Engineering strategies toward efficient CO_2 electrochemical reduction to C1 products

by

Pengfei Sui

A thesis submitted in partial fulfillment of the requirements for the degree of

Doctor of Philosophy

in

Materials Engineering

Department of Chemical and Materials Engineering
University of Alberta

Abstract

Electrochemical CO_2 reduction reaction (CO_2RR) is regarded as an attractive technology to lower the CO_2 emission level and achieve sustainable carbon neutrality by converting CO_2 to valuable chemicals. CO and HCOOH/formate are the promising products in terms of their commercial viability based on technoeconomic analysis. However, the present electrocatalysts still suffer from the high overpotential and sluggish reaction kinetics. The low solubility of CO_2 in aqueous media and broad distributions of the conversion products also account for the unsatisfactory CO_2RR performance, which need to be overcome to meet the requirement for practical implementations of CO_2RR technologies. Given that the reaction pathways for CO_2RR to C1 products can be generalized to three key points: CO_2 adsorption ability, reaction intermediates, and proton-coupled electron transfer (PCET) steps. In this thesis, various engineering strategies were investigated to have focused on these points by designing highly active, selective, and stable p-block metal-based electrocatalysts to achieve desirable CO_2RR performance.

Firstly, to effectively optimize the binding strength of the reaction intermediates, a bimetallic engineering strategy is used to improve the selectivity toward the target product. The designed electrocatalyst InOx@CuO shows high Faradaic efficiency (FE) and ultralow onset potential for CO formation. The introduced In species on Cu successfully tune the binding strength of *COOH intermediate and effectively suppress the competing hydrogen evolution reaction as revealed by computational results. Given the importance of PCET steps during CO_2RR, an interface engineering strategy is applied to synthesize interface-rich Bi_2S_3-Bi_2O_3 heterostructure. The desirable current density and selectivity towards formate with a wide

potential range of $FE_{formate}$ over 90 % are achieved in a flow cell system, which is attributed to the strengthened charge transfer ability induced by the electronic interaction between the Bi_2S_3 and Bi_2O_3 at the interface.

Considering the limited solubility of gaseous CO_2 in aqueous media, the electrocatalyst $Bi_2O_2CO_3$ nanoflowers with self-reinforced CO_2 adsorption properties are designed and demonstrate efficient formate electrosynthesis. The *in situ* measurements and theoretical calculation results reveal the self-reinforced CO_2 adsorption properties and rapid CO_2 adsorption-desorption kinetics on the catalyst surface, significantly facilitating the CO_2RR process. In addition, phase engineering has shown great potential for improving CO_2RR performance since the unconventional phase of nanomaterials usually delivers different physicochemical properties and functionalities. To this end, the stable α-Bi_2O_3 and metastable β-Bi_2O_3 phases are prepared for CO_2RR. Compared to α-Bi_2O_3, β-Bi_2O_3 possesses better abilities for CO_2 adsorption and charge transfer that consequently lead to faster reaction kinetics. Further computational results point out that the exothermic process of the key intermediate *OCHO formation on β-Bi_2O_3 benefits high formate selectivity.

Finally, the defective ultrathin Bi_5O_7I nanotubes are synthesized for the efficient CO_2RR to formate. The abundant defects offer massive uncoordinated active sites for CO_2RR to proceed and increase the CO_2 adsorption capability. Benefiting from the prominent capillary and confinement effects, the unique nanotube channel structure significantly enhances the charge transfer ability and the mass transport in aqueous media as well as stabilizes the reaction intermediates. All of these merits collectively contribute to the improved electrocatalytic performance and highlight the great potential of defect engineering for CO_2RR performance improvement.

Preface

This thesis is an original work by Pengfei Sui (P.F. Sui) under the supervision of Prof. Jing-Li Luo (J.L. Luo).

Chapter 1 is the introduction that contains the background knowledge and principles of electrochemical CO_2 reduction.

Chapter 2 covers the literature survey of different engineering strategies and catalysts for electrochemical reduction of CO_2 to C1 products.

Chapter 3 presents the employed methodologies and characterizations.

Chapter 4 has been published as **<u>P.F. Sui</u>**, S. Liu, C. Xu, J. Xiao, N. Duan, R. Feng, J.L. Luo, Directionally Maximizing CO Selectivity to Near-Unity over Cupric Oxide with Indium Species for Electrochemical CO_2 Reduction. ***Chemical Engineering Journal***, 2022, 427, 131654. Dr. C. Xu conducted the DFT calculations, Dr. J. Xiao and Dr. N. Duan helped with characterizations, Dr. R. Feng helped with X-ray absorption spectroscopy measurement, Dr. S. Liu provided comments and suggestions for manuscript writing, and Dr. J.L. Luo provided valuable discussion, suggestions and feedback for manuscript writing and revision.

Chapter 5 has been published as **<u>P.F. Sui</u>**, C. Xu, M.N. Zhu, S. Liu, Q. Liu, J.L. Luo, Interface-induced electrocatalytic enhancement of CO_2-to-formate conversion on heterostructured bismuth-based catalysts. ***Small***, 2022, 18, 2105682. Dr. C. Xu and M.N. Zhu provided suggestions on experimental design, Dr. S. Liu provided constructive comments on manuscript preparation, and Dr. Q. Liu and Dr. J.L. Luo provided valuable discussion, suggestions and feedback for manuscript writing and revision.

Chapter 6 has been published as <u>**P.F. Sui**</u>, M.R. Gao, S. Liu, C. Xu, M.N. Zhu, J.L. Luo, Carbon Dioxide Valorization via Formate Electrosynthesis in a Wide Potential Window, *Advanced Functional Materials*, 2022, 2203794. M.R. Gao conducted DFT calculations, Dr. S. Liu provided constructive suggestion on result analysis, Dr. C. Xu and M.N. Zhu helped with the *in situ* DRIFTS measurements, and Dr. J.L. Luo provided valuable discussion, suggestions and feedback for manuscript writing and revision.

Chapter 7 has been submitted to Journal as <u>**P.F. Sui**</u>, M.R Gao, C. Xu, M.N. Zhu, S. Liu, J.L. Luo, Unlocking Phase-Selective CO_2 Electroreduction over (α, β)-Bi_2O_3. M.R. Gao conducted DFT calculations, Dr. C. Xu and M.N. Zhu provided suggestions and comments on manuscript preparation, Dr. S. Liu provided constructive suggestion on result analysis, and Dr. J.L. Luo provided valuable discussion, suggestions and feedback for manuscript writing and revision.

Chapter 8 has been published as <u>**P.F. Sui**</u>, M.R. Gao, M.N. Zhu, C. Xu, Y.C. Wang, S. Liu, J.L. Luo, Unlocking Nanotubular Bismuth Oxyiodide toward Carbon-Neutral Electrosynthesis. *EES Catalysis*, 2023. M.R. Gao conducted DFT calculations, M.N. Zhu, Dr. C. Xu and Y.C. Wang provided comments on the result analysis, Dr. S. Liu provided constructive comments on manuscript preparation, and Dr. J.L. Luo provided valuable discussion, suggestions and feedback for manuscript writing and revision.

Chapter 9 includes the summary of thesis and briefly presents some future prospects.

Acknowledgements

Table of Contents

List of Tables

List of Figures

List of Symbols

E^0 — Standard potential

F — Faraday's constant

I — Total current

j — Current density

j_{CO} — Partial current density of CO

$j_{Formate}$ — Partial current density of formate

η — Overpotential

E_{eq} — Equilibrium potential

C_{dl} — Double-layer capacitance

R_s — Ohmic resistance

R_{ct} — Charge-transfer resistance

ΔG — Gibbs free energy

E_F — Fermi energy

R_f — Roughness factors

ΔE_{COOH} — Binding energy of *COOH

ΔE_{CO} — Binding energy of *CO

ΔE_H — Binding energy of *H

List of Abbreviations

CCUS	Carbon capture, utilization and storage
CO_2RR	Electrochemical reduction of CO_2
HER	Hydrogen evolution reaction
OER	Oxygen evolution reaction
ORR	Oxygen reduction reaction
SHE	Standard hydrogen electrode
FE	Faradaic efficiency
NP	Nanoparticles
NS	Nanosheets
NF	Nanoflower
NT	Nanotubes
NB	Nanobelts
NRR	Nitrogen reduction reaction
MEA	Membrane electrode assembly
RHE	Reversible hydrogen electrode
DFT	Density functional theory
SCE	Saturated calomel electrode
XAS	X-ray absorption spectroscopy
XRD	X-ray diffraction
SEM	Scanning electron microscopy
EDS	Energy-dispersive spectroscopy

TEM	Transmission electron microscopy
XPS	X-ray photoelectron spectroscopy
UPS	Ultraviolet photoelectron spectroscopy
DRIFTS	Diffuse reflectance infrared Fourier transform spectroscopy
FTIR	Fourier transform infrared spectroscopy
TGA	Thermalgravimetric analysis
ICP-OES	Inductively coupled plasma - optical emission spectrometry
LSV	Linear sweep voltammetry
CV	Cyclic voltammetry
GC	Gas chromatography
IC	Ion chromatography
ECSA	Electrochemically active surface area
EE	Energy efficiency
EIS	Electrochemical impedance spectroscopy
PDOS	Partial densities of states
CHE	Computational hydrogen electrode

Chapter 1. Introduction

1.1 CO$_2$ emissions

Global energy consumption has soared due to the development of the economy and the increasing population [1, 2]. To date, the main energy resources being consumed are still fossil fuels such as oil, coal and natural gas, which could lead to the rapid growth of CO$_2$ emission level. The high demand for energy drives the CO$_2$ emissions up by 4.8 % in 2021 to a high point of 33.0 Gt CO$_2$ [3]. As one of the major greenhouse gases, the continuous accumulation of CO$_2$ inevitably accelerates the process of global warming, leading to serious problems in environment and climate.
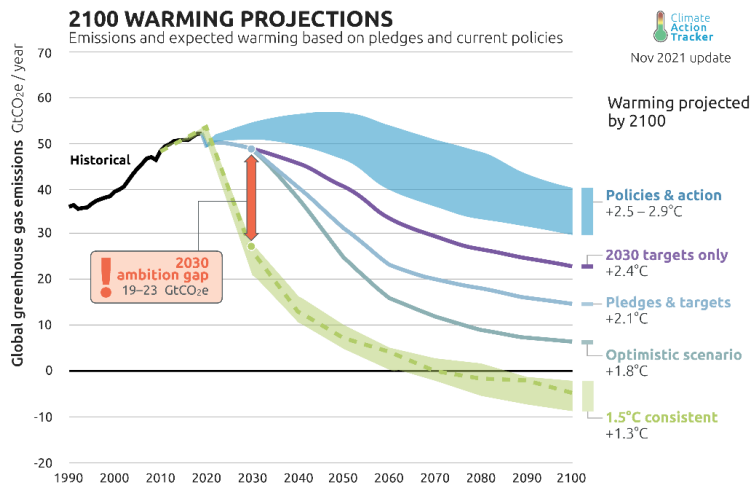
Figure 1.1 Global greenhouse gas emissions and expected warming based on pledges and current policies [3].

As shown in Figure 1.1, the CO$_2$ equivalent greenhouse gas emission will go above 55 gigatons per year under current policies and action, raising the global temperature by 2.5 to 2.9 °C. With the goal of net zero emissions target, the temperature will increase 1.8 °C instead. However, this increment is still above the critical point of 1.5 °C, which may cause disasters

and affect the existence of lives. In other words, we not only need to cut down the CO_2 emissions but also to remove the existing CO_2 from the atmosphere to achieve the aim of net zero emissions.

1.2 CO_2 utilization

Carbon capture, utilization and storage (CCUS) are a series of technologies that play an important role in meeting global energy and climate goals [4]. As shown in Figure 1.2, CO_2 is usually captured from fuel gas (pre combustion capture) or flue gas (post combustion and oxy-combustion capture) and then is compressed into liquid or supercritical state to be transported to the storage site [5]. Finally, it will be injected into geological sites or ocean for storage. This technique can mitigate CO_2 emissions and has been investigated over the past decade. However, the selection of storage sites must meet the requirements in consideration of the geological structure and safety of the ecosystem. The cost of CO_2 capture, separation, and transportation to storage site is also another critical factor to consider.
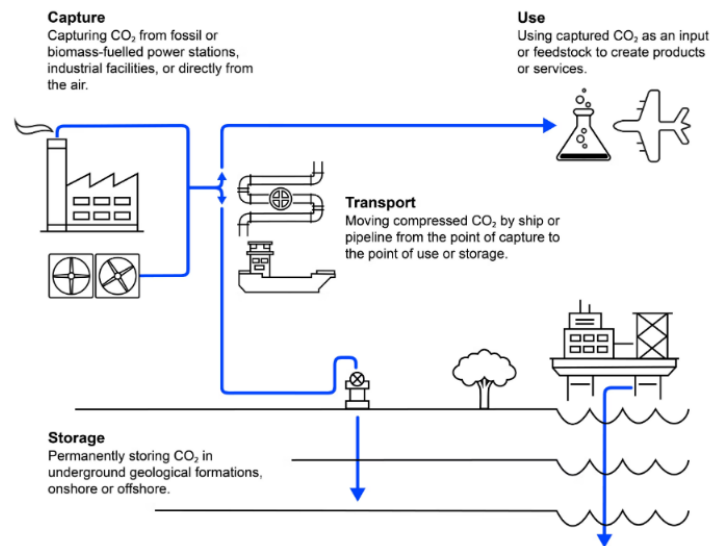
Figure 1.2 Schematic diagram of CCUS [5].

The utilization of CO_2 is considered as an effective way to mitigate the greenhouse effect and lower the CO_2 emissions. CO_2 utilization can be divided into two parts: non-conversion of CO_2 and CO_2 conversion [5], as shown in Figure 1.3. For non-conversion utilization, CO_2 alone can be used directly as fluid or solvent in different fields, e.g., enhanced oil recovery is one of typical usage of CO_2 to extract more reservoir oil, which can increase by 10% to 20% of the oil production compared with using primary and secondary recovery [6]. Another way of CO_2 utilization is to convert CO_2 to chemicals and fuels through carboxylation or reduction avenues as well as producing building materials, such as cement and concrete.
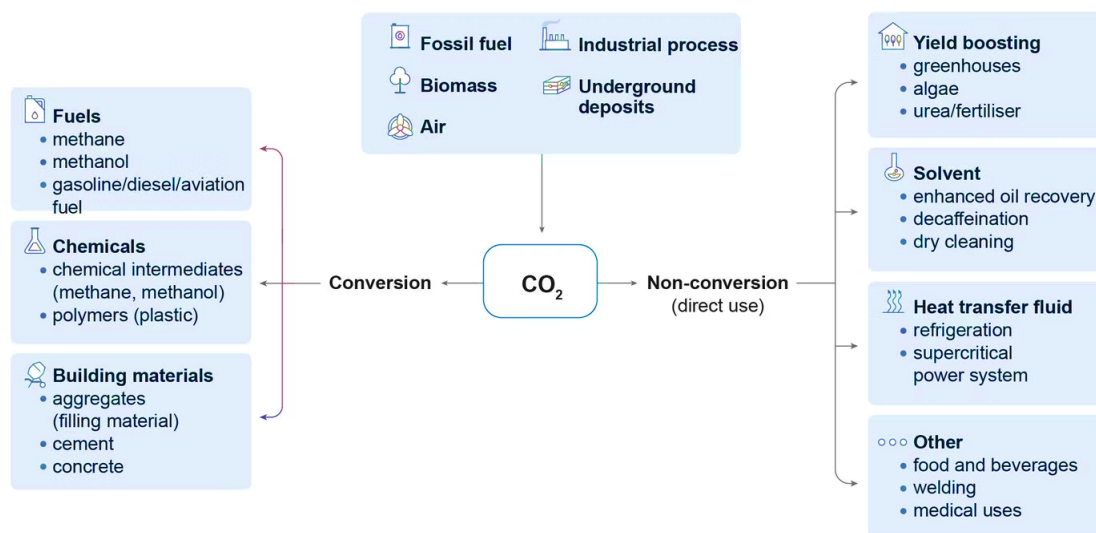
Figure 1.3 The utilization of CO_2 through conversion and non-conversion routines [5].

Typical CO_2 reduction technologies include thermochemical, biochemical, photochemical, and electrochemical catalysis [7]. Among them, CO_2 reduction using electrochemical approach has attracted much interest due to several advantages [8-10]: The reaction process is controllable by applying different potentials in aqueous solution under mild conditions. When powered by the electricity generated from renewable energy sources (e.g., wind, solar or tidal energy), it can eventually achieve sustainable carbon neutrality by converting CO_2RR

to valuable chemicals and fuels. These merits endow the electrochemical reduction of CO_2 with a great potential for simultaneously recycling carbon for utilization and renewable electricity storage.

1.3 Fundamentals of electrochemical reduction of CO_2

1.3.1 Thermodynamics of CO_2 electrochemical reduction

CO_2 electrochemical reduction (CO_2RR) involves one electron transfer to form CO_2^- with the thermodynamic potential of -1.90 V versus standard hydrogen electrode (SHE), causing the high energetic and unfavorable reduction reaction [11]. According to the relationship of Gibbs free energy and the electron transfer, a CO_2 reduction reaction will happen with a more positive E^0 according to the following expression:

$$\Delta G^0 = -nFE^0 \qquad\qquad\qquad (Eq.\ 1.1)$$

where ΔG^0 is the standard change in Gibbs free energy, n is the number of mole of electrons involved, F (96485 $C \cdot mol^{-1}$) is the Faraday constant, E^0 is the standard potential for a specific reaction.

CO_2RR involves two-, four-, six- and eight-electron transfer in gaseous, aqueous and non-aqueous phases at room temperature. The main reduced products are carbon monoxide (CO), formic acid (HCOOH) or formate ($HCOO^-$), methanol (CH_3OH), methane (CH_4), ethylene (C_2H_4), ethanol (C_2H_5OH), etc. The oxygen evolution reaction (OER) on the anode usually accompanies CO_2RR to complement the overall reaction. Table 1.1 summarizes some selected standard potentials of CO_2RR to different products and hydrogen evolution reaction (HER) under standard conditions. It can be found that the similar reduction potentials of different products make it difficult to control the target product selectivity. In addition, the HER usually competes with CO_2RR in aqueous media, further deteriorating the selectivity

4

of CO₂RR. Thus, it is challenging to achieve good selectivity toward target product with a high yield.

Table 1.1 Selected standard reduction potentials for CO_2 to various C1 and C2 products in aqueous solutions at standard conditions (1.0 atm and 25 °C) [12].

Products	Cathodic half-cell reactions	E^0 vs. SHE (V)
$HCOOH_{(l)}$	$CO_{2(g)} + 2H^+ + 2e^- \rightarrow HCOOH_{(l)}$	-0.250
$CO_{(g)}$	$CO_{2(g)} + 2H^+ + 2e^- \rightarrow CO_{(g)} + H_2O_{(l)}$	-0.106
$CH_2O_{(l)}$	$CO_{2(g)} + 4H^+ + 4e^- \rightarrow CH_2O_{(l)} + H_2O_{(l)}$	-0.070
$CH_3OH_{(l)}$	$CO_{2(g)} + 6H^+ + 6e^- \rightarrow CH_3OH_{(l)} + H_2O_{(l)}$	0.016
$CH_{4(g)}$	$CO_{2(g)} + 8H^+ + 8e^- \rightarrow CH_{4(g)} + 2H_2O_{(l)}$	0.169
$C_2H_{4(g)}$	$2CO_{2(g)} + 12H^+ + 12e^- \rightarrow C_2H_{4(g)} + 4H_2O_{(l)}$	0.064
$C_2H_5OH_{(l)}$	$2CO_{2(g)} + 12H^+ + 12e^- \rightarrow C_2H_5OH_{(l)} + 3H_2O_{(l)}$	0.084
$H_{2(g)}$	$2H^+ + 2e^- \rightarrow H_{2(g)}$	0

Among different reduced products, CO and HCOOH/formate demonstrate great potential when considering the commercial viability [13, 14]. Although higher valuable products such as C_2H_4, C_2H_5OH are more desirable, recent technoeconomic analysis concludes that the most economically viable products are C1 products with two-electron transfer steps, that is CO or HCOOH. Taking electrical energy input into consideration, C1 products are the most profitable in terms of the market prices associated with the added values per kWh electrical energy input (Figure 1.4). Therefore, the selective reduced C1 products are the best targets for CO₂RR so far and the products can be further upgraded chemically or electrochemically.
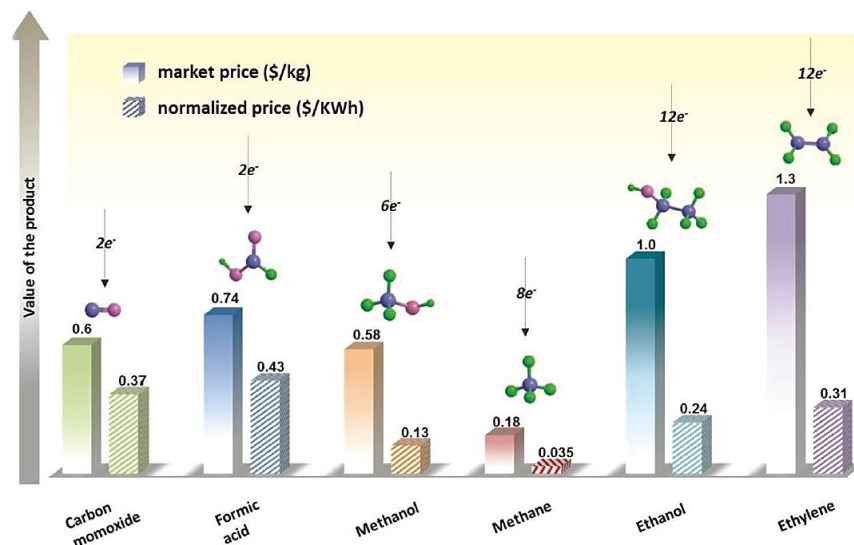
Figure 1.4 The comparison of different reduction products on market price and normalized price estimated by ideal full cells. Reprinted with permission from Reference [13]. Copyright (2019) Wiley-VCH.

1.3.2 Reaction mechanism of CO$_2$RR to C1 products

The reaction pathways for CO$_2$RR to CO and HCOOH both involve four key steps in aqueous media as shown in Figure 1.5 [15]. For CO generation, it follows the steps as below:

$$CO_2 + * + e^- \rightarrow *CO_2^- \qquad\qquad \text{(Eq. 1.2)}$$

$$*CO_2^- + H^+ \rightarrow *COOH \qquad\qquad \text{(Eq. 1.3)}$$

$$*COOH + H^+ + e^- \rightarrow *CO + H_2O \qquad\qquad \text{(Eq. 1.4)}$$

$$*CO \rightarrow CO + * \qquad\qquad \text{(Eq. 1.5)}$$
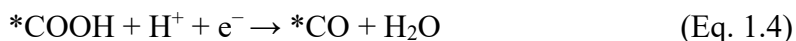
where * refers to the adsorption site on the catalyst surface. While for HCOOH formation, similar reaction steps occur except for the intermediate *OCHO formation that is summarized as below:

$$CO_2 + * + e^- \rightarrow *CO_2^- \qquad\qquad \text{(Eq. 1.6)}$$

$$*CO_2^- + H^+ \rightarrow *OCHO \qquad\qquad \text{(Eq. 1.7)}$$

6

$$*OCHO + H^+ + e^- \rightarrow *HCOOH \qquad \text{(Eq. 1.8)}$$

$$*HCOOH \rightarrow HCOOH + * \qquad \text{(Eq. 1.9)}$$

In general, the CO_2 molecule firstly adsorbs onto the catalyst surface and gains an electron to activate the initial reaction step (Eq. 1.2), which usually requires high energy input (i.e., -1.9 V vs. SHE). Then, the reaction intermediate *COOH or *OHCO is formed with the combination of one proton, followed by another proton-coupled electron transfer (PCET) step. Finally, the adsorbed *CO or *HCOOH intermediate desorbs from the catalyst surface to produce CO or HCOOH. Since the reaction usually takes place in aqueous media, HCOOH exists in the form of formate.
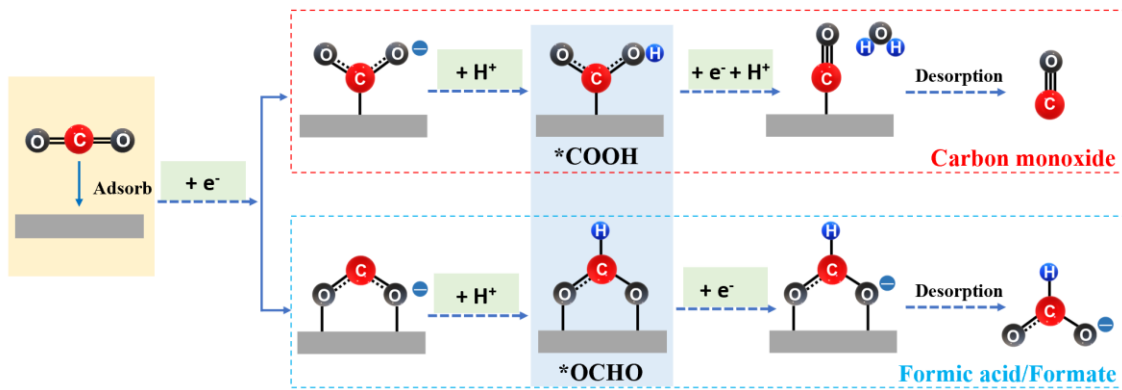
Figure 1.5 Schematic diagram of the reaction pathway for CO_2RR to CO and HCOOH formation.

The reaction pathways for C1 products can be generalized into three key points: CO_2 adsorption, reaction intermediates, and PCET steps. In aqueous media, the low solubility of CO_2 (~ 33 mM at 298 K and 1 atm) limits the sufficient reactants to participate the reaction, which significantly restrains current density and leads to the inferior formation rate. Compared with the different reaction intermediates, the appropriate binding energies of the

key intermediates (i.e., *COOH and *OCHO) can improve the selectivity towards the target product. Moreover, the proton and electron depletions of PCET steps significantly limit the reaction kinetics that requires good charge transfer ability to promote the fast reaction kinetics. Therefore, improving CO_2 adsorption ability, tuning the binding energies of these intermediates, and enhancing the charge transfer ability are the three crucial factors for designing selective and efficient catalysts for CO_2RR to C1 products.

1.3.3 Evaluation parameters for CO_2RR to C1 products

A highly active, selective and efficient CO_2RR system is very important to achieve desirable performance. To evaluate the performance of the CO_2RR system, several key parameters are summarized as follows:

1. *Faradaic efficiency*

The Faradaic efficiency (FE) can be used to describe the selectivity of the target product over CO_2RR. It is the percentage of charges used to produce the desired product over the total charges measured. The FE of gas product can be calculated by the following equation:

$$\mathrm{FE}_{\mathrm{Product}} = \frac{\alpha n F}{Q}$$

(Eq. 1.10)

where α is the number of transferred electrons, n is the number of moles of the desired product, F represents Faraday's constant (96,485 C/mol), and Q referrers to the total charge passed. Specifically, the FE can be calculated by running a set of electrolysis experiments at a fixed applied potential. It can be expressed as:

$$\text{FE}_{Product} = \frac{F n_{product} v_{product} f_v p_0}{R T_0 I_{total}} \times 100\% \qquad \text{(Eq. 1.11)}$$

where $n_{product}$ is the number of moles of electrons participating in the reaction to from certain product; $v_{product}$ is the volume concentration of certain product in the exhaust gas from the electrochemical cell; f_v is the flow rate of the exhaust gas measured at the exit of the cell at room temperature (T_0) and ambient pressure (p_0); I_{total} is the total current of the steady cell.

2. Current density

Current density (j) is obtained by dividing the total current (I_{total}) by the surface area of the working electrode and it reflects the reaction rate of CO_2RR. There are several factors influencing the j, such as catalytic surface, applied potential, electrolyte concentration and the diffusion rates of specified species. Partial current density of desired product ($j_{product}$) often reflects the catalytic activity and is used to evaluate the certain product generation rate directly. It can be expressed as

$$j_{product} = j \times \text{FE}_{product} \qquad \text{(Eq. 1.12)}$$

High j is preferred at the applied potential for the desired product of CO_2RR.

3. Onset overpotential

Onset overpotential (η) is defined as the difference between the equilibrium potential and the onset potential. Good electrocatalyst can reduce CO_2 to the target product near the standard reduction potential. It can be calculated by the following equation:

$$\eta = E - E_{eq} \qquad \text{(Eq. 1.13)}$$

where E is the minimum potential that the reaction occurs, or onset potential and E_{eq} is the equilibrium potential during CO_2RR. High η in CO_2RR is the leading kinetic barrier. Excellent catalysts are able to reduce CO_2 to desired products with a relatively low onset overpotential.

4. *Energy efficiency*

Energy efficiency (EE) describes the ratio of overall energy consumption to the desired product. Energetic efficiency can be expressed as:

$$EE = \frac{E_{cell} \times FE}{E_{cell} + \eta_{cell}} \times 100\% \qquad \text{(Eq. 1.14)}$$

where E_{cell} (V) is the measured cell potential at the current density equal to zero; FE is the Faradaic efficiency of the target product at the desired current density; η_{cell} (V) is the cell overpotential; $E_{cell} + \eta_{cell}$ is the measured cell potential at desired current density.

5. *Tafel slope*

The Tafel plot is a diagram of overpotential versus the logarithm of the partial current density. It derives from the Bulter-Volmer equation which describes how the electrical current on an electrode depends on the electrode potential. In CO_2RR, the reduction process is far away from the equilibrium state, so Tafel slope can be used to evaluate the performance of electrocatalysts. As for the desired product CO or HCOOH, Tafel slope demonstrates the reaction pathway and rate-determining step (RDS) during reactions. A slope of 118 mV dec^{-1} indicates that the one-electron reduction of CO_2 to form $*CO_2^-$ is the RDS, while the

chemical step involving protonation supplied by HCO_3^- will be the RDS with the Tafel slope of 59 mV dec^{-1}.

6. *Stability and cost*

Long-term stability of the catalyst is one of the main challenges in CO_2 reduction process. Good stability is the promotion of commercialization in industrial applications. Moreover, low process cost of catalysts is another critical requirement for industrialization application. It is desirable to synthesize highly stable with low process cost of catalysts for CO_2RR.

1.4 References

[1]   O. S. Bushuyev, P. De Luna, C. T. Dinh, L. Tao, G. Saur, J. van de Lagemaat, S. O. Kelley, E. H. Sargent, *Joule* **2018**, *2*, 825-832.

[2]   P. De Luna, C. Hahn, D. Higgins, S. A. Jaffer, T. F. Jaramillo, E. H. Sargent, *Science* **2019**, *364*.

[3]   https://climateactiontracker.org/global/temperatures/

[4]   CARBON DIOXIDE CAPTURE AND STORAGE, Cambridge University Press, United States of America, New York, **2005**.

[5]   https://www.iea.org/reports/about-ccus

[6]   E. Alper, O. Yuksel Orhan, *Petroleum* **2017**, *3*, 109-126.

[7]   D. T. Whipple, P. J. A. Kenis, *The Journal of Physical Chemistry Letters* **2010**, *1*, 3451-3458.

[8]   R. S. Weber, *ACS Catal.* **2018**, *9*, 946-950.

[9]   S. Xu, E. A. Carter, *Chem Rev* **2018**.

[10]   L. Zhang, Z. J. Zhao, T. Wang, J. Gong, *Chem. Soc. Rev.* **2018**, *47*, 5423-5443.

[11]   Y. Y. Birdja, E. Pérez-Gallent, M. C. Figueiredo, A. J. Göttle, F. Calle-Vallejo, M. T. M. Koper, *Nat. Energy.* **2019**, *4*, 732-745.

[12]   F. Li, D. R. MacFarlane, J. Zhang, *Nanoscale* **2018**, *10*, 6235-6260.

[13]   N. Han, P. Ding, L. He, Y. Li, Y. Li, *Adv. Energy Mater.* **2019**, 1902338.

[14]   S. Jin, Z. Hao, K. Zhang, Z. Yan, J. Chen, *Angew.Chem. Int. Ed.* **2021**, *60*, 20627-20648.

[15]   G. Wang, J. Chen, Y. Ding, P. Cai, L. Yi, Y. Li, C. Tu, Y. Hou, Z. Wen, L. Dai, *Chem. Soc. Rev.* **2021**, *50*, 4993-5061.

Chapter 2. Literature review of engineering strategies and catalysts for CO₂RR to C1 products

2.1 Recent advances in the engineering strategies for CO₂RR

As mentioned in *Section* 1.3.2, the CO_2RR to C1 reaction processes mainly involve three key points: CO_2 adsorption, charge transfer and intermediates binding strength. To date, various engineering strategies have been developed aiming to improve the CO_2 adsorption and charge transfer abilities and optimize the binding strength of the reaction intermediates to boost the electrocatalytic performance. Figure 2.1 shows the four common types of engineering strategies for tuning specific properties, i.e., bimetallic engineering, interface engineering, defect engineering and phase engineering. These strategies are widely used electrochemical reactions, such as HER, oxygen evolution reaction (OER), and nitrogen reduction reaction (NRR), etc., which also demonstrate their effectiveness for improving the CO_2RR performance.
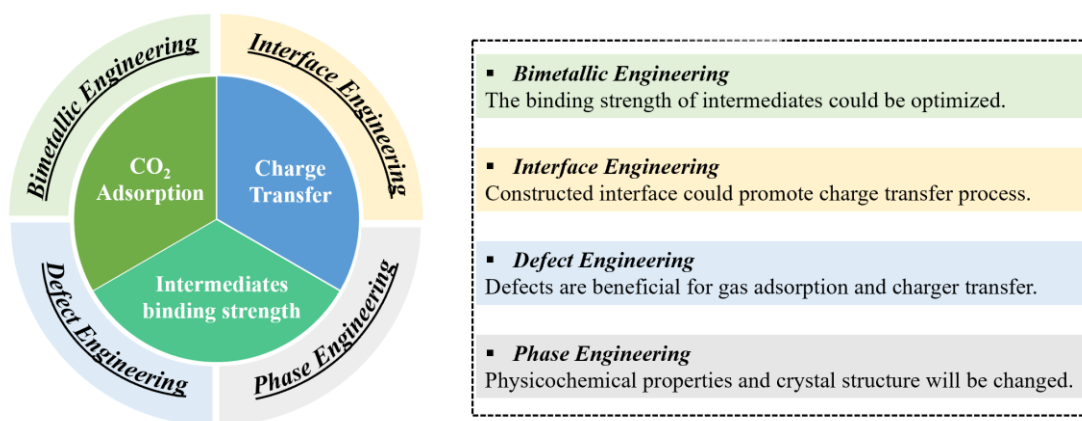
Figure 2.1 Schematic illustration of different engineering strategies in CO_2RR.

2.1.1 Bimetallic engineering

When two individual metals are mixed through alloying process, the properties of each metal changes due to the synergy effect, which can tune the binding strength of reaction intermediates on the catalyst surface to facilitate the reaction process. It is found that the atomic orbitals hybridization of two metals shifts the d-band center to the Fermi level, leading to the favorable adsorption ability of the reaction intermediates. Kim et al. [1] reported the uniform Au-Cu bimetallic nanoparticles with different compositions for CO_2RR to CO (Figure 2.1a). Their results show that Au_3Cu exhibits high activity and selectivity for CO formation with a mass activity of 230 A g^{-1} at −0.73 V, which is mainly due to the optimized binding strength of the reaction intermediate and the electronic structure (Figures 2.1b and c). Similar results were also observed on Cu/SnO_2 core-shell structure that the different ratio of Cu/Sn can effectively modulate the binding strength of *COOH and *OCHO intermediates, resulting in the different selectivity for CO_2RR [2].

In another case, Sun et al. [3] prepared the AuFe core-shell alloy nanoparticles to improve the efficiency of CO_2-to-CO conversion. The alloyed AuFe nanoparticles demonstrate an ultrahigh selectivity and mass activity for CO formation, i.e., 99% at −0.5 V vs. RHE and 150 mA mg^{-1} at −0.9 V vs. RHE. During the electrolysis, the surface defect of Fe leaching leads to the formation of the alloyed subsurface that ensures the increased selectivity and activity at low potential for CO generation (Figure 2.1d). Overall, these results firmly demonstrate that the bimetallic engineering is an attractive strategy to achieve highly selective and active CO_2RR through the binding strength optimization of the reaction intermediates.
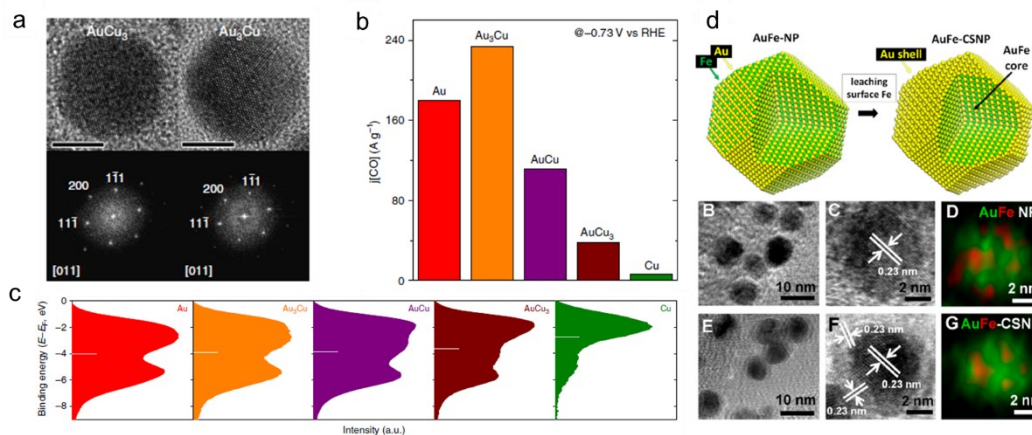
Figure 2.2 (a) High-resolution transmission electron microscopy image (HRTEM) of $AuCu_3$ and Au_3Cu. (b) Mass activity of CO at -0.73 V vs. reversible hydrogen electrode on different nanoparticles. (c) The valence band spectra of Au-Cu bimetallic nanoparticles. Reprinted with permission from Reference [1]. Copyright (2014) Springer Nature. (d) Illustration of the structural evolution of AuFe alloy nanoparticles [3]. Copyright (2017) American Chemical Society.

2.1.2 Interface engineering

Interface engineering is an effective approach to promoting electron transfer by constructing abundant interfaces within the catalysts. The introduced interfaces between the two materials with different work functions and Fermi levels would benefit the electronic interaction at the interface and assist the electron redistribution. This would then optimize the binding energy and promote the fast electron transfer through interfaces, thus ensuring the high electrocatalytic activity and selectivity. Wang et al. [4] synthesized the cube-like Zn_2SnO_4/SnO_2 heterostructure for CO_2RR by a co-precipitation method and the HRTEM image clearly shows the interface between Zn_2SnO_4 and SnO_2 (Figure 2.3a). Through experimental investigation and theoretical calculation, it is concluded that the

heterostructures with band alignment can significantly promote the charge transfer on the catalyst surface and stabilize the reaction intermediate *OCHO, thereby achieving the satisfactory CO_2RR performance.
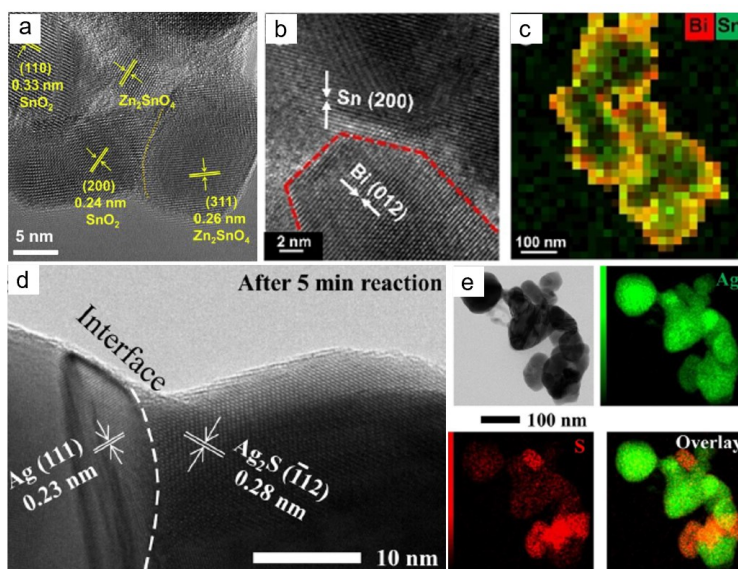
Figure 2.3 (a) HRTEM image of Zn_2SnO_4/SnO_2. Reprinted with permission from Reference [4]. Copyright (2019) Elsevier. (b) and (c) HRTEM image and the corresponding elemental mappings of BiSn bimetallic aerogel. Reprinted with permission from Reference [5]. Copyright (2021) Wiley-VCH. (d) and (e) HRTEM image and the corresponding elemental mappings of Ag_2S/Ag. Reprinted with permission from Reference [6]. Copyright (2021) Elsevier.

Similarly, the BiSn aerogel with a 3D porous structure was reported to boost the highly selective CO_2RR to HCOOH formation [5]. The abundant interfaces with interconnected channels of aerogel not only possess substantial number of active sites, but also improve the charge transfer ability that is beneficial to reaction (Figures 2.3b and c). The BiSn catalyst shows a high FE_{HCOOH} of 93.9% and achieves a FE_{HCOOH} of about 90% for 10 h in a flow cell

system, highlighting interface engineering as an approach to enhancing the CO_2RR performance. In addition, Ye et al. [6] proposed an *in situ* reconstruction method to obtain a heterogeneous Ag_2S/Ag interface structure as shown in Figures 2.3d and e. This catalyst delivers a high current density of about 420 mA cm^{-2} at -0.7 V vs. RHE and exhibits CO FE of 99% for 50 h with negligible degradation. Density functional theory (DFT) calculation results reveal that the interface active sites between Ag_2S and Ag structure favorably stabilize the reaction intermediates *COOH and lower the energy barrier towards CO formation, thus leading to the excellent electrocatalytic performance. Briefly, interface engineering can modulate the electronic structure between different components and improve the charge transfer ability on the catalyst surface, as well as optimize the binding strength of the reaction intermediates, which collectively contribute to the enhanced CO_2RR performance.

2.1.3 Defect engineering

Defects commonly exist in catalysts due to the imperfect crystal structure during practical synthesis, which can be categorized based on their dimensions, including point defect, dislocation, grain boundaries, and bulk or volume defects. The catalytic activity strongly relies on the introduced defects rather than the native ones. Recently, defect engineering has turned to hold great potential as an efficient method for tuning the electronic structure and surface morphology, enabling unique gas adsorption behaviors, and selectively enhancing the stability of the reaction intermediates. Much effort has been devoted to unraveling the defect driven CO_2RR performance by combining experimental and theoretical calculations. Zhang et al. [7] designed Cu nanosheets with nanosized defects (n-CuNS) for CO_2RR toward ethylene production (Figure 2.4a). Compared to perfect CuNS and NP, the defective n-CuNS achieves the ethylene FE of 83.2% at -1.2 V vs. RHE, outperforming most of the state-of-

the-art electrocatalysts. These abundant nanosized defects can enrich the reaction intermediates and hydroxyl ion on the catalyst surface, and can also lead to the high local pH that effectively supresses the competing HER.
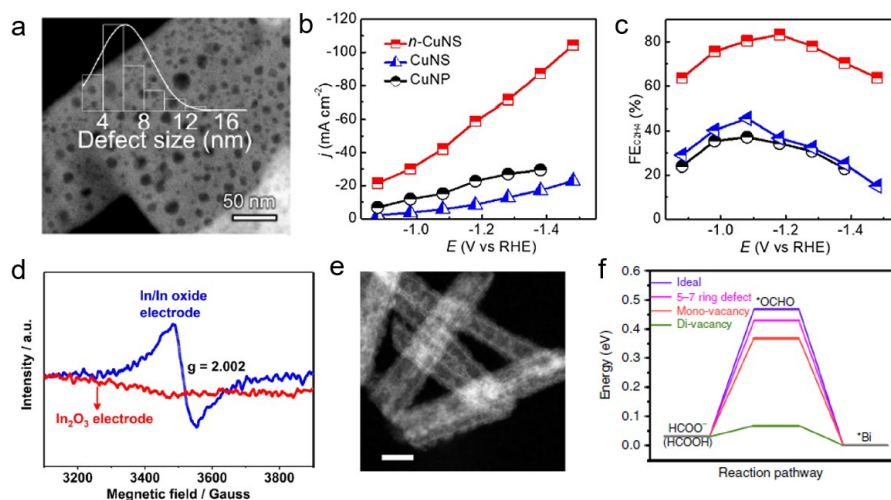
Figure 2.4 (a) High-angle annular dark-field scanning transmission electron microscopy (HAADF-STEM) of n-Cu NS. (b) Total current density and (c) FE of ethylene on different electrocatalysts. Reprinted with permission from Reference [7]. Copyright (2020) American Chemical Society. (d) EPR spectra of the fresh In_2O_3 electrode and the In/In oxide electrode. Reprinted with permission from Reference [8]. Copyright (2020) American Chemical Society. (e) HAADF-STEM image of Bi_2O_3 nanotubes. (f) Gibbs free energy for formate production on ideal and defective Bi surfaces. Reprinted with permission from Reference [9]. Copyright (2019) Springer Nature.

The enhanced CO_2RR performance was also achieved on defective In/In_2O_3 with near 100% selectivity toward C1 products [8]. The rich oxygen vacancies provide massive uncoordinated active sites for CO_2RR to proceed (Figure 2.4d) and stabilize the *OCHO intermediate to facilitate CO_2-to-formate conversion. Furthermore, *in situ* reconstruction of

nanostructure under reduction conditions can also introduce structural disorders or defects. Gong et al. [9] used the Bi_2O_3 double-walled nanotubes as a template to obtain the defective Bi nanotubes through cathodic reduction (Figure 2.4e). The converted defective Bi nanotubes demonstrate the excellent performance for CO_2RR to formate with high activity, selectivity and stability. The DFT calculation results show that the optimized defects can significantly lower the energy barrier for the formation of *OCHO to 0.07 eV, indicating that the existing defects can greatly stabilize the reaction intermediate. Similar results were also derived on the defective Bi nanosheets from the *in situ* structural reconstruction of $Bi(OH)_3$ [10]. The coordinately unsaturated sites favor the stabilization of the reaction intermediate *OCHO that facilitates the reaction kinetics for formate formation. As stated above, the defect engineering strategy is proven to be an appealing method to enhance the electrocatalytic performance owning to the exposed massive active sites and better stabilization of the reaction intermediate for the CO_2RR process.

2.1.4 Phase engineering

Besides abovementioned engineering strategies, phase engineering through regulating physiochemical properties and functionalities of nanomaterials has attracted great attention since many materials are found to possess more than one phase under different experimental conditions (i.e., high pressure and temperature) other than the thermodynamically stable phases that are the same as their bulk form [11, 12]. More importantly, these unconventional phases usually deliver the different physicochemical properties, e.g., physisorption ability, electronic property, and structural changes through phase transformation, endowing them with promising applications in electrocatalysis. Ma et al. [13] reported a crystal phase-dependent Ag_2Se for CO_2RR to formate formation. Compared to the orthorhombic (o-Ag_2Se),

monoclinic (m-Ag$_2$Se) shows the enhanced CO FE of 98.1% at -0.9 V vs. RHE and a good long-term stability. Theoretical calculation results suggest that the m-Ag$_2$Se can effectively stabilize the reaction intermediate and improve the adsorption capability. Meanwhile, the competing HER is well inhibited, which contributes to the high activity and selectivity for CO formation during CO$_2$RR. Moreover, the well-defined heterophase fcc-2H-fcc Au nanorods (fcc: face-centered cubic; 2H: hexagonal close-packed with stacking sequence of "AB") exhibit the superior electrocatalytic activity for CO$_2$RR toward CO formation. The fcc-2H-fcc Au nanorods show the lower free energies of *COOH on unconventional 2H phase and 2H/fcc interface than that of typical fcc surface, leading to the high FE of CO and mass activity. Similar conclusions were also reported on Ag-Cu Janus nanostructure [14], 2H-Pd heterophase [15], 4H/fcc Au@Cu core-shell structure [16], etc. All these results indicate the effectiveness of phase engineering as an attractive strategy to improve the CO$_2$RR performance.

2.2 Electrocatalysts for CO$_2$RR to C1 products

CO$_2$RR starts from using bulk polycrystalline metals as catalysts at the beginning. From the previous results, metal catalysts can be divided into three groups according to their reduction products. Group I consists of metals that mainly produce HCOOH/HCOO$^-$ during the reduction process, such as Sn [17, 18], Pb [19], Bi [20-22], In [23-26]and Cd [27, 28]. Ag [29, 30], Au [31], Pd [32] and Zn [33, 34] belong to Group II, which form CO as the major product [35, 36]. Besides the abovementioned materials, Cu is the only metal that can produce a wide range of products compared with other metals [37-39]. Besides CO and formate, Cu metal electrode can also produce hydrocarbons and oxygenates, such as methane, ethylene, methanol, and ethanol.

Great efforts have been devoted to noble metals used as the electrocatalysts for CO_2RR due to their high intrinsic activity and stable chemical properties. With the advantage of nanoengineering, noble metals such as Ag, Au and Pd have been studied extensively for CO_2RR to CO with different sizes and shapes. The selectivity and stability are greatly improved with different modification of catalysts. Liu et al. [29] designed the triangular silver nanoplates for CO_2RR that achieves the ultralow onset potential of 96 mV for CO formation and the excellent stability of 7 days with relatively high FE (96.8%). Further DFT calculation results reveal that the enhanced electrocatalytic activity and selectivity originate from the highly active facet of Ag (100) with the optimized edge-to-corner ratio. Similar nanostructure modulations on specific architectures were also studied on other shapes for CO_2RR to CO formation, such as Ag nanocubes [40], Ag nanowires [41], Ag nanoprisms [42] and Pd octahedra and icosahedra [32], etc. Although the noble metal-based catalysts exhibit excellent selectivity and catalytic activity for CO_2RR to CO formation, they are not suitable for large-scale industrial applications due to their high costs.

Other non-noble metal-based catalysts are further developed in light of their low prices. As one of the earth abundant elements, Zn shows the great potential to selectively produce CO for CO_2RR. Xiao et al. [34] reported the hexagonal Zn nanoplates with facets of (100) and (200) for efficient CO formation, and achieved a maximum FE of 94.2%. The exposed (100) facets with highly active sites at edge significantly lower the energy barrier for intermediate *COOH formation. In addition, the electro-reconstruction of ZnO was found to demonstrate good selectivity for CO_2RR to CO as revealed by Luo et al. [43] in that the ZnO-derived catalyst exhibits FE of over 90% with negligible degradation over 18 h. The experimental

results show that the large surface area and stable crystal structure make joint contribution to the enhanced catalytic performance.

$HCOOH/HCOO^-$ is another main C1 product that can be utilized in formate fuel cells as hydrogen carriers, in textile and pharmaceutical industries [27, 44]. So far, p-block metals such as Sn, In, Bi, and Pb are reported to favorably produce HCOOH and have been widely studied to achieve the improved CO_2RR performance. Sn is one of the mostly investigated metal materials due to its good activity, non-toxicity, and abundance. Liu et al. [17] reported the SnO_2 quantum wires (QWs) with rich grain boundaries for CO_2RR toward HCOOH formation. Compared to the ultrafine SnO_2 nanoparticles without exposed grain boundaries, the SnO_2 QWs deliver higher j and FE in a wide potential window. Similar results were also obtained by Chen et al. [45], which showed that the wavy SnO_2 with abundant oxygen vacancies, grain boundaries and low-coordinated active sites demonstrates high FE for formate formation with energy efficiency of 57.5% at -1.0 V vs. RHE. Other Sn-based catalysts such as Sn quantum sheets [46], fluorine-doped SnO_2 [47], and porous SnO_2 nanostructures [48-50] also showed the great performance improvement for CO_2RR to formate formation.

Besides Sn, In-based electrocatalysts for CO_2RR also attract much interest due to their intrinsic selectivity for HCOOH formation. By doping sulfur, the prepared S-doped In catalyst exhibits high FE of formate and rapid formation rate [51] due to sulfur induced water activation, which benefits the reaction of hydrogen species with CO_2 to produce formate. Huang et al. [26] explored the structure-property relationships of In_2O_3 and studied the size-dependent selectivity of CO_2RR; they found that r-15 nm nanocubes display the extraordinary selectivity and activity compared to r-150 nm nanocubes and In foil, where the

stronger intermediates adsorption ability was identified on smaller size nanocubes, which accounts for the improved CO_2RR performance. In addition to oxides, In-based nitrides [52] and sulfides [53] are also capable of selective formate formation during CO_2RR. Although In is also a good candidate material for CO_2RR, its high cost (about 10 times higher than that of Sn) may become a major obstacle for industrial implementation.

Compared to Sn and In, Bi-based catalysts are well-known for their low toxicity, environmental friendliness and relatively lower cost than those of Sn and In. To date, various studies on Bi-based material architectures, including Bi nanoparticles [54-56], Bi dendrites [57, 58], and Bi nanosheets [59-61]were widely studied for CO_2RR. Chen et al. [62] firstly reported 2D/0D composite of Bi_2O_3 nanosheets and nitrogen-doped graphene quantum dots for CO_2-to-formate conversion, which achieves near 100% selectivity at an overpotential of 700 mV with a good stability. Further theoretical calculations reveal that the increased adsorption energy for CO_2 and intermediate *OCHO contributes to the high activity and selectivity for formate formation. Moreover, metal-organic framework-derived carbon nanorods encapsulating Bi_2O_3 nanoparticles (Bi_2O_3@C) were synthesized for the efficient CO_2RR to formate [63]. With the benefit of carbon matrix, the high FE of 93% and current density of 200 mA cm^{-2} were achieved in a flow cell configuration due to the better charge transfer ability and rapid reaction kinetics. Liu et al. [22] also reported the similar results demonstrating that the Bi_2O_3 nanosheets grown on a conductive multiple channel carbon matrix show the desirable catalytic performance for CO_2RR to formate.

As mentioned before, Cu is the only metal that can produce hydrocarbons and oxygenates because of the suitable binding strength of intermediates on the Cu surface. This unique property endows Cu with tunable selectivity for CO_2RR by combining with other metals. Li

et al. [64] designed a series of catalysts with different Cu/Pd ratios and found that the bimetallic CuPd with Cu to Pd ratio of 3:7 could greatly improve the selectivity of CO, which was attributed to the electronic and geometric effects between Cu and Pd. Au and Ag have been widely incorporated with Cu to modify the activity and selectivity for CO_2RR. Liu et al. [65] investigated the electrocatalytic performance of Au-Cu bimetallic thin film and found that the d-band center shifts away from the Fermi level with the increasing Au atomic ratio, resulting in a weaker binding strength of *CO. Similar result was also reported by Choi et al. [66] using electrodeposited Ag-Cu dendrites for CO production. The optimized Ag atomic ratio can effectively improve the selectivity and mass activity for CO_2RR to CO formation. Apart from noble metals, other metals such as Sn [2, 67], Bi[68-70], Ce[71], and Zn [72, 73] are also well studied to improve the activity and selectivity of Cu-based electrocatalysts toward the target products.

2.3 Current status and remaining challenges

In the past few years, the studies on CO_2RR have advanced rapidly with the development of various novel catalysts. However, there is still a long way to go prior to the industrial utilization of different electrocatalysts in light of selectivity, stability, and cost. For practical CO_2 electrolysis, the desirable FE should be at least over 90% with substantial current densities (> 200 mA cm^{-2}). More importantly, a long-term safe operation of over a thousand hours is preferred to reach the economically compelling level. While the noble metals exhibit high catalytic activity for CO_2RR with relatively high selectivity and stability, their high capital costs may hinder large scale applications. Therefore, it is imperative to develop inexpensive catalysts with CO_2RR performance comparable to the noble metal-based catalysts and to meet the performance requirements of industrial applications.

In response, various non-noble metal-based materials have been developed as the CO_2RR electrocatalysts for selective C1 products formation. Different strategies have been explored to maximize the CO_2RR performance. Of note, p-block metals demonstrate the great potential for C1 products generation as the promising alternatives to noble metals. However, most of the reported FEs show the increased peak of over 90% at the moderate potential, while such high selectivity could only be maintained in a narrow potential window. In addition, it remains as a challenge to simultaneously achieve high current density and Faradaic efficiency, especially relevant to industrial condition. The engineering strategies on p-block metal-based catalysts have not been fully investigated for achieving desired CO_2RR performance on C1 products, which presents the challenges and opportunities for us to advance the research work in regards to development of p-block metal-based electrocatalysts for efficient CO_2RR.

Based on the above remaining challenges, the research objectives of this thesis are listed below:

(1) To rationally design p-block metal-based electrocatalysts to simultaneously achieve high j and FE of C1 products in a wide potential window to reach the requirements for industrial application.

(2) To investigate the effectiveness of different engineering strategies over p-block metal-based catalysts for CO_2RR technology.

2.4 References

[1]   D. Kim, J. Resasco, Y. Yu, A. M. Asiri, P. Yang, *Nat Commun* **2014**, *5*, 4948.

[2]   Q. Li, J. Fu, W. Zhu, Z. Chen, B. Shen, L. Wu, Z. Xi, T. Wang, G. Lu, J. J. Zhu, S. Sun, *J. Am. Chem. Soc.* **2017**, *139*, 4290-4293.

[3]   K. Sun, T. Cheng, L. Wu, Y. Hu, J. Zhou, A. Maclennan, Z. Jiang, Y. Gao, W. A. Goddard, 3rd, Z. Wang, *J. Am. Chem. Soc.* **2017**, *139*, 15608-15611.

[4]   K. Wang, D. Liu, P. Deng, L. Liu, S. Lu, Z. Sun, Y. Ma, Y. Wang, M. Li, B. Y. Xia, C. Xiao, S. Ding, *Nano Energy* **2019**, *64*, 103954.

[5]   Z. Wu, H. Wu, W. Cai, Z. Wen, B. Jia, L. Wang, W. Jin, T. Ma, *Angew. Chem. Int. Ed.* **2021**, *60*, 12554-12559.

[6]   K. Ye, T. Liu, Y. Song, Q. Wang, G. Wang, *Appl. Catal. B-Environ.* **2021**, *296*, 120342.

[7]   B. Zhang, J. Zhang, M. Hua, Q. Wan, Z. Su, X. Tan, L. Liu, F. Zhang, G. Chen, D. Tan, X. Cheng, B. Han, L. Zheng, G. Mo, *J. Am. Chem. Soc.* **2020**, *142*, 13606-13613.

[8]   W. Yang, Y. Zhao, S. Chen, W. Ren, X. Chen, C. Jia, Z. Su, Y. Wang, C. Zhao, *Inorg. Chem.* **2020**, *59*, 12437-12444.

[9]   Q. Gong, P. Ding, M. Xu, X. Zhu, M. Wang, J. Deng, Q. Ma, N. Han, Y. Zhu, J. Lu, Z. Feng, Y. Li, W. Zhou, Y. Li, *Nat. Commun.* **2019**, *10*, 2807.

[10]   Y. Yuan, Q. Wang, Y. Qiao, X. Chen, Z. Yang, W. Lai, T. Chen, G. Zhang, H. Duan, M. Liu, H. Huang, *Adv. Energy Mater.* **2022**, 2200970.

[11]   Y. Chen, Z. Lai, X. Zhang, Z. Fan, Q. He, C. Tan, H. Zhang, *Nat. Rev. Chem.* **2020**, *4*, 269.

[12]   H. Li, X. Zhou, W. Zhai, S. Lu, J. Liang, Z. He, H. Long, T. Xiong, H. Sun, Q. He, Z. Fan, H. Zhang, *Adv. Energy Mater.* **2020**, *10*, 2002019.

[13]   D. Ma, Y. Ying, K. Zhang, Y. Gao, L. Zhou, A. Song, Y. Zhu, K. Xie, T. Jin, H. Huang, *Appl. Catal. B-Environ.* **2022**, *316*, 121658.

[14]   Y. Ma, J. Yu, M. Sun, B. Chen, X. Zhou, C. Ye, Z. Guan, W. Guo, G. Wang, S. Lu, D. Xia, Y. Wang, Z. He, L. Zheng, Q. Yun, L. Wang, J. Zhou, P. Lu, J. Yin, Y. Zhao, Z. Luo, L. Zhai, L. Liao, Z. Zhu, R. Ye, Y. Chen, Y. Lu, S. Xi, B. Huang, C. S. Lee, Z. Fan, *Adv. Mater.* **2022**, *34*, e2110607.

[15]   Y. Ge, Z. Huang, C. Ling, B. Chen, G. Liu, M. Zhou, J. Liu, X. Zhang, H. Cheng, G. Liu, Y. Du, C. J. Sun, C. Tan, J. Huang, P. Yin, Z. Fan, Y. Chen, N. Yang, H. Zhang, *J. Am. Chem. Soc.* **2020**, *142*, 18971-18980.

[16]   Y. Chen, Z. Fan, J. Wang, C. Ling, W. Niu, Z. Huang, G. Liu, B. Chen, Z. Lai, X. Liu, B. Li, Y. Zong, L. Gu, J. Wang, X. Wang, H. Zhang, *J. Am. Chem. Soc.* **2020**, *142*, 12760-12766.

[17]   S. Liu, J. Xiao, X. F. Lu, J. Wang, X. Wang, X. W. D. Lou, *Angew. Chem. Int. Ed.* **2019**, *58*, 8499-8503.

[18]   B. Zhang, S. Chen, B. Wulan, J. Zhang, *Chem. Eng. J.* **2021**, *421*, 130003.

[19]   Y. Shi, Y. Ji, J. Long, Y. Liang, Y. Liu, Y. Yu, J. Xiao, B. Zhang, *Nat. Commun.* **2020**, *11*, 3415.

[20]   W. Zhang, S. Yang, M. Jiang, Y. Hu, C. Hu, X. Zhang, Z. Jin, *Nano Lett.* **2021**, *21*, 2650-2657.

[21]   Y. Wang, Y. Li, J. Liu, C. Dong, C. Xiao, L. Cheng, H. Jiang, H. Jiang, C. Li, *Angew. Chem. Int. Ed.* **2021**, *60*, 7681-7685.

[22]   S. Liu, X. F. Lu, J. Xiao, X. Wang, X. W. D. Lou, *Angew. Chem. Int. Ed.* **2019**, *58*, 13828-13833.

[23]   W. Guo, X. Tan, J. Bi, L. Xu, D. Yang, C. Chen, Q. Zhu, J. Ma, A. Tayal, J. Ma, Y. Huang, X. Sun, S. Liu, B. Han, *J. Am. Chem. Soc.* **2021**, *143*, 6877–6885.

[24]   Z. Zhang, F. Ahmad, W. Zhao, W. Yan, W. Zhang, H. Huang, C. Ma, J. Zeng, *Nano Lett.* **2019**, *19*, 4029-4034.

[25]   X. Yuan, Y. Luo, B. Zhang, C. Dong, J. Lei, F. Yi, T. Duan, W. Zhu, R. He, *Chem. Commun.* **2020**, *56*, 4212.

[26]   Y. Huang, X. Mao, G. Yuan, D. Zhang, B. Pan, J. Deng, Y. Shi, N. Han, C. Li, L. Zhang, L. Wang, L. He, Y. Li, Y. Li, *Angew. Chem. Int. Ed.* **2021**, *60*, 15844-15848.

[27]   N. Han, P. Ding, L. He, Y. Li, Y. Li, *Adv. Energy Mater.* **2019**, 1902338.

[28]   Z. Yang, F. E. Oropeza, K. H. L. Zhang, *APL Mater.* **2020**, *8*, 060901.

[29]   S. Liu, H. Tao, L. Zeng, Q. Liu, Z. Xu, Q. Liu, J. L. Luo, *J. Am. Chem. Soc.* **2017**, *139*, 2160-2163.

[30]   N. Han, M. Sun, Y. Zhou, J. Xu, C. Cheng, R. Zhou, L. Zhang, J. Luo, B. Huang, Y. Li, *Adv. Mater.* **2021**, *33*, 2005821.

[31]   Y. Chen, C. W. Li, M. W. Kanan, *J. Am. Chem. Soc.* **2012**, *134*, 19969-19972.

[32]   H. Huang, H. Jia, Z. Liu, P. Gao, J. Zhao, Z. Luo, J. Yang, J. Zeng, *Angew. Chem. Int. Ed.* **2017**, *56*, 3594-3598.

[33]   J. Wang, G. Wang, J. Zhang, Y. Wang, H. Wu, X. Zheng, J. Ding, X. Han, Y. Deng, W. Hu, *Angew. Chem. Int. Ed.* **2021**, *60*, 7602-7606.

[34]   J. Xiao, M. R. Gao, S. Liu, J. L. Luo, *ACS Appl. Mater. Interfaces* **2020**, *12*, 31431-31438.

[35]   T. Zheng, K. Jiang, H. Wang, *Adv. Mater.* **2018**, *30*, 1802066.

[36] S. Jin, Z. Hao, K. Zhang, Z. Yan, J. Chen, *Angew.Chem. Int. Ed.* **2021**, *60*, 20627-20648.

[37] B. Zhang, J. Zhang, *Journal of Energy Chemistry* **2017**, *26*, 1050-1066.

[38] H. Xie, T. Wang, J. Liang, Q. Li, S. Sun, *Nano Today* **2018**, *21*, 41-54.

[39] Z. Gu, H. Shen, L. Shang, X. Lv, L. Qian, G. Zheng, *Small Methods* **2018**, *2*, 1800121.

[40] S. Liu, C. Sun, J. Xiao, J.-L. Luo, *ACS Catal.* **2020**, *10*, 3158-3163.

[41] S. Liu, X.-Z. Wang, H. Tao, T. Li, Q. Liu, Z. Xu, X.-Z. Fu, J.-L. Luo, *Nano Energy* **2018**, *45*, 456-462.

[42] K. Qi, Y. Zhang, J. Li, C. Charmette, M. Ramonda, X. Cui, Y. Wang, Y. Zhang, H. Wu, W. Wang, X. Zhang, D. Voiry, *ACS Nano* **2021**, *15*, 7682-7693.

[43] W. Luo, Q. Zhang, J. Zhang, E. Moioli, K. Zhao, A. Züttel, *Appl. Catal. B-Environ.* **2020**, *273*, 119060.

[44] M. F. Philips, G.-J. M. Gruter, M. T. M. Koper, K. J. P. Schouten, *ACS Sustainable Chem. Eng.* **2020**, *8*, 15430-15444.

[45] Z. Chen, T. Fan, Y.-Q. Zhang, J. Xiao, M. Gao, N. Duan, J. Zhang, J. Li, Q. Liu, X. Yi, J.-L. Luo, *Appl. Catal. B-Environ.* **2020**, *261*, 118243.

[46] F. Lei, W. Liu, Y. Sun, J. Xu, K. Liu, L. Liang, T. Yao, B. Pan, S. Wei, Y. Xie, *Nat Commun* **2016**, *7*, 12697.

[47] Y. J. Ko, J. Y. Kim, W. H. Lee, M. G. Kim, T. Y. Seong, J. Park, Y. Jeong, B. K. Min, W. S. Lee, D. K. Lee, H. S. Oh, *Nat Commun* **2022**, *13*, 2205.

[48] B. Kumar, V. Atla, J. P. Brian, S. Kumari, T. Q. Nguyen, M. Sunkara, J. M. Spurgeon, *Angew. Chem. Int. Ed.* **2017**, *56*, 3645-3649.

[49] F. Li, L. Chen, G. P. Knowles, D. R. Macfarlane, J. Zhang, *Angew. Chem. Int. Ed.* **2017**, *129*, 520-524.

[50] G. Liu, Z. Li, J. Shi, K. Sun, Y. Ji, Z. Wang, Y. Qiu, Y. Liu, Z. Wang, P. Hu, *Appl. Catal. B-Environ.* **2020**, *260*, 118134.

[51] W. Ma, S. Xie, X. G. Zhang, F. Sun, J. Kang, Z. Jiang, Q. Zhang, D. Y. Wu, Y. Wang, *Nat. Commun.* **2019**, *10*, 892.

[52] P. Hou, X. Wang, P. Kang, *J. CO₂ Util.* **2021**, *45*, 101449.

[53] J. Feng, H. Gao, J. Feng, L. Liu, S. Zeng, H. Dong, Y. Bai, L. Liu, X. Zhang, *ChemCatChem* **2019**, *12*, 926-931.

[54]   Z. Zhang, M. Chi, G. M. Veith, P. Zhang, D. A. Lutterman, J. Rosenthal, S. H. Overbury, S. Dai, H. Zhu, *ACS Catal.* **2016**, *6*, 6255-6264.

[55]   L. Jia, M. Sun, J. Xu, X. Zhao, R. Zhou, B. Pan, L. Wang, N. Han, B. Huang, Y. Li, *Angew Chem Int Ed Engl* **2021**.

[56]   Y. Jiang, X. Zhang, D. Xu, W. Li, M. Liu, X. Qiu, *Chemical Communications* **2021**.

[57]   M. Fan, S. Prabhudev, S. Garbarino, J. Qiao, G. A. Botton, D. A. Harrington, A. C. Tavares, D. Guay, *Appl. Catal. B-Environ.* **2020**, *274*, 119031.

[58]   J. H. Koh, D. H. Won, T. Eom, N.-K. Kim, K. D. Jung, H. Kim, Y. J. Hwang, B. K. Min, *ACS Catal.* **2017**, *7*, 5071-5077.

[59]   S. X. Guo, Y. Zhang, X. Zhang, C. D. Easton, D. R. MacFarlane, J. Zhang, *ChemSusChem* **2019**, *12*, 1091-1100.

[60]   F. Li, G. H. Gu, C. Choi, P. Kolla, S. Hong, T.-S. Wu, Y.-L. Soo, J. Masa, S. Mukerjee, Y. Jung, J. Qiu, Z. Sun, *Appl. Catal. B-Environ.* **2020**, *277*, 119241.

[61]   J. Yang, X. Wang, Y. Qu, X. Wang, H. Huo, Q. Fan, J. Wang, L. M. Yang, Y. Wu, *Adv. Energy Mater.* **2020**, *10*, 2001709.

[62]   Z. Chen, K. Mou, X. Wang, L. Liu, *Angew. Chem. Int. Ed.* **2018**, *57*, 12790-12794.

[63]   P. Deng, F. Yang, Z. Wang, S. Chen, Y. Zhou, S. Zaman, B. Y. Xia, *Angew. Chem. Int. Ed.* **2020**, *59*, 10807-10813.

[64]   M. Li, J. Wang, P. Li, K. Chang, C. Li, T. Wang, B. Jiang, H. Zhang, H. Liu, Y. Yamauchi, N. Umezawa, J. Ye, *Journal of Materials Chemistry A* **2016**, *4*, 4776-4782.

[65]   K. Liu, M. Ma, L. Wu, M. Valenti, D. Cardenas-Morcoso, J. P. Hofmann, J. Bisquert, S. Gimenez, W. A. Smith, *ACS Appl Mater Interfaces* **2019**.

[66]   J. Choi, M. J. Kim, S. H. Ahn, I. Choi, J. H. Jang, Y. S. Ham, J. J. Kim, S.-K. Kim, *Chemical Engineering Journal* **2016**, *299*, 37-44.

[67]   S. N. Zhang, M. Li, B. Hua, N. Duan, S. Ding, S. Bergens, K. Shankar, J. L. Luo, *ChemCatChem* **2019**, *11*, 4147-4153.

[68]   L. Peng, Y. Wang, Y. Wang, N. Xu, W. Lou, P. Liu, D. Cai, H. Huang, J. Qiao, *Appl. Catal. B-Environ.* **2021**, 120003.

[69]   X. Zhang, X. Sun, S.-X. Guo, A. M. Bond, J. Zhang, *Energy & Environmental Science* **2019**, *12*, 1334-1340.

[70] X. An, S. Li, A. Yoshida, T. Yu, Z. Wang, X. Hao, A. Abudula, G. Guan, *ACS Appl Mater Interfaces* **2019**, *11*, 42114-42122.

[71] Y. Wang, Z. Chen, P. Han, Y. Du, Z. Gu, X. Xu, G. Zheng, *ACS Catalysis* **2018**, *8*, 7113-7119.

[72] Y. Feng, Z. Li, H. Liu, C. Dong, J. Wang, S. A. Kulinich, X. Du, *Langmuir* **2018**, *34*, 13544-13549.

[73] Y. Peng, T. Wu, L. Sun, J. M. V. Nsanzimana, A. C. Fisher, X. Wang, *ACS Appl Mater Interfaces* **2017**, *9*, 32782-32789.

Chapter 3. Methodologies and Characterizations

3.1 The specifications of chemicals and gases

The following chemicals used in the thesis work were all purchased from Sigma-Aldrich: Copper (II) sulfate pentahydrate (ACS reagent, ≥98.0%), indium (III) chloride hydrate (99.99% metals basis), urea, sodium dodecylbenzene sulfonate (SDBS), sulfuric acid (96%), hydrochloric acid (ACS reagent, 37%), nitric acid (68.0-70.0%), thioacetamide (TAA, reagent grade, 98%), bismuth (III) nitrate pentahydrate (ACS reagent, ≥98.0%), cetyltrimethylammonium bromide (CTAB), bismuth citrate (99.99% trace metals basis), ammonium hydroxide solution (ACS reagent, 28.0 ~ 30.0%), sodium carbonate solution (ACS reagent, anhydrous), potassium iodide (ACS reagent, ≥99.0%), sodium hydroxide (ACS reagent, ≥97.0%), potassium hydroxide (reagent grade, 90%), polyvinylpyrrolidone (PVP10, Mw. 10000), sodium chloride (ACS reagent, ≥99.0%), Nafion perfluorinated ion-exchange resin solution (5 wt% in mixture of lower aliphatic alcohol and H_2O) and Nafion® N-117 membrane (0.18 mm of thickness). Potassium bicarbonate (>99.99%), isopropanol, and ethanol were purchased from Fisher Scientific Company. Carbon papers (Toray TGP-H-060), gas diffusion electrode (Sigracet 22BB and 39BB) were purchased from Fuel Cell Store. Deionized water was taken from a Millipore Autopure system. All chemicals are of analytical grade and used without further purification. Hydrogen (99.995%), argon (99.999%), compressed air (extra dry) and carbon dioxide (99.999%) were purchased from Linde Canada Inc.

3.2 Materials synthesis

3.2.1 Synthesis of CuO, InOx@CuO and In$_2$O$_3$ nanoparticles

Firstly, carbon paper (Toray TGP-H-060) was cut into small pieces with the size of 2 cm × 1 cm, pretreated by sonication in 0.1 M HCl solution and then washed with deionized water for 10 minutes and dried in air. The electrodeposition was conducted with a two-electrode cell by galvanostatic method. Pretreated carbon paper was directly used as a working electrode with the surface area of 1 cm^2 and Pt mesh as a counter electrode. The solution for electrodeposition was a mixture of 0.0333 M CuSO$_4$ and 0.1667 M H$_2$SO$_4$. During the electrodeposition, the current density was kept at 23 mA cm^{-2} for 15 minutes at ambient pressure and room temperature. After electrodeposition, the sample was washed with deionized water and ethanol, then dried in air. The prepared sample was annealed in air at 300 °C for 210 min with a ramping rate of 5 °C min^{-1} and cooled down to room temperature to obtain the CuO.

To prepare InO$_x$@CuO, indium was deposited on the prepared sample through a simple method. The prepared electrodeposited Cu samples were immersed into the 10, 50, 100, 150 and 200 mM InCl$_3$ solutions for half a minute respectively and dried in air. Then, the same annealing treatment was used to obtain the electrocatalysts of CuO with In species. The obtained catalysts are noted as InO$_x$-10@CuO, InO$_x$-50@CuO, InO$_x$@CuO, InO$_x$-150@CuO and InO$_x$-200@CuO, respectively. Following the same procedure, the In-free catalyst containing Cl$^-$ (In-free CuO), was prepared using 100 mM KCl instead of InCl$_3$.

To prepare In$_2$O$_3$ nanoparticles, 0.6 g In(NO$_3$)$_3$, 0.8 g urea and 0.17 g sodium dodecylbenzene sulfonate (SDBS) were added into a beaker mixed with 50 ml DI water and stirred vigorously

for 1 h. The homogenous mixture was refluxed at 100 °C for 3 h to obtain the precursor. Subsequently, the precursor was heated to 550 °C for 4 h in air with a heating rate of 2 °C min^{-1}. After naturally cooling down to room temperature, the In_2O_3 nanoparticles were obtained.

3.2.2 Synthesis of Bi_2O_3, Bi_2S_3 and Bi_2S_3-Bi_2O_3 nanosheets

To prepare Bi_2S_3-Bi_2O_3 NSs, 0.6 mmol of $Bi(NO_3)_3 \cdot 5H_2O$ and 0.2 mL of HNO_3 were added into 5 mL of DI water to form a milky suspension. Then, a sulfurization agent solution was prepared by dissolving 0.15 g of cetyltrimethylammonium bromide and 0.1 g of thioacetamide in 60 mL DI water through ultrasonication. The prepared solution of dissolved bismuth salt was added into the sulfurization agent dropwise under constant stirring. Finally, the mixture was stirred at room temperature for 3 h with the color changing from white to dark brown. The product was collected by washing and centrifuging with DI water and ethanol three times respectively, and dried at 60 °C overnight. Bi_2S_3 NPs were prepared with excessive TAA (0.4g) using the same method. Without adding TAA, Bi_2O_3 NSs were obtained.

3.2.3 Synthesis of bismuth subcarbonate nanoflowers

The bismuth subcarbonate nanoflowers (BOC NFs) were prepared via a one-pot synthesis method at room temperature. The 2 mmol bismuth citrate was added to the 15 mL 0.5 M ammonium hydroxide solution under stirring conditions to form a clear solution. Then, the prepared 15 mL 1.0 M sodium carbonate solution was dropwise added to form the white precipitate. After reacting for 24 hours, the product was collected by centrifugation and washed with deionized water and ethanol three times respectively, and dried in air.

3.2.4 Synthesis of β-Bi$_2$O$_3$ and α-Bi$_2$O$_3$ polymorphs

The β-Bi$_2$O$_3$ and α-Bi$_2$O$_3$ polymorphs were prepared by heating the Bi$_2$O$_2$CO$_3$ precursor (Section 3.2.3). The as-prepared Bi$_2$O$_2$CO$_3$ powder was placed in a crucible and heated in a muffle furnace in air at certain temperature for 3 hours with a ramping rate of 5 °C min^{-1}. The temperatures for pure β-Bi$_2$O$_3$ and α-Bi$_2$O$_3$ synthesis were 420 and 550 °C, respectively.

3.2.5 Synthesis of Bi$_5$O$_7$I nanotubes and nanobelts

Bi$_5$O$_7$I nanotubes were prepared via the hydrothermal method. Firstly, 2 mmol Bi(NO$_3$)$_3$·5H$_2$O and 3.2 g PVP were added into 40 mL deionized water under stirring condition to form a uniform solution. Then, 20 mL KI-saturated solution was added dropwise into the precursor solution with continuous stirring and a red solution was formed. After stirring for 10 minutes, the NaOH solution (3 M) was added into the mixture to adjust the pH to 10.5. Subsequently, the resulting solution mixture was transferred into a 100 mL Teflon-line stainless steel autoclave and heated at 160 °C for 3 hours. After cooling down to room temperature, the products were collected by centrifugation and washed with DI water and ethanol four times respectively to remove the residuals. The obtained product was dried at 60 °C overnight before further usage. Bi$_5$O$_7$I nanobelts were prepared with the same procedure except adjusting the pH to 12.5.

3.3 Materials characterizations

The material characterization methods used in this work are summarized as follows:

(1) X-ray diffraction (XRD): The crystalline structures of catalysts were identified by XRD using a Rigaku Rotaflex Cu Kα radiation at 40 kV, 44 mA and the diffraction patterns are analyzed using Jade 6.5 software.

(2) Scanning electron microscopy (SEM): The microstructures and morphologies were observed using a high-resolution Zeiss Sigma field emission scanning electron microscopy (FESEM) and Hitachi S4800 FESEM.

(3) Transmission electron microscopy (TEM): The TEM characterization was performed using a JEOL JEM-ARM200CF electron microscopy equipped with an EDS detector. TEM with a cold field emission gun was operated at an accelerating voltage of 200 kV. Images were achieved using a Gatan digital imaging system through Digital Micrograph software.

(4) X-ray photoelectron spectroscopy (XPS): XPS was employed to investigate the surface chemical states of catalysts using Kratos AXIS Ultra with monochromatic Al Kα source (hv = 1486.6 eV). The binding energies of XPS spectra were calibrated by referencing to the adventitious C 1s peak at 284.8 eV.

(5) Ultraviolet photoelectron spectroscopy (UPS): The work functions of catalysts were measured by UPS using the Kratos AXIS Ultra with He I source (hv =21.2 eV) at –10 V.

(6) X-ray absorption spectroscopy (XAS): The X-ray absorption measurements were carried out at Canadian Light Source (CLS) using the Very Sensitive Elemental and Structural Probe Employing Radiation from a Synchrotron (VESPERS, 07B2-1) beamline.

(7) CO_2/N_2 adsorption/desorption: The CO_2 adsorption isotherms were measured using an Autosorb iQ apparatus. The pore size of BOC NFs was measured by N_2 adsorption/desorption method using the same apparatus.

(8) Thermalgravimetric analysis (TGA): The weight losses of BOC NFs were determined by TGA on a TA SDT Q600 instrument at a heating rate of 5 °C min^{-1} from room temperature to 600 °C in air.

(9) Raman spectroscopy: Renishaw inVia Qontor Confocal Raman Microscope was used with the excitation laser of 532 nm (50 mW). The monochromator was calibrated before each set of measurements using the zero-order peak and the Si lattice peak at 520.5 cm^{-1} of a Si wafer reference sample.

(10) UV/vis spectrophotometer: The measurement of optical property was conducted by using a Spectrophotometer UV/VIS (Hitachi U-3900H, 240 nm to 850 nm). The UV-vis diffuse reflectance was measured by Hitachi U-3900H using the integrating sphere coated with a highly reflective barium sulfate.

3.4 Electrochemical measurements and product analysis

3.4.1 Electrochemical performance measurements in H-cell

The electrochemical measurements were performed with an electrochemical interface (Solartron 1287) and an impedance/gain-phase analyzer (Solartron 1255) or Gamry Reference 3000. For each kind of catalyst, three-electrode cell was used for measurements for the performance and product analyses to ensure the repeatability. The error ranges are derived by calculating the deviations from the average Faradaic efficiencies, the mean values for all the measurements at each applied potential.

The electrochemical measurement was carried out with a typical three-electrode H-type cell, where the saturated calomel electrode (SCE) and platinum plate/graphite rod served as

reference electrode and counter electrode, respectively. Before measurement, each compartment of cell was filled with 40 ml electrolyte. CO_2 was bubbled into the 0.1/0.5M $KHCO_3$ solution at a flow rate of 20 ml min^{-1} for at least 30 minutes before each experiment to remove all the oxygen and achieve a saturated CO_2 condition. All the potentials versus SCE were recorded and converted the reversible hydrogen electrode (RHE) reference scale by the equation:

$$E(\text{V vs. RHE}) = E(\text{V vs. SCE}) + 0.241 + 0.0592\text{pH} \qquad \text{(Eq. 3.1)}$$

Liner sweep voltammetry (LSV) curves were recorded at a scan rate of 20 mV s^{-1}. Electrochemical impedance spectroscopy (EIS) measurements were carried out at -1.0 V vs. RHE in CO_2-saturated 0.5 M $KHCO_3$ aqueous solution with a three-electrode configuration with the AC voltage signal of a 10 mV amplitude over the frequency range 0.1-10^5 Hz.

3.4.2 Electrochemical performance measurements in the flow cell system

The flow cell was built with a gas diffusion layer (GDL, Sigracet 22BB/39BC) and Pt foil as cathode and anode, separated by the anion exchange membrane. The Hg/HgO (1.0 M KOH) was used as the reference electrode. All the potentials versus Hg/HgO electrode were recorded and converted the reversible hydrogen electrode (RHE) reference scale by the equation:

$$E\ (\text{V vs. RHE}) = E\ (\text{V vs. Hg/HgO, 1.0 M}) + 0.098\ \text{V} + 0.0592\text{pH} \quad \text{(Eq. 3.2)}$$

The flow rate of CO_2 gas was 20 mL min^{-1}. The electrolyte 1.0 M KOH was circulated in both cathode and anode respectively with flow rate of 10 mL min^{-1} pumped by Precision Peristaltic Pump (BINACA PUMPS).

3.4.3 Electrochemical performance measurements in MEA system

The custom-built two-electrode MEA system consisting of titanium plates with serpentine flow channels was used to evaluate the CO_2RR performance. The cathode and anode were separated by an anion exchange membrane (Sustainion X37-50 Grade RT. Dioxide Materials). The humidified CO_2 was fed into the cathode at 50 mL min^{-1} controlled by the mass flow controller, while the anode was circulated with 0.1 M $KHCO_3$ electrolyte at a rate of 5 mL min^{-1}. The cathode was prepared using the same method as flow cell preparation. The anode was prepared by depositing IrO_2 on a titanium mesh support by a dip coating followed by calcination.

3.4.3 Electrochemically active surface area measurement

The ECSA of a material with similar composition is proportional to its electrochemical double-layer capacitance (C_{dl}), which was measured by CV in a non-Faradaic region at different scan rates of 20, 40, 60, 80, 100, 120 mV s^{-1}. Then, the double-layer capacitance (C_{dl}) was determined by plotting the $\Delta j=(j_a-j_c)/2$ at certain potential as a function of the scan rate. It can be calculated by the following equation:

$$C_{dl} = \frac{d(\Delta j)}{2dV_s}$$
(Eq. 3.3)

The roughness factor R_f was estimated from the ratio of double-layer capacitance (C_{dl}) for the working electrode and the corresponding smooth catalyst.

3.4.3 Product analysis

Gaseous products analysis: The gas products from cathode were identified by an online Hewlett-Packard model Agilent 6890N gas chromatograph (GC) equipped with a packed bed column (HaySep D) operated at 100 °C with a thermal conductivity detector and a flame

ionization detector. Argon was used as the carrier gas with a flow rate of 30 ml min^{-1}. At each applied potential, the cathodic gas was injected into GC three times with a time interval of 6 min to get the average value of the products. Faradaic efficiency of gas products can be calculated as follows:

$$\text{FE}_{Product} = \frac{F n_{product} v_{product} f_v p_0}{RT_0 I_{total}} \times 100\%$$

(Eq. 3.4)

where F is the Faradaic constant; $n_{product}$ is the number of mole of electrons participating in the reaction to form certain product; $v_{product}$ is the volume concentration of certain product in the exhaust gas from the cell; f_v is the flow rate of the exhaust gas measured at the exit of the cell at room temperature (T_0) and ambient pressure (p_0); I_{total} is the total current of the steady cell.

Liquid products analysis: The liquid product of formate was measured by using 850 Professional IC with Metrosep Organic Acids-250/7.8 column. The eluent was 0.5 mmol L^{-1} sulfuric acid mixed with 10% acetone with the standard flow rate of 0.5 mL min^{-1}. The Faradaic efficiency of formic acid can be calculated by using the following equation:

$$\text{FE}_{formate} = \frac{2c_{(formate)} V F}{Q_{total}} \times 100\%$$

(Eq. 3.5)

where $c_{(formate)}$ is the concentration of formic acid determined by IC; V is the total volume of electrolyte in cathode chamber; F is the Faradaic constant; Q_{total} is the total amount of charge passing through the system.

3.5 *In situ*/Operando measurements

3.5.1 *In situ* Raman spectroscopy measurement

The *in situ* electrochemical Raman spectroscopy was conducted using a Renishaw inVia Qontor Confocal Raman Microscope. As the excitation source, a laser of 532 nm (50 mW) was used. The monochromator was calibrated before each set of measurements using the zero-order peak and the Si lattice peak at 520.5 cm^{-1} of a Si wafer reference sample. The measurement was conducted in a three-electrode electrochemical cell made by polytetrafluoroethylene (PTFE) with a quartz window. The spectra were measured from the open circuit potential (OCP) to cathodic potentials (V vs. RHE). The cathodic limit is defined by the interference of HER because the formation of bubbles on the electrode can lead to the signal loss. Before measurement, the CO_2 gas was bubbled through the electrolyte for 30 minutes to ensure that the solution reached saturation. Each spectrum was accumulated for 1 min after the 10 min electrolysis, allowing the system to achieve a steady-state condition after each change of potential.

3.5.2 *In situ* diffuse reflectance infrared Fourier transform spectroscopy measurement

The *in situ* diffuse reflectance infrared Fourier transform spectroscopy (DRIFTS) spectra were collected on a Nicolet 8700 spectrometer equipped with a deuterated-triglycine sulfate (DTGS) detector cooled by liquid nitrogen. A reaction chamber manufactured by Harrick Scientific was used to obtain the *in situ* DRIFTS data in a Praying Mantis DRIFTS accessory. All spectra were obtained with a resolution of 4 cm^{-1} and an accumulation of 32 scans. The sample cup of the cell was filled with a finely powdered sample. Prior to the CO_2 adsorption studies, catalyst samples were pre-treated *in situ* in a pure He stream (30 mL min^{-1}) and kept for 2 h to remove adsorbed impurities. After the pre-treatment, a gas mixture flow of 1% CO_2

and 99% He stream was purged into the chamber at a rate of 30 ml min^{-1} at room temperature. The spectra were collected at a certain time until the adsorption peak was stable.

3.5.3 *In situ* heating X-ray diffraction measurement

The *in situ* heating X-ray diffraction measurements were performed on Bruker D8 Discover diffraction system equipped with Cu-source and high throughput LynxEYE 1-dimensional detector with high intensity and speed. The precursor $Bi_2O_2CO_3$ powder was placed on the heating stage and covered by a dome. The heating rate was 1 °C s^{-1} and the temperature was held for 10 minutes every 50 °C to record the XRD patterns. The heating range was from room temperature 22 to 600 °C.

3.5.3 *In situ* heating scanning electron microscopy measurement

The *in situ* heating scanning electron microscopy measurement was carried out using Zeiss Sigma FESEM with a MEMS *in situ* heating stage (NORCADA). The $Bi_2O_2CO_3$ powder was directly dispersed on the heating stage and loaded into the chamber. The heating rate was 1 °C s^{-1} and the chamber maintained the vacuum state throughout the measurement.

3.6 Density functional theory calculation

Density functional theory (DFT) calculations were carried out with the Vienna Ab initio Simulation Program (VASP) [1-3]. Perdew-Burke-Ernzerhof (PBE) generalized gradient approximation (GGA) function was employed to model the exchange correlation interactions [4]. Gaussian smearing of 0.1eV was set for surface calculations while for gas-phase species, it was set at 0.01eV. The convergence criterion for electronic structure iteration was set at 10^{-6} eV. Relaxation of degree of ions was not terminated until a maximum force component

of 0.05eV/Angstrom was reached. Different adsorption geometries were considered and the one with the lowest energy was chosen.

The Cu (111) surface was modeled using a three-layer (6 × 6) periodic unit cell. The Cu-supported In surface was simplified by using an In atom island on the three-layer (6 × 6) Cu (111) surface. In all cases, the bottom layer was fixed during optimization, while the remaining atoms were relaxed until the energies and forces in the system were less than 10^{-4} eV and 0.01 eV/Å, respectively. The total energy of gas-phase CO_2 was corrected by + 0.45 eV and a solvation effect correction of -0.1 eV was added to total energy of *COOH and *CO. A plane-wave cut-off energy of 400 eV was set and spin polarization was selected for all the computations. The Fermi-level smearing was set at 0.2 eV.

A (2×2×3) Bi_2O_3 and a (2×2×3) $Bi_2O_2CO_3$ model were built based on the optimized Bi_2O_3 and $Bi_2O_2CO_3$ unit cell, respectively. For geometry optimization of Bi_2O_3 and $Bi_2O_2CO_3$ with and without the adsorption of intermediate species, the three atomic layers at the top were fully relaxed while the remaining layers were fixed. Brillouim Zone k points were sampled by Monkhorst-Pack (4×4×1). The cut-off energy was set at 520 eV for spin polarized calculation.

A (2×2×3) β-Bi_2O_3 (110) surface model was built based on the optimized Bi_2O_3 unit cell. For geometry optimization of Bi_2O_3 with and without the adsorption of intermediate species, the three atomic layers at the top were fully relaxed while the remaining layers were fixed. Brillouim Zone k points were sampled by Monkhorst-Pack (4×4×1). The cut-off energy was set at 520 eV for spin polarized calculation.

A (3×3) surface model with six atomic layers were built based an optimized unit cell of Bi. To avoid the interaction between the neighbouring slabs, a vacuum layer with at least 15 Å was added. Monkhorst-Pack (4×4×1) was set for k points sampling of Brillouim zone. The cut-off energy was set at 520 eV for spin polarized calculation. The Bi surface model with one Bi vacancy is denoted as "Mono-Bi (Bi-V_1)" and the Bi surface model with two Bi vacancies is the Monkhorst-Pack denoted as "Dino-Bi (Bi-V_2)".

The Gibbs free energy diagram for CO_2RR was built according to Eq. 3.6,

$$G=E+ZPE+\int C_p dT-TS \qquad \text{(Eq. 3.6)}$$

where E, ZPE, $\int C_p dT$ and -TS represent the DFT calculated electronic energy, zero-point energy, enthalpy correction and entropy correction individually. PV contribution was neglected. 3N freedom degrees were treated as frustrated harmonic vibrations to calculate ZPE and enthalpy correction while a proposed standard method was used to calculate entropy contribution and transfer it to thermodynamic data at room temperature [5, 6]. The computational hydrogen electrode (CHE) model [7] describing each electrochemical reaction step as a simultaneous transfer of proton and electron was employed. The CO_2RR for CO route can be divided into three steps as shown in Eqs. 3.7 to 3.9,

$$CO_2 + * + 2(H^+ + e^-) \leftrightarrow *COOH + H^+ + e^- \qquad \text{(Eq. 3.7)}$$

$$*COOH + H^+ + e^- \leftrightarrow *CO + H_2O \qquad \text{(Eq. 3.8)}$$

$$*CO + H_2O \leftrightarrow * + CO + H_2O \qquad \text{(Eq. 3.9)}$$
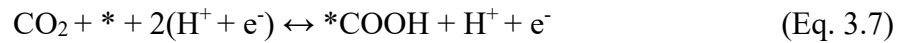
where * means the corresponding surface on which the species adsorbed.

The CO_2RR for HCOOH route can be divided into three steps shown in Eqs. 3.10 to 3.12,

$$CO_2 + * + 2(H^+ + e^-) \leftrightarrow *HCOO + H^+ + e^- \qquad \text{(Eq. 3.10)}$$

$$*HCOO + H^+ + e^- \leftrightarrow *HCOOH \qquad \text{(Eq. 3.11)}$$

$$*HCOOH \leftrightarrow * + HCOOH \qquad \text{(Eq. 3.12)}$$

Taking the initial state where CO_2 molecular is freely above on clean surface as the reference, the Gibbs free energy change for each step is expressed in Eqs. 3.13 to 3.18,

$$\Delta G[*COOH] = G[*COOH] - G[*] - G[CO_2] - G[H^+ + e^-] \qquad \text{(Eq. 3.13)}$$

$$\Delta G[*CO] = G[*CO] + G[H_2O] - G[*] - G[CO_2] - 2 \times G[H^+ + e^-] \qquad \text{(Eq. 3.14)}$$

$$\Delta G[CO] = G[CO] + G[H_2O] - G[CO_2] - 2 \times G[H^+ + e^-] \qquad \text{(Eq. 3.15)}$$

$$\Delta G[*HCOO] = G[*HCOO] - G[*] - G[CO_2] - G[H^+ + e^-] \qquad \text{(Eq. 3.16)}$$

$$\Delta G[*HCOOH] = G[*HCOOH] - G[*] - G[CO_2] - 2 \times G[H^+ + e^-] \qquad \text{(Eq. 3.17)}$$

$$\Delta G[HCOOH] = G[HCOOH] - G[CO_2] - 2 \times G[H^+ + e^-] \qquad \text{(Eq. 3.18)}$$

The Gibbs free energy for hydrogen evolution reaction shown in Eqs. 3.19 and 3.20.

$$* + H^+ + e^- \leftrightarrow H* \qquad \text{(Eq. 3.19)}$$

$$H* \leftrightarrow * + 0.5H_2 \qquad \text{(Eq. 3.20)}$$

can also be represented by Eq. 3.21

$$\Delta G[H*] = G[H*] - G[*] - G[H^+ + e^-] \qquad \text{(Eq. 3.21)}$$

The Gibbs free energy of $H^+ + e^-$ can be calculated by Eq. 3.22

$$G[H^+ + e^-] = 0.5 \times G[H_2] - G[*] \qquad \text{(Eq. 3.22)}$$

3.7 References

[1]   G. Kresse, J. Hafner, *Phys. Rev. B* **1993**, *47*, 558-561.

[2]   G. Kresse, J. Hafner, *Phys. Rev. B* **1994**, *49*, 14251-14269.

[3]   G. Kresse, J. Furthmüller, *Phys. Rev. B* **1996**, *54*, 11169-11186.

[4]   B. Hammer, L. B. Hansen, J. K. Nørskov, *Phys. Rev. B* **1999**, *59*, 7413-7421.

[5]   V. Tripković, E. Skúlason, S. Siahrostami, J. K. Nørskov, J. Rossmeisl, *Electrochim. Acta* **2010**, *55*, 7975-7981.

[6]   C. J. Cramer, Essentials of computational chemistry: theories and models, John Wiley & Sons, England, **2013**.

[7]   W. J. Durand, A. A. Peterson, F. Studt, F. Abild-Pedersen, J. K. Nørskov, *Surf. Sci.* **2011**, *605*, 1354-1359.

Chapter 4. Directionally Maximizing CO Selectivity to Near-Unity over Cupric Oxide with Indium Species for Electrochemical CO$_2$ Reduction

4.1 Introduction

The excessive exploration and consumption of fossil fuels inevitably result in the record-breaking level of CO$_2$ emission into the atmosphere [1-4]. CO$_2$ reduction reaction (CO$_2$RR) using renewable energies (e.g., solar, wind or tidal power) is a sustainable and economical way to convert CO$_2$ to various carbon-neutral fuels [5-9]. CO$_2$RR has been extensively investigated in order to uncover the reaction mechanisms under various conditions, so that CO$_2$RR can proceed more efficiently and cost-effectively to eventually reduce CO$_2$ emission and alleviate the greenhouse gas effect. However, the practical application and commercialization of CO$_2$RR are severely limited by the high overpotential, sluggish kinetics, broad distribution of target products, the competitive hydrogen evolution reaction (HER) in aqueous media and the multi-electron transfer steps over most catalysts during CO$_2$RR [10-12]. It is thus desirable to develop highly selective and active electrocatalysts for CO$_2$RR.

It is well known that CO is an important industrial raw chemical for Fischer-Tropsch synthesis and methanol production. Thus, CO formation with a high selectivity during CO$_2$RR is highly desirable [13, 14]. So far, various materials, mostly the noble metals (e.g., Ag [15, 16], Au [17, 18] and Pd [19]), have been extensively studied and utilized for converting CO$_2$ to CO via CO$_2$RR, but the low earth abundance and high costs of noble metals impede their large-scale applications. In addition, the non-precious metal Zn is also utilized for CO$_2$RR toward CO formation whereas the relatively high applied potential and

unsatisfactory selectivity still restricts the desirable CO_2RR performance [20-22]. As an alternative, the earth-abundant Cu has attracted much attention for CO_2RR due to its unique properties of having the binding strength with the intermediates during CO_2RR [23]. Previous studies have been mainly focused on the formation of hydrocarbon on the Cu-based electrocatalysts [24-27], whereas the activity and selectivity of CO_2RR to CO on Cu-based electrocatalysts still remain challenging as compared to those on Au and Ag [28, 29]. Post-transition metals (In, Sn and Bi) have been demonstrated to selectively produce HCOOH because of their weak binding strength of the $CO_2^{\bullet -}$ intermediate [30-33]. These materials are attractive candidates to tune the activity and selectivity of Cu-based materials for CO_2RR due to their relatively high overpotentials for HER [34]. Throughout the literature, there is a volcano-like profile for HER catalytic activity versus metal-H bond energy, which strongly demonstrates that the post-transition metals have high overpotential toward HER [35]. Furthermore, the binding energy of intermediate (i.e., *H) is much stronger than that of *HCOO on most post-transition metals, which further verifies their low selectivity towards HER, i.e., the high selectivity for CO_2RR [23]. However, fast deactivation of pure metals induced by external power during CO_2RR weakens their catalytic performance. The combination of post-transition metal and Cu-based electrocatalyst holds the potential to effectively tune the binding strength of the key reaction intermediates, which could well address the abovementioned issues with the Cu-based materials for CO_2RR toward CO formation. The previously published work for Cu-In binary catalysts employed the different techniques, such as defect engineering, gas diffusion electrode fabrication, interface engineering, to enhance CO_2RR performance. Devi et al. [36] showed that the oxygen vacancy defects could improve the CO_2 adsorption and served as the active sites for CO_2

reduction. The maximum Faradaic efficiency of 85% for CO under relatively high potential (-0.895 V vs. RHE) was achieved. Luo et al. [37] studied the benefits of the metal-metal interface structure created in Cu/In bimetallic catalysts and showed that both selectivity and stability were enhanced with the aid of interface. In order to overcome the limit of CO_2 mass transport in aqueous electrolyte, Xiang et al. [38] reported a gas diffusion electrode (GDE) in a strong alkaline solution (1.0 M KOH) for CO_2RR toward CO formation and the Faradaic efficiency of 90 % with the current density of about 200 mA cm^{-2} was reached at -1.17 V vs. RHE. Despite the enhanced catalytic performance achieved on Cu-In binary electrocatalysts using different approaches, the high overpotential and low current density still restrict the energy efficiency for CO_2RR. Thus, it is worth improving the performance of Cu-In binary catalysts to achieve the high energy efficiency and further exploring the reaction mechanism.

Herein, a composite of In species on CuO ($InO_x@CuO$) was synthesized through a facile method and exhibits a superior performance for CO_2RR to CO with a maximum Faradaic efficiency (FE) of 97.8 % at -0.6 V, a high CO partial current density [$j_{(CO)}$] of 7.2 mA cm^{-2}, and a good stability of 50 h with negligible degradation, outperforming previously reported Cu-based materials for CO_2RR toward CO formation. More importantly, CO starts to be observed at an ultralow potential of -0.196 V, further demonstrating the superiority of $InO_x@CuO$ for CO_2RR toward CO formation. Benefited from the introduction of In species, the increased active sites, enhanced CO_2 adsorption capability and strengthened electron transfer ability were achieved over $InO_x@CuO$, which collectively contribute to the superior electrocatalytic performance for CO_2RR to CO.

4.2 Results and discussion

4.2.1 Characterization of electrocatalysts

The $InO_x@CuO$ was synthesized through a three-step process and the illustration on the formation evolution is presented in Figure 4.1a. Specifically, Cu dendrites were first obtained by an electrodeposition method, followed by a simple dipping step and an eventual annealing treatment. To confirm the chemical states of the as-prepared material, the X-ray absorption near-edge structure (XANES) spectrum in the Cu K-edge of this material was obtained and the result is displayed in Figure 4.1b with Cu foil, Cu_2O and CuO as the references. The near-edge spectra of $InO_x@CuO$ are found to be well located at the position of CuO, which confirms the chemical state of Cu as Cu^{2+}. The Fourier transform k^2-weighted function of the extended X-ray absorption fine structure (EXAFS) spectra in R space of this material shows the dominating peaks of Cu-O and Cu-Cu in oxide, indicative of the existence of Cu-O bonds and Cu-Cu in oxide bonds of CuO (Figure 4.1c) [39, 40]. To further study the crystallinity of this material, the crystal structure is identified by X-ray diffraction (XRD) where the high intensity peak at $26.3°$ is attributed to the substrate of carbon paper (Figures 4.1d and S4.1a). The diffraction peaks at $35.2°$ and $38.5°$ agree well with the standard pattern of CuO (PDF #44-0706), whereas no diffraction peaks of In species are found due to the trace amount of In species. With increasing concentration of $InCl_3$ solution, the XRD patterns of the prepared catalysts show the crystal phase of In_2O_3 after being immersed in 150 and 200 mM $InCl_3$ solutions. As shown in Figure S4.1c, the peaks at 30.6°, 51.0° and 56.0° are well matched with the standard patterns of In_2O_3 (PDF #06-0416). The increasing concentration of $InCl_3$ promotes the crystallization of In_2O_3 during annealing treatment, which further influences the structure of the catalysts.
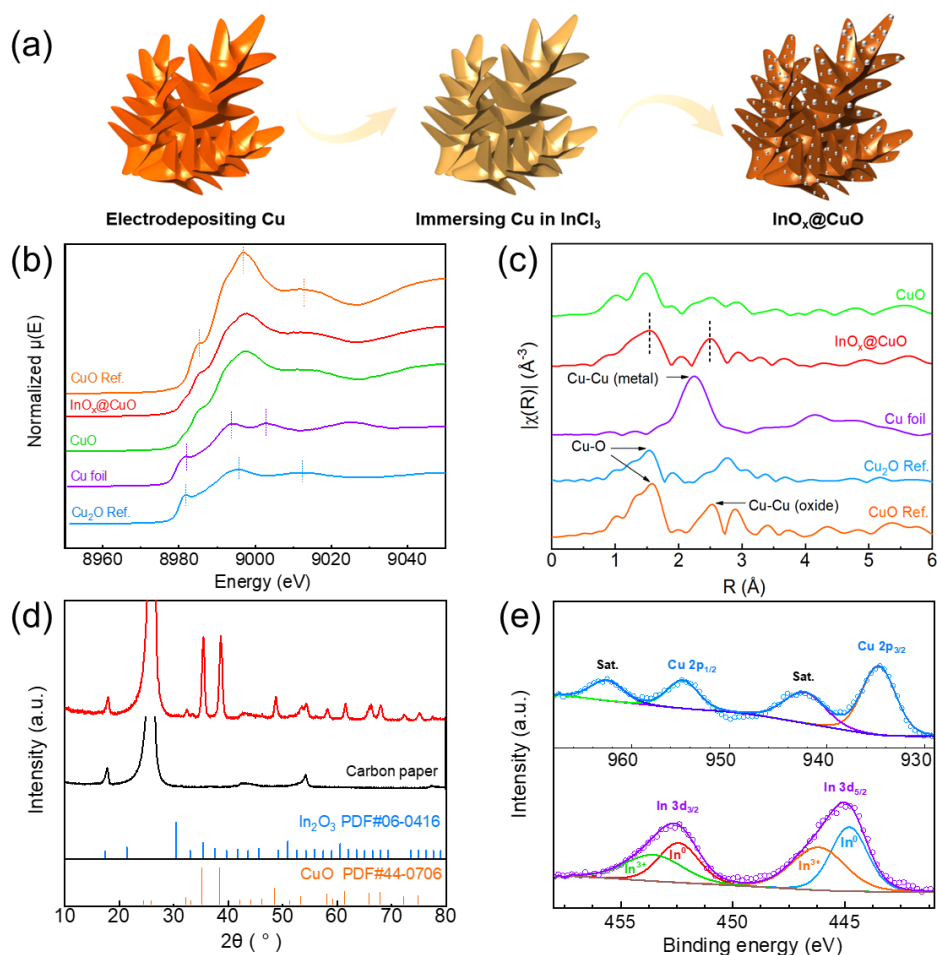
Figure 4.1 (a)Schematic illustration of the formation process of the InO$_x$@CuO; (b) Cu K-edge XANES spectra of CuO, InO$_x$@CuO and reference standard of Cu foil, Cu$_2$O and CuO before CO$_2$RR; (c) The k^2-weighted EXAFS data in R space of CuO and InO$_x$@CuO; (d) XRD pattern of InO$_x$@CuO before CO$_2$RR; (e) High-resolution XPS spectra of Cu 2p and In 3d of InO$_x$@CuO electrocatalyst before CO$_2$RR.

To further confirm the existence of crystal phase of In$_2$O$_3$, the Raman spectroscopy measurement was conducted. As shown in Figure S4.1d, the CuO displays the peaks at 282, 334 and 622 cm^{-1} that agree with CuO results [41]. It can also be found that a new peak at 130 cm^{-1} is observed when In species incorporate on CuO, which is assigned to the In-O

vibration on In_2O_3 crystal [42]. These results further confirm the formation of In_2O_3 within the In species. To examine the presence of In species on $InO_x@CuO$ catalyst, X-ray photoelectron spectrometer (XPS) was used to confirm the surface chemical states of this material (Figure 4.1e). The peaks at 934.7 and 954.8 eV correspond to the Cu $2p_{3/2}$ and Cu $2p_{1/2}$, suggesting the pure chemical state of Cu^{2+}, while the peaks at 452.4 and 444.8 eV agree with the In^0 and the peaks at 453.5 and 446.2 eV point to the chemical state of In^{3+}, an indication of the mixture of In^0 and In^{3+} species. More importantly, an In^0/In^{3+} molar ratio of 1 based on the XPS fitting results persuasively implies that the In species exist in the forms of In_2O_3 and metallic In.

To observe the morphological features, field-emission scanning electron microscopy (FESEM) was performed on $InO_x@CuO$. Clearly, substantial amounts of fine nanoparticles were formed on the CuO (Figure S4.2) where the dendritic structure of sharp leaves changed to aggregated nanoparticles after addition of In species. A close inspection on the transmission electron microscope (TEM) image of $InO_x@CuO$ (Figure 4.2a) and the crystal lattice on the selected square regions found that the d-spacings of the selected regions on the small and large nanoparticles are 0.292 (Figure 4.2b) and 0.252 nm (Figure 4.2c), respectively, which agrees well with values for the (222) plane of cubic In_2O_3 and the $(11\bar{1})$ plane of crystalline CuO. Additionally, the metallic In was also observed from HRTEM images shown in Figure S4.3. The lattice fringes of 0.272 and 0.230 nm are assigned to the planes of (101) and (110) on metallic In. This demonstrates the successful formation of In species on CuO. The EDX elemental mappings of Cu, O and In over $InO_x@CuO$ (Figure 4.2d) also confirm the incorporation of In species on CuO.
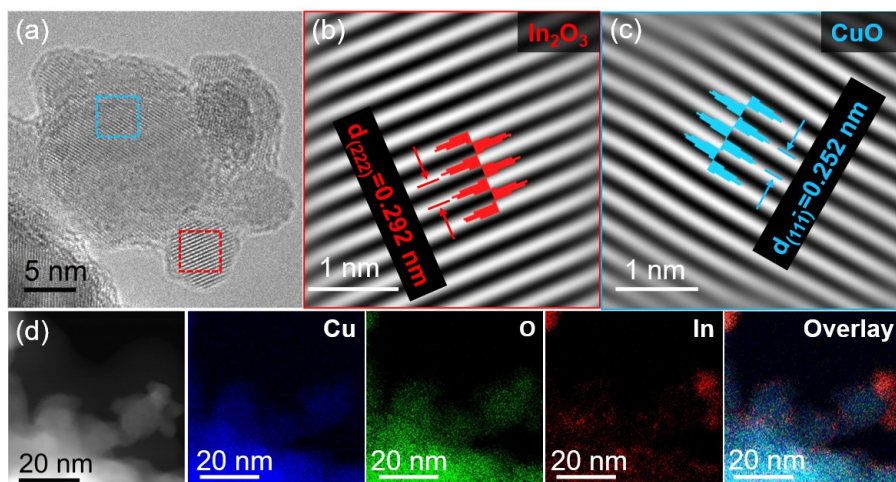
Figure 4.2 (a) High-resolution TEM image of as-prepared InOx@CuO; (b) and (c) the enlarged square regions in (a) showing the crystal lattice; (d) HAADF-STEM image and the corresponding elemental mappings of Cu, O and In.

4.2.2 Effect of InCl$_3$ solution on morphology evolution

To examine the morphology change of the prepared catalysts, different amount of In was prepared during synthesis process. It is found that the concentration of InCl$_3$ solution plays an important role in altering the morphology. The dendrite morphology is well preserved by using low concentration (10 mM), where the dendrite with sharp leaves is clearly observed in SEM images (Figure S4.4). Upon increasing amount of In, the sharp leaves start to aggregate, and the typical morphology of InO$_x$@CuO with 100 mM InCl$_3$ is nanoparticles. Furthermore, to exclude the effect of chloride ion on the morphology change, the 100 mM KCl solution was used during immersion process. The result clearly shows that the dendrite morphology is well maintained compared with the InCl$_3$ immersed samples. Therefore, it can be concluded that the morphology change is attributed to the In species during the synthesis. To demonstrate the amount of In species in the as-prepared catalysts, energy dispersive X-ray spectrometry (EDX) analysis was conducted to confirm the atomic ratios of In/Cu. As

shown in Figure S4.5, the atomic ratio of In/Cu presents a linear relationship with the concentration of $InCl_3$ solution, the In/Cu ratio of 0.047 is obtained on InO_x@CuO with an $InCl_3$ solution of 100 mM. The atomic ratios of In/Cu in InO_x@CuO with different concentrations of $InCl_3$ solution were measured using ICP-OES (Table S4.1). However, the ratio of InO_x@CuO is only 0.027 that is comparatively lower than the one measured by EDX analysis, which is attributed to the formation of In species on the catalyst surface during the immersion process. This result further verifies that trace amount of In species incorporated on CuO would lead to unobservable XRD patterns of In species.

4.2.3 Electrocatalytic performance for CO_2RR

The CO_2RR catalytic activity was examined in a two-compartment cell with CO_2-saturated 0.1 M $KHCO_3$ electrolyte with all the potentials referred to the reversible hydrogen electrode (RHE). To demonstrate the preferential occurrence of CO_2RR rather than HER, constant electrolysis at various potentials was carried out. The gaseous and liquid products were quantitatively detected using online gas chromatography (GC) and ion chromatography (IC), respectively. The prepared InO_x@CuO catalysts with different concentrations of $InCl_3$ solution as well as In-free CuO were first tested to examine the CO_2RR performance toward CO formation. The results indicate that CO and H_2 are the dominating gaseous products, together with minor amounts of C_2H_4 and HCOOH. As shown in Figure S4.6, for In-free CuO, the CO_2RR performance toward CO formation is quite poor and the main product is H_2 and the maximum FE of CO only reaches 15 % at -0.7 V. Comparatively, the maximum FE of CO is about 80 % at -0.6 V on InO_x-10@CuO. The FE of CO is improved upon increasing the amount of deposited In species, and InO_x-50@CuO shows FEs of around 90% from -0.5 to -0.7 V. When the concentration of $InCl_3$ reached 100 mM, the best catalytic performance

for CO_2RR was achieved on $InO_x@CuO$ with an enhanced CO selectivity in a wide potential range. However, with the concentration of $InCl_3$ increasing to 150 and 200 mM, the FE of CO shows downtrend compared to $InO_x@CuO$, accompanied by the decreasing total current densities (Figure S4.7). In comparison with the over 90% FE of CO in a wide potential range on $InO_x@CuO$, the maximum FE of CO is less than 90 % on InO_x-200$@CuO$. Additionally, all the In species incorporated CuO catalysts show the low selectivity for HCOOH formation at less negative potentials. The In-free CuO also exhibits less than 10 % FE of HCOOH at various applied potentials, suggesting that the incorporated In species mainly affect the selectivity between CO and H_2. Therefore, the optimal concentration of $InCl_3$ is 100 mM to achieve the best catalytic performance for CO_2RR toward CO.

To further demonstrate the role of In species for CO_2RR, electrodeposited Cu, CuO, and In_2O_3 nanoparticles (NPs) as well as carbon paper as the representative references were also evaluated. Apparently, the electrodeposited Cu shows poor selectivity toward CO formation, where H_2 is the dominating gas product during CO_2RR (Figure S4.7f), while the as-prepared In_2O_3 NPs prefer HCOOH formation with a total CO FE of 25 % at -0.7 V (Figure S4.8). However, the $InO_x@CuO$ is highly selective toward CO formation with FEs of over 90 % in a wide potential window from -0.3 to -0.7 V (Figure S4.9) and achieves its maximum value of 97.8% at -0.6 V (Figures 4.3a). This persuasively confirms the importance of In species on CuO for the directional manipulation of CO selectivity. It is noteworthy that HER is significantly suppressed with the introduction of In species, indicating a very high preference of $InO_x@CuO$ for CO_2RR over HER. Figure 4.3b exhibits the $j_{(CO)}$ of carbon paper, CuO and $InO_x@CuO$, determined by the steady-state j in potentiostatic mode and FE, it clearly demonstrates the very high catalytic activity of $InO_x@CuO$ towards CO formation during

CO$_2$RR. It is also found that the InO$_x$@CuO shows a $j_{(CO)}$ of about 7.2 mA cm^{-2}, around 7 times higher than that of CuO (ca. 1 mA cm^{-2}) at -0.6 V. Most significantly, the InO$_x$@CuO starts to generate CO with a detectable level at an onset potential of -0.196 V, which is only 86 mV higher than the theoretical equilibrium potential. The energy efficiency (EE) of InO$_x$@CuO was determined to evaluate the conversion efficiency of electrical energy to target product at the applied potentials for CO$_2$RR. The maximum EE of 34.14% is achieved at -0.3 V vs. RHE and still maintains at around 32% at -0.6 V vs. RHE, as shown in Table S4.2.
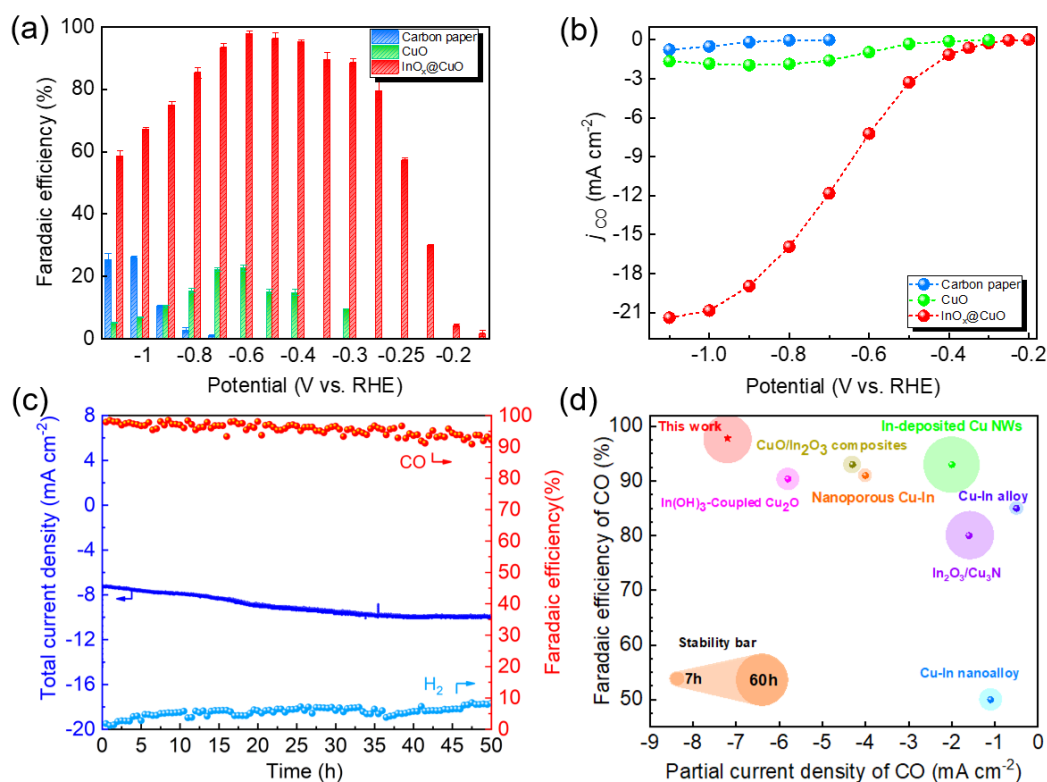
Figure 4.3 Comparisons of (a) FEs of CO and (b) jCO of carbon paper, CuO and InOx@CuO at various potentials; (c) Long-term stability test of the InOx@CuO; (d) Overview of various reported Cu-In electrocatalysts for CO$_2$ conversion to CO in 0.1 M KHCO3. (Note: The

circular area represents the stability of electrocatalysts, the larger area corresponds to the better stability.)

As a crucial factor for practical application of electrocatalysts, the long-term stability of $InO_x@CuO$ was tested at a fixed potential of -0.6 V over an extended period of time (Figure 4.3c). The FEs of CO experience slight fluctuations but still remain at over 90% with little formation of HCOOH during the 50 h test, implying a good stability of $InO_x@CuO$ for CO_2RR. The total current density slightly increases due to the accumulation of HCOOH during the long-term electrolysis. Remarkably, the morphology of $InO_x@CuO$ after CO_2RR is still well maintained as shown in Figure S4.10. To evaluate the loss of catalyst during CO_2RR, the concentration of Cu in electrolyte was measured by ICP-OES after the stability test. The extremely low concentration of Cu (0.082 mg L^{-1}) indicates the negligible corrosion of the catalysts, further confirming the excellent stability of the catalyst. Figure 4.3d and Table S4.3 summarize the performances of the electrochemical reduction of CO_2 to CO for the $InO_x@CuO$ from this work and all the previous Cu-In related electrocatalysts, which clearly shows that the performance of $InO_x@CuO$ comparably exceeds those of carbon paper and CuO as well as many benchmarking Cu-In electrocatalysts [43-46].

4.2.4 *In situ* XAS measurement and reaction mechanism for CO_2RR

To identify the chemical state change and clarify the origins of the enhanced catalytic performance over $InO_x@CuO$, the *in situ* XAS measurement was carried out using a home-made operando XAS electrochemical cell. Figure 4.4a shows the Cu K-edge time-resolved XANES spectra of $InO_x@CuO$ at -0.6 V in 0.1 M $KHCO_3$. The Cu K-edge position shifts to lower energies with time, and an observable shoulder at around 8979.5 eV appears at 46 min till the end. The edge negatively shifts to a lower binding energy, which is an indication of

the reduction of Cu species under the testing conditions. In the initial 2 hours of CO_2RR, CuO starts to be reduced to Cu, demonstrating the mixture of Cu^{2+} and Cu^0 at the beginning. To further confirm the contents of Cu^{2+} and Cu^0 species, the linear combination fitting is conducted based on the *in situ* measured spectra. As shown in Figure S4.11, the decrement of CuO shows a near-linear relationship with the increase of reduced Cu species. From the fitting results (Table S4.4), about 12 % CuO is reduced to Cu in the first 5 min and the ratio of Cu^{2+}/Cu^0 reaches around 1 at about 80 min, which further indicates that both CuO and reduced Cu serve as active sites and take part in the reaction at the initial stage. Notably, the complete CuO reduction takes near 2 h during CO_2RR, much slower than the reported Cu-based electrocatalysts [47, 48]. This ensures the excellent stability and the negligible changes on the morphology of InO_x@CuO during reduction. After initial 2 h reduction of CuO, Cu^0 became the main species serving as the active site to the end.

To determine the time required to complete the reduction of CuO to Cu at different potentials, the InO_x@CuO was firstly reduced at -1.8 and -0.6 V vs. RHE, respectively. As shown in Figures S4.12a and c, the total current densities can be divided to two stages in both cases, fast reduction of CuO to Cu (stage I) and steady state of CO_2RR (stage II). The increment of current density in stage I indicates the reduction of CuO to Cu. Comparison of Figure S4.12a and c indicates that the reduction process is faster at a more negative potential. It takes about 100 s for the total reduction of CuO to Cu at -1.8 V vs. RHE. To better reveal the effect of reduction rate of CuO on CO_2RR performance, the samples were reduced at -0.6 and -1.8 V vs. RHE, respectively, for their corresponding stage I and then tested at -0.6 V vs. RHE to evaluate their CO_2RR performances. It can be found that the FE of CO shows the higher value and higher total current density in Stage II for the sample being directly reduced at -

0.6 V vs. RHE in the stage I, suggesting an improved selectivity for CO formation (Figure S4.12b). However, the catalyst initially reduced at -1.8 V vs. RHE in Stage I shows inferior CO selectivity in Stage II at -0.6 V vs. RHE (Figure S4.12d). After the CO_2RR tests shown in Figures S4.12b and d, the morphologies of both catalysts were observed to demonstrate the effect of reduction rate on the catalyst structure. As shown in Figure S4.13, the catalyst with a fast reduction process shows larger particles of the reduced Cu, whereas it is the slow reduction of CuO that forms the smaller and uniformly distributed Cu particles which provide more active sites for CO_2RR. Thus, the increased active sites and negligible change of the catalyst structure jointly ensure the good selectivity and stability of the catalyst for CO_2 to CO conversion.

Wavelet transforms of EXAFS spectra (WT-EXAFS) at Cu K-edge demonstrate the local atomic structures of InO_x@CuO. Apparently, the highest intensity of the fresh sample is assigned to the lobe centered at (6.3 Å^{-1}, 1.5 Å), corresponding to the oxygen atoms which surround the central copper atom, as shown in Figure 4.4d. After CO_2RR, the local atomic structure demonstrates the central copper atom without any surrounding oxygen atoms, which verifies the reduction of CuO to Cu (Figure 4.4e). Additionally, the XRD result of InO_x@CuO after CO_2RR also reveals that the CuO is reduced to metallic Cu, as further verified by the Fourier transform k^2-weighted function of the EXAFS spectra in R space, where only Cu-Cu metallic bond is observed in the InO_x@CuO (Figure S19). Nevertheless, a little difference in the chemical states of Cu with the presence of small peaks of Cu^{2+} is observed in the XPS results (Figure 4.4f), which might be caused by the re-oxidation of the metastable Cu^0 on the surface of the material after CO_2RR. Concurrently, the binding energies of In 3d demonstrate the complete reduction of In species to metallic In (Figure

4.4g). Although CuO and In species are both reduced to metallic state, the morphology of the

catalyst and FE of CO show negligible changes.
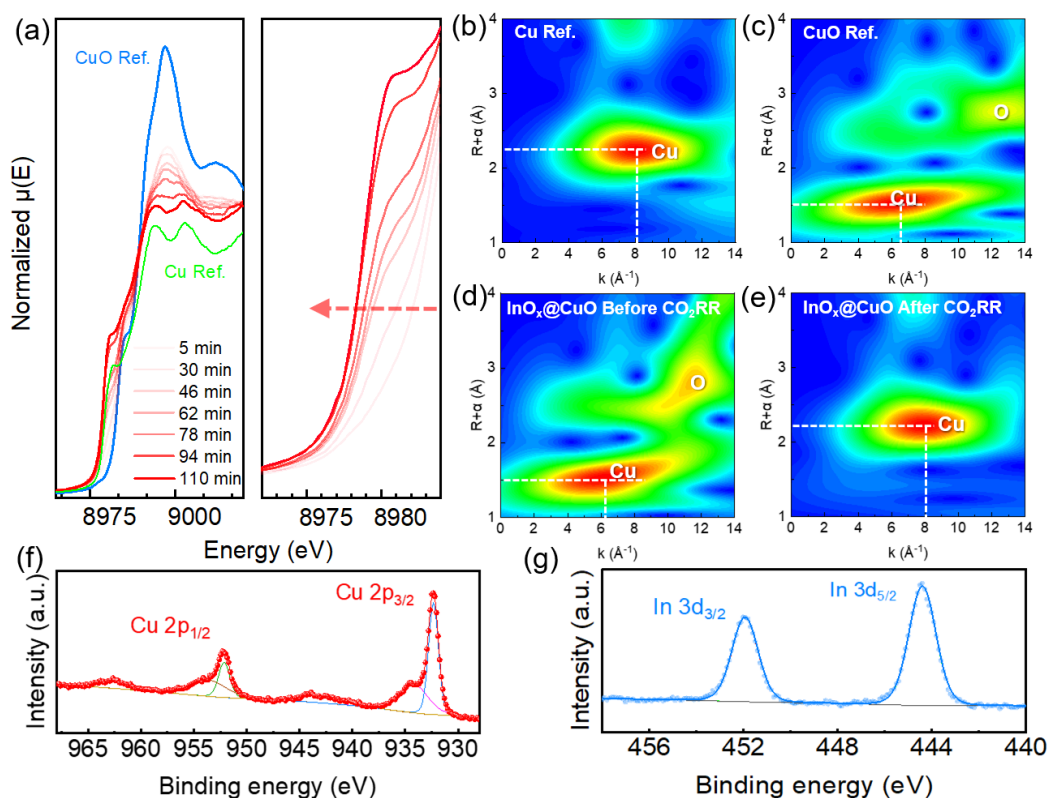
Figure 4.4 (a) *In situ* Cu K-edge XAS spectra of InO$_x$@CuO at the applied potential of -0.6

V over the course of 2 h; Wavelet transforms of EXAFS spectra (WT-EXAFS) at Cu K-edge

for (b) Cu reference, (c) CuO reference, (d) InO$_x$@CuO before CO$_2$RR and (e) InO$_x$@CuO

after CO$_2$RR; High-resolution XPS spectra of (f) Cu 2p and (g) In 3d of InO$_x$@CuO

electrocatalyst after CO$_2$RR.

It is believed that the synergism of Cu and In makes the dominant contribution to the

selectivity for CO formation, as has also been reported in the relevant studies [40, 43, 46]. It

is noteworthy that the core level binding energies of Cu and In in XPS results slightly shift

after CO$_2$RR as compared to the reported values. The binding energy of In 3d shifts 0.6 eV

to a higher value, while the peak of Cu 2p shifts to the lower binding energy. These changes indicate the existence of electron relocation between Cu and In during CO_2RR. The strong electronegativity of Cu guarantees the electron transfer from In to Cu, which further improves the CO_2RR performance.

To better understand the reaction mechanism of CO_2RR on $InO_x@CuO$, the DFT calculations were performed on the pathways of CO formation and HER. As the slow reduction of CuO at applied negative potential, metallic Cu and In will serve as the main active sites till the end. Thus, the DFT calculations for CO_2RR were performed on metallic Cu and In incorporated metallic Cu (In@Cu) accordingly. As shown in Figure 4.5a, the Gibbs free energies (ΔG) for *COOH formation are 0.88 and 0.50 eV on Cu and In@Cu, respectively. The incorporation of In on Cu significantly decreases the intermediate *COOH formation energy by 0.38 eV. The ΔG for *CO formation decreases on both Cu and In@Cu, suggesting the energetically favorable step from *COOH to *CO. Moreover, the desorption energy barrier of *CO on In@Cu (0.03 eV) is much lower than that on Cu (0.30 eV), ensuring the better desorption of *CO on In@Cu. Thus, the lower energy barrier for CO formation proves the higher selectivity of CO with incorporation of In species. In addition, Figure 4.5b shows the ΔG for the competitive HER. It can be found the formation energy of *H is 0.4 eV on In@Cu, which is considerably higher than that on Cu surface (0.02 eV). The higher energy barrier of *H formation on In@Cu leads to the lower catalytic activity toward HER, indicating that the incorporation of In on Cu significantly suppresses the H_2 production, which are beneficial to CO_2RR. Figure 4.5c shows the schematic diagram for CO_2RR to CO on $InO_x@CuO$. The CO_2 will adsorb on the catalyst surface first with the fast-initial electron transfer step to form *CO_2^-. Subsequently, an additional electron and a proton transfer to the

adsorbed $*CO_2^-$ to form $*COOH$ and finally, the CO and H_2O will be produced. Based on the above discussion, the lower energy barrier of $InO_x@CuO$ for CO_2RR and effective suppression of HER jointly contribute to the high selectivity towards CO formation, and thereby guarantees the enhanced CO_2RR performance on $InO_x@CuO$.
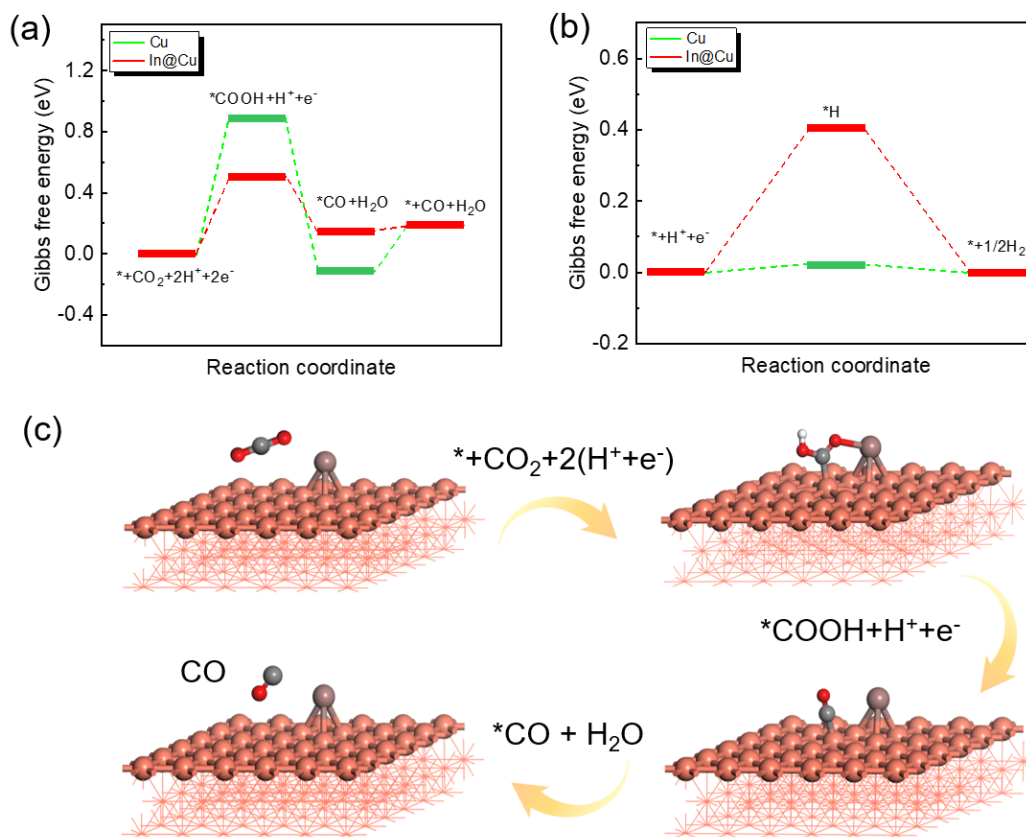
Figure 4.5 Gibbs free energies for (a) CO_2 to CO and (b) H_2 evolution on Cu and In@Cu; (c) Schematic reaction mechanism diagram of CO_2RR to CO over $InO_x@CuO$.

4.2.5 The origins of enhanced catalytic performance

To rule out the size effect, the electrochemical active surface areas (ECSAs) of CuO and $InO_x@CuO$ were determined (Figures 4.6a). It is found that the CuO with In species possesses a larger ECSA than dendrites CuO, which consequently offers substantial amount of active sites and good accessibility of CO_2-saturated media to these active sites. These

account for the comparably higher specific catalytic activity and eventually, the enhanced CO_2RR performance of $InO_x@CuO$. To gain more insights into the kinetics of CO_2RR to CO, ECSA-corrected Tafel plots were analyzed and shown in Figure 4.6b based on the $j_{(CO)}$ at various overpotentials. The results show two different rate-determining steps for CO formation during CO_2RR. Clearly, the Tafel slope of 146.65 mV dec^{-1} on CuO is closer to the theoretical value of 118 mV dec^{-1}, consistent with a rate-determining initial electron transfer to CO_2 for the formation of an adsorbed $*CO_2^-$ intermediate, i.e., $CO_2 + e^- \rightarrow *CO_2^-$ [49, 50]. In contrast, the Tafel slope of 70.45 mV dec^{-1} on $InO_x@CuO$ is closer to the theoretical value of 59 mV dec^{-1}, in support of a mechanism that involves a reversible electron transfer to CO_2 for the formation of $*CO_2^-$, followed by a rate-determining proton transfer with HCO_3^- serving as the proton donor, i.e., $*CO_2^- + HCO_3^- \rightarrow *COOH + CO_3^{2-}$ [51, 52]. The fast pre-equilibrium of CO_2 to $*CO_2^-$ during CO_2RR provides a better stability of electrocatalyst to stabilize the intermediates. The Tafel slope of 70.45 mV dec^{-1} well illustrates a better $*CO_2^-$ stabilization ability on $InO_x@CuO$ than that on CuO, which ensures the excellent performance of $InO_x@CuO$ for CO_2RR. To further verify that the rate-determining step of $InO_x@CuO$ is the proton transfer from HCO_3^-, the catalytic performance was also evaluated in CO_2-saturated 0.5 M $KHCO_3$ electrolyte. Clearly, both current densities and FEs of CO increase compared to that in 0.1 M $KHCO_3$ (Figure S4.14). The $InO_x@CuO$ shows a wider potential range from -0.8 to -0.3 V for CO FE of over 90%, with the maximum value of 98.5% at -0.6 V. The result demonstrates a better catalytic performance in a high concentration of electrolyte, further indicating the benefits of the increment of HCO_3^- during CO_2RR.
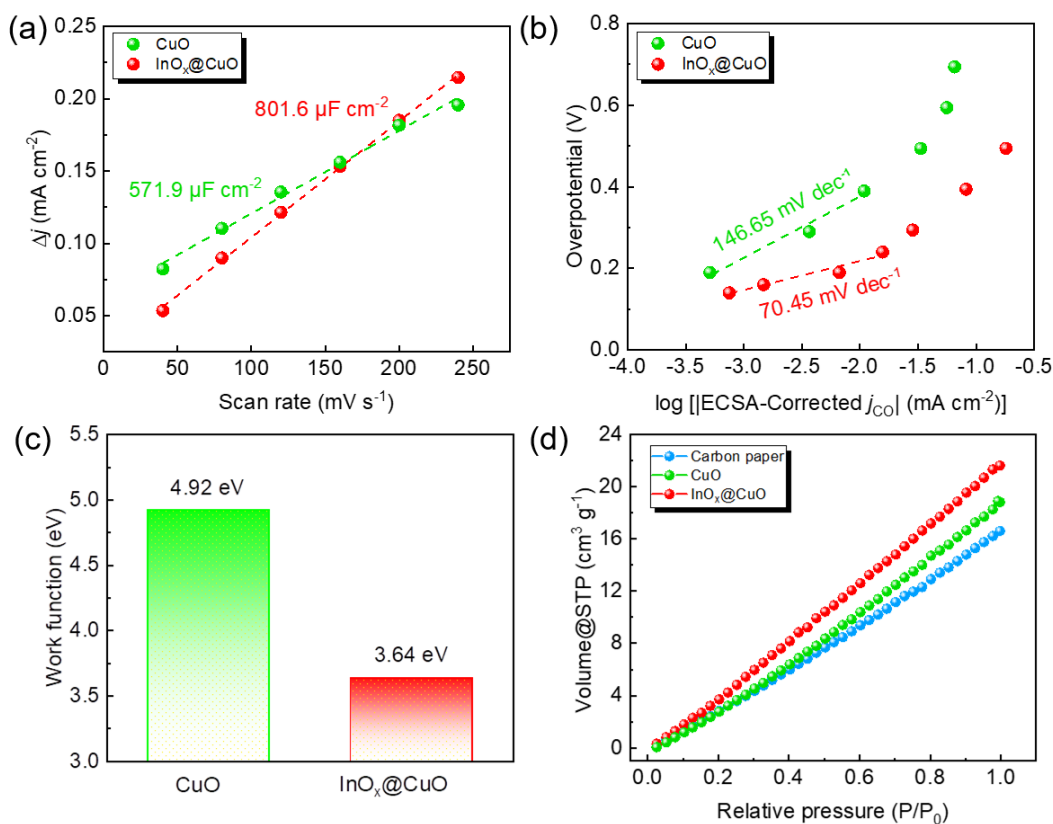
Figure 4.6 (a) Charging current density differences (Δj) plotted against scan rates; (b) ECSA-corrected Tafel plots for CO production; (c) Work functions based on experimental calculations; (d) CO_2 adsorption isotherms of carbon paper, CuO and $InO_x@CuO$.

It is well known that a quick electron transfer ability of a material is crucial to ensure a high CO_2RR performance, therefore, electrochemical impedance spectroscopy (EIS) was carried out at a fixed potential of -0.6 V in CO_2-saturated 0.1 M $KHCO_3$. The Nyquist plots show a smaller charge transfer resistance over $InO_x@CuO$ than that over CuO, where the identical semicircles position indicate the similar Ohmic resistance in the cell (Figure S4.15). Clearly, the introduction of In species on CuO could accelerate electron transfer and largely lower the polarization resistance for CO_2RR, which consequently enhances the catalytic performance. This was further confirmed by the work functions of CuO and $InO_x@CuO$, measured by

ultraviolet photoelectron spectroscopy (UPS). It has been widely accepted that the work function is strongly correlated to catalytic activity. Apparently, $InO_x@CuO$ shows a lower work function (i.e., 3.64 eV) than CuO (i.e., 4.92 eV, Figures 4.6c and S4.16), demonstrating a superior electron transfer ability of $InO_x@CuO$, this also accounts for the fast pre-equilibrium of CO_2 to $CO_2^{•-}$ that promotes the better stabilization of the intermediates during CO_2RR. It is also commonly known that the low solubility of CO_2 in aqueous media limits its mass transfer during CO_2RR and as a result, restrains the current density. Hence, improving CO_2 adsorption capability plays a key role in CO_2RR. To that end, volumetric CO_2 adsorption-desorption isotherms were thus carried out to evaluate the CO_2 adsorption capability over carbon paper, CuO and $InO_x@CuO$ (Figures 4.6d). Apparently, CuO exhibits a comparably larger CO_2 adsorption capacity (i.e., 18.9 cm^3 g^{-1} at P/P_0 of 1.0) as compared to carbon paper (i.e., 16.7 cm^3 g^{-1} at P/P_0 of 1.0), indicating that the electrodeposited dendritic morphology could greatly improve the CO_2 adsorption ability. By introducing the In species on CuO, the CO_2 adsorption capability of $InO_x@CuO$ (i.e., 21.7 cm^3 g^{-1} at P/P_0 of 1.0) is improved to about 1.4 times higher than that of carbon paper at P/P_0 of 1.0, and slightly higher than that of CuO, suggesting that the coverage of In species on CuO actually improves the accessibility of CO_2 to active sites, i.e., more efficient mass transfer. The enhanced CO_2 adsorption capacity of $InO_x@CuO$ can certainly offer good mass transfer in aqueous media and consequently, increase the current density. All these factors collectively contribute to the outstanding performance of $InO_x@CuO$ with high activity and selectivity for CO_2RR to CO and more impressively, it outperforms most of the state-of-the-art Cu-based materials. In light of the above results, utilizing earth-abundant metals to synthesize highly selective/stable

electrocatalysts via incorporating a secondary material has been proven to be an effective strategy to design catalysts for more efficient and cost effective CO_2RR to CO.

4.3 Conclusions

In summary, the electrocatalyst CuO with In species is successfully synthesized and exhibits good electrocatalytic performance for CO_2RR to CO. More specifically, a current density of 7.2 mA cm^{-2} is obtained at -0.6 V with a near-unity Faradaic efficiency of CO. Moreover, the $InO_x@CuO$ shows an ultralow onset potential for CO formation and exhibits an excellent stability of over 50 h. The introduction of In species on CuO is found to accelerate electron transfer and stabilize the reaction intermediates. Furthermore, the synthesized $InO_x@CuO$ offers more abundant active sites, the lower work function and larger CO_2 adsorption capacity, all jointly contributing to the outstanding electrocatalytic performance. The research outputs of this work present an attractive approach to designing the electrocatalysts using earth-abundant materials and achieving enhanced electrocatalytic activity and good stability for CO_2RR.

4.4 References

[1]   X. Li, J. Yu, M. Jaroniec, X. Chen, *Chem Rev* **2019**, *119*, 3962-4179.

[2]   Y. Li, M. Zhang, L. Zhou, S. Yang, Z. Wu, Y. Ma, *Acta Physico Chimica Sinica* **2020**, *0*, 2009030-2009030.

[3]   O. S. Bushuyev, P. De Luna, C. T. Dinh, L. Tao, G. Saur, J. van de Lagemaat, S. O. Kelley, E. H. Sargent, *Joule* **2018**, *2*, 825-832.

[4]   P. De Luna, C. Hahn, D. Higgins, S. A. Jaffer, T. F. Jaramillo, E. H. Sargent, *Science* **2019**, *364*.

[5]   L. Cheng, D. Zhang, Y. Liao, J. Fan, Q. Xiang, *Chinese Journal of Catalysis* **2021**, *42*, 131-140.

[6]   J. Qiao, Y. Liu, F. Hong, J. Zhang, *Chem. Soc. Rev.* **2014**, *43*, 631-675.

[7]   C. Xu, J. Hong, P. Sui, M. Zhu, Y. Zhang, J.-L. Luo, *Cell Reports Physical Science* **2020**, *1*, 100101.

[8]   R. Francke, B. Schille, M. Roemelt, *Chem. Rev.* **2018**, *118*, 4631-4701.

[9]   C. Chen, J. F. Khosrowabadi Kotyk, S. W. Sheehan, *Chem* **2018**, *4*, 2571-2586.

[10]   M. G. Kibria, J. P. Edwards, C. M. Gabardo, C. T. Dinh, A. Seifitokaldani, D. Sinton, E. H. Sargent, *Adv. Mater.* **2019**, *31*, 1807166.

[11]   Z. Chen, M.-R. Gao, N. Duan, J. Zhang, Y.-Q. Zhang, T. Fan, J. Zhang, Y. Dong, J. Li, Q. Liu, X. Yi, J.-L. Luo, *Appl. Catal. B-Environ.* **2020**, *277*, 119252.

[12]   C. Costentin, M. Robert, J. M. Saveant, *Chem. Soc. Rev.* **2013**, *42*, 2423-2436.

[13]   R. S. Weber, *ACS Catal.* **2018**, *9*, 946-950.

[14]   Y. Hou, Y.-L. Liang, P.-C. Shi, Y.-B. Huang, R. Cao, *Appl. Catal. B-Environ.* **2020**, *271*, 118929.

[15]   S. Liu, H. Tao, L. Zeng, Q. Liu, Z. Xu, Q. Liu, J. L. Luo, *J. Am. Chem. Soc.* **2017**, *139*, 2160-2163.

[16]   S. Liu, X.-Z. Wang, H. Tao, T. Li, Q. Liu, Z. Xu, X.-Z. Fu, J.-L. Luo, *Nano Energy* **2018**, *45*, 456-462.

[17]   Y. Chen, C. W. Li, M. W. Kanan, *J. Am. Chem. Soc.* **2012**, *134*, 19969-19972.

[18]   J.-H. Kim, H. Woo, S.-W. Yun, H.-W. Jung, S. Back, Y. Jung, Y.-T. Kim, *Appl. Catal. B-Environ.* **2017**, *213*, 211-215.

[19]   H. Huang, H. Jia, Z. Liu, P. Gao, J. Zhao, Z. Luo, J. Yang, J. Zeng, *Angew. Chem. Int. Ed.* **2017**, *56*, 3594-3598.

[20]   K. Liu, J. Wang, M. Shi, J. Yan, Q. Jiang, *Advanced Energy Materials* **2019**, *9*, 1900276.

[21]   W. Luo, J. Zhang, M. Li, A. Züttel, *ACS Catalysis* **2019**, *9*, 3783-3791.

[22]   J. Xiao, M. R. Gao, S. Liu, J. L. Luo, *ACS Appl. Mater. Interfaces* **2020**, *12*, 31431-31438.

[23]   A. Bagger, W. Ju, A. S. Varela, P. Strasser, J. Rossmeisl, *Chemphyschem* **2017**, *18*, 3266-3273.

[24]   X. Su, Y. Sun, L. Jin, L. Zhang, Y. Yang, P. Kerns, B. Liu, S. Li, J. He, *Appl. Catal. B-Environ.* **2020**, *269*, 118800.

[25]   Q. Zhu, X. Sun, D. Yang, J. Ma, X. Kang, L. Zheng, J. Zhang, Z. Wu, B. Han, *Nat Commun* **2019**, *10*, 3851.

[26]   D. Wakerley, S. Lamaison, F. Ozanam, N. Menguy, D. Mercier, P. Marcus, M. Fontecave, V. Mougel, *Nat. Mater.* **2019**, *18*, 1222-1227.

[27]   C. Choi, T. Cheng, M. Flores Espinosa, H. Fei, X. Duan, W. A. Goddard, Y. Huang, *Adv. Mater.* **2019**, *31*, 1805405.

[28]   S. N. Zhang, M. Li, B. Hua, N. Duan, S. Ding, S. Bergens, K. Shankar, J. L. Luo, *ChemCatChem* **2019**, *11*, 4147-4153.

[29]   Q. Li, J. Fu, W. Zhu, Z. Chen, B. Shen, L. Wu, Z. Xi, T. Wang, G. Lu, J. J. Zhu, S. Sun, *J. Am. Chem. Soc.* **2017**, *139*, 4290-4293.

[30]   S. Liu, J. Xiao, X. F. Lu, J. Wang, X. Wang, X. W. D. Lou, *Angew. Chem. Int. Ed.* **2019**, *58*, 8499-8503.

[31]   Q. Gong, P. Ding, M. Xu, X. Zhu, M. Wang, J. Deng, Q. Ma, N. Han, Y. Zhu, J. Lu, Z. Feng, Y. Li, W. Zhou, Y. Li, *Nat. Commun.* **2019**, *10*, 2807.

[32]   D. Wu, G. Huo, W. Chen, X.-Z. Fu, J.-L. Luo, *Appl. Catal. B-Environ.* **2020**, *271*, 118957.

[33]   R. Hegner, L. F. M. Rosa, F. Harnisch, *Appl. Catal. B-Environ.* **2018**, *238*, 546-556.

[34]   D. D. Zhu, J. L. Liu, S. Z. Qiao, *Adv. Mater.* **2016**, *28*, 3423-3452.

[35]   B. E. Conway, G. Jerkiewicz, *Electrochimica Acta* **2000**, *45*, 4075-4083.

[36]   P. Devi, K. Malik, E. Arora, S. Bhattacharya, V. Kalendra, K. V. Lakshmi, A. Verma, J. P. Singh, *Catalysis Science & Technology* **2019**, *9*, 5339-5349.

[37]   W. Luo, W. Xie, R. Mutschler, E. Oveisi, G. L. De Gregorio, R. Buonsanti, A. Züttel, *ACS Catalysis* **2018**, *8*, 6571-6581.

[38]   H. Xiang, S. Rasul, B. Hou, J. Portoles, P. Cumpson, E. H. Yu, *ACS Appl Mater Interfaces* **2020**, *12*, 601-608.

[39]   J.Y.Kim, J. A. Rodriguez, J. C. Hanson, A. I. Frenkel, P. L. Lee, *J. Am. Chem. Soc.* **2003**, *125*, 10684-10692.

[40]   X. Wang, J. C. Hanson, A. I. Frenkel, J. Y. Kim, J. A. Rodriguez, *J. Phys. Chem. B* **2004**, *108*, 13667-13673.

[41]   J. F. Xu, W. Ji, Z. X. Shen, W. S. Li, S. H. Tang, X. R. Ye, X. Q. Xin, *J. Raman Spectrosc.* **1999**, *30*, 413-415.

[42]   H. Zhu, X. Wang, F. Yang, X. Yang, *Cryst. Growth Des.* **2008**, *8*, 950-956.

[43]   T. Li, H. Wei, T. Liu, G. Zheng, S. Liu, J. L. Luo, *ACS. Appl. Mater. Interfaces* **2019**, *11*, 22346-22351.

[44]   F. L. P. Veenstra, A. J. Martin, J. Perez-Ramirez, *ChemSusChem* **2019**, *12*, 3501-3508.

[45]   Y. J. Jang, J. Lee, J. H. Kim, B. J. Lee, J. S. Lee, *Journal of Power Sources* **2018**, *378*, 412-417.

[46]   G. O. Barasa, T. Yu, X. Lu, X. Zhou, H. Wang, L. Qian, Y. Yu, L. Liu, P. Lei, *Electrochim. Acta* **2019**, *295*, 584-590.

[47]   P. De Luna, R. Quintero-Bermudez, C.-T. Dinh, M. B. Ross, O. S. Bushuyev, P. Todorović, T. Regier, S. O. Kelley, P. Yang, E. H. Sargent, *Nat. Catal.* **2018**, *1*, 103-110.

[48]   H. Mistry, A. S. Varela, C. S. Bonifacio, I. Zegkinoglou, I. Sinev, Y. W. Choi, K. Kisslinger, E. A. Stach, J. C. Yang, P. Strasser, B. R. Cuenya, *Nat. Commun.* **2016**, *7*, 12123.

[49]   Y. Chen, M. W. Kanan, *J. Am. Chem. Soc.* **2012**, *134*, 1986-1989.

[50]   X. Zhang, Z. Chen, M. Jiao, X. Ma, K. Mou, F. Cheng, Z. Wang, X. Zhang, L. Liu, *Appl. Catal. B-Environ.* **2020**, *279*, 119383.

[51]   C. W. Lee, N. H. Cho, S. W. Im, M. S. Jee, Y. J. Hwang, B. K. Min, K. T. Nam, *J. Mater. Chem. A* **2018**, *6*, 14043-14057.

[52]   L. Zhang, Z. J. Zhao, J. Gong, *Angew. Chem. Int. Ed.* **2017**, *56*, 11326-11353.

4.5 Supporting Information

4.5.1 Supporting figures and tables
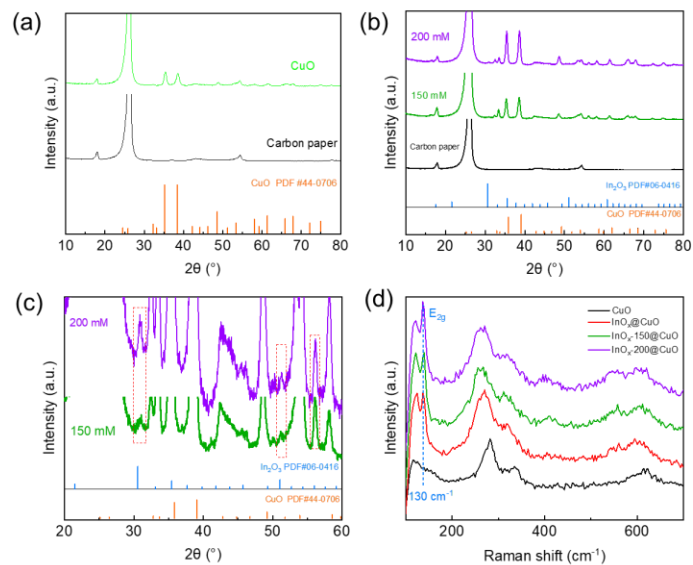
Figure S4.1 (a) XRD patterns of carbon paper and CuO before CO_2RR; (b) XRD patterns and (c) enlargement of InO_x-150@CuO and InO_x-200@CuO; (d) Raman spectra of prepared CuO, InO_x@CuO, InO_x-150@CuO and InO_x-200@CuO.
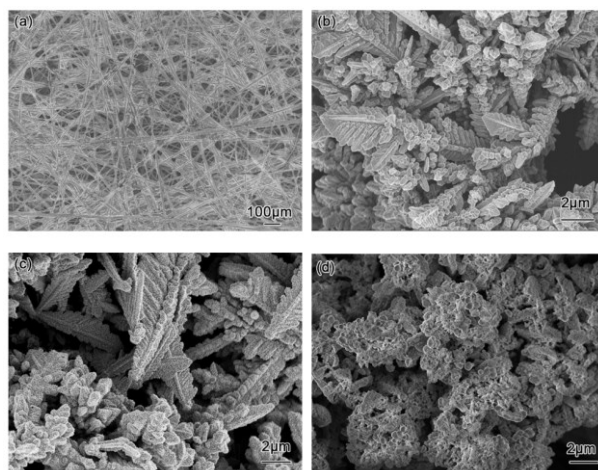
Figure S4.2 SEM images of (a) carbon paper, (b) electrodeposited Cu, (c) CuO and (d) InO_x@CuO.
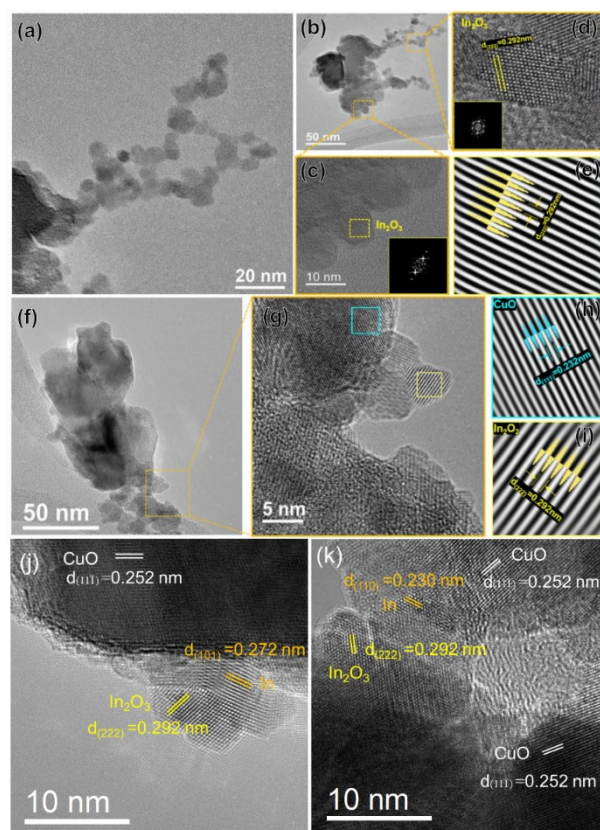
Figure S4.3 TEM images of $InO_x@CuO$ electrocatalyst and the HRTEM of selected corresponding areas with fast Fourier transformation.
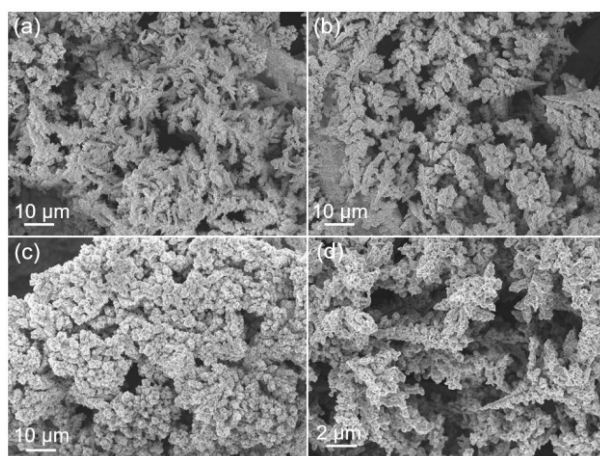
Figure S4.4 SEM images of (a) InO_x-10@CuO; (b) InO_x-50@CuO; (c) $InO_x@CuO$; (d) In-free CuO.
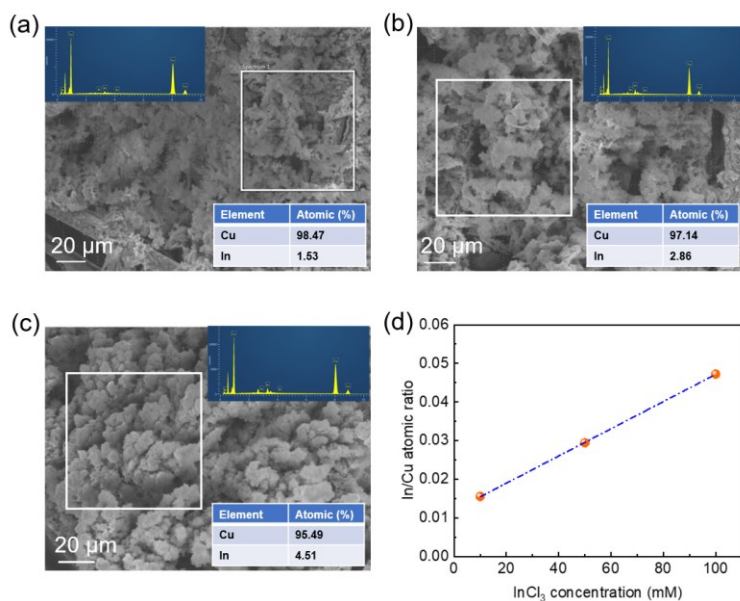
Figure S4.5 EDX analyses of (a) InO_x-10@CuO; (b) InO_x-50@CuO; (c) InO_x@CuO and (d) the In/Cu atomic ratio of the obtained catalysts.
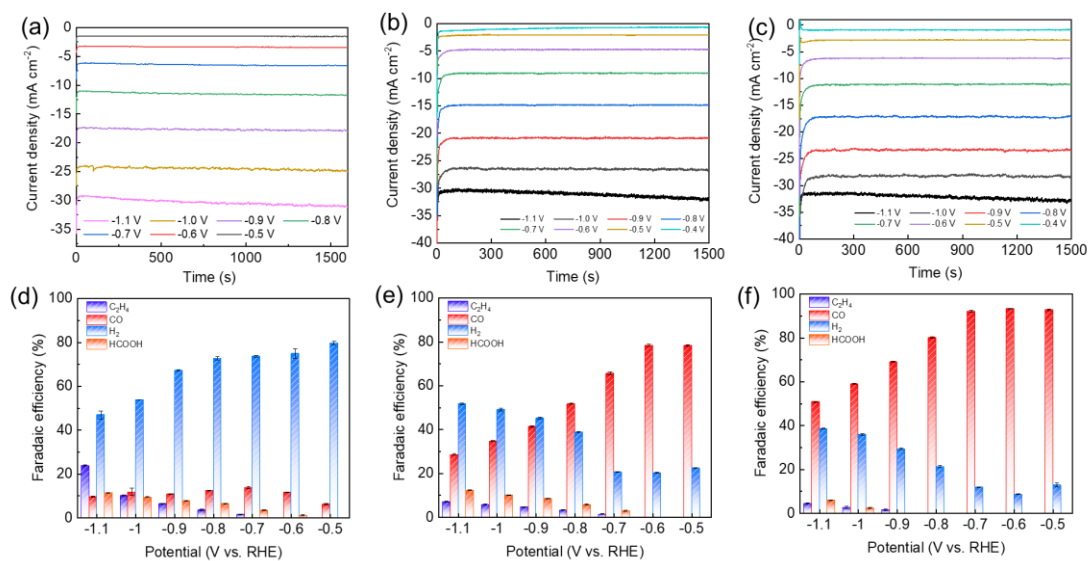
Figure S4.6 Plots of current densities as a function of time and Faradaic efficiencies for (a) and (d) In-free CuO; (b) and (e) InO_x-10@CuO; (c) and (f) InO_x-50@CuO.
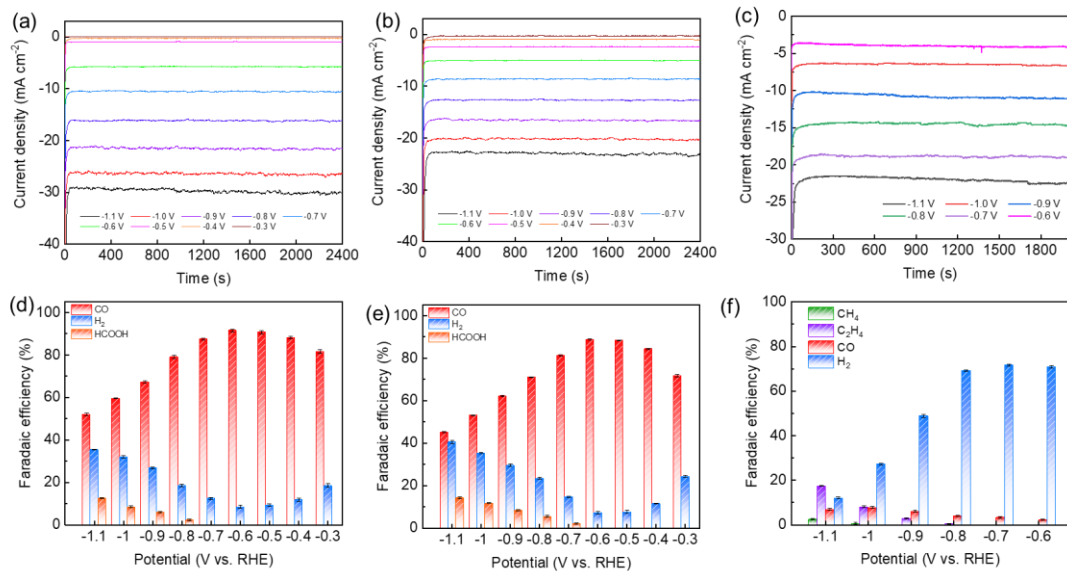
Figure S4.7 Plots of current densities as a function of time and Faradaic efficiencies for (a) and (d) InO$_x$-150@CuO; (b) and (e) InO$_x$-200@CuO; (c) and (f) electrodeposited Cu.
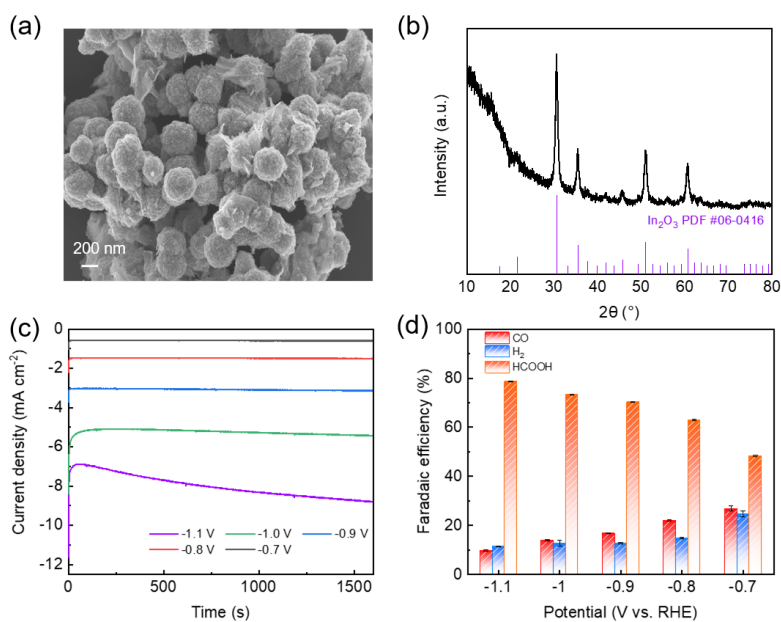
Figure S4.8 (a) SEM image of the as-prepared In$_2$O$_3$ nanoparticles; (b) XRD pattern of the In$_2$O$_3$ nanoparticles; (c) plots of current densities as a function of time at various potentials; (d) FEs of In$_2$O$_3$ nanoparticles at various potentials.
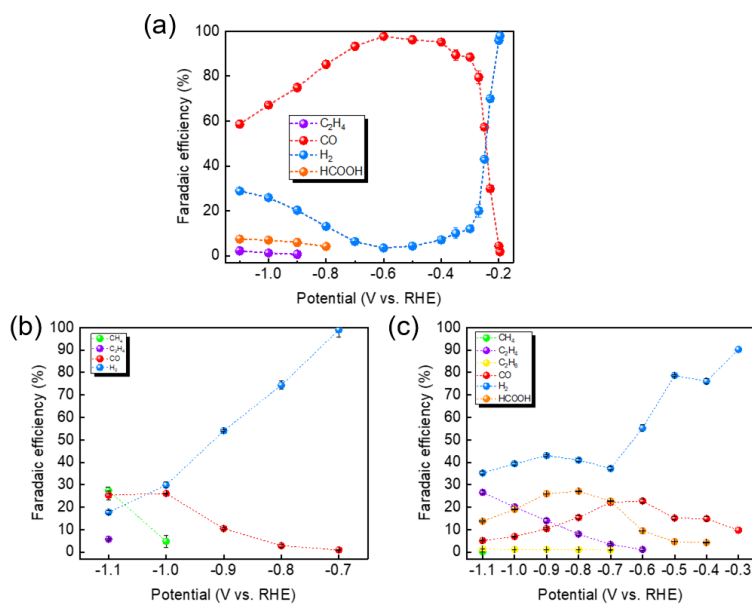
Figure S4.9 FEs of products over (a) InO$_x$@CuO, (b) carbon paper and (c) CuO at various potentials.
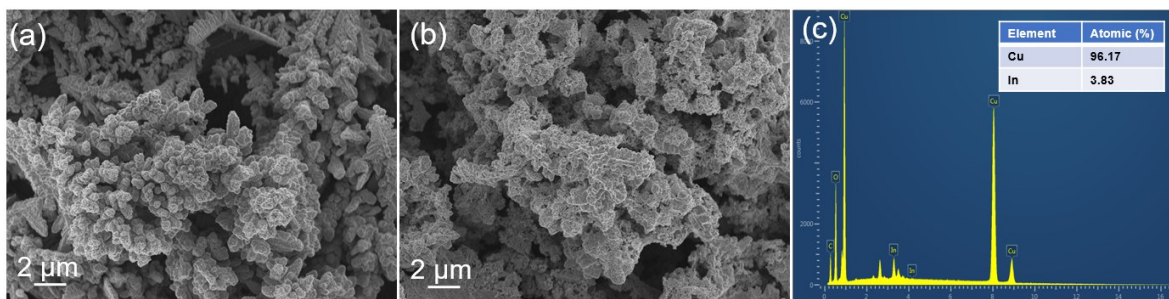
Figure S4.10 SEM images of electrocatalysts after CO$_2$RR (a) CuO; (b) InO$_x$@CuO; (c) EDX analysis of InO$_x$@CuO after CO$_2$RR.
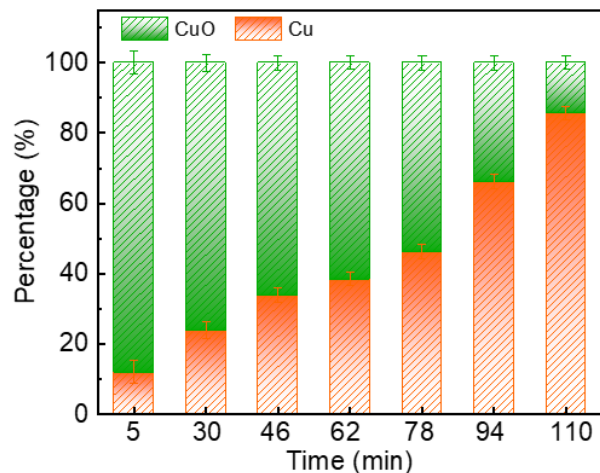
Figure S4.11 Percentage of each species over $InO_x@CuO$ during *in situ* measurement obtained from linear combination fitting analysis.
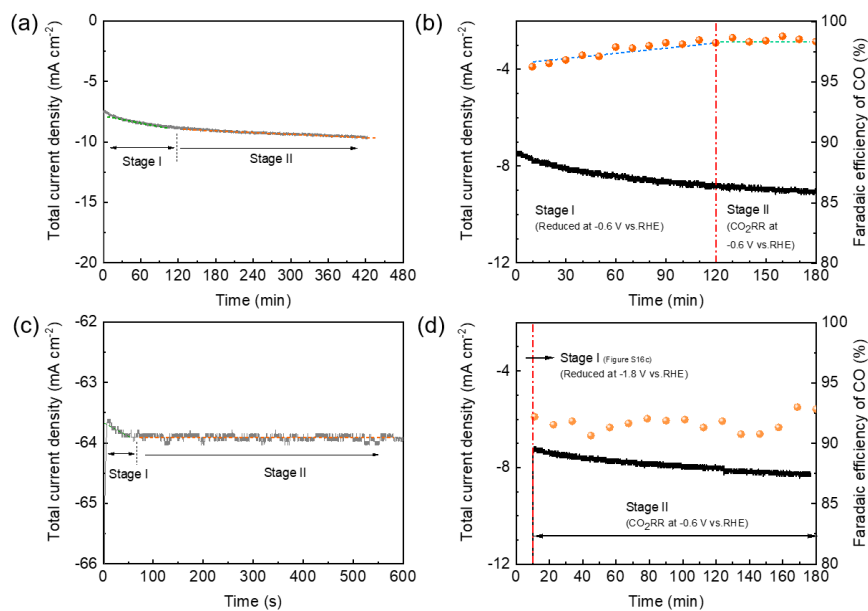
Figure S4.12 (a) The total current density of $InO_x@CuO$ at -0.6 V vs. RHE; (b) The total current density and FE of CO at -0.6 V vs. RHE; (c) The total current density of $InO_x@CuO$ at -1.8 V vs. RHE; (d) The total current density and FE of CO at -0.6 V vs. RHE for the $InO_x@CuO$ initially reduced at -1.8 V for 10 min.
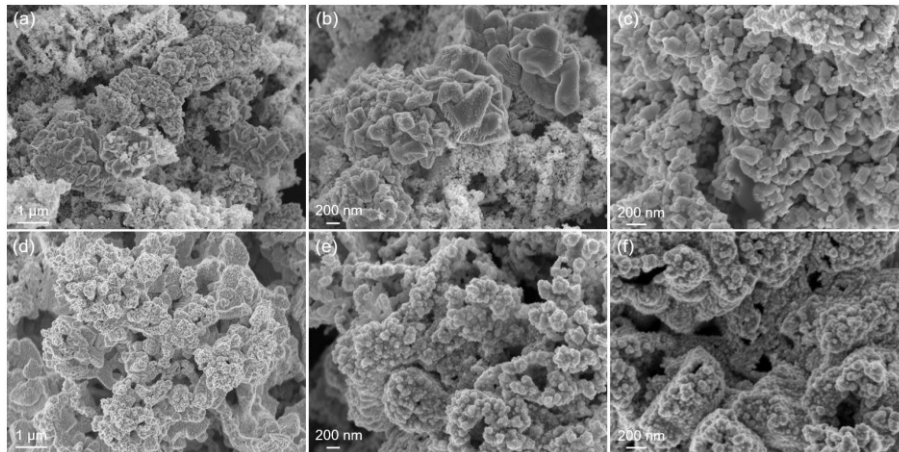
Figure S4.13 SEM images of (a), (b) and (c) InO$_x$@CuO after CO$_2$RR shown in Figure S16 d (initially reduced at -1.8 V for 10 min and then tested at -0.6 V); (d), (e) and (f) InO$_x$@CuO after CO$_2$RR test shown in Figure S 16 b (reduced and tested at -0.6 V).
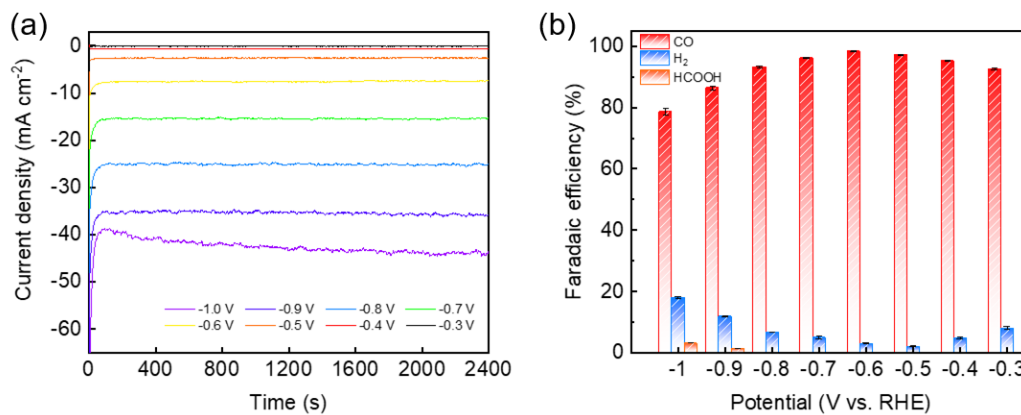
Figure S4.14 Plots of current densities as a function of time and Faradaic efficiencies for InO$_x$@CuO in CO$_2$-saturated 0.5 M KHCO$_3$ electrolyte.

75
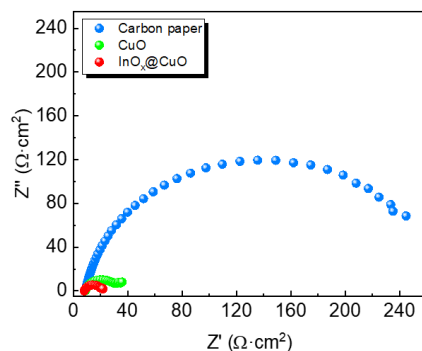
Figure S4.15 Nyquist plots of the electrochemical impedance spectra of electrocatalysts at -0.6 V vs. RHE in CO_2-satured 0.1 M $KHCO_3$ electrolyte.
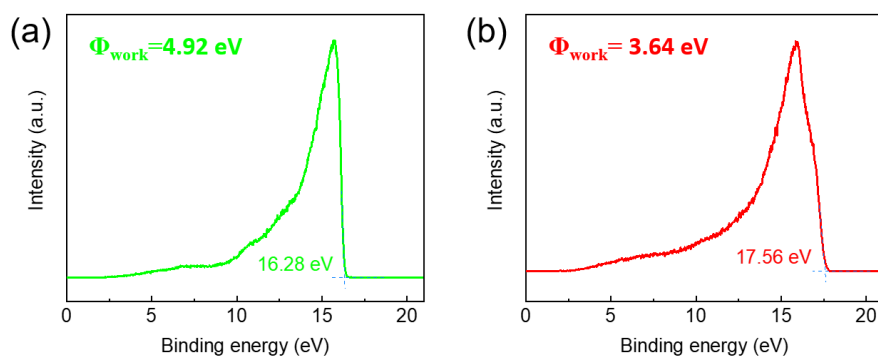
Figure S4.16 UPS plots of (a) CuO and (b) InO_x@CuO.

Determination of work function

The work functions of CuO and InO_x@CuO were measured through the use of ultraviolet photoelectron spectroscopy. UPS data were acquired with a Kratos AXIS Ultra photoelectron spectrometer using He I (21.2 eV) ultraviolet radiation and pass energy of 10 eV. Each sample has a distinct Fermi edge for various V_{bias} values, and by extrapolating the cut-off energies to $V_{bias}= 0$, we then determined the work function values.

Table S4.1 ICP-OES results of atomic ratio on In/Cu over different electrocatalysts.

Catalyst	Atomic ratio of In/Cu
InO_x-10@CuO	0.008
InO_x-50@CuO	0.014
InO_x@CuO	0.027
InO_x-150@CuO	0.039
InO_x-200@CuO	0.050

Table S4.2 Energy efficiency calculation results based on the measured potentials and FEs of CO.

Applied cathode potential (V vs. RHE)	Measured cell potential (V)	FE of CO (%)	Energy efficiency (%)
-0.20	-1.96	4.32	1.90
-0.25	-2.13	57.30	23.14
-0.30	-2.28	90.42	34.14
-0.40	-2.41	95.19	33.97
-0.50	-2.55	96.20	32.44
-0.60	-2.62	97.80	32.10
-0.70	-2.78	93.37	28.88
-0.80	-2.83	85.32	25.93
-0.90	-2.98	74.97	21.64
-1.00	-3.04	67.15	19.00
-1.10	-3.17	58.63	15.91

*Measured cell potential at current density equal to zero, E_{cell} = -0.86 V; all the measured potentials are without *iR* compensation.

Table S4.3 Summary of metal-based catalysts for CO production in CO_2RR.

Catalyst	Onset potential (V vs. RHE)	Potential range of FE_{CO} over 90% (mV)	FE_{COmax} (%)	j_{CO} at FE_{COmax} (mA cm^{-2})	Stability (h)	Ref.
Cu-In alloy	-0.3	None	90	0.5	7	[1]
In-deposited Cu NWs	-0.4	300	93	2.5	60	[2]
Nanoporous Cu-In	-0.45	200	91	4.1	7	[3]
CuO/In$_2$O$_3$ composites	-0.5	None	93	4.3	10	[4]
In(OH)$_3$-Coupled Cu$_2$O	-0.3	200	90.37	2.1	12	[5]
In$_2$O$_3$/Cu$_3$N	None	None	80	1.6	50	[6]
CuO/In$_2$O$_3$ composites	-0.4	None	85	None	None	[7]
H-Zn-NPs	-0.66	400	94.2	5.2	12	[8]
L25-Ag-NCs	-0.256	300	99	1.7	18	[9]
Sponge-like porous Ag	-0.3	100	93	7	24	[10]
SnO$_x$/Ag	-0.6	None	85	1	12	[11]
Zn/ZnS	-0.55	200	94.2	4.28	15	[12]
Porous Zn nanosheets	-0.6	None	88	8.5	12	[13]
Sn-decorated Cu$_x$O NWs	-0.5	None	90	4.5	12	[14]
ZnGa$_2$O$_4$	-0.7	None	96	0.5	10	[15]
CdS	-0.7	None	81	21.9	10	[16]
Fe-N-C	-0.35	None	65	2.5	None	[17]
NiN$_x$CNT-900	-0.35	500	98	9	44	[18]
InO$_x$@CuO	**-0.196**	**400**	**97.8**	**7.2**	**50**	**This work**

Table S4.4 Linear combination fitting results of each species over InO$_x$@CuO during *in situ* measurement.

Time (min)	CuO (%)	Cu (%)	Error (%)	R-factor
5	87.86	12.14	3.26	0.0581805
30	75.95	24.05	2.44	0.033582
46	66.12	33.88	2.12	0.0260207
62	61.43	38.57	1.94	0.0217796
78	53.57	46.43	2.01	0.0248868
94	33.72	66.28	2.15	0.0299469
110	14.28	85.72	1.94	0.0250946

4.5.2 Supporting references

[1]   S. Rasul, D. H. Anjum, A. Jedidi, Y. Minenkov, L. Cavallo, K. Takanabe, *Angew Chem Int Ed Engl* **2015**, *54*, 2146-2150.

[2]   W. Luo, W. Xie, R. Mutschler, E. Oveisi, G. L. De Gregorio, R. Buonsanti, A. Züttel, *ACS Catalysis* **2018**, *8*, 6571-6581.

[3]   G. O. Barasa, T. Yu, X. Lu, X. Zhou, H. Wang, L. Qian, Y. Yu, L. Liu, P. Lei, *Electrochim. Acta* **2019**, *295*, 584-590.

[4]   S. Chu, S. Hong, J. Masa, X. Li, Z. Sun, *Chem Commun (Camb)* **2019**, *55*, 12380-12383.

[5]   T. Li, H. Wei, T. Liu, G. Zheng, S. Liu, J. L. Luo, *ACS. Appl. Mater. Interfaces* **2019**, *11*, 22346-22351.

[6]   F. L. P. Veenstra, A. J. Martin, J. Perez-Ramirez, *ChemSusChem* **2019**, *12*, 3501-3508.

[7]   P. Devi, K. Malik, E. Arora, S. Bhattacharya, V. Kalendra, K. V. Lakshmi, A. Verma, J. P. Singh, *Catalysis Science & Technology* **2019**, *9*, 5339-5349.

[8]   J. Xiao, M. R. Gao, S. Liu, J. L. Luo, *ACS Appl. Mater. Interfaces* **2020**, *12*, 31431-31438.

[9]   S. Liu, C. Sun, J. Xiao, J.-L. Luo, *ACS Catal.* **2020**, *10*, 3158-3163.

[10]   T. Fan, Q. Wu, Z. Yang, Y. Song, J. Zhang, P. Huang, Z. Chen, Y. Dong, W. Fang, X. Yi, *ChemSusChem* **2020**, *13*, 2677-2683.

[11]   Z. Cai, Y. Wu, Z. Wu, L. Yin, Z. Weng, Y. Zhong, W. Xu, X. Sun, H. Wang, *ACS Energy Letters* **2018**, *3*, 2816-2822.

[12]   C. Li, G. Shen, R. Zhang, D. Wu, C. Zou, T. Ling, H. Liu, C. Dong, X.-W. Du, *J. Mater. Chem. A* **2019**, *7*, 1418-1423.

[13]   K. Liu, J. Wang, M. Shi, J. Yan, Q. Jiang, *Advanced Energy Materials* **2019**, *9*, 1900276.

[14]   Y. Zhao, C. Wang, G. G. Wallace, *Journal of Materials Chemistry A* **2016**, *4*, 10710-10718.

[15]   M. Zhao, Y. Gu, P. Chen, Z. Xin, H. Zhu, B. Wang, K. Zhu, S. Yan, Z. Zou, *Journal of Materials Chemistry A* **2019**, *7*, 9316-9323.

[16]   R. He, A. Zhang, Y. Ding, T. Kong, Q. Xiao, H. Li, Y. Liu, J. Zeng, *Adv Mater* **2018**, *30*.

[17]   W. Ju, A. Bagger, G. P. Hao, A. S. Varela, I. Sinev, V. Bon, B. Roldan Cuenya, S. Kaskel, J. Rossmeisl, P. Strasser, *Nat Commun* **2017**, *8*, 944.

[18]   X. Wang, D. Wu, C. Dai, C. Xu, P. Sui, R. Feng, Y. Wei, X.-Z. Fu, J.-L. Luo, *Journal of Materials Chemistry A* **2020**, *8*, 5105-5114.

Chapter 5. Interface-induced electrocatalytic enhancement of CO_2-to-formate conversion on heterostructured bismuth-based catalysts

5.1 Introduction

The ever-increasing utilization of carbon-based fuels to meet the growing energy demand has caused the excessive CO_2 emission into the atmosphere, inevitably causing global greenhouse effect and other environmental issues. So far, various strategies, such as photocatalysis, thermal catalysis and chemical catalysis, among others, have been invoked to battle the record-breaking CO_2 emission. Electrochemical CO_2 reduction reaction (CO_2RR), when utilizing the electric power from renewable energy, has drawn particular attentions to sustainably and economically lower the level of atmospheric CO_2, alleviate greenhouse gas effect and to simultaneously convert CO_2 to value-added industrial products [1-5]. However, the inertness of CO_2 molecule, the sluggish multi-electron transfer kinetics and the competitive hydrogen evolution reaction (HER) during CO_2RR result in the high overpotential (η) to various degrees, which jeopardizes CO_2RR performance [6, 7]. Therefore, it is highly desirable to develop the electrocatalysts that are capable of compromising the above impediments and simultaneously achieving the optimal CO_2RR performance through specific optimization process.

Formic acid (HCOOH) or formate, as an important liquid product from CO_2RR, has been widely employed as chemical intermediates in various industrial processes [8]. The common industrial manufacture of HCOOH involves the carbonylation of methanol prior to the hydrolyzing of methyl formate. This process is performed in the liquid phase at elevated

pressure, which is an energy-intensive and high-cost process [9]. In contrast, CO_2RR to HCOOH requires a quite mild reduction condition. Currently, some metal-based materials (e.g., Sn [10-12], Pb [13-15], In [16, 17], and Cd [18, 19]) have been studied for HCOOH formation during CO_2RR because of their suitable binding energy for the intermediate HCOO* [20, 21]. However, the high cost and toxicity of these heavy metals (e.g., Pb, Cd, In etc.) preclude their scalability. Remarkably, Bi-based materials have attracted much attention owing to their low toxicity, earth-abundance, and good selectivity towards formate formation. Various features of Bi-based materials, such as size, morphology and electrocatalysts with conductive support, have been widely investigated to achieve enhanced electrocatalytic activity and selectivity [22-24]. Nevertheless, their low current density and high overpotential are still the bottlenecks that restrict their practical applications at industrial level [25, 26]. Therefore, it is of great importance to fabricate the highly effective and stable Bi-based electrocatalysts, to explore the associated reaction mechanism in order to achieve an improved selectivity towards formate.

The complicated multi-electron transfer steps during CO_2RR suggest the importance of charge transfer ability of electrocatalyst [27, 28]. Various studies on Bi-based electrocatalysts, including the construction of Bi_2O_3 nanosheets (NSs) on multi-channel carbon matrix support [29], the fabrication of Bi_2O_3@C derived from metal-organic framework [30], graphene [31] and multiwalled carbon nanotubes [32], have demonstrated the effectiveness of using conductive carbon support to improve CO_2RR performance toward HCOOH formation to different extent through lowering the contact resistance and accelerating electron transfer. However, the issues of low current density, narrow potential range and relatively high but still unsatisfactory HCOOH selectivity still exist and need to be thoroughly addressed for Bi-

based materials to be practical electrocatalysts for efficient CO_2RR. Interface engineering is an effective approach to prompting electron transfer by constructing abundant interfaces within the catalysts [33-35]. This strategy has been proven to be effective in many electrochemical reactions, such as HER [36], oxygen evolution reaction [37, 38] and nitrogen reduction reaction [39]. The introduced interfaces between the two materials with different work functions and Fermi levels would benefit the electronic interaction at the interface and assist the electron redistribution. This would then optimize the binding energy and promote the fast electron transfer through interfaces, thus ensuring the high electrocatalytic activity and stability. Therefore, it is important to get more insights into the interface engineering over specific configuration of Bi-based electrocatalysts and its underlying intrinsic mechanism for CO_2RR.

In this study, the heterostructure of Bi_2S_3-Bi_2O_3 NSs was prepared for CO_2RR to formate through a facile synthesis method. Benefiting from the enhanced charge transfer ability, the Bi_2S_3-Bi_2O_3 NSs exhibit high Faradic efficiency ($FE_{formate}$) of over 90% in a wide potential window, where the maximum $FE_{formate}$ value of 93.82% is achieved at -1.1 V versus reversible hydrogen electrode (vs. RHE). Moreover, the high partial current density of about 200 mA cm^{-2} at -1.1 V, together with a small onset potential of -0.4 V for formate formation is obtained in a flow cell. The enhanced electrocatalytic performance of Bi_2S_3-Bi_2O_3 NSs could be attributed to the strengthened electron transfer ability induced by the electronic interaction between the Bi_2S_3 and Bi_2O_3 at the interface. Together with the increased number of active sites and improved CO_2 adsorption capacity, the Bi_2S_3-Bi_2O_3 NSs prove to be quite beneficial to improve the reaction kinetics and selectivity for CO_2RR toward formate formation. More importantly, this study demonstrates an attractive approach to designing

electrocatalysts via constructing specific configuration of heterostructure with substantial amounts of interfaces for fast charge transfer and strong electrocatalytic activity.

5.2 Results and discussion

5.2.1 Characterizations of Bi_2O_3-Bi_2S_3 nanosheets

The Bi_2O_3-Bi_2S_3 NSs were synthesized *via* a simple wet chemical method, as shown in Figure 5.1a. Briefly, the precursor of milky suspension bismuth salt was added dropwise into the sulfurization agent under stirring condition and the resulting mixture was then incubated to form the final product Bi_2S_3-Bi_2O_3 NSs at room temperature. The X-ray diffraction (XRD) patterns (Figures 5.1b and S5.1) were collected to characterize the crystalline structure of the prepared materials (e.g., Bi_2S_3-Bi_2O_3 NSs, the individual Bi_2O_3 NSs and Bi_2S_3 NPs). Clearly, the peaks of Bi_2S_3-Bi_2O_3 NSs match well with the standard patterns of the cubic phase Bi_2O_3 (JCPDS 52-1007) and the orthorhombic phase Bi_2S_3 (JCPDS 17-0320), suggesting the successful preparation of the Bi_2S_3-Bi_2O_3 NSs. This is further confirmed by the Fourier-transform infrared spectroscopy (FTIR) spectra (Figure S5.2c), where the bands at 528, 718 (716) and 961 cm^{-1} are assigned to the vibration of the bond between Bi and O, and the band at 619 cm^{-1} on Bi_2S_3-Bi_2O_3 NSs is attributed to the partial transformation of Bi-S, further confirming the successful preparation of Bi_2S_3-Bi_2O_3 NSs.

X-ray photoelectron spectroscopy (XPS) was utilized to further get insights into the electronic properties and chemical compositions. A high-resolution XPS spectrum of Bi 4f is presented in Figure 5.1c where the peaks at 164.3 and 159.0 eV correspond to the Bi $4f_{5/2}$ and Bi $4f_{7/2}$ in Bi_2O_3 NSs, respectively, while the emerging new peak at around 225 eV is assigned to S 2s in Bi_2S_3-Bi_2O_3 NSs (Figure S5.2d). Clearly, the binding energy of Bi 4f in

Bi_2S_3-Bi_2O_3 NSs shifts positively compared to that of Bi_2O_3 NSs, an indication of the existence of electronic interaction between Bi_2S_3 and Bi_2O_3 in the as-prepared Bi_2S_3-Bi_2O_3 NSs.
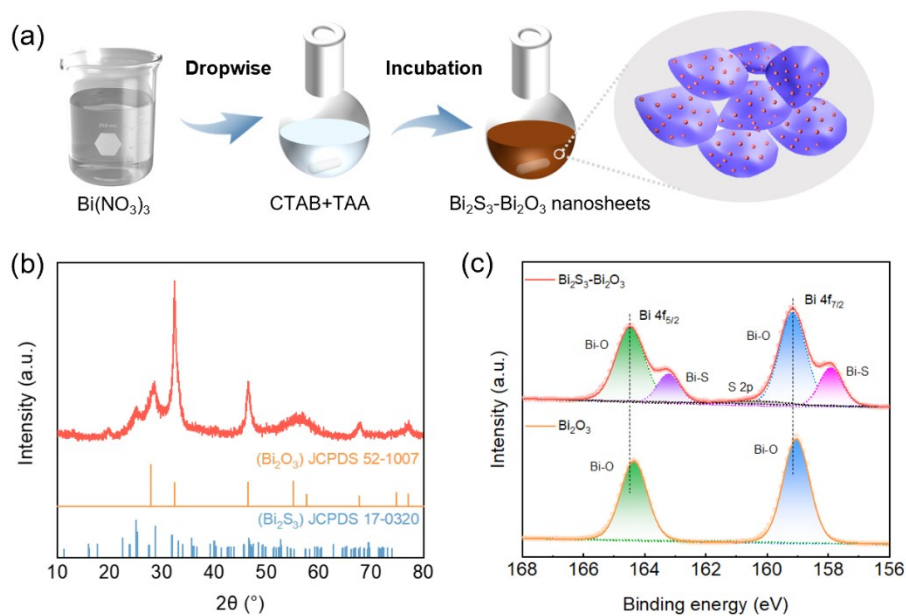
Figure 5.1 (a) Schematic illustration of the synthesis process of Bi_2S_3-Bi_2O_3 NSs; (b) XRD pattern of Bi_2S_3-Bi_2O_3 NSs; (c) High-resolution Bi 4f XPS spectra of Bi_2O_3 NSs and Bi_2S_3-Bi_2O_3 NSs.

To observe the morphologies and nanostructures of Bi_2S_3-Bi_2O_3 NSs, the field emission scanning electron microscopy (FESEM) and transmission electron microscope (TEM) were performed, and it is found that the prepared Bi_2S_3-Bi_2O_3 NSs clearly show the nanostructure of NSs possessing an average thickness of around 30 nm with the coarse and rough surface (Figures 5.2a and S5.2). Further TEM inspections on Bi_2S_3-Bi_2O_3 NSs display wrinkles existing with a darker color (Figure 5.2b), and the high-resolution TEM (HRTEM) image clearly presents the lattice fringes of 0.23 nm for the (041) facet of Bi_2S_3 and 0.32 nm for

(111) facet of Bi_2O_3. The close contact between Bi_2S_3 and Bi_2O_3 yields abundant interfaces as displayed in Figures 5.2d and e. The high-angle annular dark-field (HADDF) STEM image, together with energy dispersive X-ray (EDX) spectroscopy, further confirms the presence of Bi_2S_3 NPs on the surface of Bi_2O_3 NSs and the successfully prepared interface-abundant Bi_2S_3-Bi_2O_3 NSs (Figures 5.2f and g).
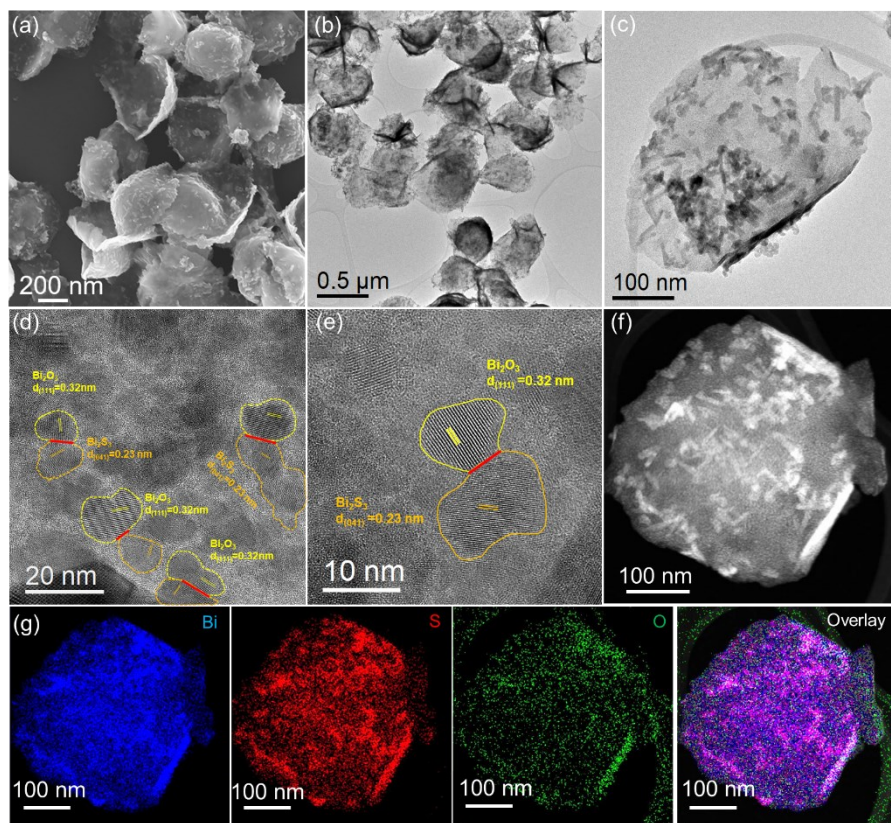
Figure 5.2 (a) SEM image, (b) and (c) TEM images, (d) and (e) HRTEM image; (f) HAADF-STEM image and (g) corresponding EDX mapping images of Bi_2S_3-Bi_2O_3 NSs.

5.2.2 Electrocatalytic CO_2 reduction performances

The electrocatalytic CO_2RR performances over the as-prepared Bi_2O_3 NSs, Bi_2S_3 NPs and Bi_2S_3-Bi_2O_3 NSs were first evaluated in 0.1 M CO_2-saturated $KHCO_3$ electrolyte within a gas-tight H-type cell. To demonstrate the effect of the interface between Bi_2S_3-Bi_2O_3 for

CO$_2$RR, a physically mixed mixture of Bi$_2$O$_3$ and Bi$_2$S$_3$ (noted as Bi$_2$S$_3$/Bi$_2$O$_3$) was also tested to exclude the direct mixture effect. The linear sweep voltammetry (LSV) curves of all the materials were recorded between -1.6 and 0 V at a scan rate of 20 mV s^{-1}. Apparently, the Bi$_2$S$_3$/Bi$_2$O$_3$ shows higher current density as compared with the individual Bi$_2$O$_3$ NSs and Bi$_2$S$_3$ NPs, while the Bi$_2$S$_3$-Bi$_2$O$_3$ NSs present the highest current densities among all the materials (Figure 5.3a), demonstrating a better electrocatalytic activity toward CO$_2$RR. To quantify the product distribution of Bi$_2$S$_3$-Bi$_2$O$_3$ NSs for CO$_2$RR, the constant electrolysis was conducted at different applied potentials, where the liquid and gaseous products were measured and evaluated using online gas chromatography (GC) and ion chromatography (IC), respectively. The results show that formate is the only liquid product with minor gaseous products of CO and H$_2$, when the potential is more negative than -0.8 V (Figure S5.3). Bi$_2$O$_3$ NSs and Bi$_2$S$_3$ NPs present the lower FEs of less than 90% for formate formation within the applied potential range, while the Bi$_2$S$_3$/Bi$_2$O$_3$ demonstrates a better performance compared to the individual Bi$_2$O$_3$ NSs and Bi$_2$S$_3$ NPs for CO$_2$RR with a maximum FE$_{formate}$ of 89.7 % at -1.2 V. The improved selectivity demonstrates the effectiveness of the interaction between Bi$_2$O$_3$ and Bi$_2$S$_3$, which is further revealed by the interface-dependent enhancement of the electrocatalytic CO$_2$RR performance over Bi$_2$S$_3$-Bi$_2$O$_3$ NSs. Apparently, the Bi$_2$S$_3$-Bi$_2$O$_3$ NSs are highly selective toward formate formation with FE greater than 90 % in a wide potential range from -1.4 to -1.0 V (Figure 5.3b) and a maximum FE$_{formate}$ of 93.8 % at -1.1 V (e.g., -0.86 V with jR compensation; Figure S5.4a). This shows a comparable electrocatalytic performance among the previously reported Bi-based electrocatalysts [23, 31, 40-44]. Remarkably, the total FEs for C1 products (e.g., formate and CO) reach a value of over 90 % from -1.4 to -0.9 V and achieve the maximal near-unity at -1.1 V, suggesting the

high selectivity of Bi_2S_3-Bi_2O_3 NSs for CO_2RR relative to the parasitic HER (Figure S5.4b). Figure 5.3c shows the potential window with high FE of formate over Bi_2S_3-Bi_2O_3 NSs against the recently reported high-performance Bi-based electrocatalysts (Table S5.1). Clearly, the Bi_2S_3-Bi_2O_3 NSs possess an extended potential window of 400 mV with FE of formate over 90 %, further demonstrating the preferential selectivity for formate formation.
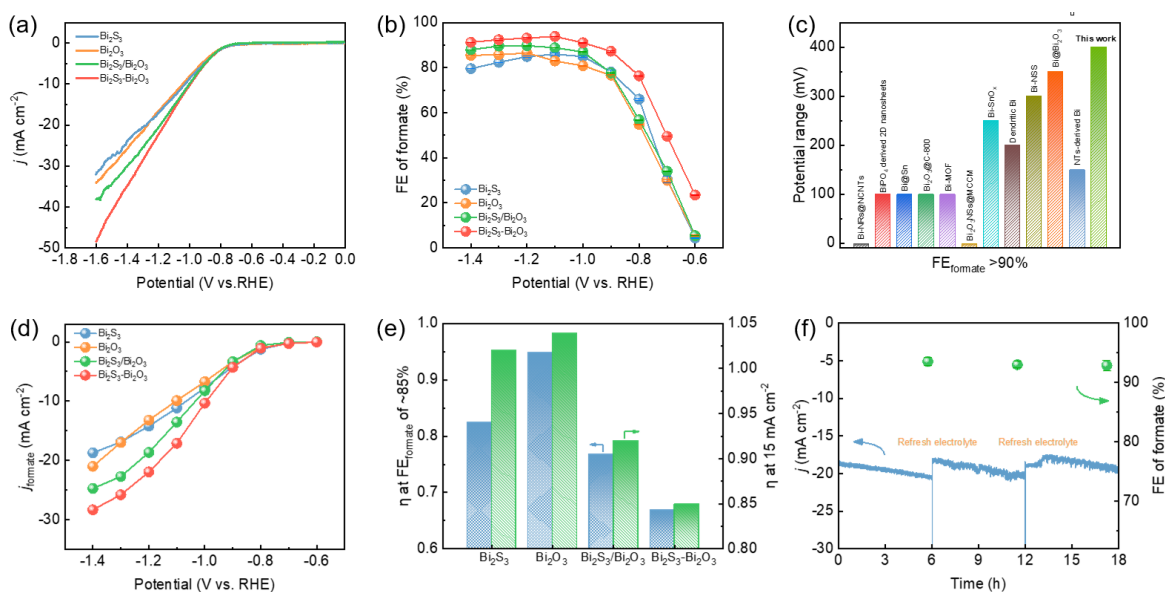
Figure 5.3 (a) LSV curves in 0.1 M CO_2-saturated $KHCO_3$ electrolyte, (b) FEs of formate product over Bi_2S_3 NPs, Bi_2O_3 NSs, Bi_2S_3/Bi_2O_3 and Bi_2S_3-Bi_2O_3 NSs; (c) Comparison of the-state-of-the-art Bi-based electrocatalysts with FE of formate over 90 %; (d) $j_{formate}$ and (e) η at FE of about 85 % and 15 mA cm^{-2} over Bi_2S_3 NPs, Bi_2O_3 NSs, Bi_2S_3/Bi_2O_3 and Bi_2S_3-Bi_2O_3 NSs; (f) Long-term stability test of Bi_2S_3-Bi_2O_3 NSs at -1.1 V in 0.1 M CO_2-saturated $KHCO_3$ electrolyte.

The partial current densities ($j_{formate}$) were derived from the j and $FE_{formate}$ during steady electrolysis to exclusively show the electrocatalytic activities for formate formation during CO_2RR, as shown in Figure 5.3d. The Bi_2S_3-Bi_2O_3 NSs reach approximately a $j_{formate}$ of 28.3

mA cm^{-2} at -1.4 V, higher than those of other as-prepared electrocatalysts. At -1.1 V with the maximum FE of formate of 93.8%, the $j_{formate}$ is 17.1 mA cm^{-2}, which reflects the good electrocatalytic activity for CO_2RR. More importantly, the minimum η of 669 mV is required for Bi_2S_3-Bi_2O_3 NSs to achieve the $FE_{formate}$ of 85 %, remarkably lower than the Bi_2O_3 NSs (948 mV), the Bi_2S_3 NPs (825 mV) and the Bi_2S_3/Bi_2O_3 (768 mV), as shown in Figure 5.3e. To achieve a $j_{formate}$ of about 15.0 mA cm^{-2}, the Bi_2S_3-Bi_2O_3 NSs require a smaller η of 850 mV, whereas a higher value is required to achieve the equivalent performance over the other as-prepared electrocatalysts. This obvious difference in η indicates that lower external energy is required to stride over the energy barrier to effectively proceed the CO_2RR on Bi_2S_3-Bi_2O_3 NSs. Finally, the long-term electrolysis at a fixed potential of -1.1 V was conducted to evaluate the stability of Bi_2S_3-Bi_2O_3 NSs. Apparently, the j slightly decreases due to the accumulation of $HCOO^-$ in the electrolyte, which can be quickly restored when refreshing the cathode electrolyte (Figure 5.3f), together with a negligible change of formate FE at about 93 % during the 18 h stability test, suggesting a superior stability of Bi_2S_3-Bi_2O_3 NSs for CO_2RR. To better reveal the origins of the good stability of Bi_2S_3-Bi_2O_3 NSs, the post-catalysis characterizations were conducted. As shown in Figure S5.5, the morphology of nanosheets is well retained after CO_2RR measurement, indicating that Bi_2S_3-Bi_2O_3 NSs have good morphological stability. In addition, the TEM images (Figure S5.6) display the nanosheet structure where the interface between Bi_2S_3 and Bi_2O_3 can be observed in the HRTEM image. Furthermore, the corresponding EDX elemental mappings show the evenly distributed elements Bi, O and S, confirming the composition stability of Bi_2S_3-Bi_2O_3 NSs. The XRD result (Figure S5.7) also shows the main remaining phase composition of Bi_2O_3

and Bi_2S_3 after CO_2RR measurement. All these results verify the good stability of Bi_2S_3-Bi_2O_3 NSs for CO_2RR.

5.2.3 Characterizations of Bi_2O_3-Bi_2S_3 nanosheets

It is worth mentioning that the low solubility of CO_2 in aqueous electrolyte inevitably restricts the mass transfer during CO_2RR, which significantly limits the current density. Hence, improving CO_2 adsorption ability is a critical step to improve the CO_2RR electrocatalytic performance. Volumetric CO_2 adsorption-desorption isotherms were conducted to evaluate the CO_2 adsorption ability over the as-prepared electrocatalysts. As shown in Figure 5.4a, the CO_2 uptake volume of Bi_2S_3-Bi_2O_3 NSs rises with increasing relative pressure of CO_2 gas, reaching a value of about 10 cm^3 g^{-1} at P/P_0 of 1.0. In comparison with Bi_2S_3 NPs and Bi_2O_3 NSs, the enhancement of CO_2 adsorption on Bi_2S_3-Bi_2O_3 NSs is apparent, which allows an easier access of CO_2 molecules to the Bi_2S_3-Bi_2O_3 NSs catalyst and faster transport on the electrode surface, thus facilitating the subsequent reaction steps for CO_2 conversion. The enhanced CO_2 adsorption capacity could also offer a better mass transfer in the aqueous media, and consequently increase the current density. However, the increased current density is still far lower than the required value in terms of practical CO_2RR electrolysis at an industrial scale. Previous studies have claimed that the current density to meet the industrial requirement should be around 200 mA cm^{-2} for CO_2RR toward HCOOH formation [45]. To overcome the drawbacks caused by the limited CO_2 mass transport in a conventional H-type cell, the flow cell configuration should be such that it could separate the CO_2 gas and electrolyte to increase the current density. Thus, the Bi_2S_3-Bi_2O_3 NSs were further examined in a flow cell with 1.0 M KOH electrolyte.
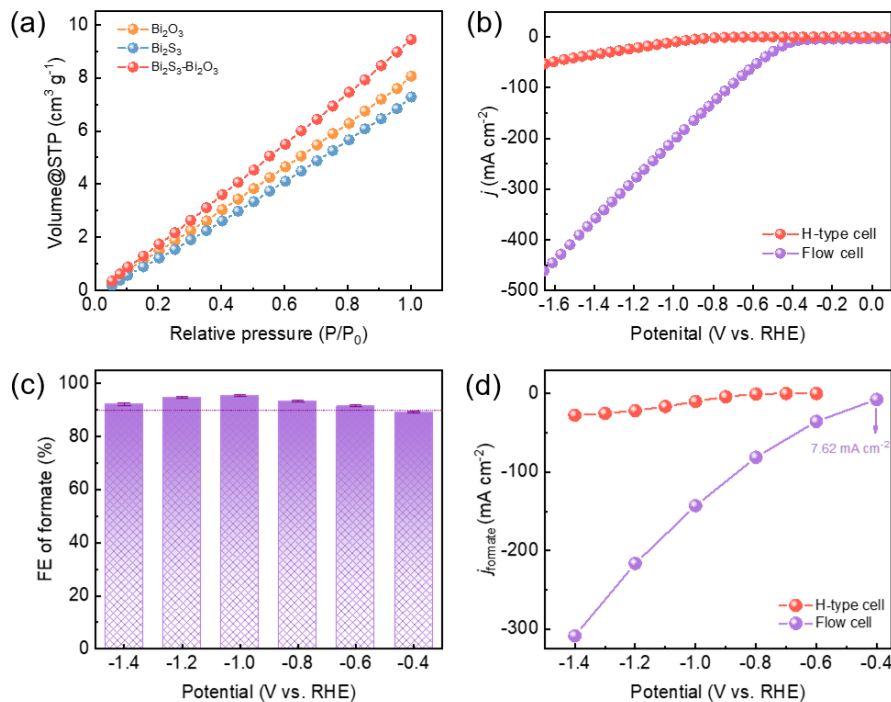
Figure 5.4 (a) Volumetric CO_2 adsorption isotherms of Bi_2O_3, Bi_2S_3 and Bi_2S_3-Bi_2O_3 NSs; (b) LSV curves of Bi_2S_3-Bi_2O_3 NSs at a scan rate of 20 mV s^{-1} in H-type cell and flow cell; (c) FE of formate and (d) $j_{formate}$ for Bi_2S_3-Bi_2O_3 NSs in all potentials range in flow cell configuration.

Figure 5.4b shows the LSV curves of Bi_2S_3-Bi_2O_3 NSs in a H-type cell and a flow cell configuration. It can be found that the onset potential for formate formation is achieved at about -0.4 V, more positive than that in the H-type cell (-0.6 V). Additionally, the total current density in the flow cell is one order of magnitude higher in comparison with that in H-type cell. The total current density reaches a value of around 350 mA cm^{-2} at -1.4 V, about 12-fold higher than the value measured in the H-type cell. Notably, the current density of around 9 mA cm^{-2} is maintained at -0.4 V, revealing the high intrinsic electrocatalytic activity on Bi_2S_3-Bi_2O_3 NSs. As implied in Figure 5.4c, the FEs of formate display a wide potential range of over 90% from -1.4 to -0.4 V on Bi_2S_3-Bi_2O_3 NSs, demonstrating the high selectivity

for formate formation. More importantly, the $FE_{formate}$ is still around 90 % at a quite small onset potential of -0.4 V, further proving the enhanced electrocatalytic performance for CO_2RR. The partial current density of formate is about 7.6 mA cm^{-2} at -0.4 V, which is comparable to most of the state-of-the-art materials for CO_2RR to formate (Figure 5.4d and Table S5.2). The excellent selectivity and high current density both demonstrate the promising future of Bi_2S_3-Bi_2O_3 NSs catalyst for practical application of CO_2RR to formate formation.

5.2.4 Investigation on the electrocatalytic enhancement

To better understand the enhanced electrocatalytic performance and to confirm the improved charge transfer ability, a systematical investigation was conducted on the as prepared electrocatalysts. Firstly, double-layer capacitance (C_{dl}) was measured to rule out the ECSA effect considering the different morphologies (Figure S5.8). Figure 5.5a shows the ECSA results, and the Bi_2S_3-Bi_2O_3 NSs possess a higher value of capacitance (2.91 mF cm^{-2}) than Bi_2O_3 NSs (1.43 mF cm^{-2}), Bi_2S_3 NPs (2.46 mF cm^{-2}) and Bi_2S_3/Bi_2O_3 (2.72 mF cm^{-2}), indicating the larger ECSA for CO_2RR. The enlarged ECSA of Bi_2S_3-Bi_2O_3 NSs is perhaps owing to the interconnections of Bi_2O_3 and Bi_2S_3, which creates more interfaces and eventually facilitates the reaction kinetics and promotes the electrocatalytic activity towards CO_2RR. In addition, the Tafel plots were fitted to gain insight into the reaction kinetics. It is generally accepted that the slope of 118 mV dec^{-1} suggests the initial electron transfer to CO_2 as the rate-determining step (RDS), whereas the value of 59 mV dec^{-1} indicates that the transfer of chemical proton from HCO_3^- served as the RDS [46]. Compared with Bi_2O_3 NSs (145.79 mV dec^{-1}) and Bi_2S_3 NPs (137.51 mV dec^{-1}), a lower Tafel slope of 95.76 mV dec^{-1} on Bi_2S_3-Bi_2O_3 NSs suggests the accelerated reaction kinetics (Figure 5.5b). Clearly, all the

Tafel slopes close to the theoretical value of 118 mV dec^{-1} confirm the initial electron transfer

to form $CO_2^{\cdot-}$ intermediate and match with the RDS. The crucial role of interface-promoted

reaction kinetics is further confirmed in comparison with the Tafel slope of Bi_2S_3/Bi_2O_3

(104.33 mV dec^{-1}). The lower Tafel slope of Bi_2S_3-Bi_2O_3 NSs implies a faster reaction

kinetics that speeds up the CO$_2$RR and improves its performance.
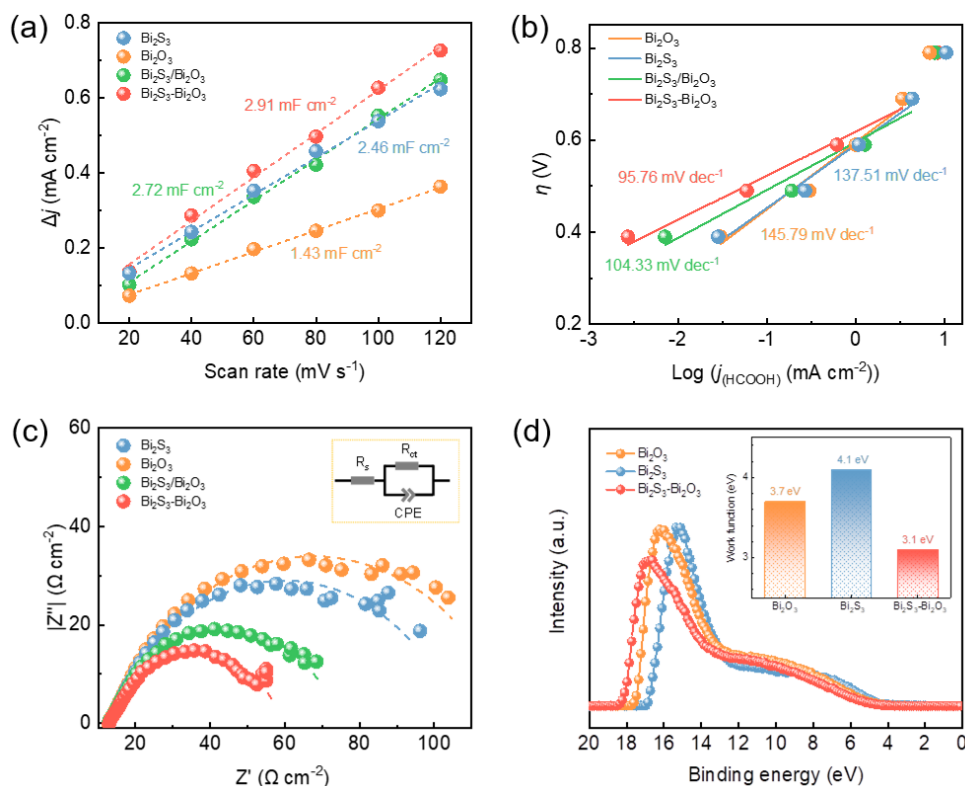
Figure 5.5 (a) Linear fitting of double-layer capacitive currents versus scan rates to estimate

ECSA; (b) Tafel plots; (c) Nyquist plots (inset: equivalent circuit); (d) UPS spectra of Bi_2O_3,

Bi_2S_3 and Bi_2S_3-Bi_2O_3 NSs (inset: work function).

Furthermore, electrochemical impedance spectroscopy (EIS) was studied to investigate the

electron transfer properties (Figure 5.5c). Randle's equivalent circuit was employed to fit the

experimental results and to obtain the interfacial charge transfer resistance (R_{ct}). As shown

in Table S5.3, the electrolyte resistance (R_s) is about 13 Ω. The R_{ct} of Bi_2S_3-Bi_2O_3 NSs is comparably smaller (46.7 Ω) than those of Bi_2O_3 NSs (109.2 Ω) and Bi_2S_3 NPs (93.8 Ω), indicating an improved electron transfer ability. It is worth noting that the physical mixture of Bi_2S_3/Bi_2O_3 could also partially reduce the R_{ct} (72.3 Ω) due to the direct contact of Bi_2S_3 and Bi_2O_3. Although the charge transfer ability could be reinforced through physical mixing, the loose contact is inferior to the chemically prepared high-quality abundant interfaces of Bi_2S_3-Bi_2O_3 NSs. The fast electron transfer guarantees the formation of $CO_2^{\bullet-}$ intermediate from CO_2 through the first electron transfer step. Additionally, the enhancement of charge transfer ability was further confirmed by the measurement of ultraviolet photoelectron spectroscopy (UPS). It has been commonly recognized that the work function strongly correlates to the electrocatalytic activity, and is conveniently used to illustrate electron transfer on the electrode [47]. Specifically, the lower work function indicates the higher tunneling probability of electrons, which assures an easier electron transfer from the electrocatalyst to the reactant. Remarkably, Figure 5.5d presents the UPS spectra where the Bi_2S_3-Bi_2O_3 NSs show a higher cut-off binding energy as compared with the other two electrocatalysts, suggesting a lower work function of Bi_2S_3-Bi_2O_3 NSs (3.1 eV) than those of Bi_2O_3 NSs (3.7 eV) and Bi_2S_3 NPs (4.1 eV) and indicating an enhanced electron transfer ability. Given the abovementioned results, it can be persuasively concluded that the abundance of interfaces on Bi_2S_3-Bi_2O_3 NSs can significantly boost the charge transfer ability, which could accelerate the CO_2RR kinetics and consequently enhance the electrocatalytic performance.

5.2.5 Proposed reaction mechanism for CO₂RR

Figure 5.6a shows a schematic diagram of the mechanistic pathways over Bi_2S_3-Bi_2O_3 NSs to better understand the involved mechanism. CO_2 will firstly adsorb onto the surface, accompanied by the fast-interfacial induced electron transfer to $CO_{2\ (ads)}$, which is regarded as the RDS. Then, the intermediate $CO_2^{•-}{}_{(ads)}$ further accepts one proton (H^+) with another electron to form $HCOO^{•-}{}_{(ads)}$. Finally, the $HCOO^{•-}{}_{(ads)}$ will desorb from the catalyst surface and generate $HCOO^-$. The improved electron transfer capability facilitates the whole processes for CO_2RR on Bi_2S_3-Bi_2O_3 NSs as confirmed by the fast reaction kinetics.
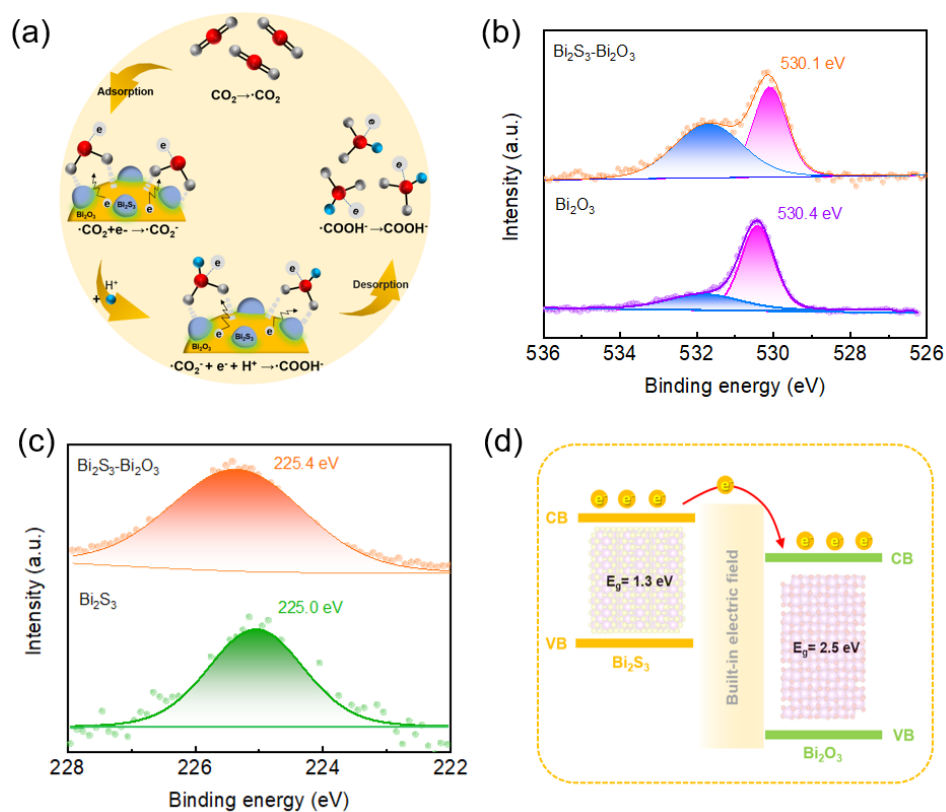
Figure 5.6 (a) Illustration of reaction mechanism over Bi_2S_3-Bi_2O_3 NSs for CO_2RR; XPS spectra of (b) O 1s and (c) S 2s in Bi_2S_3-Bi_2O_3 NSs, Bi_2S_3 NPs and Bi_2O_3 NSs; (d) Schematic diagram of the band alignment of Bi_2S_3-Bi_2O_3 NSs.

To reveal the origin of the enhanced electron transfer ability of Bi_2S_3-Bi_2O_3 NSs, high-resolution XPS measurement was performed to investigate the surface electronic states with the individual Bi_2O_3 NSs and Bi_2S_3 NPs as references. Apparently, the electron binding energy of O 1s has a negative shift of about 0.3 eV after the formation of Bi_2S_3-Bi_2O_3 NSs relative to that of Bi_2O_3 NSs (Figure 5.6b). Correspondingly, the binding energy of S 2s positively shifts from 225.0 to 225.4 eV, this confirms the charge transfer between the two components in Bi_2S_3-Bi_2O_3 NSs (Figure 5.6c). The electronic interaction between Bi_2S_3 and Bi_2O_3 at the interface plays an important role in tuning the electronic structure of each individual component, thus affecting the reaction kinetics for CO_2RR. Based on the above results, it is believed that the interface of the as-prepared Bi_2S_3-Bi_2O_3 NSs is beneficial to the electrocatalytic activity towards CO_2RR. The Bi_2S_3 is a n-type semiconductor with a band gap of 1.3 eV, while the p-type Bi_2O_3 has a band gap of about 2.5 eV [48, 49]. According to the experimental results of work function, the Bi_2O_3 (3.7 eV) shows a lower value as compared with Bi_2S_3 (4.1 eV). When Bi_2S_3 directly contacts with Bi_2O_3, a built-in electric field at the interface would generate electrons flowing from Bi_2S_3 to Bi_2O_3 until the work function reaches an equilibrium state, as shown in Figure 5.6d. Furthermore, the absolute electronegativity usually reflects the attraction of electrons to the materials. The absolute electronegativity values of Bi_2O_3 and Bi_2S_3 are about 6.23 and 5.3 eV, respectively [48, 50]. The lower absolute electronegativity of Bi_2S_3 ensures an easier free flow of electrons to Bi_2O_3 on surface to achieve the equilibrium of the work function. The optimized electronic structure at the interface induces an increased charge transfer to the adsorbates, thus accelerating the kinetics of CO_2RR and enhancing the electrocatalytic performance. In light of the above results and discussions, the faster electron transfer over Bi_2S_3-Bi_2O_3 NSs, the abundant active

sites and enhanced intrinsic activity collectively promote the faster reaction kinetics and the good electrocatalytic performance for CO_2RR to formate.

5.3 Conclusions

In summary, the Bi_2S_3-Bi_2O_3 NSs have been successfully prepared and its electrocatalytic performance was explored for CO_2RR to formate. The direct mixture of Bi_2O_3 NSs and Bi_2S_3 NPs has demonstrated effectiveness of the interaction between the two components for CO_2RR enhancement, while the Bi_2S_3-Bi_2O_3 NSs with rich interface show a much higher current density and selectivity towards formate formation. A partial current density of 17.1 mA cm^{-2} is obtained at the potential of -1.1 V, together with an optimal $FE_{formate}$ of 93.8 %. Additionally, a wide potential range of $FE_{formate}$ over 90 % with large current density is achieved in a flow cell system. The superior performance for CO_2RR originates from the fast-interfacial charge transfer induced by the abundant interfaces, which not only improves the reaction kinetics, but also improves the electrocatalytic activity and selectivity. These research outputs from this study shed light on the interface engineering of CO_2RR electrocatalysts and offer an effective approach to fabricating the electrocatalysts suitable for industrial applications.

5.4 References

[1]   J. Qiao, Y. Liu, F. Hong, J. Zhang, *Chem. Soc. Rev.* **2014**, *43*, 631-675.

[2]   C. Xu, J. Hong, P. Sui, M. Zhu, Y. Zhang, J.-L. Luo, *Cell Reports Physical Science* **2020**, *1*, 100101.

[3]   P. De Luna, C. Hahn, D. Higgins, S. A. Jaffer, T. F. Jaramillo, E. H. Sargent, *Science* **2019**, *364*.

[4]   M. G. Kibria, J. P. Edwards, C. M. Gabardo, C. T. Dinh, A. Seifitokaldani, D. Sinton, E. H. Sargent, *Adv. Mater.* **2019**, *31*, 1807166.

[5]   R. S. Weber, *ACS Catal.* **2018**, *9*, 946-950.

[6]   L. Zhang, Z. J. Zhao, T. Wang, J. Gong, *Chem. Soc. Rev.* **2018**, *47*, 5423-5443.

[7]   F. Li, D. R. MacFarlane, J. Zhang, *Nanoscale* **2018**, *10*, 6235-6260.

[8]   T. Vo, K. Purohit, C. Nguyen, B. Biggs, S. Mayoral, J. L. Haan, *ChemSusChem* **2015**, *8*, 3853-3858.

[9]   A. S. Agarwal, Y. Zhai, D. Hill, N. Sridhar, *ChemSusChem* **2011**, *4*, 1301-1310.

[10]   F. Li, L. Chen, G. P. Knowles, D. R. MacFarlane, J. Zhang, *Angew. Chem. Int. Ed.* **2017**, *56*, 505-509.

[11]   S. Liu, J. Xiao, X. F. Lu, J. Wang, X. Wang, X. W. D. Lou, *Angew. Chem. Int. Ed.* **2019**, *58*, 8499-8503.

[12]   X. Liu, Y. Jiao, Y. Zheng, M. Jaroniec, S. Z. Qiao, *J. Am. Chem. Soc.* **2019**, *141*, 9664-9672.

[13]   Q. Zhu, J. Ma, X. Kang, X. Sun, H. Liu, J. Hu, Z. Liu, B. Han, *Angew. Chem. Int. Ed.* **2016**, *55*, 9012-9016.

[14]   M. J. W. Blom, V. Smulders, W. P. M. van Swaaij, S. R. A. Kersten, G. Mul, *Appl. Catal. B-Environ.* **2020**, *268*, 118420.

[15]   Y. Shi, Y. Ji, J. Long, Y. Liang, Y. Liu, Y. Yu, J. Xiao, B. Zhang, *Nat. Commun.* **2020**, *11*, 3415.

[16]   Z. Zhang, F. Ahmad, W. Zhao, W. Yan, W. Zhang, H. Huang, C. Ma, J. Zeng, *Nano Lett.* **2019**, *19*, 4029-4034.

[17]   R. Hegner, L. F. M. Rosa, F. Harnisch, *Appl. Catal. B-Environ.* **2018**, *238*, 546-556.

[18]   H. W. Yoshio Hori, Toshio Tsukamoto, Osamu, Koga, *Electrochim. Acta* **1994**, *39*, 1833-1839.

[19]   Z. Chen, N. Wang, S. Yao, L. Liu, *J. CO_2 Util.* **2017**, *22*, 191-196.

[20]   N. Han, P. Ding, L. He, Y. Li, Y. Li, *Adv. Energy Mater.* **2019**, 1902338.

[21]   Z. Yang, F. E. Oropeza, K. H. L. Zhang, *APL Mater.* **2020**, *8*, 060901.

[22]   T. Tran-Phu, R. Daiyan, Z. Fusco, Z. Ma, R. Amal, A. Tricoli, *Adv. Funct. Mater.* **2019**, *30*, 1906478.

[23]   X. Zhang, T. Lei, Y. Liu, J. Qiao, *Appl. Catal. B-Environ.* **2017**, *218*, 46-50.

[24]   C. W. Lee, J. S. Hong, K. D. Yang, K. Jin, J. H. Lee, H.-Y. Ahn, H. Seo, N.-E. Sung, K. T. Nam, *ACS Catal.* **2018**, *8*, 931-937.

[25]   H. Ju, G. Kaur, A. P. Kulkarni, S. Giddey, *J. CO₂ Util.* **2019**, *32*, 178-186.

[26]   B. Endrődi, G. Bencsik, F. Darvas, R. Jones, K. Rajeshwar, C. Janáky, *Prog. Energy Combust. Sci.* **2017**, *62*, 133-154.

[27]   Y. Y. Birdja, E. Pérez-Gallent, M. C. Figueiredo, A. J. Göttle, F. Calle-Vallejo, M. T. M. Koper, *Nat. Energy.* **2019**, *4*, 732-745.

[28]   Y. J. Sa, C. W. Lee, S. Y. Lee, J. Na, U. Lee, Y. J. Hwang, *Chem. Soc. Rev.* **2020**, *49*, 6632-6665.

[29]   S. Liu, X. F. Lu, J. Xiao, X. Wang, X. W. D. Lou, *Angew. Chem. Int. Ed.* **2019**, *58*, 13828-13833.

[30]   P. Deng, F. Yang, Z. Wang, S. Chen, Y. Zhou, S. Zaman, B. Y. Xia, *Angew. Chem. Int. Ed.* **2020**, *59*, 10807-10813.

[31]   D. Wu, W. Chen, X. Wang, X.-Z. Fu, J.-L. Luo, *J. CO₂ Util.* **2020**, *37*, 353-359.

[32]   X. Zhang, J. Fu, Y. Liu, X.-D. Zhou, J. Qiao, *ACS Sustain. Chem. Eng.* **2020**, *8*, 4871-4876.

[33]   H. Li, C. Chen, D. Yan, Y. Wang, R. Chen, Y. Zou, S. Wang, *J. Mater. Chem. A* **2019**.

[34]   F. Pan, Y. Yang, *Energy Environ. Sci.* **2020**, *13*, 2275-2309.

[35]   A. Vasileff, C. Xu, Y. Jiao, Y. Zheng, S.-Z. Qiao, *Chem* **2018**, *4*, 1809-1831.

[36]   Z. Niu, C. Qiu, J. Jiang, L. Ai, *ACS Sustain. Chem. Eng.* **2018**, *7*, 2335-2342.

[37]   L. An, Z. Zhang, J. Feng, F. Lv, Y. Li, R. Wang, M. Lu, R. B. Gupta, P. Xi, S. Zhang, *J. Am. Chem. Soc.* **2018**, *140*, 17624-17631.

[38]   Y. Liu, X. Luo, C. Zhou, S. Du, D. Zhen, B. Chen, J. Li, Q. Wu, Y. Iru, D. Chen, *Appl. Catal. B-Environ.* **2020**, *260*, 118197.

[39]   K. Chu, Y. P. Liu, Y. B. Li, Y. L. Guo, Y. Tian, *ACS Appl. Mater. Interfaces* **2020**, *12*, 7081-7090.

[40]   F. Li, G. H. Gu, C. Choi, P. Kolla, S. Hong, T.-S. Wu, Y.-L. Soo, J. Masa, S. Mukerjee, Y. Jung, J. Qiu, Z. Sun, *Appl. Catal. B-Environ.* **2020**, *277*, 119241.

[41]   Y. Wang, L. Cheng, J. Liu, C. Xiao, B. Zhang, Q. Xiong, T. Zhang, Z. Jiang, H. Jiang, Y. Zhu, Y. Li, C. Li, *ChemElectroChem* **2020**, *7*, 2864-2868.

[42]   D. Wu, X. Wang, X.-Z. Fu, J.-L. Luo, *Appl. Catal. B-Environ.* **2021**, *284*, 119723.

[43]   P. Deng, H. Wang, R. Qi, J. Zhu, S. Chen, F. Yang, L. Zhou, K. Qi, H. Liu, B. Y. Xia, *ACS Catal.* **2019**, *10*, 743-750.

[44]   D. Wu, G. Huo, W. Chen, X.-Z. Fu, J.-L. Luo, *Appl. Catal. B-Environ.* **2020**, *271*, 118957.

[45]   K. Liu, W. A. Smith, T. Burdyny, *ACS Energy Lett.* **2019**, *4*, 639-643.

[46]   C. W. Lee, N. H. Cho, S. W. Im, M. S. Jee, Y. J. Hwang, B. K. Min, K. T. Nam, *J. Mater. Chem. A* **2018**, *6*, 14043-14057.

[47]   Z.-Z. Wu, F.-Y. Gao, M.-R. Gao, *Energy Environ. Sci.* **2021**, *14*, 1121-1139.

[48]   E. Pineda, M. E. Nicho, P. K. Nair, H. Hu, *Sol. Energy* **2012**, *86*, 1017-1022.

[49]   Y. Huang, W. Wang, Q. Zhang, J. J. Cao, R. J. Huang, W. Ho, S. C. Lee, *Sci. Rep.* **2016**, *6*, 23435.

[50]   Yong Xu, M. A. A. Schoonen, *Am. Mineral* **2000**, *85*, 543-556.

5.5 Supporting Information

5.5.1 Supporting figures and tables
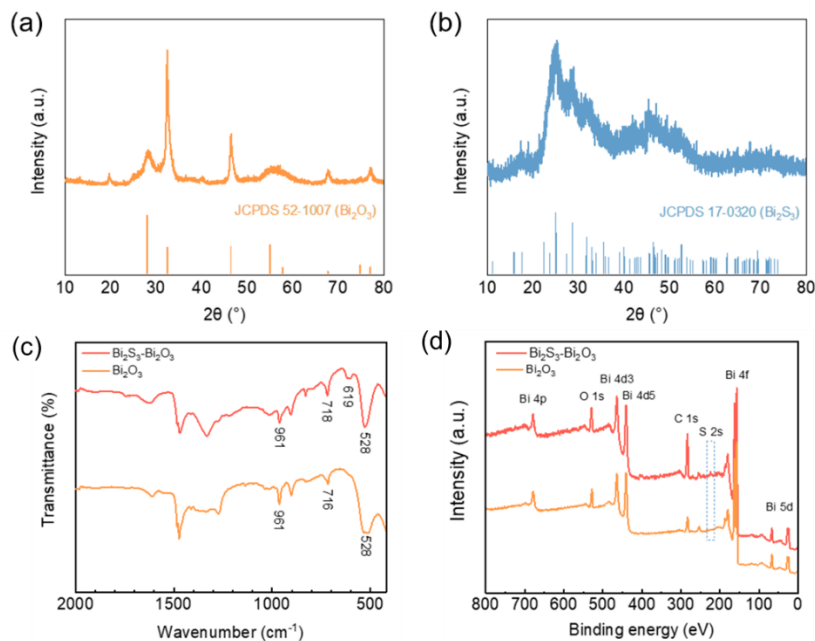
Figure S5.1 XRD patterns of (a) Bi_2O_3 NSs; (b) Bi_2S_3 NPs; (c) FTIR spectra of Bi_2O_3 NSs and Bi_2S_3-Bi_2O_3 NSs; (d) XPS survey spectra of Bi_2O_3 NSs and Bi_2S_3-Bi_2O_3 NSs.
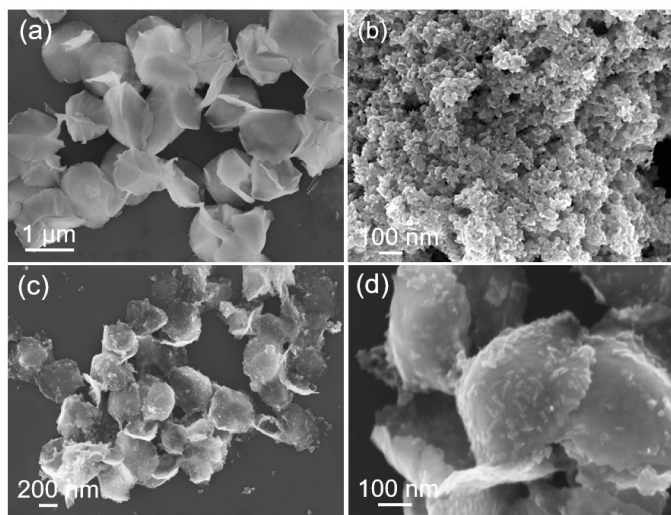
Figure S5.2 SEM images of (a) Bi_2O_3 NSs, (b) Bi_2S_3 NPs, (c) and (d) Bi_2S_3-Bi_2O_3 NSs.
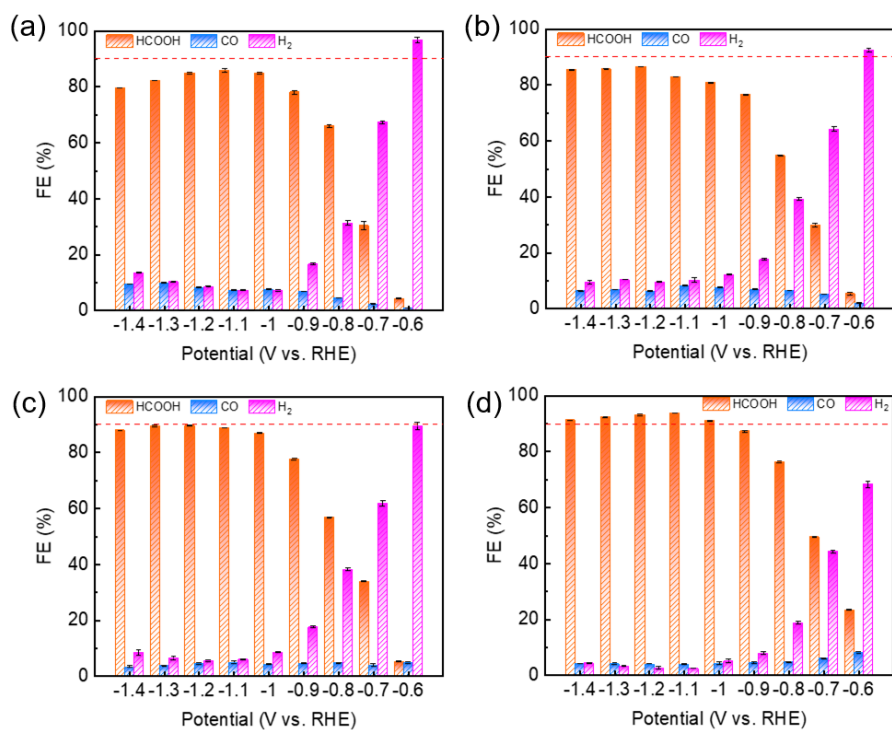
Figure S5.3 Faradaic efficiencies of products over (a) Bi_2O_3 NSs, (b) Bi_2S_3 NPs, (c) Bi_2S_3/Bi_2O_3 and (d) Bi_2S_3-Bi_2O_3 NSs.
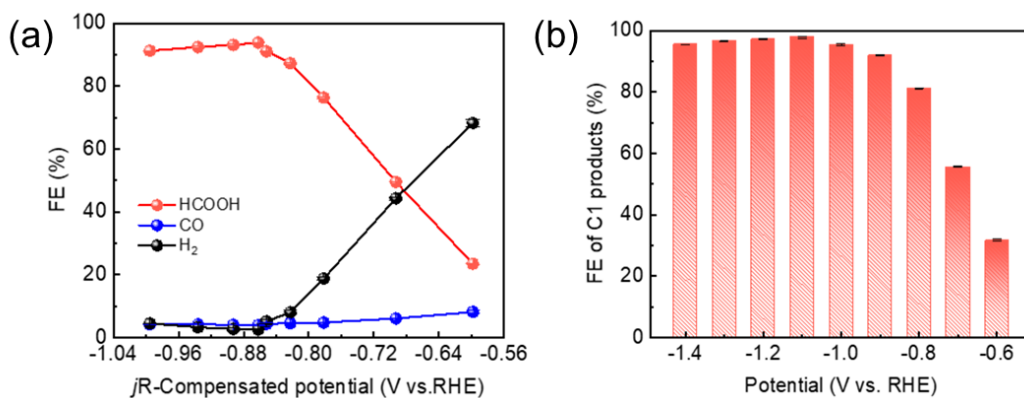
Figure S5.4 (a) Faradaic efficiencies over the Bi_2S_3-Bi_2O_3 NSs at different potentials with jR compensation; (b) Faradaic efficiencies of C1 products over Bi_2S_3-Bi_2O_3 NSs.
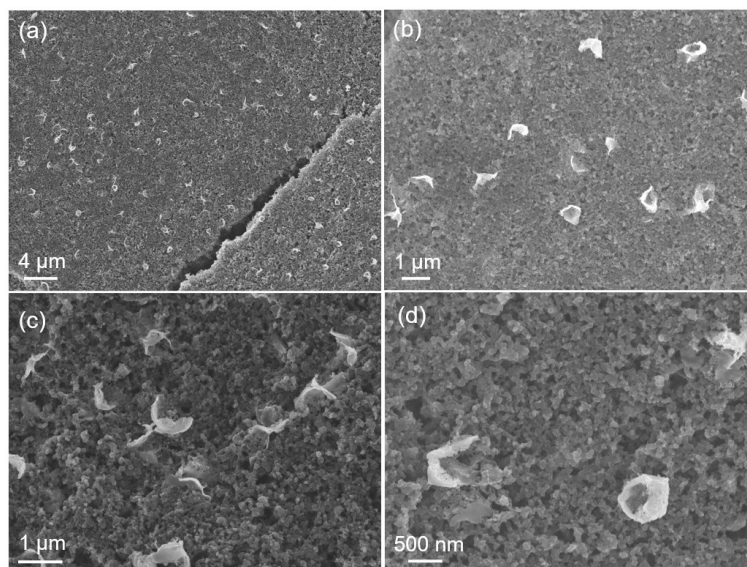
Figure S5.5 SEM images of Bi$_2$S$_3$-Bi$_2$O$_3$ NSs after CO$_2$RR measurement.
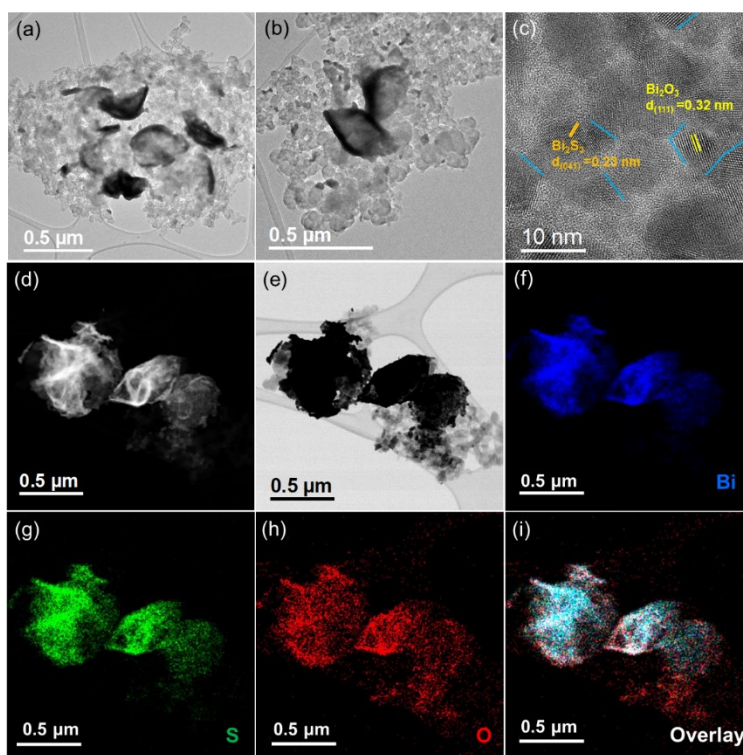
Figure S5.6 (a) and (b) TEM images, (c) HRTEM image, (d) and (e) HAADF-STEM images and (f) to (i) EDX elemental mappings of Bi$_2$S$_3$-Bi$_2$O$_3$ NSs after CO$_2$RR.
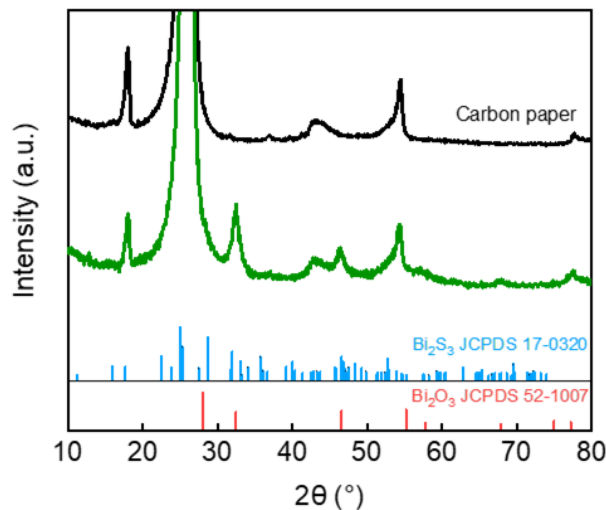
Figure S5.7 XRD pattern of Bi_2S_3-Bi_2O_3 NSs after CO_2RR.
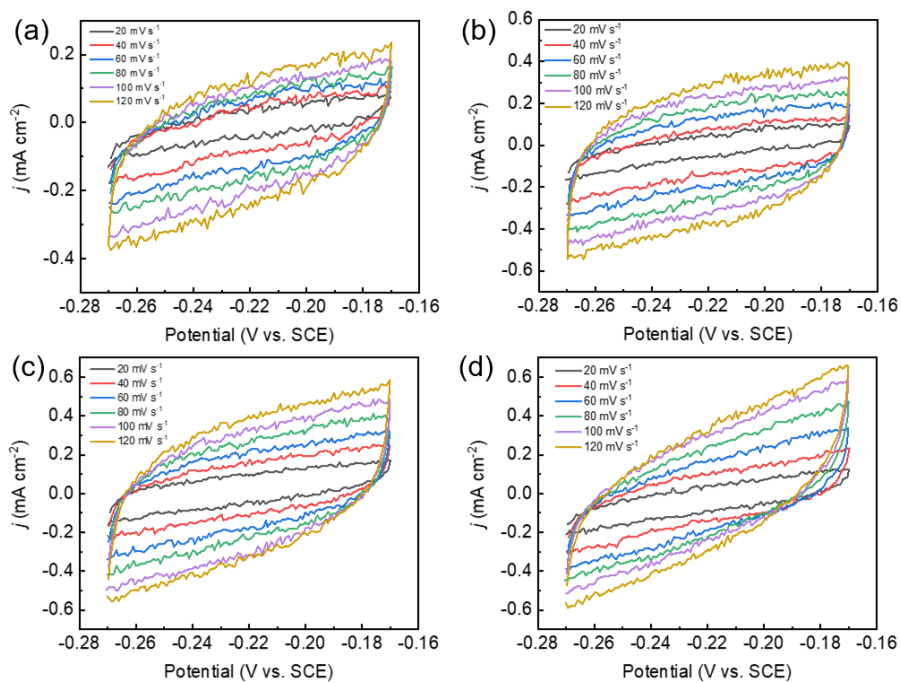
Figure S5.8 Cyclic voltammograms of (a) Bi_2O_3 NSs, (b) Bi_2S_3 NPs and (c) Bi_2S_3/Bi_2O_3 NSs and (d) Bi_2S_3-Bi_2O_3 NSs between -0.27V and -0.17 V vs. SCE in CO_2-saturated 0.1 M $KHCO_3$.

Table S5.1 Comparison of potential range on some reported Bi-based electrocatalysts for the electrochemical reduction of CO_2 to formate.

Catalyst	Electrolyte	Potential range (FE > 90%)	Ref
Bi-NRs@NCNTs	0.1 M $KHCO_3$	-0.9 V	[1]
$BiPO_4$ derived 2D nanosheets	0.2 M Na_2SO_4	-0.9 V ~ -1.0 V	[2]
Bi@Sn	0.5 M $KHCO_3$	-1.0 V ~ -1.1 V	[3]
Bi_2O_3@C-800	0.5 M $KHCO_3$	-0.8 V ~ -0.9 V	[4]
Bi-MOF	0.1 M $KHCO_3$	-0.9 V ~ -1.0 V	[5]
Bi_2O_3NSs@MCCM	0.1 M $KHCO_3$	-1.256 V	[6]
Bi-SnO_x	0.5 M $KHCO_3$	-0.67 V~ -0.92 V	[7]
Dendritic Bi	0.5 M $KHCO_3$	-0.72 V ~ -0.92 V	[8]
Bi-NSS	0.1 M $KHCO_3$	-1.0 V ~ -1.3 V	[9]
Bi@Bi_2O_3	0.5 M $KHCO_3$	-0.65 V ~ -1.0 V	[10]
NTs-derived Bi	0.5 M $KHCO_3$	-0.75 V ~ -0.9 V	[11]
Bi_2S_3-Bi_2O_3 NSs	0.1 M $KHCO_3$	-1.0 V ~ -1.4 V	This work

Table S5.2 Comparison of some reported metal-based electrocatalysts for the electrochemical reduction of CO_2 to formate.

Catalyst	Electrolyte	Potential (V vs RHE)	FE$_{formate}$ (%)	$j_{formate}$ (mA cm^{-2})	Ref.
In-In$_2$S$_3$ nanosheets	1.0 M KHCO$_3$	-1.0	76	20	[12]
In/In$_2$O$_{3-x}$	0.5 M NaHCO$_3$	-0.82	89.2	2.7	[13]
In$_2$O$_3$−rGO	0.1 M KHCO$_3$	-1.2	84.6	22.4	[14]
NC-SnO$_2$@CC-3	0.5 M KHCO$_3$	-0.7	93	44	[15]
VO-SnO$_2$	0.5 M NaHCO$_3$	-0.7	92.4	2.3	[16]
V$_O$-rich N-SnO$_2$ NS	0.1 M KHCO$_3$	-1.2	89	15.5	[17]
NW-SnO$_2$	0.5 M KHCO$_3$	-1.0	87.4	22	[18]
Bi nanosheets	0.1 M KHCO$_3$	-1.1	86	14	[19]
Bi$_2$S$_3$ derived Bi/Bi$_2$O$_3$	0.5 M KHCO$_3$	-1.0	82	7.0	[20]
Bi$_2$O$_3$NSs@MCCM	0.1 M KHCO$_3$	−1.256 (*−0.909)	93.8	15.0	[6]
β-Bi$_2$O$_3$ fractals	0.1 M KHCO$_3$	-1.20	87	22	[21]
Bi dendrite	0.5 M KHCO$_3$	-0.74	89	2.3	[22]
Bi-MOF	0.1 M KHCO$_3$	-0.9	92.2	4.5	[5]
Bi@Sn NPs	0.5 M KHCO$_3$	-1.1	91	31	[3]
	2.0 M KHCO$_3$[a]	-1.1	92	250	
Bi$_2$O$_3$@C-800	0.5 M KHCO$_3$	-0.90	92	7.5	[4]
	1.0 M KOH[a]	-1.1	93	208	
Bi$_2$S$_3$-Bi$_2$O$_3$ NSs	0.1 M KHCO$_3$	-1.1 (*-0.86)	93.8	17.1	This work
	1.0 M KOH[a]	-1.0	95.3	145	

Note: * indicates jR compensation; [a] indicates the measurement in flow cell.

Table S5.3 The corresponding impedance by fitting circuit at the potential of -1.1 V vs. RHE in the H-type cell.

Catalyst	Ohmic resistance R_s (Ω)	Charge transfer resistance R_{ct} (Ω)
Bi_2S_3	13.07	93.83
Bi_2O_3	13.00	109.20
Bi_2S_3/Bi_2O_3	12.95	72.32
Bi_2S_3-Bi_2O_3	13.21	46.65

5.5.2 Supporting references

[1]   X. Zhang, J. Fu, Y. Liu, X.-D. Zhou, J. Qiao, *ACS Sustain. Chem. Eng.* **2020**, *8*, 4871-4876.

[2]   Y. Wang, Y. Li, J. Liu, C. Dong, C. Xiao, L. Cheng, H. Jiang, H. Jiang, C. Li, *Angew. Chem. Int. Ed.* **2021**, *60*, 7681-7685.

[3]   Y. Xing, X. Kong, X. Guo, Y. Liu, Q. Li, Y. Zhang, Y. Sheng, X. Yang, Z. Geng, J. Zeng, *Adv. Sci.* **2020**, 1902989.

[4]   P. Deng, F. Yang, Z. Wang, S. Chen, Y. Zhou, S. Zaman, B. Y. Xia, *Angew. Chem. Int. Ed.* **2020**, *59*, 10807-10813.

[5]   F. Li, G. H. Gu, C. Choi, P. Kolla, S. Hong, T.-S. Wu, Y.-L. Soo, J. Masa, S. Mukerjee, Y. Jung, J. Qiu, Z. Sun, *Appl. Catal. B-Environ.* **2020**, *277*, 119241.

[6]   S. Liu, X. F. Lu, J. Xiao, X. Wang, X. W. D. Lou, *Angew. Chem. Int. Ed.* **2019**, *58*, 13828-13833.

[7]   Q. Yang, Q. Wu, Y. Liu, S. Luo, X. Wu, X. Zhao, H. Zou, B. Long, W. Chen, Y. Liao, L. Li, P. K. Shen, L. Duan, Z. Quan, *Adv Mater* **2020**, e2002822.

[8]   M. Fan, S. Prabhudev, S. Garbarino, J. Qiao, G. A. Botton, D. A. Harrington, A. C. Tavares, D. Guay, *Appl. Catal. B-Environ.* **2020**, *274*, 119031.

[9]   F. L. Meng, Q. Zhang, Y. X. Duan, K. H. Liu, X. B. Zhang, *Chinese Journal of Chemistry* **2020**, *38*, 1752-1756.

[10]   Y.-R. Wang, R.-X. Yang, Y. Chen, G.-K. Gao, Y.-J. Wang, S.-L. Li, Y.-Q. Lan, *Science Bulletin* **2020**, *65*, 1635-1642.

[11]   Q. Gong, P. Ding, M. Xu, X. Zhu, M. Wang, J. Deng, Q. Ma, N. Han, Y. Zhu, J. Lu, Z. Feng, Y. Li, W. Zhou, Y. Li, *Nature Communications* **2019**, *10*, 2807.

[12]   X. Yuan, Y. Luo, B. Zhang, C. Dong, J. Lei, F. Yi, T. Duan, W. Zhu, R. He, *Chem. Commun.* **2020**, *56*, 4212.

[13]   Y. Liang, W. Zhou, Y. Shi, C. Liu, B. Zhang, *Science Bulletin* **2020**, *65*, 1547-1554.

[14]   Z. Zhang, F. Ahmad, W. Zhao, W. Yan, W. Zhang, H. Huang, C. Ma, J. Zeng, *Nano Lett.* **2019**, *19*, 4029-4034.

[15]   B. Zhang, S. Chen, B. Wulan, J. Zhang, *Chem. Eng. J.* **2021**, *421*, 130003.

[16]   G. Liu, Z. Li, J. Shi, K. Sun, Y. Ji, Z. Wang, Y. Qiu, Y. Liu, Z. Wang, P. Hu, *Appl. Catal. B-Environ.* **2020**, *260*, 118134.

[17]   Z. Li, A. Cao, Q. Zheng, Y. Fu, T. Wang, K. T. Arul, J. L. Chen, B. Yang, N. M. Adli, L. Lei, C. L. Dong, J. Xiao, G. Wu, Y. Hou, *Adv Mater* **2020**, e2005113.

[18]   Z. Chen, T. Fan, Y.-Q. Zhang, J. Xiao, M. Gao, N. Duan, J. Zhang, J. Li, Q. Liu, X. Yi, J.-L. Luo, *Appl. Catal. B-Environ.* **2020**, *261*, 118243.

[19]   W. Zhang, Y. Hu, L. Ma, G. Zhu, P. Zhao, X. Xue, R. Chen, S. Yang, J. Ma, J. Liu, Z. Jin, *Nano Energy* **2018**, *53*, 808-816.

[20]   Y. Wang, L. Cheng, J. Liu, C. Xiao, B. Zhang, Q. Xiong, T. Zhang, Z. Jiang, H. Jiang, Y. Zhu, Y. Li, C. Li, *ChemElectroChem* **2020**, *7*, 2864-2868.

[21]   T. Tran-Phu, R. Daiyan, Z. Fusco, Z. Ma, R. Amal, A. Tricoli, *Adv. Funct. Mater.* **2019**, *30*, 1906478.

[22]   J. H. Koh, D. H. Won, T. Eom, N.-K. Kim, K. D. Jung, H. Kim, Y. J. Hwang, B. K. Min, *ACS Catal.* **2017**, *7*, 5071-5077.

Chapter 6. Carbon Dioxide Valorization via Formate Electrosynthesis in a Wide Potential Window

6.1 Introduction

The ever-increasing energy consumption of fossil fuels has led to excessive emissions of CO_2, causing environmental problems and exacerbating the greenhouse gas effect [1-5]. Electrochemical reduction reaction of CO_2 (CO_2RR) appears to be a promising strategy to alleviate these problems and sustainably produce value-added chemicals and fuels [6-10]. As one of the typical reduction products, formic acid (HCOOH)/formate ($HCOO^-$) shows great potential in energy-dense fuels based on the techno-economic analysis and it can be utilized as feedstock for fuel cells and chemical intermediates in various industrial processes [11, 12].

Previous studies have reported the preferential formate formation on p-block metals, and great efforts have been devoted to developing various metal-based electrocatalysts [13]. Although some heavy metals are capable of catalyzing CO_2-to-formate conversion, such as Hg, Cd, Pb and Tl [14-16], the high toxicity and cost of these metals limit their large-scale applications for CO_2RR. Sn-based materials have also attracted great interests due to their nontoxicity and low cost, but their poor selectivity and relatively high overpotential make them the unsatisfactory candidates for meeting the application requirements [17-20]. It is worth mentioning that Bi-based materials have been shown to be the promising candidates for the formate formation during CO_2RR [20-25]. In addition to their abundant reserves and low toxicity, Bi-based materials are also relatively inert to hydrogen evolution reaction (HER). Despite much effort having been devoted to the enhancement of catalytic activity and selectivity on Bi-based materials for formate formation, designing the effective and selective

Bi-based catalysts for practical CO_2RR applications still remains challenging due to the uneasy task of achieving good current density, selectivity and durability simultaneously [21]. Normally, the high formate Faradaic efficiencies are attained at the expense of low current density, and it would quickly deteriorate as cathodic potentials increase, i.e., a high formate selectivity can only occur within a narrow potential window. Therefore, it is of great importance to design and fabricate the low cost catalysts possessing high selectivity and activity in a wide potential window for formate formation to advance CO_2RR technology toward its practical implementations at industrial scale.

It is generally accepted that the CO_2 adsorption on the catalyst surface coupled with a transferred electron serves as the initial reaction step in CO_2RR process. However, the chemical inertness of CO_2 results in a high energy barrier in the $CO_2/*CO_2^-$ formation step at a high reduction potential of $E° = -1.90$ V vs standard hydrogen electrode [26]. This thermodynamic bottleneck severely hinders the reaction rate and leads to unsatisfactory performance of CO_2RR [27]. Moreover, the low solubility of CO_2 in aqueous media (approximately 33 mM under a standard condition) strongly limits the mass transfer and restrains the current density during CO_2RR [28, 29]. Given the importance of access to the CO_2 reactant on the catalyst surface during CO_2RR, enhancing CO_2 adsorption capability is considered a feasible approach to improving the electrocatalytic performance. Bocarsly et al. reported an interesting phenomenon for CO_2RR to HCOOH formation on In and Sn electrodes using *in situ* attenuated total reflectance infrared spectroscopy (ATR-IR) [30-32]. They showed that the generation of the surface-bound electroactive carbonate species from the CO_2 intercalated on the catalyst surface is the first step in CO_2 conversion and these carbonate species serve as intermediates for subsequent reactions for formate formation.

Jiang et al. reported that the cadmium carbonate catalyzed selective production of CO and attributed the high selectivity to the strong affinity of CO_2 to the catalyst surface having lower potential of the intermediate formation [27]. These results suggest the important role of the existing carbonate species during CO_2RR process. Inspired by this, designing electrocatalysts with structurally bonded carbonates is expected to demonstrate the different CO_2 adsorption behavior that may facilitate the CO_2RR process, thereby improving the catalytic performance. Bismuth subcarbonate, $(BiO)_2CO_3$ (BOC), is a Sillén-type layered crystal structure material composed of CO_3^{2-} and $[Bi_2O_2]^{2+}$. The unique composition and crystal structure make it a possible candidate for CO_2RR to address the above-mentioned concerns. Therefore, it is worthwhile to study the electrocatalytic performance of BOC in CO_2RR and explore its reaction mechanism to achieve both high selectivity and activity in a wide potential window, which is crucial for the practical applications of CO_2RR technologies.

In this work, we report a nanoflower-like bismuth subcarbonate electrocatalyst (BOC NFs) prepared through a facile one-pot synthesis method toward high formate selectivity in CO_2RR. The unique self-reinforced CO_2 adsorption property and fast CO_2 adsorption-desorption kinetics of BOC NFs are revealed through the *in situ* characterizations and theoretical calculations. As a result, the maximum Faradaic efficiency (FE) of 98.9 % with a current density (*j*) of 10.0 mA cm^{-2} is achieved at a moderate potential (-1.0 V vs. reversible hydrogen electrode, RHE) in 0.1 M KHCO$_3$, along with a good stability of 36 h with negligible degradation for formate formation. Moreover, a high current density of 230 mA cm^{-2} at -1.1 V and good durability for efficient CO_2-to-formate conversion are achieved in the flow cell configuration, outperforming most of the state-of-the-art Bi-based electrocatalysts. This work offers a promising strategy to design environmentally friendly

111

electrocatalysts with self-reinforced CO_2 adsorption capability for highly efficient CO_2RR to formate production.

6.2 Results and discussion

6.2.1 Structural Characterizations of $(BiO)_2CO_3$ Nanoflowers

As illustrated in Figure 6.1a, the BOC NFs were synthesized via a wet chemical method. The bismuth citrate was first dissolved in ammonia to form a transparent precursor, followed by adding sodium bicarbonate solution under continuous stirring and reacting for 24 h at room temperature.
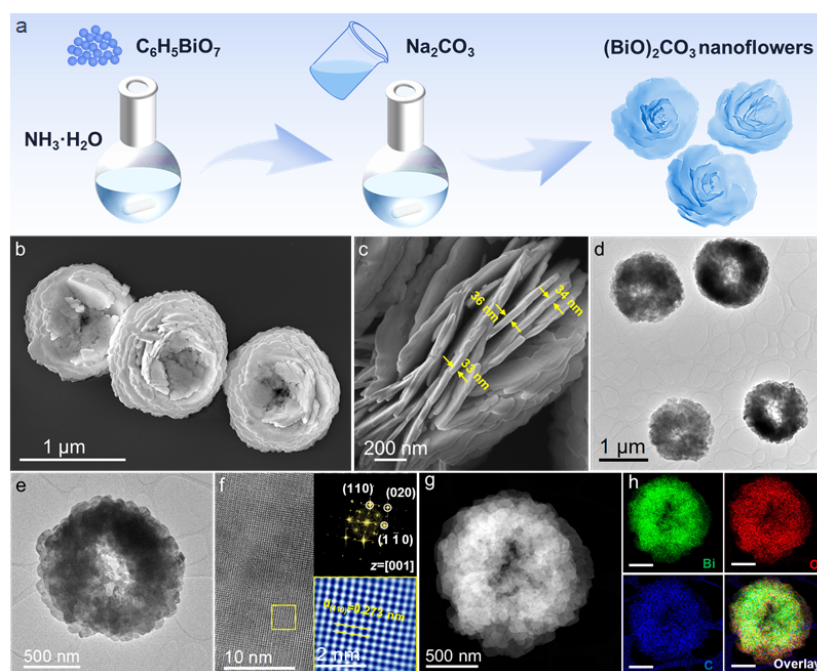
Figure 6.1 (a) Schematical illustration of the synthesis of BOC NFs; (b) and (c) SEM images, (d) and (e) TEM images, (f) HRTEM image (inset: corresponding FFT pattern and lattice fringe), and (g) HAADF-STEM image and (h) corresponding EDS elemental mappings (scale bar 500 nm) of prepared BOC NFs.

The field-emission scanning electron microscopy (FESEM) and transmission electron microscopy (TEM) were carried out to probe the morphological features of the as-prepared catalysts. The BOC NFs are observed with a uniform diameter of about 1 μm (Figure 6.1b), which are stacked by nanosheets with a thickness of about 30 nm (Figure 6.1c). As confirmed by TEM, a hollow area with the size of 0.2 μm is found in the center of BOC NFs (Figures 6.1d and e). It is expected that the hollow structure is beneficial for gas adsorption during the electrochemical reactions. The atomic lattice fringe of 0.273 nm as shown in Figure 1f corresponds to the (110) lattice spacing of tetragonal BOC, and the corresponding fast Fourier transform pattern (FFT) with a four-fold symmetry further confirms the presence of (001) basal planes. In addition, the high-angle annular dark-field scanning TEM (HAADF-STEM) images with energy-dispersive X-ray spectroscopy (EDS) elemental mappings also show the uniform distribution of elements Bi, C and O throughout the whole BOC NFs, further demonstrating the successful preparation of BOC NFs (Figures 6.1g and h).

The phase composition of BOC NFs was confirmed by powder X-ray diffraction (XRD) and all measured peaks can be indexed to the standard patterns of tetragonal BOC (PDF # 25-1464) as shown in Figure 6.2a. In addition, the Fourier-transformed infrared spectroscopy (FTIR) measurement was performed to identify the chemical bonds of the as-prepared catalysts. The four vibration modes of carbonate (CO_3^{2-}) are all observed in BOC NFs (Figure 6.2b). The intensive peaks at 1380 cm^{-1} and 844 cm^{-1} are ascribed to the antisymmetric vibration mode v_3 and out-of-plane bending mode v_2 of CO_3^{2-} respectively, while the peaks at 690 and 670 cm^{-1} are assigned to the in-plane deformation mode v_4. Moreover, the symmetric stretching vibration mode v_1 is identified at 1066 cm^{-1}, together with the stretching vibration of Bi=O bond at 540 cm^{-1}. These results firmly demonstrate the existence of

abundant carbonate species in BOC NFs. To reveal the chemical state of BOC NFs, X-ray photoelectron spectroscopy (XPS) was carried out and the survey spectrum indicates the spectroscopic features of Bi, O and C (Figure S6.1). The high resolution XPS spectrum of Bi shows a spin-orbit splitting doublet of Bi 4f, where the binding energies of 164.4 and 159.0 eV are assigned to Bi $4f_{5/2}$ and Bi $4f_{7/2}$ respectively (Figure 6.2c) [33]. Additionally, the O 1s spectrum exhibits the peaks at 529.3 and 530.3 eV associated with Bi-O and C-O bonds in CO_3^{2-}, and the peak at 532.3 eV corresponds to the adsorbed oxygen species. The characteristic peak in C 1s at 288.7 eV is attributed to the carbonate ions in BOC NFs. Overall, the characterization results collectively confirm the formation of the highly crystalline BOC NFs.
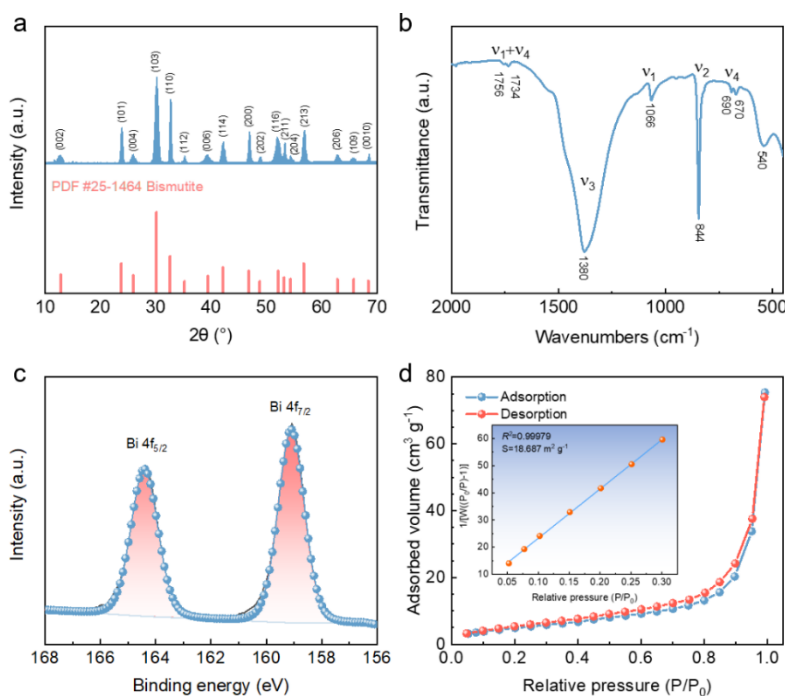
Figure 6.2 (a) XRD pattern, (b) FTIR spectrum, (c) High resolution XPS Bi 4f spectrum and (d) N_2 adsorption-desorption isotherm curve of prepared BOC NFs (inset: the BET surface area).

Further physical characterization was performed by N_2 adsorption-desorption isotherm to reveal the pore structure and specific surface area (SSA) of the as-prepared catalyst (Figure 6.2d). According to the Brunauer-Deming-Deming-Teller (BDDT) classification of physical adsorption isotherms, the adsorption curve of BOC NFs belongs to the type IV, indicating the existence of mesoporous structure. In addition, the type of H3 hysteresis loop demonstrates the formation of slit-like pores, which corresponds to the stacked nanosheet structure. The SSA derived from the isotherm by Brunauer-Emmett-Teller (BET) equation shows a value of about 18.7 m^2 g^{-1}, suggesting the large surface area of the stacked nanosheets in BOC NFs. These results are consistent with the morphological features of the BOC NFs.

6.2.2 CO$_2$RR Performance of (BiO)$_2$CO$_3$ Nanoflowers

The CO$_2$RR electrocatalytic performance evaluation of the BOC NFs, with Bi_2O_3 as the reference (Figures S6.2 and S6.3), was first carried out in CO_2-saturated 0.1 M KHCO$_3$ electrolyte within a gas-tight H-type cell separated by Nafion 117 membrane, and all the potentials were converted to the reversible hydrogen electrode (RHE) unless specified otherwise. As shown in Figure 6.3a, the linear sweep voltammetry (LSV) results demonstrate the better overall electrocatalytic activities of BOC NFs with higher j than that of Bi_2O_3. However, these high activities include both CO$_2$RR and the competing HER, where the preference to CO$_2$RR should be further identified. Thus, the chronoamperometry measurements at different potentials were carried out to exclude the contribution of HER by quantitative analysis of CO$_2$RR products as shown in Figures S6.4a. The gaseous and liquid products were determined by online gas chromatography (GC) and ion chromatography (IC), respectively.
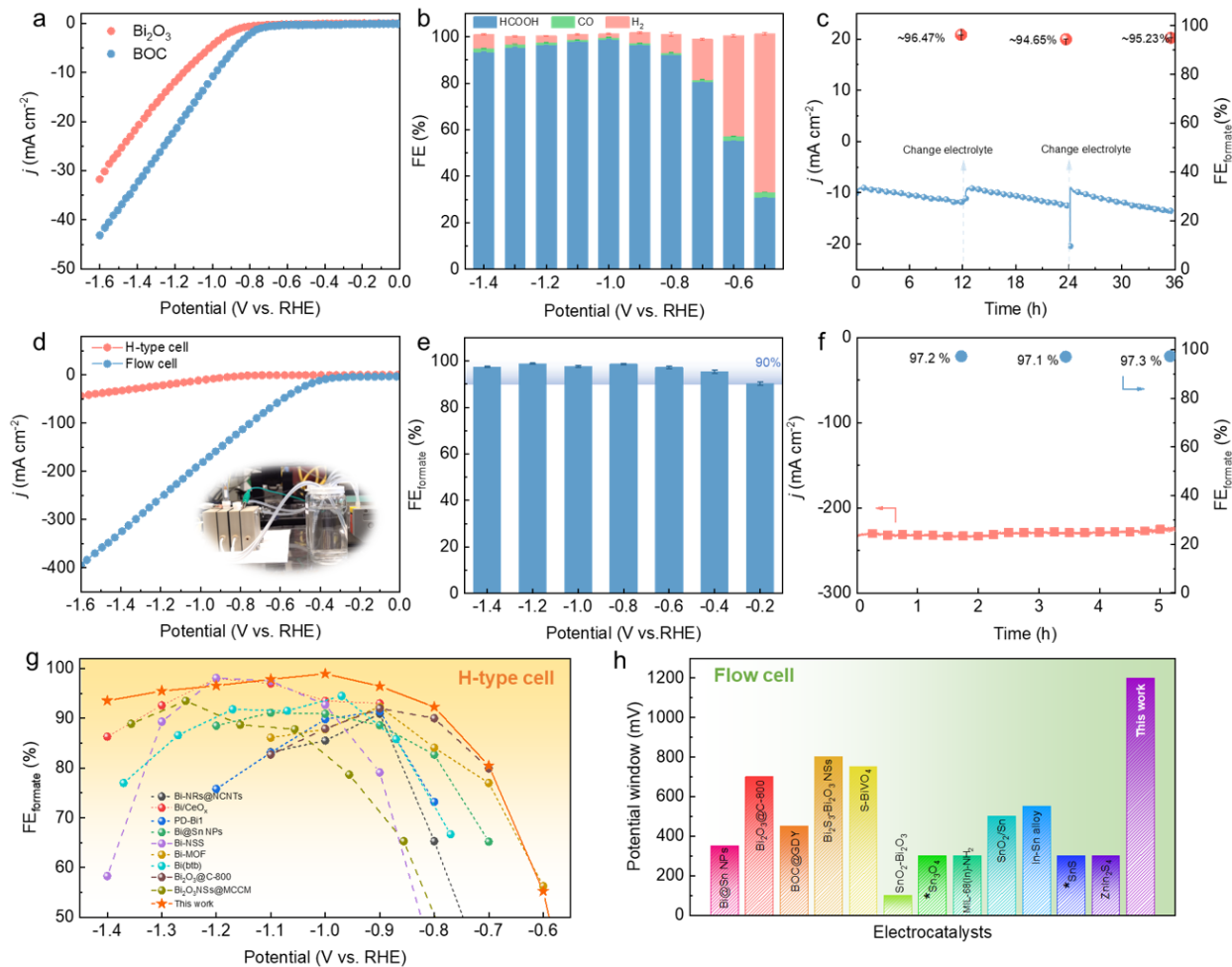
Figure 6.3 (a) LSV curves of Bi_2O_3 and BOC NFs in CO_2-saturated 0.1 M $KHCO_3$ in H-type cell; (b) FEs of product distributions at different applied potentials on BOC NFs; (c) Stability test of BOC at -1.0 V vs. RHE in H-type cell; (d) Comparison of LSV curves of BOC NFs in the H-type cell and flow cell; (e) $FE_{formate}$ at different applied potentials and (f) Stability test of BOC NFs at -1.1 V vs. RHE in 1.0 M KOH using the flow cell. (g) Comparison of FEs of formate at the various applied potentials with recently reported Bi-based electrocatalysts in a H-type cell; (h) Comparison of potential window range with $FE_{formate}$ > 90% with reported metal-based electrocatalysts for formate production using a flow cell (* indicates the $FE_{formate}$ > 80%).

116

Figure 6.3b shows the product distributions of BOC NFs at different applied potentials where formate is the dominating liquid product with minor amounts of gaseous products of CO and H_2. Specifically, the BOC NFs are highly selective toward formate formation with $FE_{formate}$ of over 90% in a wide potential window from -0.8 to -1.4 V, in which a maximum $FE_{formate}$ of 98.9% at -1.0 V was achieved. Although Bi_2O_3 also shows a preference for formate formation, the selectivity is much inferior to the BOC NFs (Figure S6.4b). Moreover, the minimum potential for formate detection reaches -0.5 V on BOC NFs, indicating a low onset overpotential (η) for formate formation during CO_2RR.

Furthermore, the partial current density ($j_{formate}$) was determined to exclusively show the electrocatalytic activities for formate formation during CO_2RR (Figure S6.4c). At a moderate potential, the BOC NFs show a $j_{formate}$ of 22.2 mA cm^{-2}, around 3.8 times higher than that of Bi_2O_3 (5.9 mA cm^{-2}) at -1.2 V. This high $j_{formate}$ further confirms the good electrocatalytic activity for the conversion of CO_2 to formate. As a key factor for the practical application of electrocatalysts, the stability test was performed at a fixed potential of -1.0 V over an extended period of time with electrolyte being refreshed every 12 h. As shown in Figure 6.3c, the stably maintained j and $FE_{formate}$ indicate the good stability of BOC NFs for CO_2RR. The $FE_{formate}$ shows negligible changes from 98.4% to 96.7% after 36 h measurement, further confirming the good stability of BOC NFs. It can be found that j slightly increases over 12 h due to the accumulation of $HCOO^-$ in the electrolyte, which could be quickly restored after refreshing the cathode electrolyte. To elucidate the origins of good durability, the morphology and structure features of BOC NFs after CO_2RR were further identified. The post-catalysis XRD shows the new phase of bismuth (PDF # 44-1246) with mostly retained pristine BOC after CO_2RR, which is ascribed to the electroreduced Bi species (Figure S6.4d).

In addition, as confirmed by SEM and TEM characterizations, the morphology of BOC NFs shows slight changes after CO_2RR that only a small fraction of BOC NFs is reduced to Bi nanosheets (Figures S6.5). The similar results have been reported in the previous work that the BOC structure is well maintained after CO_2RR measurement [34, 35]. This is mainly due to the dynamic transformation of BOC structure under the CO_2RR conditions [36, 37]. The negligible degradation of BOC NFs proves the good durability of both structure and morphology, which accounts for the outstanding stability for CO_2RR.

The economically compelling application of CO_2RR technology toward formate conversion requires a high j of over 200 mA cm^{-2} and $FE_{formate}$ higher than 90% [8, 38]. However, the limitation of CO_2 mass transport in aqueous electrolyte within the H-type cell significantly restricts the j for CO_2RR [39, 40]. As an alternative, the gas diffusion electrode (GDE) in a flow cell configuration was used to shorten the CO_2 diffusion path and reduce ohmic resistance compared to that in an H-type cell, this achieved high j and better CO_2RR performance [41]. Thus, the as-prepared BOC NFs were further evaluated using a flow cell. The LSV results show that the BOC NFs deliver a j of 200 mA cm^{-2} at -1.0 V (Figures 6.3d and S6.6a) and at a more positive onset potential of -0.2 V for formate formation in comparison with the values from the H-type cell. As confirmed by the electrochemical impedance spectroscopy (EIS) measurements (Figure S6.6b), the enhancement of electrocatalytic performance is attributed to the rapid CO_2 diffusion to the catalysts surface and the reduced ohmic resistance of flow cell using a high-concentration alkaline electrolyte. The highly conductive alkaline electrolyte not only reduces the ohmic resistance especially at high j, but also suppresses the parasitic HER during CO_2RR [39]. As a result, the $FE_{formate}$ of BOC NFs maintains at over 95% in the potential range from -0.4 to -1.4 V and only slightly

118

decreases to 90% at a lower onset potential of -0.2 V (Figure 6.3e). The $j_{formate}$ increases from 3.6 to 316 mA cm^{-2} under the applied potentials correspondingly (Figure S6.6c). The extremely wide potential window of 1200 mV with high formate selectivity of over 90% demonstrates the superior electrocatalytic performance of BOC NFs for efficient formate electrosynthesis. Moreover, the commercially feasible j of about 230 mA cm^{-2} and FE$_{formate}$ of over 97 % are achieved by conducting electrolysis at -1.1 V for 5 h shown in Figure 3f. The negligible changes of j and FE$_{formate}$ signify the good stability of BOC NFs, further demonstrating the great potential for their practical applications in advancing CO$_2$RR technology. Such high FE$_{fomrate}$ and j of BOC NFs for CO$_2$RR within an extremely wide potential window also make it stand out among most formate-producing electrocatalysts in both H-type cell and flow cell (Figures 6.3g and 6.3h, Tables S6.1 and S6.2).

6.2.3 Investigation of Self-Reinforced CO$_2$ Adsorption Capability on (BiO)$_2$CO$_3$ Nanoflowers

As mentioned earlier, the adsorption of CO$_2$ to the catalyst surface is regarded as the initial step during CO$_2$RR. Due to the presence of the structurally bonded carbonate species and the layered crystal structure configuration, as well as a hollow structure favorable for gaseous CO$_2$ adsorption, BOC NFs are expected to exhibit unique CO$_2$ adsorption properties. To this end, the *in situ* diffuse reflectance infrared Fourier transform spectroscopy (DRIFTS) was first performed to identify the dynamic CO$_2$ gas adsorption process on the as-prepared catalysts. Figures 6.4a and 6.4d show the overall measured spectra with the feed gas CO$_2$ at the room temperature and pressure. BOC NFs are found to have two distinct bands at approximately 2350 cm^{-1} and 1600 cm^{-1}, while there is only one band at 2350 cm^{-1} for Bi$_2$O$_3$. Considering the different CO$_2$ adsorption types, i.e., physisorption and chemisorption, the

spectra are further analyzed with enlarged selected areas of A and B. The high intensity bands at 2350 cm^{-1} of BOC NFs and Bi_2O_3 belong to the physisorption of CO_2 gas [42] (Figures 6.4b and 6.4e). Both electrocatalysts demonstrate the strong CO_2 physisorption capability, while the higher peak intensity and shorter time to reach CO_2 adsorption equilibrium on BOC NFs indicate the better physisorption capability.
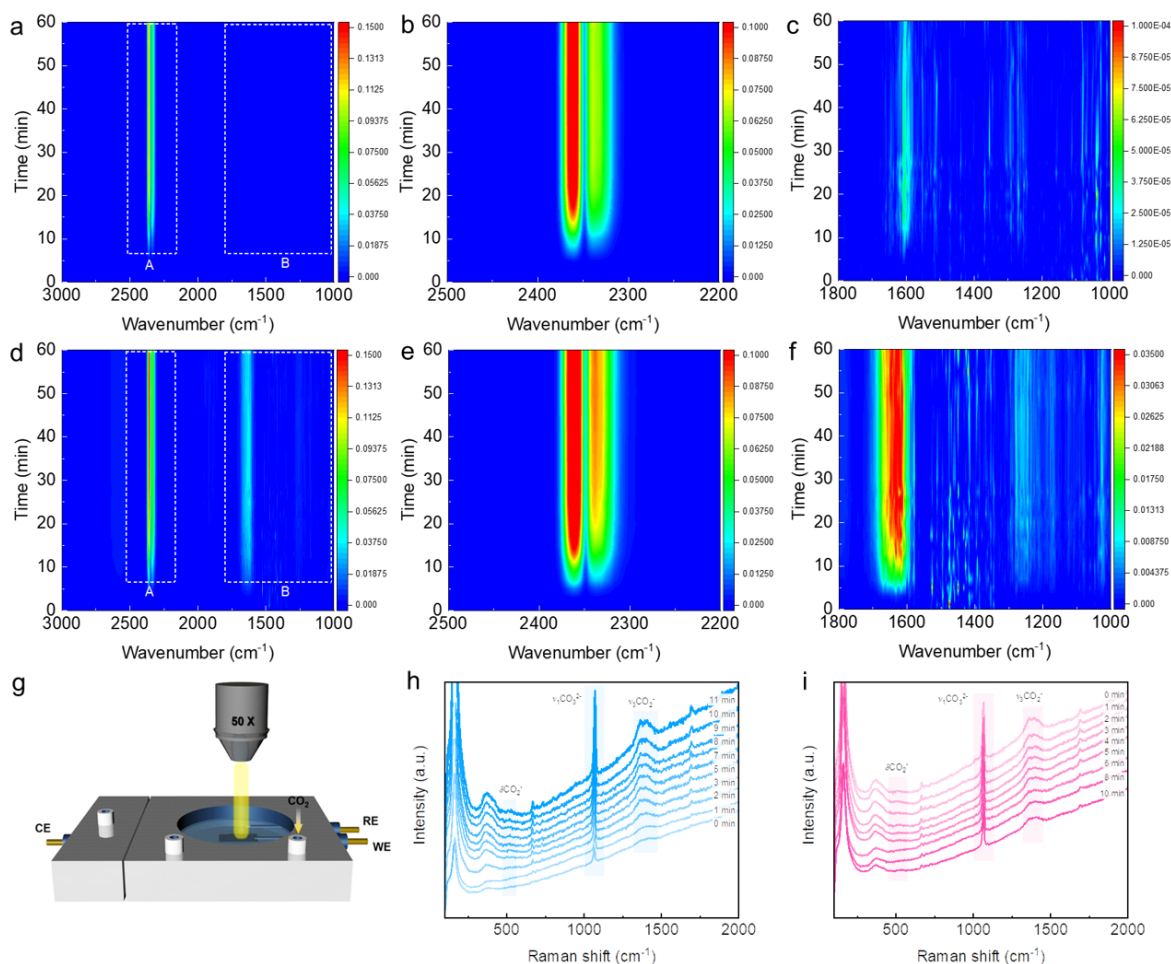
Figure 6.4 *In situ* DRIFTS spectra of CO_2 adsorbed on (a), (b) and (c) Bi_2O_3 surface; (d), (e) and (f) BOC NFs surface; (g) Schematic illustration of *in situ* Raman spectroscopy measurement during CO_2RR; Time-resolved *in situ* Raman spectra of BOC NFs in 0.1 M KHCO$_3$ at OCP (h) with CO_2 bubbling and (i) stop the CO_2 bubbling.

Furthermore, the magnified band from 1000 to 1800 cm^{-1} is assigned to the adsorption of carbonate and bicarbonate species that belongs to the CO_2 chemisorption [43, 44]. These bands are usually broadly overlapped. As shown in Figure 6.4c, the band located at 1686 cm^{-1} of Bi_2O_3 corresponds to the v_2 vibration mode of the adsorbed carbonate species, but the extremely low peak intensity indicates that almost no CO_2 chemisorption occurs. In contrast, the BOC NFs demonstrate the overlapped bands with higher intensity compared to that of Bi_2O_3, indicating the stronger CO_2 chemisorption capability (Figure 6.4f). The CO_2 chemisorption of BOC NFs reaches saturation state within 30 min, whereas the Bi_2O_3 maintains a low intensity throughout the entire measurement (Figure S6.6d). Moreover, the density functional theory (DFT) calculations were performed to verify the CO_2 chemisorption on BOC NFs. The negative binding energies of all the optimized adsorption sites for CO_2 onto the (110) surface prove the energetically favorable CO_2 chemisorption on BOC NFs (Figure S6.7). Based on the above results, it can be concluded that BOC NFs possess superior CO_2 adsorption capability with fast adsorption kinetics, and the self-reinforced adsorption properties ensure sufficient CO_2 reactant that can fast reach the electrocatalyst surface for CO_2RR to proceed.

Given that the *in situ* DRIFTS measurement was carried out in an atmospheric environment, the *in situ* electrochemical Raman spectroscopy in 0.1 M $KHCO_3$ electrolyte was further performed on BOC NFs to confirm the excellence of CO_2 adsorption properties (Figure 6.4g). As shown in Figure 4h, the time-resolved Raman spectra were first acquired at open circuit potential (OCP) with the constant CO_2 gas bubbling. At the beginning, two Raman peaks located at about 1070 and 1350~1430 cm^{-1} can be observed that are related to structurally bonded carbonate species within the catalyst. These peak intensities gradually increase with

the continuous bubbling of CO_2 gas, suggesting the increment of adsorbed carbonate species on the catalyst surface. Specifically, the high intensity peak at 1070 cm^{-1} is attributed to $v_1CO_3^{2-}$ of the chemisorbed carbonate, which corresponds to the symmetrical C-O stretching vibration [45]. The vibration peaks at 1350~1430 cm^{-1} are assigned to $v_3CO_3^{2-}$ symmetric stretching of η^2(C, O)-CO_2^- of carboxylate anion. It is also worth noting that the new peak located at 450~550 cm^{-1} (Figure 6.4h) corresponds to the in-plane vibration of δCO_2^-, an indication of the adsorbed CO_2 on the catalyst surface [46]. Once the CO_2 gas bubbling is stopped, all Raman peak intensities associated with the surface bonded carbonate species starts to decrease to a steady state in 10 minutes (Figure 6.4i). This result firmly proves the rapid CO_2 adsorption-desorption kinetics on the BOC NFs in an aqueous electrolyte. In general, the above results not only verify the self-reinforced CO_2 adsorption properties, especially the chemisorption of BOC NFs, but also reveal the fast CO_2 adsorption-desorption kinetics on the catalyst surface in aqueous electrolyte. All of these merits are beneficial to the CO_2RR process and guarantee the excellent catalytic performance of the formate electrosynthesis.

6.2.4 Reaction Mechanism Study of the Enhanced Electrocatalytic Performance

It is well accepted that the electrocatalytic activity improvement is usually related to the increased number of active sites [3]. In that regard, the electrochemically active surface area (ECSA) was determined by measuring the double-layer capacitance. It is found that BOC NFs possess a significantly larger ECSA than Bi_2O_3, suggesting the substantial number of active sites over the as-prepared BOC NFs (Figure S6.8a). The increased ECSA is owing to the sheet-stacked structure of BOC NFs, which subsequently contributes to the excellent CO_2 adsorption behavior and leads to a rather high electrocatalytic activity toward CO_2RR. To

gain deep insights into the electrokinetic mechanism of CO_2RR to formate formation, the ECSA-corrected Tafel slopes were determined as shown in Figure 6.5a. The Bi_2O_3 and BOC NFs exhibit a similar Tafel slope of around 118 mV dec^{-1}, indicating that the initial one electron transfer process is the rate-determining step on the catalysts [47]. Additionally, the charge transfer ability is of great importance to the electrocatalytic performance due to the involvement of the proton-coupled electron transfer step during CO_2RR process. The Nyquist plot of BOC NFs measured at -1.0 V vs. RHE in CO_2-satured 0.1 M $KHCO_3$ electrolyte shows the two semicircles, one semicircle at high frequencies and the other at low frequencies (Figure 6.5b). The potential dependent EIS measurements were further carried out on BOC NFs as shown in Figure S6.8b. It can be clearly seen that the semicircles at high frequencies are independent of the applied potential, while the diameter of low frequencies semicircles significantly decreases as the applied potential moves to the more negative range. The results indicate that the semicircles at high frequencies mainly represent the resistance of ionic migration through the electrolyte film formed on the electrode/electrolyte interface and the inner active sites. The low frequencies semicircles reflect the charge transfer resistance that is dependent on the kinetics of reaction. Therefore, the BOC NFs show the smaller charge transfer resistance based on the radius of the Nyquist plots, suggesting a faster electron transfer between the interface of electrocatalyst and electrolyte. Subsequently, the work functions of Bi_2O_3 and BOC NFs were experimentally calculated by measuring ultraviolet photoelectron spectroscopy (UPS), since it can be used to evaluate the intrinsic electron transfer capability of electrocatalysts [48]. As shown in Figure 6.5c, the cut-off binding energy of BOC NFs is higher than that of Bi_2O_3, suggesting the lower work function of BOC NFs, which is consistent with the EIS results (Figure S6.8c). This implies the higher electron

tunneling property of BOC NFs that makes it easier for the electrons to transfer to the catalyst surface, so as to enable fast CO_2RR reaction process. Briefly, the superior electron transfer ability of BOC NFs accounts for the rapid pre-equilibrium of CO_2 to $*CO_2^-$ and consequently leads to an enhanced electrocatalytic activity of CO_2RR.
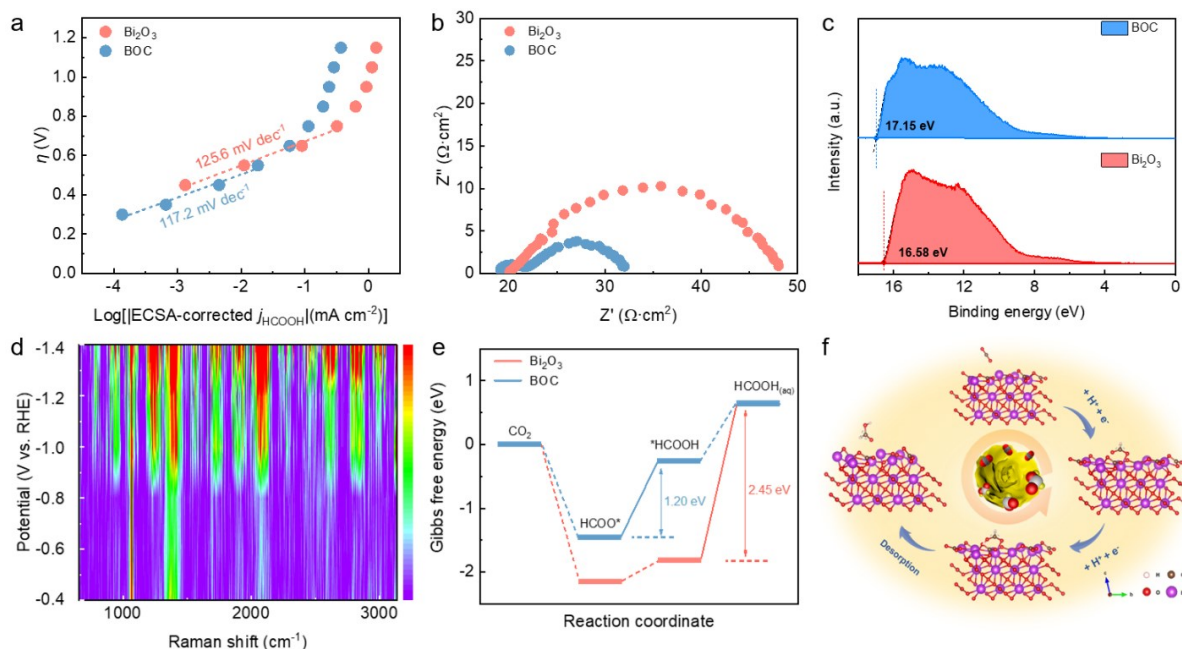
Figure 6.5 (a) ECSA-corrected Tafel plots for formate formation, (b) Nyquist plots of the EIS at -1.0 V vs. RHE in CO_2-satured 0.1 M $KHCO_3$ electrolyte and (c) UPS plots on Bi_2O_3 and BOC NFs; (d) Potential-resolved *in situ* Raman spectra of BOC NFs in CO_2-saturated 0.1 M $KHCO_3$; (e) DFT calculation results of Gibbs free energy for CO_2RR to formate on Bi_2O_3 and BOC NFs; (f) Schematic diagram of formate formation on BOC NFs.

To gain deeper insights, the potential-resolved *in situ* electrochemical Raman spectroscopy was performed toward the more negative cathodic potential to track the reaction process and intermediates for CO_2 to formate conversion. As displayed in Figure 6.5d, the two distinct Raman peaks at 1070 and 1350-1430 cm^{-1} are detected at -0.8 V or lower potentials. This can

be attributed to the C-O stretching vibrations from $v_1CO_3^{2-}$ and $v_3CO_3^{2-}$ of the BOC NFs, in consistence with the previous measured results at OCP. It is worth noting that as the applied potential moves towards the more negative range, the peak intensity gradually increases, with several new Raman peaks appearing at the same time. More specifically, the bands located at 785 and 1770 cm^{-1} belong to the carbonyl group stretching mode of formate, and the bands of 1595 and 2880 cm^{-1} correspond to the modes of O-C-O antisymmetric stretching and C-H stretching of formate, respectively [49]. This result confirms the formation of HCOO intermediate during the CO_2 to formate conversion. In addition, the presence of CO as a product is also confirmed by the vibration signal of vCO at 2060 cm^{-1} [50], and the high intensity is mainly due to the adsorbed CO bubbles accumulated on the catalyst surface.

To theoretically deepen our understanding on the reaction mechanism, the DFT calculations were performed on Bi_2O_3 and BOC NFs for CO_2RR toward formate formation. As shown in Figure 6.5e, the Gibbs free energy changes (ΔGs) for HCOO* formation are -1.45 and -2.16 eV on BOC NFs and Bi_2O_3 respectively, suggesting the exothermic reaction steps. Although the HCOO* formation energy of Bi_2O_3 is lower than that of BOC NFs, the higher energy barrier of 2.45 eV for *HCOOH desorption step significantly hinders the reaction process. Thus, BOC NFs are more favorable for formate formation. Based on *in situ* Raman measurements and DFT calculation results, the CO_2RR process of formate formation on BOC NFs can be schematically illustrated as shown in Figure 6.5f. Firstly, the superior CO_2 adsorption capability and fast adsorption kinetics of BOC NFs make it easier for CO_2 molecules to access the catalyst surface to form *CO_2 which is subsequently combined with a proton-coupled electron transfer step to form the intermediate HCOO*. Then, the

intermediate of HCOO* further gains another electron and proton to generate *HCOOH that finally undergoes a desorption step to form HCOOH.

According to the above results, the high electrocatalytic performance of BOC NFs should be related to their unique crystal structure and CO_2 adsorption behavior. The structurally bonded carbonate species of BOC NFs facilitates the CO_2 adsorption-desorption kinetics on the catalyst surface, thus ensuring a fast CO_2RR reaction process. Besides, the layer-stacked nanoflower structure endows the catalyst with a considerably larger surface area that provides an increased number of active sites for CO_2RR. Lastly, the good charge transfer ability of BOC NFs results in the rapid proton-coupled electron transfer steps, leading to a more efficient CO_2RR process. All these advantages collectively contribute to the favorable electrocatalytic performance of CO_2RR for formate formation.

6.3 Conclusions

In summary, the electrocatalyst BOC NFs are successfully synthesized through a facile method and demonstrate the good electrocatalytic performance for formate electrosynthesis. More specifically, the near-unity formate selectivity and a good stability are achieved at -1.0 V. The high $FE_{formate}$ of over 90% is obtained in a potential window as wide as 1200 mV, outperforming many other reported formate-producing electrocatalysts. The experimental and theoretical results demonstrate the self-reinforced CO_2 adsorption property and fast adsorption-desorption kinetics of BOC NFs, which could greatly facilitate the CO_2RR process through improving the overall electrocatalytic performance. This study exemplifies a promising strategy to design highly active, efficient and robust catalysts with self-

reinforced CO_2 adsorption capability for formate electrosynthesis especially under industrial relevant conditions.

6.4 References

[1]   P. De Luna, C. Hahn, D. Higgins, S. A. Jaffer, T. F. Jaramillo, E. H. Sargent, *Science* **2019**, *364*.

[2]   C. Xu, J. Hong, P. Sui, M. Zhu, Y. Zhang, J.-L. Luo, *Cell Reports Physical Science* **2020**, *1*, 100101.

[3]   F. Pan, Y. Yang, *Energy Environ. Sci.* **2020**, *13*, 2275-2309.

[4]   G. Wang, J. Chen, Y. Ding, P. Cai, L. Yi, Y. Li, C. Tu, Y. Hou, Z. Wen, L. Dai, *Chem. Soc. Rev.* **2021**, *50*, 4993-5061.

[5]   L. Zhou, R. Lv, *J. Energy Chem.* **2022**, *70*, 310-331.

[6]   S. Jin, Z. Hao, K. Zhang, Z. Yan, J. Chen, *Angew.Chem. Int. Ed.* **2021**, *60*, 20627-20648.

[7]   N. Han, P. Ding, L. He, Y. Li, Y. Li, *Adv. Energy Mater.* **2019**, 1902338.

[8]   S. Overa, B. H. Ko, Y. Zhao, F. Jiao, *Acc. Chem. Res.* **2022**, *55*, 638-648.

[9]   H. Liu, Y. Zhu, J. Ma, Z. Zhang, W. Hu, *Adv. Funct. Mater.* **2020**, *30*, 1910534.

[10]   T.-J. Wang, W.-S. Fang, Y.-M. Liu, F.-M. Li, P. Chen, Y. Chen, *J. Energy Chem.* **2022**, *70*, 407-413.

[11]   Q. Gong, P. Ding, M. Xu, X. Zhu, M. Wang, J. Deng, Q. Ma, N. Han, Y. Zhu, J. Lu, Z. Feng, Y. Li, W. Zhou, Y. Li, *Nat. Commun.* **2019**, *10*, 2807.

[12]   M. Fan, S. Prabhudev, S. Garbarino, J. Qiao, G. A. Botton, D. A. Harrington, A. C. Tavares, D. Guay, *Appl. Catal. B-Environ.* **2020**, *274*, 119031.

[13]   Z. Yang, F. E. Oropeza, K. H. L. Zhang, *APL Mater.* **2020**, *8*, 060901.

[14]   M. Azuma, K. Hashimoto, M. Hiramoto, M. Watanabe, T. Sakata, *J. Electrochem. Soc.* **1990**, *137*, 1772-1778.

[15]   H. W. Yoshio Hori, Toshio Tsukamoto, Osamu, Koga, *Electrochim. Acta* **1994**, *39*, 1833-1839.

[16]   J. Xiao, S. Liu, P.-F. Sui, C. Xu, L. Gong, H. Zeng, J.-L. Luo, *Chem. Eng. J.* **2022**, *433*, 133785.

[17]   F. Cheng, X. Zhang, K. Mu, X. Ma, M. Jiao, Z. Wang, P. Limpachanangkul, B. Chalermsinsuwan, Y. Gao, Y. Li, Z. Chen, L. Liu, *Energy Technol.* **2021**, *9*, 2000799.

[18]   B. Zhang, S. Chen, B. Wulan, J. Zhang, *Chem. Eng. J.* **2021**, *421*, 130003.

[19]   Z. Chen, T. Fan, Y.-Q. Zhang, J. Xiao, M. Gao, N. Duan, J. Zhang, J. Li, Q. Liu, X. Yi, J.-L. Luo, *Appl. Catal. B-Environ.* **2020**, *261*, 118243.

[20]   S. Liu, J. Xiao, X. F. Lu, J. Wang, X. Wang, X. W. D. Lou, *Angew. Chem. Int. Ed.* **2019**, *58*, 8499-8503.

[21]   Y. Guan, M. Liu, X. Rao, Y. Liu, J. Zhang, *J. Mater. Chem. A* **2021**, *9*, 13770-13803.

[22]   X. Zhang, T. Lei, Y. Liu, J. Qiao, *Appl. Catal. B-Environ.* **2017**, *218*, 46-50.

[23]   K. Fan, Y. Jia, Y. Ji, P. Kuang, B. Zhu, X. Liu, J. Yu, *ACS Catal.* **2019**, *10*, 358-364.

[24]   P. Deng, H. Wang, R. Qi, J. Zhu, S. Chen, F. Yang, L. Zhou, K. Qi, H. Liu, B. Y. Xia, *ACS Catal.* **2019**, *10*, 743-750.

[25]   P. F. Sui, C. Xu, M. N. Zhu, S. Liu, Q. Liu, J. L. Luo, *Small* **2021**, e2105682.

[26]   Y. Y. Birdja, E. Pérez-Gallent, M. C. Figueiredo, A. J. Göttle, F. Calle-Vallejo, M. T. M. Koper, *Nat. Energy.* **2019**, *4*, 732-745.

[27]   X. Jiang, X. Wang, Q. Wang, X. Xiao, J. Chen, M. Wang, Y. Shen, *ACS Appl. Energy Mater.* **2021**, *4*, 2073-2080.

[28]   R. M. Aran-Ais, D. Gao, B. Roldan Cuenya, *Acc. Chem. Res.* **2018**, *51*, 2906-2917.

[29]   M. Konig, J. Vaes, E. Klemm, D. Pant, *iScience* **2019**, *19*, 135-160.

[30]   M. F. Baruch, J. E. Pander, J. L. White, A. B. Bocarsly, *ACS Catal.* **2015**, *5*, 3148-3156.

[31]   J. E. Pander, M. F. Baruch, A. B. Bocarsly, *ACS Catal.* **2016**, *6*, 7824-7833.

[32]   Z. M. Detweiler, J. L. White, S. L. Bernasek, A. B. Bocarsly, *Langmuir* **2014**, *30*, 7593-7600.

[33]   L. Chen, R. Huang, S.-F. Yin, S.-L. Luo, C.-T. Au, *Chem. Eng. J.* **2012**, *193-194*, 123-130.

[34]   Y. Wang, B. Wang, W. Jiang, Z. Liu, J. Zhang, L. Gao, W. Yao, *Nano Res.* **2021**, *15*, 2919-2927.

[35]   L. G. Puppin, M. Khalid, G. T. T. da Silva, C. Ribeiro, H. Varela, O. F. Lopes, *J. Mater. Res.* **2020**, *35*, 272-280.

[36] T. Fan, W. Ma, M. Xie, H. Liu, J. Zhang, S. Yang, P. Huang, Y. Dong, Z. Chen, X. Yi, *Cell Reports Physical Science* **2021**, 100353.

[37] W. Lv, J. Bei, R. Zhang, W. Wang, F. Kong, L. Wang, W. Wang, *ACS Omega* **2017**, *2*, 2561-2567.

[38] Y. Cheng, P. Hou, X. Wang, P. Kang, *Acc. Chem. Res.* **2022**, *55*, 231-240.

[39] H. Rabiee, L. Ge, X. Zhang, S. Hu, M. Li, Z. Yuan, *Energy Environ. Sci.* **2021**, *14*, 1959-2008.

[40] K. Yang, R. Kas, W. A. Smith, T. Burdyny, *ACS Energy Lett.* **2020**, 33-40.

[41] R. I. Masel, Z. Liu, H. Yang, J. J. Kaczur, D. Carrillo, S. Ren, D. Salvatore, C. P. Berlinguette, *Nat. Nanotechnol.* **2021**, *16*, 118-128.

[42] Y. Yang, L. Ohnoutek, S. Ajmal, X. Zheng, Y. Feng, K. Li, T. Wang, Y. Deng, Y. Liu, D. Xu, V. K. Valev, L. Zhang, *J. Mater. Chem. A* **2019**, *7*, 11836-11846.

[43] C. Xu, X. Zhang, M.-N. Zhu, L. Zhang, P.-F. Sui, R. Feng, Y. Zhang, J.-L. Luo, *Appl. Catal. B-Environ.* **2021**, *298*, 120533.

[44] J. Baltrusaitis, J. Schuttlefield, E. Zeitler, V. H. Grassian, *Chem. Eng. J.* **2011**, *170*, 471-481.

[45] I. V. Chernyshova, P. Somasundaran, S. Ponnurangam, *Proc. Natl. Acad. Sci.* **2018**, *115*, E9261-E9270.

[46] C. He, S. Chen, R. Long, L. Song, Y. Xiong, *Sci. China Chem.* **2020**, *63*, 1721-1726.

[47] C. W. Lee, N. H. Cho, S. W. Im, M. S. Jee, Y. J. Hwang, B. K. Min, K. T. Nam, *J. Mater. Chem. A* **2018**, *6*, 14043-14057.

[48] Z.-Z. Wu, F.-Y. Gao, M.-R. Gao, *Energy Environ. Sci.* **2021**, *14*, 1121-1139.

[49] A. M. Ismail, G. F. Samu, Á. Balog, E. Csapó, C. Janáky, *ACS Energy Lett.* **2018**, *4*, 48-53.

[50] J. Wang, G. Wang, J. Zhang, Y. Wang, H. Wu, X. Zheng, J. Ding, X. Han, Y. Deng, W. Hu, *Angew. Chem. Int. Ed.* **2021**, *60*, 7602-7606.

6.5 Supporting Information

6.5.1 Supporting figures and tables
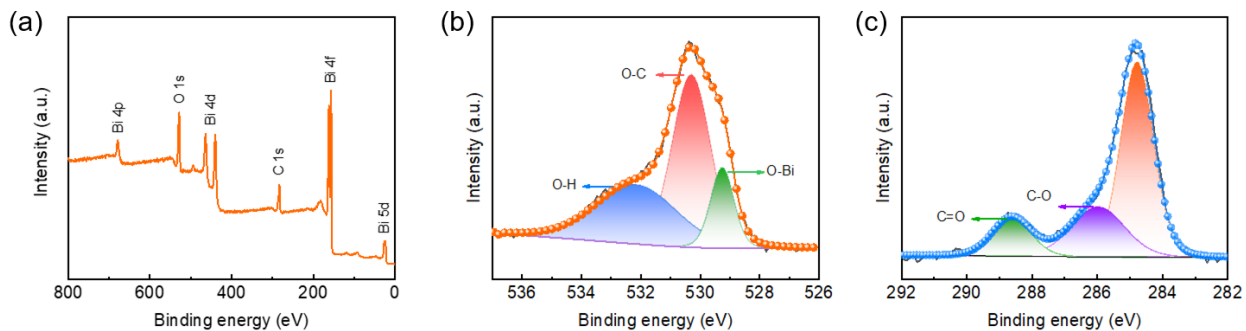
Figure S6.1 (a) XPS survey scan, (b) O 1s and (c) C 1s XPS spectra of BOC NFs.
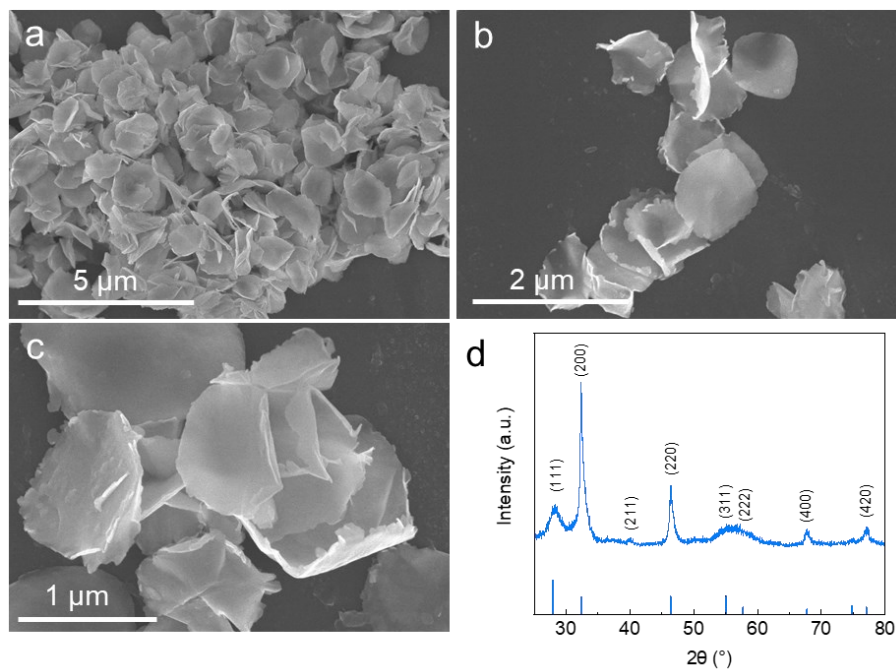
Figure S6.2 (a), (b) and (c) SEM images of as-prepared Bi_2O_3 nanosheets; (d) XRD pattern of Bi_2O_3.
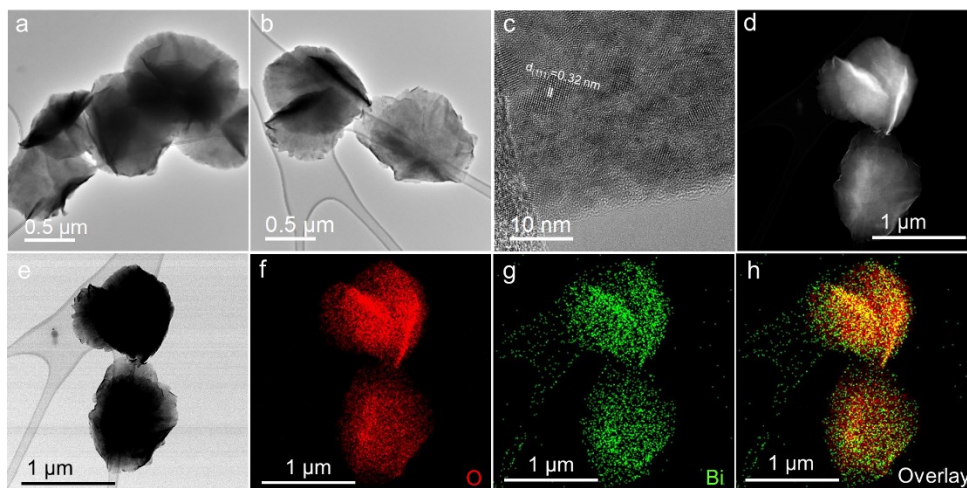
Figure S6.3 (a) and (b) TEM images, (c) HRTEM image, (d) and (e) HAADF-STEM images and (f) to (h) corresponding EDS elemental mappings of Bi_2O_3 nanosheets.
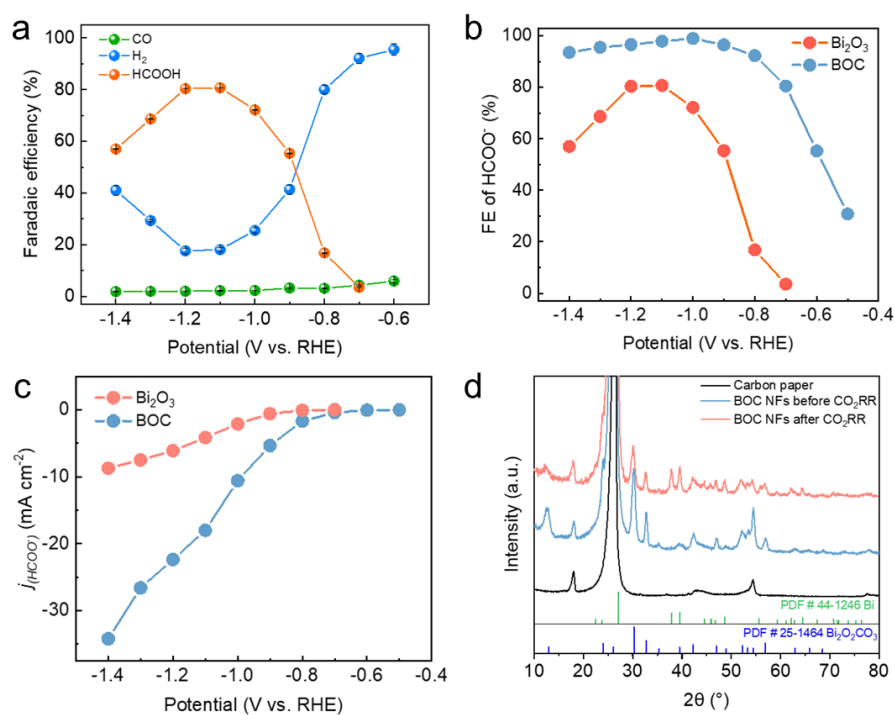
Figure S6.4 (a) Faradaic efficiencies of reduction products for Bi_2O_3; (b) FE of formate on Bi_2O_3 and BOC NFs at different applied potentials; (c) Partial current densities toward formate at different applied potentials; (d) XRD patterns of fresh and post-catalysis electrode.
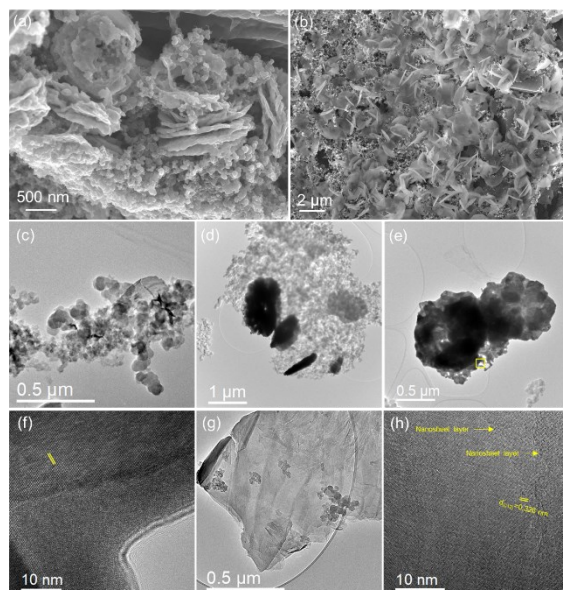
Figure S6.5 (a) and (b) SEM images of BOC NFs after CO_2RR; (c) to (h) TEM images of BOC NFs after CO_2RR.
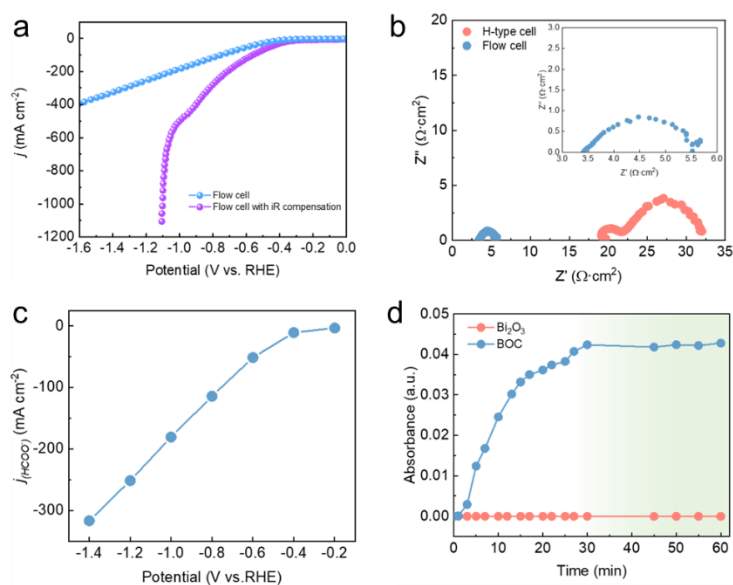
Figure S6.6 (a) LSV curves of BOC NFs in the flow cell measured with/without iR compensation; (b) Nyquist plots of BOC NFs (inset: the enlarge result in flow cell) in the H-type cell and flow cell; (c) $j_{(HCOO-)}$ of BOC NFs at different applied potentials measured in a flow cell; (d) The absorbance intensity of CO_2 at the band of 1686 cm^{-1} as time measured on Bi_2O_3 and BOC NFs.
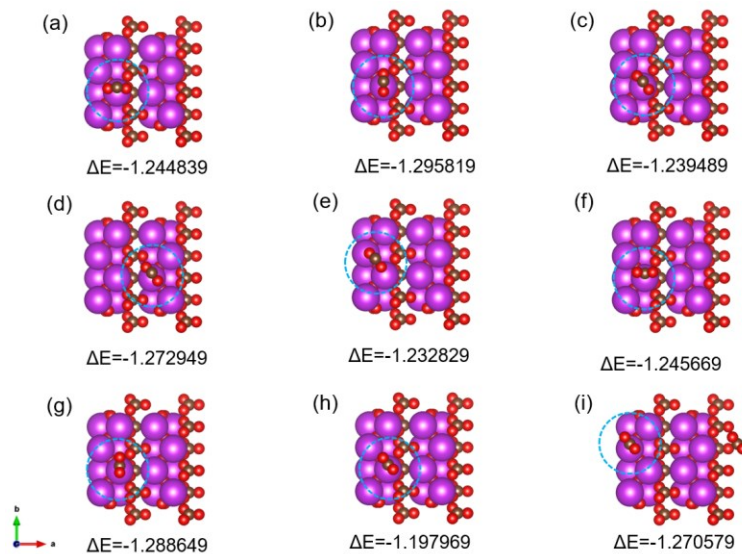
Figure S6.7 The optimized adsorption sites for CO_2 onto the $(BiO)_2CO_3$ (110) surface and the corresponding binding energy ΔE (eV).
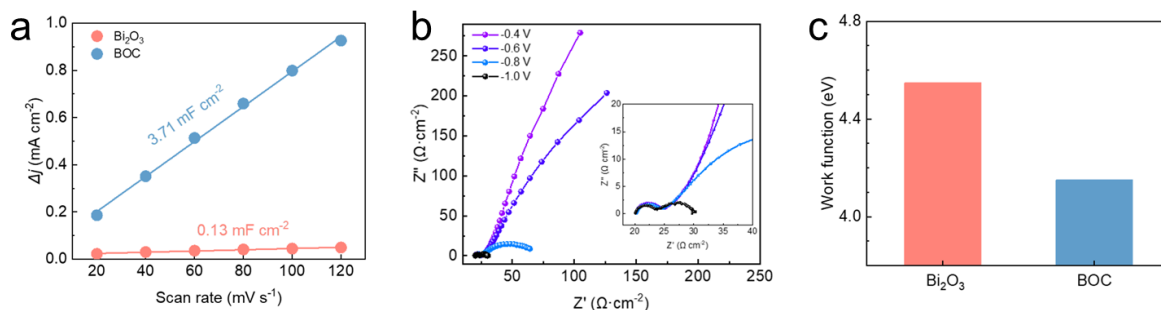
Figure S6.8 (a) Charging current density differences (Δj) plotted against scan rates on Bi_2O_3 and BOC NFs; (b) Nyquist plots for the BOC NFs at different applied potentials in CO_2-satured 0.1 M $KHCO_3$ electrolyte; (c) Work functions based on experimental calculations.

Table S6.1 Summary of our and previously Bi-based electrocatalysts for formate production based on electrochemical reduction of CO_2.

Catalyst	Electrolyte	Maximum $FE_{formate}$ (%)	Potential range for $FE_{formate}$ >90% (mV)	Reference
Bi-NRs@NCNTs	0.1 M KHCO$_3$	90.9 (-0.9 V)	-	[9]
Bi/CeO$_x$	0.2 M Na$_2$SO$_4$	98 (-1.2 V)	400	[10]
PD-Bi1	0.5 M KHCO$_3$	91.4 (-0.9 V)	100	[11]
Bi@Sn NPs	0.5 M KHCO$_3$	91 (-1.1 V)	100	[12]
Bi-NSS	0.1 M KHCO$_3$	98.4 (-1.2V)	200	[13]
Bi-MOF	0.1 M KHCO$_3$	92.2 (-0.9 V)	-	[14]
Bi(btb)	0.5 M KHCO$_3$	95.3 (-0.97 V)	200	[15]
Bi$_2$O$_3$@C-800	0.5 M KHCO$_3$	92 (-0.9 V)	100	[16]
Bi$_2$O$_3$NSs@MCCM	0.1 M KHCO$_3$	93.8 (-1.26 V)	-	[17]
Bi NTs	0.5 M KHCO$_3$	97 (-1.0 V)	450	[18]
Bi-SnO$_x$	0.5 M KHCO$_3$	95.8 (-0.88 V)	250	[19]
f-Bi$_2$O$_3$	0.1 M KHCO$_3$	87 (-1.2 V)	-	[20]
β-Bi$_2$O$_3$ NTs	0.5 M KHCO$_3$	97 (-0.9 V)	350	[21]
Bi-Sn aerogel	0.1 M KHCO$_3$	93.9 (-1.0 V)	300	[22]
BOC@GDY	0.5 M NaHCO$_3$	95.5 (-0.85 V)	300	[23]
Bi$_2$S$_3$-Bi$_2$O$_3$ NSs	0.1 M KHCO$_3$	93.8 (-1.1 V)	400	[24]
S-Bi$_2$O$_3$-CNT	0.5 M KHCO$_3$	97.06 (-0.9 V)	500	[25]
BOC NFs	**0.1 M KHCO$_3$**	**93.52 (-1.4 V)** **95.48 (-1.3 V)** **96.56 (-1.2 V)** **97.83 (-1.1 V)** **98.93 (-1.0 V)** **96.43 (-0.9 V)** **92.28 (-0.8 V)**	**600**	**This work**

Table S6.2 Summary and comparison of recently reported electrocatalysts for CO₂RR to formate formation in a flow cell.

Catalyst	Electrolyte	Maximum FE$_{formate}$ with the applied potential (vs. RHE)	Potential window (mV)	Ref.
Bi@Sn NPs	2.0 M KHCO₃	95% at -1.02 V	350 (FE$_{formate}$ > 90%)	[12]
Bi₂O₃@C-800	1.0 M KOH	95% at -0.7 V	700 (FE$_{formate}$ > 90%)	[16]
BOC@GDY	1.0 M KOH	97% at -0.85 V	450 (FE$_{formate}$ > 90%)	[23]
Bi₂S₃-Bi₂O₃ NSs	1.0 M KOH	95% at -1.0 V	800 (FE$_{formate}$ > 90%)	[24]
S-BiVO₄ (#)	1.0 M KHCO₃	97.5 % at -1.0 V	750 (FE$_{formate}$ > 90%)	[26]
SnO₂-Bi₂O₃ (#)	1.0 M KOH	91% at -1.29 V	100 (FE$_{formate}$ > 90%)	[27]
Sn₃O₄	1.0 M KOH	91.1% at -1.02 V	300 (FE$_{formate}$ > 80%)	[28]
MIL-68(In)-NH₂	1.0 M KOH	94.4% at -1.1 V	300 (FE$_{formate}$ > 90%)	[29]
SnO₂/Sn	1.0 M KOH	93% at -0.98 V	500 (FE$_{formate}$ > 90%)	[30]
In-Sn alloy	1.0 M KOH	94% at -0.98 V	550 (FE$_{formate}$ > 90%)	[31]
SnS	1.0 M KOH	88 ± 2% at -1.3 V	300 (FE$_{formate}$ > 80%)	[32]
ZnIn₂S₄ (#)	1.0 M KHCO₃	99.3% at -1.18 V	300 (FE$_{formate}$ > 90%)	[33]
BOC NFs	**1.0 M KOH**	**98.7 (-0.8 V)** **98.7 (-0.5 V) (#)**	**1200 (FE$_{formate}$ > 90%)**	**This work**

Note: **(#)** indicates the electrochemical measurements with iR compensation.

6.5.2 Supporting references

[1] G. Kresse, J. Hafner, *Phys. Rev. B* **1993**, 47, 558.

[2] G. Kresse, J. Hafner, *Phys. Rev. B* **1994**, 49, 14251.

[3] G. Kresse, J. Furthmüller, *Phys. Rev. B* **1996**, 54, 11169.

[4] B. Hammer, L.B. Hansen, J.K. Nørskov, *Phys. Rev. B* **1999**, 59, 7413.

[5] H. Monkhorst, J. Pack, *Phys. Rev. B* **1976**, 13, 5188.

[6] C. J. Cramer, Essentials of computational chemistry: theories and models, John Wiley & Sons, 2013.

[7] V. Tripković, E. Skúlason, S. Siahrostami, J. K. Nørskov, J. Rossmeisl, *Electrochimica Acta.* **2010**, 55, 7975.

[8] W. J. Durand, W. J.; Peterson, A. A, Studt, F.; Abild-Pedersen, F.; Nørskov, J. K. *Surf. Sci.* **2011**, 605, 1354.

[9] W. Zhang, S. Yang, M. Jiang, Y. Hu, C. Hu, X. Zhang, Z. Jin, *Nano Lett.* **2021**, *21*, 2650-2657.

[10] J. Yan, Y. X. Duan, Z. Yu, Q. Jiang, Y. T. Zhou, D. X. Liu, Z. Wen, *Angew. Chem. Int. Ed.* **2021**, 60, 8798-8802.

[11] Y. Wang, Y. Li, J. Liu, C. Dong, C. Xiao, L. Cheng, H. Jiang, H. Jiang, C. Li, *Angew. Chem. Int. Ed.* **2021**, *60*, 7681-7685.

[12] Y. Xing, X. Kong, X. Guo, Y. Liu, Q. Li, Y. Zhang, Y. Sheng, X. Yang, Z. Geng, J. Zeng, *Adv. Sci.* **2020**, 1902989.

[13] F. L. Meng, Q. Zhang, Y. X. Duan, K. H. Liu, X. B. Zhang, *Chin. J. Chem.* **2020**, *38*, 1752-1756.

[14] F. Li, G. H. Gu, C. Choi, P. Kolla, S. Hong, T.-S. Wu, Y.-L. Soo, J. Masa, S. Mukerjee, Y. Jung, J. Qiu, Z. Sun, *Appl. Catal. B-Environ.* **2020**, *277*, 119241.

[15] P. Lamagni, M. Miola, J. Catalano, M. S. Hvid, M. A. H. Mamakhel, M. Christensen, M. R. Madsen, H. S. Jeppesen, X. M. Hu, K. Daasbjerg, T. Skrydstrup, N. Lock, *Adv. Funct. Mater.* **2020**, 1910408.

[16] P. Deng, F. Yang, Z. Wang, S. Chen, Y. Zhou, S. Zaman, B. Y. Xia, *Angew. Chem. Int. Ed.* **2020**, *59*, 10807-10813.

[17] S. Liu, X. F. Lu, J. Xiao, X. Wang, X. W. D. Lou, *Angew. Chem. Int. Ed.* **2019**, *58*, 13828-13833.

[18] K. Fan, Y. Jia, Y. Ji, P. Kuang, B. Zhu, X. Liu, J. Yu, *ACS Catal.* **2019**, *10*, 358-364.

[19] Q. Yang, Q. Wu, Y. Liu, S. Luo, X. Wu, X. Zhao, H. Zou, B. Long, W. Chen, Y. Liao, L. Li, P. K. Shen, L. Duan, Z. Quan, *Adv. Mater.* **2020**, e2002822.

[20] T. Tran-Phu, R. Daiyan, Z. Fusco, Z. Ma, R. Amal, A. Tricoli, *Adv. Funct. Mater.* **2019**, *30*, 1906478.

[21] Q. Gong, P. Ding, M. Xu, X. Zhu, M. Wang, J. Deng, Q. Ma, N. Han, Y. Zhu, J. Lu, Z. Feng, Y. Li, W. Zhou, Y. Li, *Nat. Commun.* **2019**, *10*, 2807.

[22] Z. Wu, H. Wu, W. Cai, Z. Wen, B. Jia, L. Wang, W. Jin, T. Ma, *Angew. Chem. Int. Ed.* **2021**, *60*, 12554-12559.

[23] S.-F. Tang, X.-L. Lu, C. Zhang, Z.-W. Wei, R. Si, T.-B. Lu, *Sci. Bull.* **2021**, *66*, 1533-1541.

[24] P. F. Sui, C. Xu, M. N. Zhu, S. Liu, Q. Liu, J. L. Luo, *Small* **2021**, e2105682.

[25] S.-Q. Liu, M.-R. Gao, R.-F. Feng, L. Gong, H. Zeng, J.-L. Luo, *ACS Catal.* **2021**, 7604-7612.

[26] W. Ma, J. Bu, Z. Liu, C. Yan, Y. Yao, N. Chang, H. Zhang, T. Wang, J. Zhang, *Adv. Funct. Mater.* **2020**, 2006704.

[27] X. Wang, W. Wang, J. Zhang, H. Wang, Z. Yang, H. Ning, J. Zhu, Y. Zhang, L. Guan, X. Teng, Q. Zhao, M. Wu, *Chem. Eng. J.* **2021**, 426, 131867.

[28] L.-X. Liu, Y. Zhou, Y.-C. Chang, J.-R. Zhang, L.-P. Jiang, W. Zhu, Y. Lin, *Nano Energy* **2020**, 77, 105296.

[29] Z. Wang, Y. Zhou, C. Xia, W. Guo, B. You, B. Y. Xia, *Angew. Chem. Int. Ed.* **2021**, 60, 19107-19112.

[30] S. Ning, J. Wang, D. Xiang, S. Huang, W. Chen, S. Chen, X. Kang, *J. Catal.* **2021**, 399, 67-74.

[31] J. Wang, S. Ning, M. Luo, D. Xiang, W. Chen, X. Kang, Z. Jiang, S. Chen, *Appl. Catal. B-Environ.* **2021**, 288, 119979.

[32] J. Zou, C. Y. Lee, G. G. Wallace, *Adv. Sci.* **2021**, 8, e2004521.

[33] L. P. Chi, Z. Z. Niu, X. L. Zhang, P. P. Yang, J. Liao, F. Y. Gao, Z. Z. Wu, K. B. Tang, M. R. Gao, *Nat. Commun.* **2021**, 12, 5835.

Chapter 7. Unlocking Phase-Selective CO$_2$ Electroreduction over (α, β)-Bi$_2$O$_3$

7.1 Introduction

The ever-increasing energy consumption relying on fossil fuels has caused excessive CO$_2$ emission into the atmosphere and its associated environmental issues. Of all the potential roadmaps to achieve net-zero emission and carbon neutrality, electrochemical reduction of CO$_2$ (CO$_2$RR), especially when combined with renewable power generations, appears to be an attractive approach to reducing CO$_2$ emissions and simultaneously producing carbon-neutral fuels, which is beneficial to promoting carbon neutrality. However, the chemical inertness of CO$_2$ molecules and the competing hydrogen evolution reaction (HER) deteriorate the selectivity toward target products, which leads to the imperative exploration for the efficient CO$_2$RR electrocatalysts [1, 2].

Various strategies, e.g., structure engineering [1, 3] interface engineering [4], defects engineering [5, 6], have been devoted to improving CO$_2$RR performance with varying degrees of success toward different aiming products. Of particular note, phase engineering through regulating physiochemical properties and functionalities of nanomaterials has attracted great attention since many materials are found to present more than one phase under different experimental conditions (i.e., high pressure and temperature) other than the thermodynamically stable phases that are the same as their bulk form [7, 8]. More importantly, these unconventional phases usually deliver different physicochemical properties, e.g., physisorption ability, electronic property, and structural changes through phase transformation, endowing them with promising applications in electrocatalysis. Zhang et al.

demonstrated the enhanced catalytic performance for HER on heterophase 4H/ face cubic centered (fcc) Ru nanotubes due to the abundant structural defects of atomic steps/kinks and crystal phase boundaries[9], while annealing the fcc-FePt to form face centered tetragonal (fct)-FePt exhibited the unique electronic structure where the strong spin-orbit coupling and hybridization of Fe 3d and Pt 5d states could effectively stabilize the structure, and prevent Fe leaching during oxygen reduction reaction (ORR) [10]. Additionally, phase engineering has also shown its effectiveness in CO_2RR that the well-defined fcc-2H-fcc Au nanorods show the lower free energies of *COOH on unconventional 2H phase and 2H/fcc interface than typical fcc surface [11]. Clearly, the unconventional phases are responsible for the enhanced electrocatalytic performance and highlight the promising potential of phase engineering.

Currently, most studies on phase engineering are mainly focused on noble-metals or bimetallic metals (i.e., Au [11], Ru [9], Pd [12], AuPd [13], and PdSn [14]) for HER and ethanol oxidation reaction, but barely on unconventional phases of metal oxides for CO_2RR. Bismuth oxide (Bi_2O_3), due to its selective conversion of CO_2 to formate, as well as their earth abundance and low toxicity and cost compared to other materials, has generated much research interest in CO_2RR [15], but almost all of them are δ-Bi_2O_3 [16-18]. In fact, four different phases of Bi_2O_3, i.e., stable monoclinic α-phase and face-centered cubic δ-phase, and metastable tetragonal β-phase and body-centered cubic γ-phase commonly exist. Nevertheless, the metastable β-Bi_2O_3 has been proved to be the most active phase in photocatalysis [19], implying that the study on phase dependence of metal oxides toward CO_2RR is of pronounced significance and could bring new opportunities.

To this end, a thermal treatment approach is utilized to synthesize pure α- and β-Bi_2O_3. The structure and phase changes of Bi_2O_3 could be easily tuned from β to α by heating $Bi_2O_2CO_3$, which are probed by *in situ* heating X-ray diffraction (HT-XRD) and scanning electron microscope (SEM). The prepared β-Bi_2O_3 owns substantial amounts of defects and grain boundaries compared to α-Bi_2O_3, which are beneficial to electrocatalysis. As a result, β-Bi_2O_3 delivers higher current densities (j) and formate Faradaic efficiencies ($FE_{formate}$) than α-Bi_2O_3 for CO_2RR, as well as the good durability. Experimental and density functional theory (DFT) calculation results suggest that the β-Bi_2O_3 possesses faster reaction kinetics and a lower energy barrier toward formate formation, which jointly contribute to the high activity and selectivity toward CO_2RR.

7.2 Results and Discussion

Pure α- and β-Bi_2O_3 are obtained with an easy route by heating the precursor $Bi_2O_2CO_3$[20] and the dynamic phase transition is probed through *in situ* HT-XRD measurement (Figure 7.1a). Figure 7.1b shows an overview of the temperature resolved XRD patterns where the peak at around 20° belongs to the dome pattern (Figure S7.1a).

In the beginning, the patterns are well indexed to $Bi_2O_2CO_3$ and remain unchanged when the temperature is below 300 °C (Figure 7.1c). Then, it starts to decompose as the temperature gradually increases to 340 °C and ends at around 400 °C. Notably, the $Bi_2O_2CO_3$ is completely converted to β-Bi_2O_3 after releasing CO_2 following the reaction, $Bi_2O_2CO_3 \rightarrow \beta$-$Bi_2O_3 + CO_2$. The thermogravimetric analysis (TGA) (Figure S7.1b) suggests that the decomposition temperature is above 300 °C where the weight loss comes from the released CO_2 during the heating process. As the temperature further increases, β-Bi_2O_3 undergoes a

phase transformation at around 450 °C and it is fully transformed to α-Bi$_2$O$_3$ when the temperature reaches 500 °C (Figures 7.1d and 7.1e).
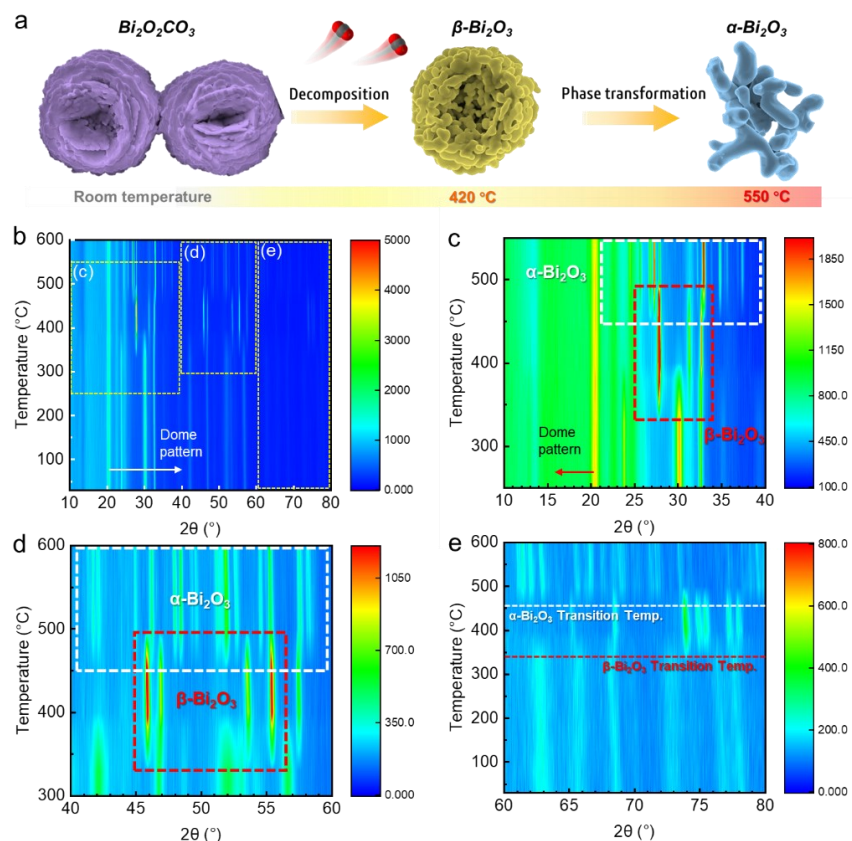
Figure 7.1 (a) Schematic illustration for materials preparation; (b) The overview of temperature-resolved *in situ* XRD patterns; (c), (d) and (e) The XRD patterns of the corresponding marked areas in Figure 1b.

The pure Bi$_2$O$_3$ phases were obtained at 420 °C (α) and 550 °C (β), respectively (Figure S7.2). The β-Bi$_2$O$_3$ shows that the nanoflower structure of the precursor is well maintained, accompanied by the stacked nanosheets shrinking into a coral-like morphology (Figures 7.2a and S7.3). The hollow area in the center of the nanoflower can be observed and the further high-resolution transmission electron microscopy (HRTEM) image demonstrates the

interplanar distance of 0.320 nm that agrees well with (201) plane of β-Bi_2O_3 (Figures 7.2b and 7.2c). Additionally, obvious grain boundaries can be found that are attributed to the recrystallization after $Bi_2O_2CO_3$ decomposition (Figures 7.2d and S7.4). It is interesting to note that some nanovoids are formed on the β-Bi_2O_3 surface and it can be speculated that the released CO_2 during the decomposition of $Bi_2O_2CO_3$ is responsible for the formation of the nanovoids (Figures 7.2e and 7.2f). $Bi_2O_2CO_3$ is more like a Sillén-type compound composed of $[Bi_2O_2]^{2+}$ layers and intercalated $[CO_3]^{2-}$ triangular groups. During heating, the structurally bonded carbonate species begin to release gaseous CO_2. When the accumulated CO_2 within the nanoparticles builds up to a certain pressure level, it is released to form nanovoids on the surface. Moreover, the high-angle annular dark-field scanning TEM (HAADF-STEM) image and the corresponding EDS elemental mappings confirm the successful preparation of β-Bi_2O_3 (Figure 7.2g). Compared to β-Bi_2O_3, the nanoflower structure completely disappears over α-Bi_2O_3 as the temperature increases to 550 °C. The morphologies of α-Bi_2O_3 show the larger size of the coral-like structure with no nanovoids, which accounts for a reduction in structural defects (Figure S7.5). Further the *in situ* heating SEM was performed to observe the morphology evolution during the decomposition and phase transition processes (Figure S7.6). At the initial stage, the nanoflower-like $Bi_2O_2CO_3$ is stable with the sheet-stacked structure while the nanosheets begin to shrink with the increase in temperature, forming small nanopores on the surface. As the heating temperature and time increase, these nanopores become larger, which allow the interconnected materials to form a coral-like network. When the temperature heats above 500 °C, the nanoflower structure begins to collapse, eventually forming a large size coral-like structure.
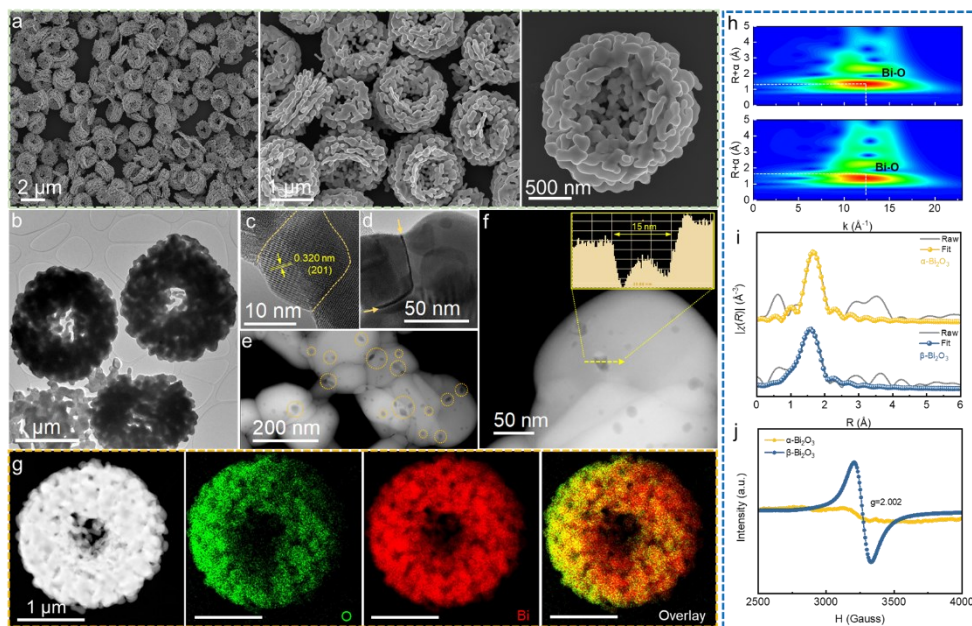
Figure 7.2 (a) SEM images; (b) TEM image; (c) and (d) HRTEM images; (e) and (f) HAADF-STEM images (inset: intensity change with line scan); (g) The corresponding EDS elemental maps and overlay images; (h) WT-EXAFS at Bi L_3-edge; (i) Fitting results of EXAFS spectra to R space; (j) EPR spectra of α-Bi$_2$O$_3$ and β-Bi$_2$O$_3$.

The X-ray photoelectron spectroscopy (XPS) results show that peaks at 163.7 and 158.3 eV in high resolution Bi 4f spectra correspond to the Bi 4f$_{5/2}$ and Bi 4f$_{7/2}$ (Figure S7.7a), suggesting the Bi^{3+} of the synthesized materials [21]. Figure S7.7b displays the spectra of the X-ray absorption near-edge structure spectroscopy (XANES), in which the prepared α-Bi$_2$O$_3$ aligns well with commercial Bi$_2$O$_3$ (α). Both prepared α-Bi$_2$O$_3$ and β-Bi$_2$O$_3$ exhibit positive energy shifts compared to the Bi-metal reference, indicating a higher Bi valance state. Furthermore, the wavelet transforms of the extended X-ray absorption fine structure (WT-EXAFS) spectra at Bi L_3-edge for α-Bi$_2$O$_3$ and β-Bi$_2$O$_3$ confirm that the highest intensity points are attributed to the oxygen atoms surrounding the central Bi atom, in which both α-Bi$_2$O$_3$ and β-Bi$_2$O$_3$ demonstrate similar features as the commercial Bi$_2$O$_3$ (α) (Figures 7.2h

and S7.7c). Subsequently, the Fourier transform k^2-weighted function of the EXAFS spectra in R space was derived where the dominating peaks are attributed to the Bi-O bonds of the prepared Bi_2O_3 (Figure 7.2i). The fitted spectra show that the Bi-O coordination number (CN) of β-Bi_2O_3 is about 3.7, which is remarkably smaller than the ideal value of Bi_2O_3 (CN = 5) (Table S7.1). The lower CN value indicates the presence of uncoordinated Bi atoms in β-Bi_2O_3, revealing its defective nature corresponding to the observed morphologies. However, the CN of 4.9 suggests the existence of few defects in α-Bi_2O_3. Considering the uncoordinated Bi atoms, the oxygen vacancies are expected in β-Bi_2O_3. The further electron paramagnetic resonance (EPR) spectroscopy results confirm the oxygen vacancy defects in β-Bi_2O_3 with an obvious signal at g = 2.002 compared with that of α-Bi_2O_3 (Figure 7.2j). Based on the above results, pure β-Bi_2O_3 with abundant structural defects can be obtained by thermal treatment of $Bi_2O_2CO_3$, after which the nearly perfect α-Bi_2O_3 can be formed through the phase transition of β-Bi_2O_3.

The CO_2RR electrocatalytic performance of α-Bi_2O_3 and β-Bi_2O_3 was evaluated in a gas-tight H-type cell. All the potentials are converted to the reversible hydrogen electrode (RHE). Figure 7.3a displays the linear sweep voltammetry (LSV) results that both α-Bi_2O_3 and β-Bi_2O_3 show the increment of j and more positive onset potentials in the CO_2-saturated electrolyte, suggesting the occurrence of CO_2RR. To demonstrate the preference for CO_2RR rather than HER, the constant potentiostatic electrolysis was further conducted by quantitative analysis of the products. The results show that formate is the predominant product, together with minor amounts of CO and H_2 for both α-Bi_2O_3 and β-Bi_2O_3 (Figure S7.8). Specifically, β-Bi_2O_3 shows a high plateau for formate Faradaic efficiencies ($FE_{formate}$) of over 90% across a broad potential window from -1.4 to -0.9 V, where a maximum of 98.1%

was achieved at −1.1 V (Figure 7.3b). The FE of competing HER is suppressed to below 8% within this potential window. Compared with β-Bi$_2$O$_3$, α-Bi$_2$O$_3$ exhibits a lower FE$_{formate}$ at all applied potentials, and the maximum value of 94.1% was reached at −1.2 V. Furthermore, the partial current densities of formate ($j_{formate}$) were derived to reveal the electrocatalytic activities toward CO$_2$-to-formate conversion.
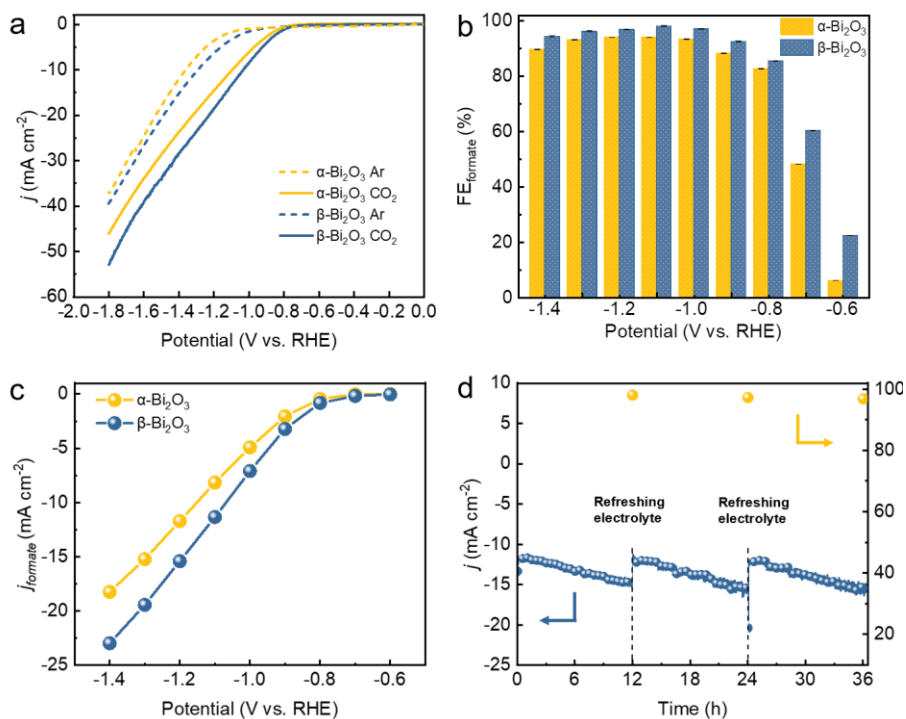
Figure 7.3 (a) LSV curves in Ar- and CO$_2$-saturated 0.1 M KHCO$_3$; (b) FE$_{formate}$ and (c) $j_{formate}$ at different applied potentials; (d) Stability test of β-Bi$_2$O$_3$ measured at -1.1 V in 0.1 M KHCO$_3$.

As shown in Figure 7.3c, β-Bi$_2$O$_3$ demonstrates the higher catalytic activity for CO$_2$RR toward formate formation compared to α-Bi$_2$O$_3$ and it delivers a $j_{formate}$ of 23 mA cm^{-2} at −1.4 V, about 1.3 times higher than that of α-Bi$_2$O$_3$ (18.2 mA cm^{-2}). Apart from the electrocatalytic activity and selectivity, stability is also an important parameter for practical

application. The constant electrolysis of β-Bi$_2$O$_3$ was carried out at a fixed potential of -1.1 V and the electrolyte was refreshed every 12 hours to exclude the influence of formate accumulation on the stability. It is found that the total j slightly changes from 12.5 to 15 mA cm^{-2} after 12 h electrolysis, while the FE$_{formate}$ remains at a high value of above 95%, indicating the good stability of the electrocatalyst β-Bi$_2$O$_3$ (Figure 7.3d). After 36 h of electrolysis, the FE$_{formate}$ is still around 96%, which further confirms the good stability of the electrocatalyst. The post-catalysis characterizations were performed after CO$_2$RR and both α-Bi$_2$O$_3$ and β-Bi$_2$O$_3$ were reduced to the ultrathin nanosheets, where the corresponding HRTEM confirms the existence of metallic Bi (Figures S7.9 and S7.10). In addition, the XRD result suggests a mixture of dominant metallic Bi and minor Bi$_2$O$_2$CO$_3$ that are also reported in previous studies (Figure S7.11) [17, 22, 23].

To better understand the origin of the electrocatalytic performance, the electrochemical active surface areas (ECSAs) were determined to estimate the active site numbers after CO$_2$RR. As shown in Figure S7.12a, β-Bi$_2$O$_3$ possesses a slightly larger C$_{dl}$ compared to α-Bi$_2$O$_3$, indicating more catalytic active sites for CO$_2$RR to proceed, but the similar morphology and structure result in little difference on the actual number of active sites under reduction condition. Then, the ECSA normalized $j_{foramte}$ was derived to exclude the effect of the morphology difference on CO$_2$RR performance (Figure S7.12b). Clearly, β-Bi$_2$O$_3$ still delivers higher $j_{formate}$ than α-Bi$_2$O$_3$, confirming its better intrinsic catalytic activity toward CO$_2$RR. To gain a deeper insight into the reaction kinetics for CO$_2$RR toward formate, the Tafel slopes were determined to identify the rate-determining step (RDS). Figure 7.4a shows the ECSA-corrected Tafel plots where β-Bi$_2$O$_3$ exhibits a smaller slope of 82.03 mV dec^{-1} compared to α-Bi$_2$O$_3$ (104.48 mV dec^{-1}), implying the faster reaction kinetics of β-Bi$_2$O$_3$ for

formate formation. By comparing the different Tafel slopes, two types of RDSs were identified on the prepared Bi_2O_3. The Tafel slope of α-Bi_2O_3 is closer to the theoretical value of 118 mV dec^{-1}, suggesting the first electron transfer to the CO_2 as the RDS, i.e., $* + CO_{2(aq)} + e^- \rightarrow {}^*CO_2{}^{\bullet-}$ [24]. In contrast, the slope of β-Bi_2O_3 is closer to 59 mV dec^{-1}, in support of the RDS that involves a chemical proton transfer from bicarbonate, i.e., $^*CO_2{}^{\bullet-} + HCO_3^- \rightarrow {}^*OCHO + CO_3^{2-}$ [25, 26].

Given the importance of CO_2 participation and charge transfer ability in the reaction kinetics, the two factors were further investigated to elucidate the induced difference in RDS. The volumetric CO_2 adsorption-desorption isotherms were carried out to evaluate the CO_2 adsorption capability (Figure 7.4b). Apparently, β-Bi_2O_3 exhibits a comparably three times larger CO_2 adsorption capability than α-Bi_2O_3, promoting sufficient CO_2 reactants to the catalyst surface for the CO_2RR process. In comparison, the inferior CO_2 adsorption capability of α-Bi_2O_3 results in the sluggish reaction kinetics on the RDS of $* + CO_{2(aq)} + e^- \rightarrow {}^*CO_2{}^{\bullet-}$ due to the limited supplement of CO_2. Apart from the benefits of larger ECSA on β-Bi_2O_3, the nanovoids and oxygen vacancies are also responsible for the faster reaction kinetics as they promote the adsorption and reactivity of gaseous CO_2 [4, 27]. Moreover, the electron transfer ability was evaluated by the measurement of ultraviolet photoelectron spectroscopy (UPS) as displayed in Figure S7.12c. The higher cut-off binding energy of β-Bi_2O_3 demonstrates a better electron transfer ability as further confirmed by the calculation of work functions [28, 29]. The lower work function of β-Bi_2O_3 (4.9 eV) corresponds to the higher tunneling probability for electrons transferring from the catalyst to the reactant (Figure S7.12d). Compared with α-Bi_2O_3, the superior electron transfer ability of β-Bi_2O_3 mainly originates from the abundance of defects that the oxygen vacancies can effectively lower the

work function [30]. Thus, the better CO_2 adsorption capability and charge transfer ability of β-Bi_2O_3 jointly contribute to the faster reaction kinetics and better electrocatalytic performance of CO_2RR.
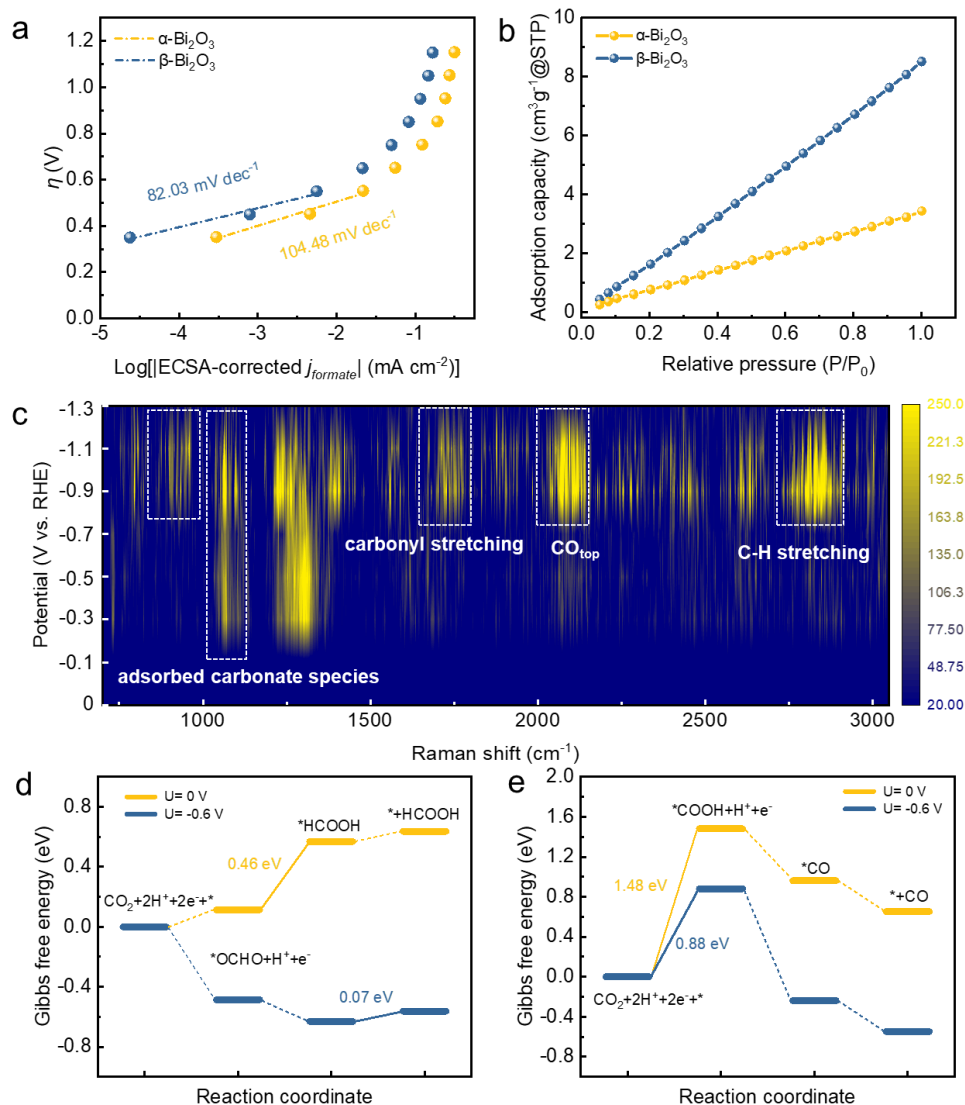
Figure 7.4 (a) ECSA-corrected Tafel plots; (b) CO_2 isotherms curves; (c) Potential-dependent Raman spectra of β-Bi_2O_3 measured in CO_2-staturated 0.1 M $KHCO_3$; Gibbs free energy changes of β-Bi_2O_3 at U = 0 and -0.6 V for (d) CO_2 to HCOOH pathway and (e) CO_2 to CO pathway.

Furthermore, *in situ* Raman spectroscopy measurements were performed on β-Bi$_2$O$_3$ to monitor the reaction process and the reaction intermediates (Figure 7.4c). In the beginning, no obvious Raman signals are detected at the potential of 0 V, while as the applied potential moves to the negative range, two bands appear at 1060 and 1330 cm^{-1} that are ascribed to the adsorbed carbonate species [31]. When the applied potential reaches −0.7 V, several new bands are observed where the bands at 1595 and 2880 cm^{-1} correspond to carbonyl O-C-O antisymmetric stretching and C-H stretching modes of formate [32], suggesting the formation of intermediate *OCHO during CO$_2$RR. The broad bands at 1335 cm^{-1} further confirm the formation of formate intermediate *OCHO as it belongs to the carbonyl O-C-O symmetric stretching mode of formate. In addition, the adsorbate *CO is detected at the band of 2060 cm^{-1} which is mainly caused by the accumulation of generated CO bubbles on the catalyst surface during CO$_2$RR [33].

Density functional theory (DFT) calculations were performed on β-Bi$_2$O$_3$ to deepen our understanding of the high activity and selectivity toward formate during CO$_2$RR. Figures 7.4d and 7.4e show the Gibbs free energy diagrams of CO$_2$RR to HCOOH and CO formation, respectively. At the external potential of 0 V (U = 0 V), β-Bi$_2$O$_3$ exhibits an uphill process for CO$_2$ to HCOOH formation with endothermic energy barriers, in which the Gibbs free energy change (ΔG) of *OCHO to *HCOOH shows a high barrier of 0.46 eV compared to those of the other reaction steps. However, the higher energy barrier of 1.48 eV for intermediate *COOH formation significantly hinders the pathway of CO formation, which favors the high selectivity for formate. Moreover, when applying the external potential U = −0.6 V to the reaction processes, the pathway for CO$_2$ to HCOOH shows a downhill trend of Gibbs free energy, suggesting the exothermic and spontaneous processes for formate

formation. Although the desorption step of *HCOOH still requires energy of 0.07 eV, it is comparably lower than the energy barrier at U = 0 V for HCOOH formation, which is consistent with the experimental results that formate could be detected at a low onset potential. By contrast, the pathway for CO_2 to CO still experiences a similar energy change as U = 0 V and the formation of the intermediate *COOH still shows a high energy barrier of 0.88 eV at U = −0.6 V. More importantly, the competing HER is significantly suppressed at U = −0.6 V with a high energy barrier of 0.75 eV (Figure S7.13a), which is beneficial to the CO_2RR and guarantees good selectivity for formate formation. Given the existence of competing HER during CO_2RR, the limiting potential difference (ΔU) between CO_2RR and HER was also determined to reveal the selectivity toward CO_2RR [16, 34]. The $ΔU_L(HCOOH)$ of −0.78 V is more positive than $ΔU_L(CO)$ of −1.62 V, further indicating the higher formate selectivity during CO_2RR (Figure S7.13b). All the results demonstrate the faster reaction kinetics and lower energy barrier of the metastable $β$-Bi_2O_3 toward formate formation, which enables it to serve as a highly active and selective catalyst to boost the CO_2RR electrocatalytic performance.

Moreover, Bi_2O_3 is also a good candidate for photocatalysis, and the photocatalytic performance was further evaluated through the photocatalytic degradation of Rhodamine B (RhB) under visible light irradiation (Figure S7.14). Figure 7.5a shows the relative concentration (C/C_0) of RhB as a function of time and it is found that $β$-Bi_2O_3 exhibits better photocatalytic performance than $α$-Bi_2O_3 with a degradation efficiency of 90% within 160 min, while only 45% RhB is decomposed by $α$-Bi_2O_3. The kinetic rates (k) were further determined using the pseudo-first-order kinetics equation on $α$-Bi_2O_3 and $β$-Bi_2O_3. Clearly, $β$-Bi_2O_3 shows a k of 0.0163 min^{-1} that is 3.6 times higher than that of $α$-Bi_2O_3 (0.0045 min^{-1}),

implying the fast reaction kinetics of β-Bi$_2$O$_3$ for RhB degradation (Figure 7.5b). Then, the recycling tests were carried out on β-Bi$_2$O$_3$ to evaluate the photostability and reusability. As shown in Figure 7.5c, the degradation efficiencies of β-Bi$_2$O$_3$ are still maintained at around 90% after recycling five times, indicating the good durability of β-Bi$_2$O$_3$ for RhB degradation.
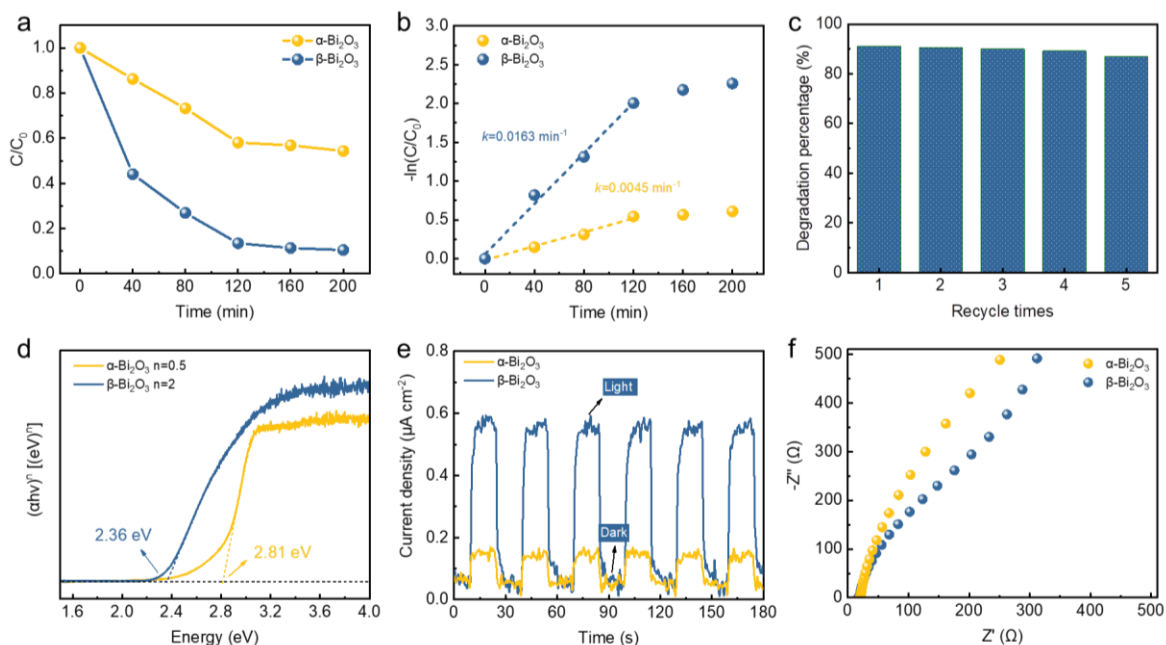
Figure 7.5 (a) Photocatalytic degradation efficiency under visible light irradiation; (b) Kinetic rate constants; (c) Photocatalytic degradation of RhB cycling test on β-Bi$_2$O$_3$; (d) Tauc plots curves; (e) Transient photocurrent response with visible-light on/off; (f) EIS Nyquist plots with visible light on.

To elucidate the intrinsic origins credited for the enhanced photocatalytic performance, the optical properties and band gaps were investigated (Figure S7.15a). Both α-Bi$_2$O$_3$ and β-Bi$_2$O$_3$ show strong absorption in UV range with the absorption edges near the visible light region. The calculated band gaps of α-Bi$_2$O$_3$ and β-Bi$_2$O$_3$ are 2.81 and 2.36 eV, respectively (Figure 7.5d). The narrower band gap of β-Bi$_2$O$_3$ ensures a higher visible light absorption,

which is beneficial for the enhancement of photocatalytic activity under visible light irradiation. In addition, the energy band structures were further studied through the VB-XPS measurement that both α-Bi$_2$O$_3$ and β-Bi$_2$O$_3$ demonstrate a similar value for the difference between the Fermi level and the valence band (Figure S7.15b). The photocurrent response of α-Bi$_2$O$_3$ and β-Bi$_2$O$_3$ was tested in 0.5 M Na$_2$SO$_4$ electrolyte using the fluorine-doped tin oxide (FTO) glass as the substrate. The photocurrent density of β-Bi$_2$O$_3$ is five times higher than that of α-Bi$_2$O$_3$ with visible light irradiation (Figure 7.5e), demonstrating the effective separation of photogenerated electron-hole pairs on β-Bi$_2$O$_3$ for RhB degradation. As depicted in Figure 7.5f, the results of electrochemical impedance spectra (EIS) measurement show the smaller interfacial charge carriers transfer resistance of β-Bi$_2$O$_3$, which could effectively suppress the recombination of electrons and holes. Aside from the abovementioned merits, the hierarchical structures and pore channels within the structure of β-Bi$_2$O$_3$ also contribute to the excellent adsorption of dye molecules, promoting a higher kinetic rate and photocatalytic performance. Briefly, the increased visible light adsorption, promoted electron-hole pairs separation and enhanced dye adsorption ability collectively contribute to better photocatalytic performance for RhB degradation on β-Bi$_2$O$_3$.

7.3 Conclusions

In summary, the dynamic structure and phase transition of Bi$_2$O$_3$ are probed by *in situ* characterizations, where β-Bi$_2$O$_3$ starts to form at 340 °C followed by the phase transformation to α-Bi$_2$O$_3$ at 450 °C. The decomposition of Bi$_2$O$_2$CO$_3$ leads to the formation of a substantial number of defects and grain boundaries on the prepared β-Bi$_2$O$_3$, which are beneficial for catalysis. As a result, β-Bi$_2$O$_3$ demonstrates a higher selectivity for CO$_2$-to-formate conversion than α-Bi$_2$O$_3$, and the FE$_{formate}$ of over 90% in a potential window of 500

mV is achieved on β-Bi_2O_3, with the maximum FE$_{formate}$ of 98.1% at −1.1 V. Compared to α-Bi_2O_3, the better CO_2 adsorption and charge transfer abilities of β-Bi_2O_3 are accounted for the fast reaction kinetics, as well as the lower energy barriers toward formate formation, both of which synergistically contribute to the good electrocatalytic performance toward CO_2RR. Meanwhile, β-Bi_2O_3 also exhibits better performance for photocatalytic RhB dye degradation than α-Bi_2O_3, manifesting its high activity in photocatalysis. Overall, this work unravels the phase dependence of oxide materials on catalysis and emphasizes the effectiveness of phase engineering for rationally designing high-efficiency catalysts.

7.4 References

[1]   G. Wang, J. Chen, Y. Ding, P. Cai, L. Yi, Y. Li, C. Tu, Y. Hou, Z. Wen, L. Dai, *Chem. Soc. Rev.* **2021**, *50*, 4993-5061.

[2]   L. Li, X. Li, Y. Sun, Y. Xie, *Chem. Soc. Rev.* **2022**, *51*, 1234.

[3]   R. M. Aran-Ais, D. Gao, B. Roldan Cuenya, *Acc. Chem. Res.* **2018**, *51*, 2906-2917.

[4]   Y. Wang, P. Han, X. Lv, L. Zhang, G. Zheng, *Joule* **2018**, *2*, 2551-2582.

[5]   Q. Wang, y. lei, D. Wang, Y. Li, *Energy Environ. Sci.* **2019**, *12*, 1730-1750.

[6]   Z. Wu, Y. Zhao, W. Jin, B. Jia, J. Wang, T. Ma, *Adv. Funct. Mater.* **2020**, 2009070.

[7]   Y. Chen, Z. Lai, X. Zhang, Z. Fan, Q. He, C. Tan, H. Zhang, *Nat. Rev. Chem.* **2020**, *4*, 269.

[8]   H. Li, X. Zhou, W. Zhai, S. Lu, J. Liang, Z. He, H. Long, T. Xiong, H. Sun, Q. He, Z. Fan, H. Zhang, *Adv. Energy Mater.* **2020**, *10*, 2002019.

[9]   Q. Lu, A. L. Wang, H. Cheng, Y. Gong, Q. Yun, N. Yang, B. Li, B. Chen, Q. Zhang, Y. Zong, L. Gu, H. Zhang, *Small* **2018**, *14*, e1801090.

[10]   J. Kim, Y. Lee, S. Sun, *J. Am. Chem. Soc.* **2010**, *132*, 4996-4997.

[11]   Z. Fan, M. Bosman, Z. Huang, Y. Chen, C. Ling, L. Wu, Y. A. Akimov, R. Laskowski, B. Chen, P. Ercius, J. Zhang, X. Qi, M. H. Goh, Y. Ge, Z. Zhang, W. Niu, J. Wang, H. Zheng, H. Zhang, *Nat. Commun.* **2020**, *11*, 3293.

[12]   H. Cheng, N. Yang, G. Liu, Y. Ge, J. Huang, Q. Yun, Y. Du, C. J. Sun, B. Chen, J. Liu, H. Zhang, *Adv. Mater.* **2020**, *32*, e1902964.

[13]   X. Zhou, Y. Ma, Y. Ge, S. Zhu, Y. Cui, B. Chen, L. Liao, Q. Yun, Z. He, H. Long, L. Li, B. Huang, Q. Luo, L. Zhai, X. Wang, L. Bai, G. Wang, Z. Guan, Y. Chen, C. S. Lee, J. Wang, C. Ling, M. Shao, Z. Fan, H. Zhang, *J. Am. Chem. Soc.* **2022**, *144*, 547-555.

[14]   M. Zhou, J. Liu, C. Ling, Y. Ge, B. Chen, C. Tan, Z. Fan, J. Huang, J. Chen, Z. Liu, Z. Huang, J. Ge, H. Cheng, Y. Chen, L. Dai, P. Yin, X. Zhang, Q. Yun, J. Wang, H. Zhang, *Adv. Mater.* **2022**, *34*, e2106115.

[15]   Y. Guan, M. Liu, X. Rao, Y. Liu, J. Zhang, *J. Mater. Chem. A* **2021**, *9*, 13770-13803.

[16]   Z. Chen, K. Mou, X. Wang, L. Liu, *Angew. Chem. Int. Ed.* **2018**, *57*, 12790-12794.

[17]   S. Liu, X. F. Lu, J. Xiao, X. Wang, X. W. D. Lou, *Angew. Chem. Int. Ed.* **2019**, *58*, 13828-13833.

[18]   S. Q. Liu, E. Shahini, M. R. Gao, L. Gong, P. F. Sui, T. Tang, H. Zeng, J. L. Luo, *ACS Nano* **2021**, *15*, 17757-17768.

[19]   H. Cheng, B. Huang, J. Lu, Z. Wang, B. Xu, X. Qin, X. Zhang, Y. Dai, *Phys. Chem. Chem. Phys* **2010**, *12*, 15468-15475.

[20]   P. F. Sui, M. R. Gao, S. Liu, C. Xu, M. N. Zhu, J. L. Luo, *Adv. Funct. Mater.* **2022**, 2203794.

[21]   T. Tran-Phu, R. Daiyan, Z. Fusco, Z. Ma, R. Amal, A. Tricoli, *Adv. Funct. Mater.* **2019**, *30*, 1906478.

[22]   Y. Shi, C. F. Wen, X. Wu, J. Y. Zhao, F. Mao, P. F. Liu, H. G. Yang, *Mater. Chem. Front.* **2022**, *6*, 1091-1097.

[23]   S.-Q. Liu, M.-R. Gao, R.-F. Feng, L. Gong, H. Zeng, J.-L. Luo, *ACS Catal.* **2021**, *11*, 7604-7612.

[24]   C. W. Lee, N. H. Cho, S. W. Im, M. S. Jee, Y. J. Hwang, B. K. Min, K. T. Nam, *J. Mater. Chem. A* **2018**, *6*, 14043-14057.

[25]   S. Zhang, P. Kang, T. J. Meyer, *J. Am. Chem. Soc.* **2014**, *136*, 1734-1737.

[26]   P.-F. Sui, S. Liu, C. Xu, J. Xiao, N. Duan, R. Feng, J.-L. Luo, *Chem. Eng. J.* **2022**, *427*, 131654.

[27]   R. Daiyan, W. H. Saputera, Q. Zhang, E. Lovell, S. Lim, Y. H. Ng, X. Lu, R. Amal, *Adv. Sustain. Syst.* **2018**, *3*, 1800064.

[28]   Z.-Z. Wu, F.-Y. Gao, M.-R. Gao, *Energy Environ. Sci.* **2021**, *14*, 1121-1139.

[29]   T. Liu, C. Xi, C. Dong, C. Cheng, J. Qin, S. Hu, H. Liu, X.-W. Du, *J. Phys. Chem. C* **2019**, *123*, 28319-28326.

[30]   P. Gayen, S. Saha, K. Bhattacharyya, V. K. Ramani, *ACS Catal.* **2020**, *10*, 7734-7746.

[31]   I. V. Chernyshova, P. Somasundaran, S. Ponnurangam, *Proc. Natl. Acad. Sci.* **2018**, *115*, E9261-E9270.

[32]   A. M. Ismail, G. F. Samu, Á. Balog, E. Csapó, C. Janáky, *ACS Energy Lett.* **2018**, *4*, 48-53.

[33]   C. Zhan, F. Dattila, C. Rettenmaier, A. Bergmann, S. Kuhl, R. Garcia-Muelas, N. Lopez, B. R. Cuenya, *ACS Catal.* **2021**, *11*, 7694-7701.

[34]   E. Zhang, T. Wang, K. Yu, J. Liu, W. Chen, A. Li, H. Rong, R. Lin, S. Ji, X. Zheng, Y. Wang, L. Zheng, C. Chen, D. Wang, J. Zhang, Y. Li, *J. Am. Chem. Soc.* **2019**, *141*, 16569-16573.

7.5 Supporting Information

7.5.1 Supporting figures and tables
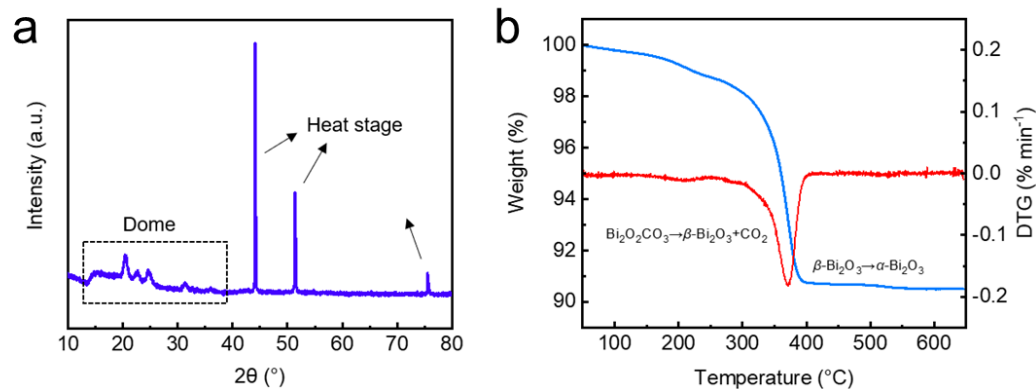
Figure S7.1 (a) XRD pattern of heat stage with dome; (b) The TGA/DTG measurement of $Bi_2O_2CO_3$ (heating rate: 5 °C min^{-1} in air). The overall weight loss can be attributed to the release of CO_2.
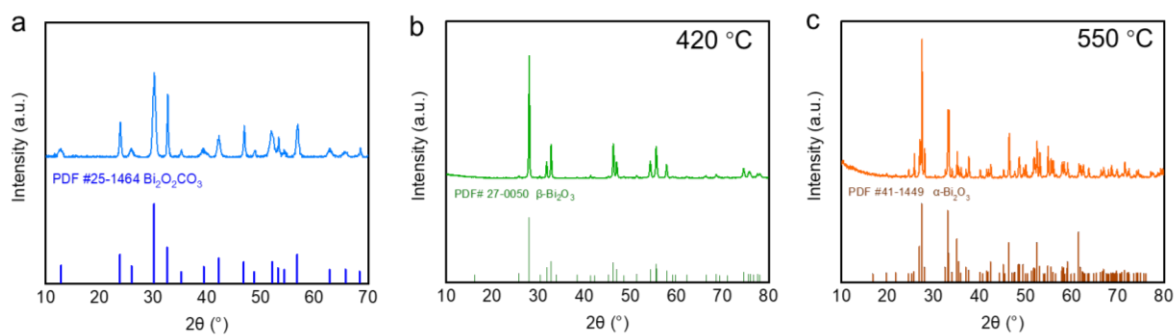
Figure S7.2 XRD patterns of (a) $Bi_2O_2CO_3$, (b) β-Bi_2O_3 and (c) α-Bi_2O_3.
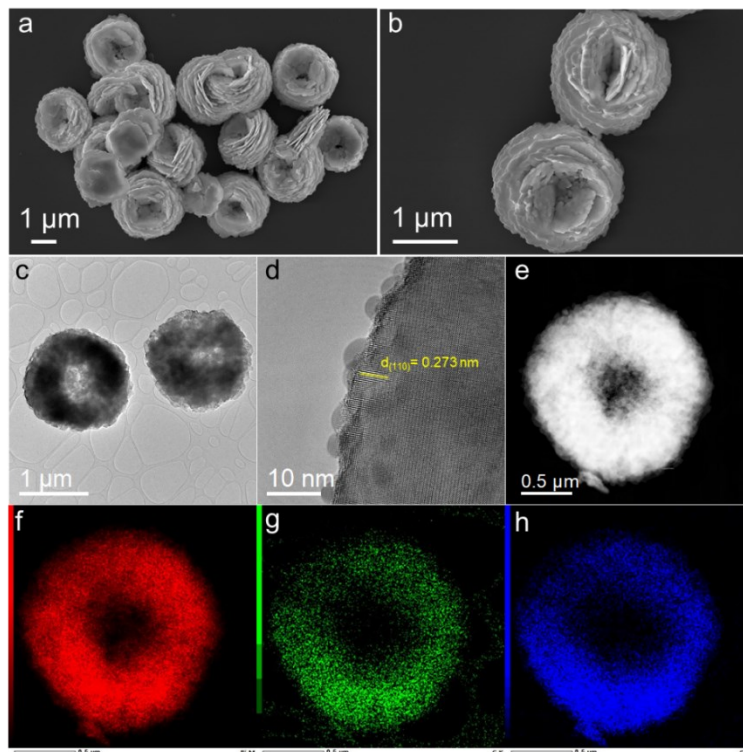
Figure S7.3 Morphologies of Bi$_2$O$_2$CO$_3$. (a) and (b) SEM images; (c) TEM image; (d) HRTEM image; (e) HAADF-STEM image; (f) to (h) The corresponding EDS elemental maps.
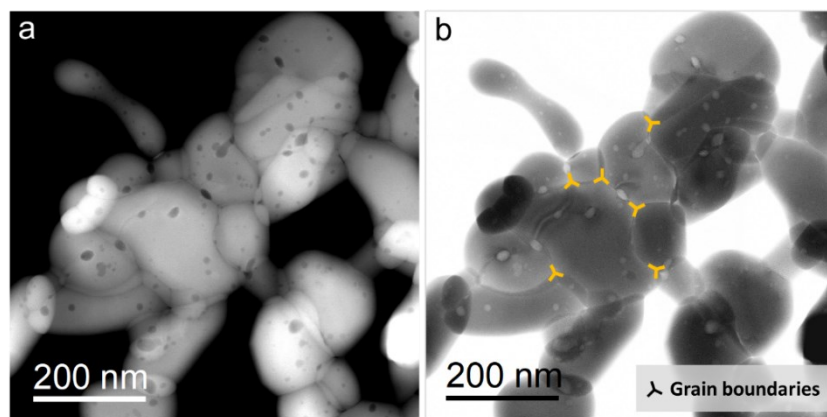
Figure S7.4 (a) Dark-field and (b) bright-field STEM images of β-Bi$_2$O$_3$.
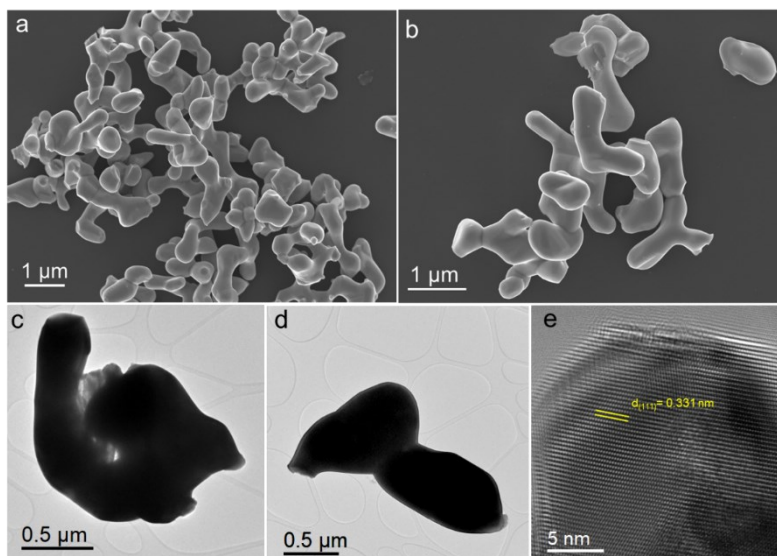
Figure S7.5 (a) and (b) SEM images; (c) and (d) TEM images; (e) HRTEM images of α-Bi$_2$O$_3$.
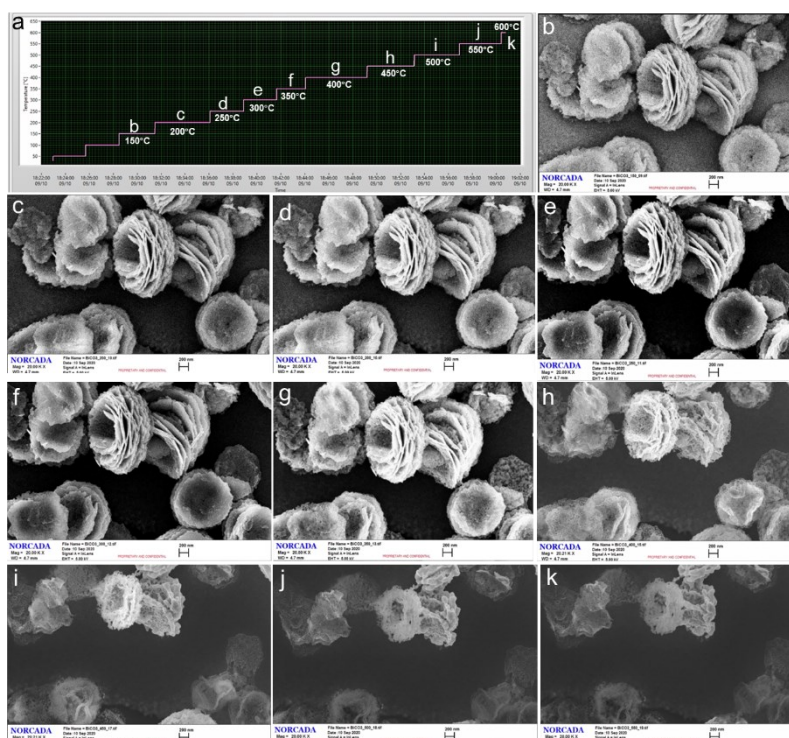
Figure S7.6 (a) Diagram of programmable temperature for *in situ* heating SEM; (b) to (k) The corresponding SEM images at different temperatures.
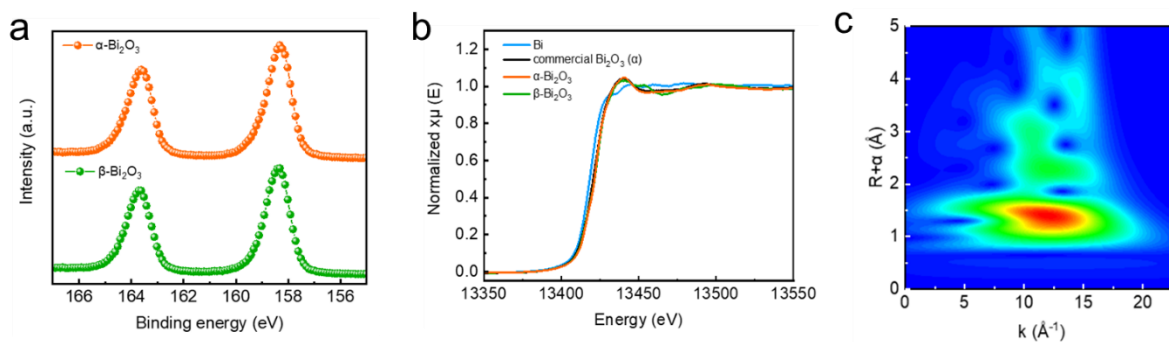
Figure S7.7 (a) High resolution XPS spectra of Bi 4f on α-Bi$_2$O$_3$ and β-Bi$_2$O$_3$; (b) The normalized Bi L$_3$-edge XANES spectra of prepared α-Bi$_2$O$_3$ and β-Bi$_2$O$_3$ in comparison with Bi and commercial Bi$_2$O$_3$ (α) standards; (c) Wavelet transforms of EXAFS spectrum (WT-EXAFS) of commercial Bi$_2$O$_3$ (α) at Bi L$_3$-edge.
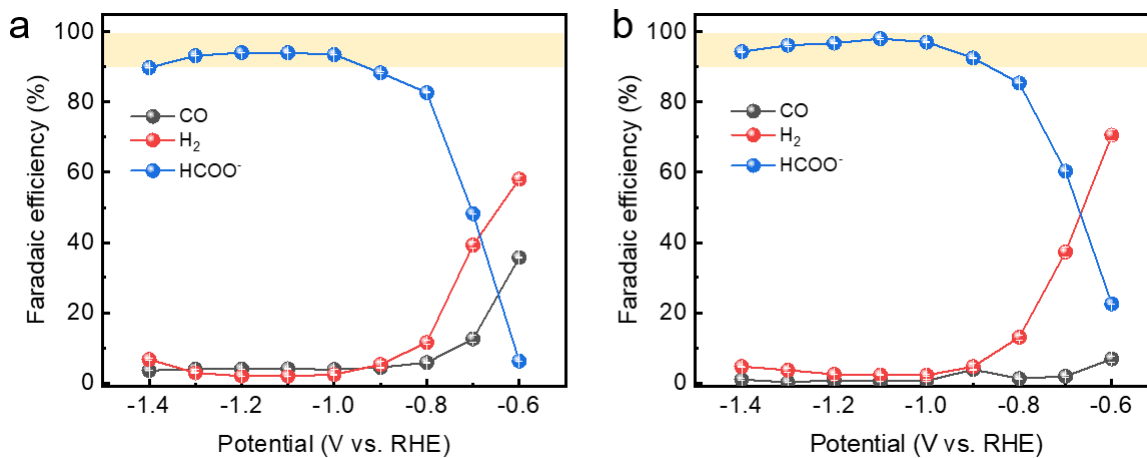
Figure S7.8 Faradaic efficiencies of products at different applied potentials (a) α-Bi$_2$O$_3$ and (b) β-Bi$_2$O$_3$.
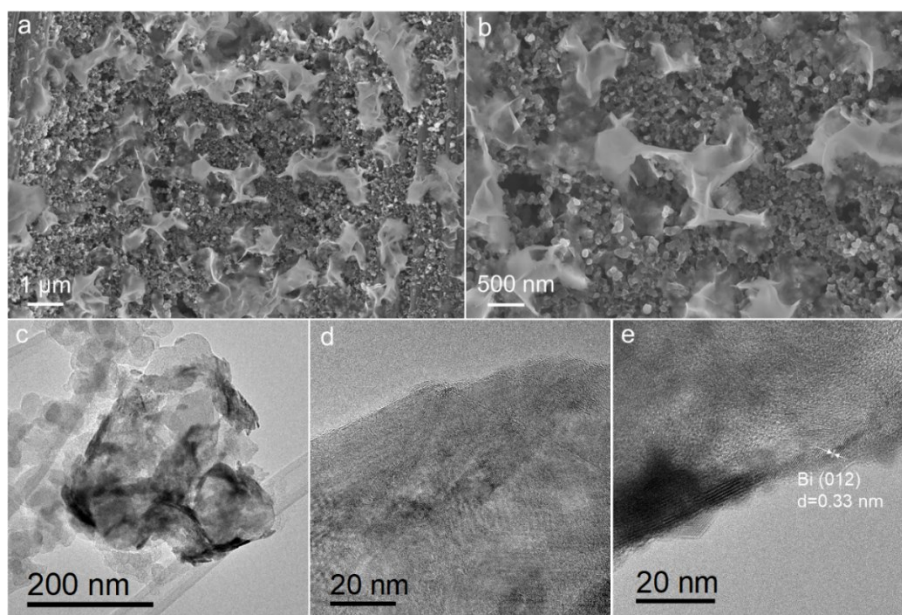
Figure S7.9 (a) and (b) SEM images, (c)TEM image; (d) and (e) HRTEM images of β-Bi$_2$O$_3$ after CO$_2$RR measurement.
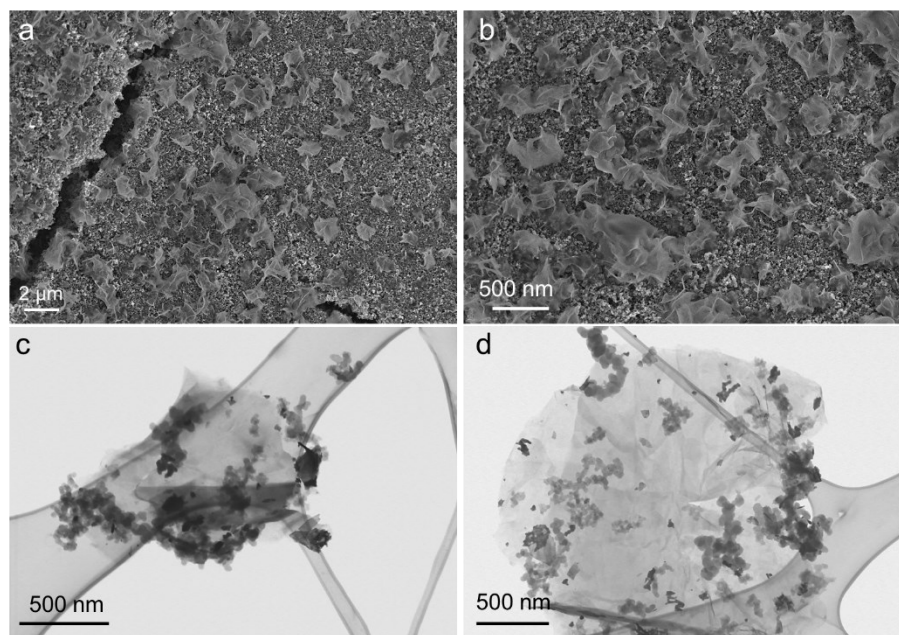
Figure S7.10 (a) and (b) SEM images, and (c) and (d) TEM images of α-Bi$_2$O$_3$ after CO$_2$RR measurement.
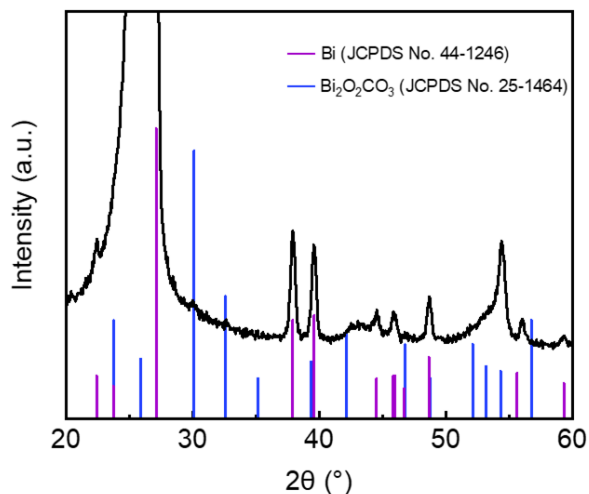
Figure S7.11 XRD pattern of β-Bi_2O_3 after CO_2RR measurement.
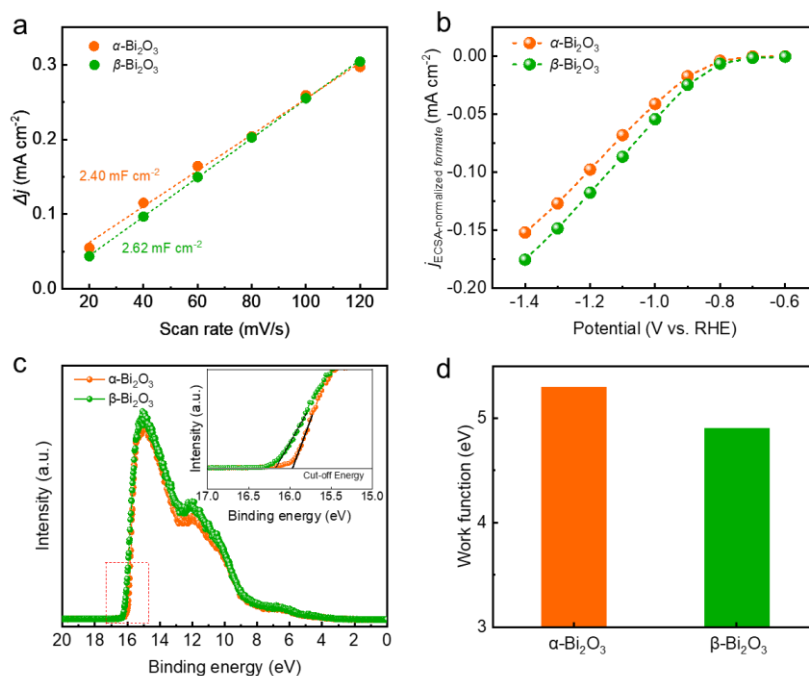
Figure S7.12 (a) The plots of charging current density differences $\Delta j/2$ vs. scan rates and (b) ECSA-normalized partial current density of formate on α-$Bi_2O_3$and β-Bi_2O_3; (c) UPS plots and (d) Work function of α-Bi_2O_3 and β-Bi_2O_3.
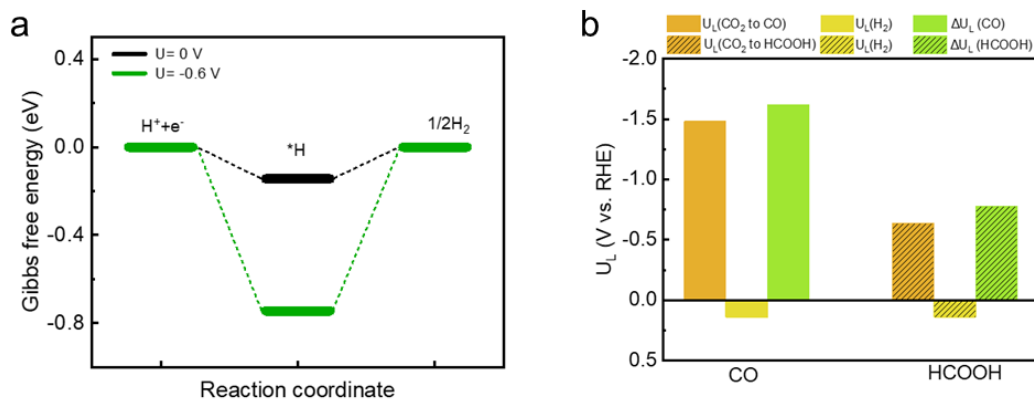
Figure S7.13 (a) Gibbs free energies for the formation of H* at different potentials U on β-Bi$_2$O$_3$; **(b)** Calculated difference in limiting potentials (ΔU_L) for CO$_2$RR to CO and HER, and CO$_2$RR to HCOOH and HER. ΔU_L is directly related to the selectivity of the CO$_2$ reaction, and a more positive value indicates a higher selectivity.
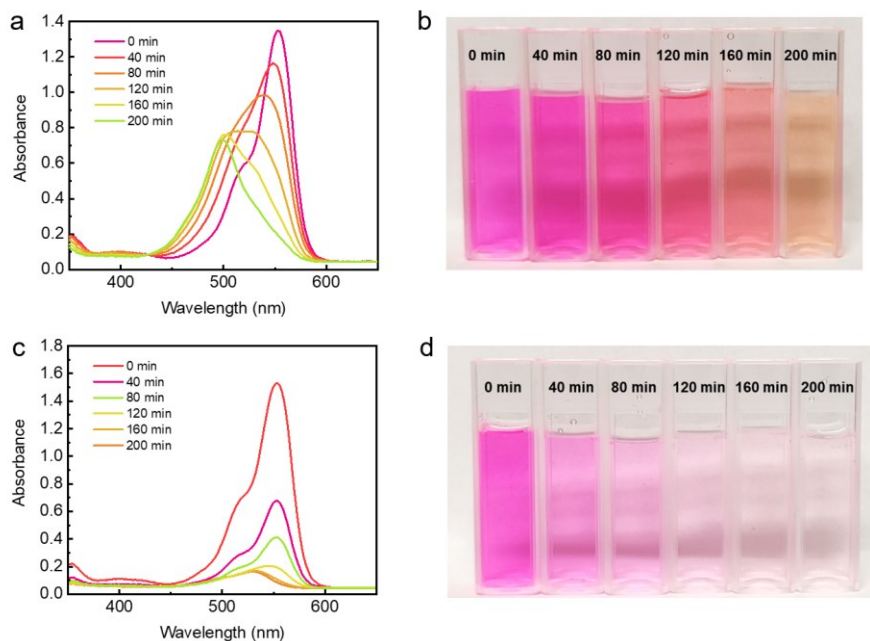
Figure S7.14 (a) The absorbance of dye solution measured at different time and **(b)** The corresponding color changes of α-Bi$_2$O$_3$; **(c)** The absorbance of dye solution measured at different time and **(d)** The corresponding color changes of β-Bi$_2$O$_3$.
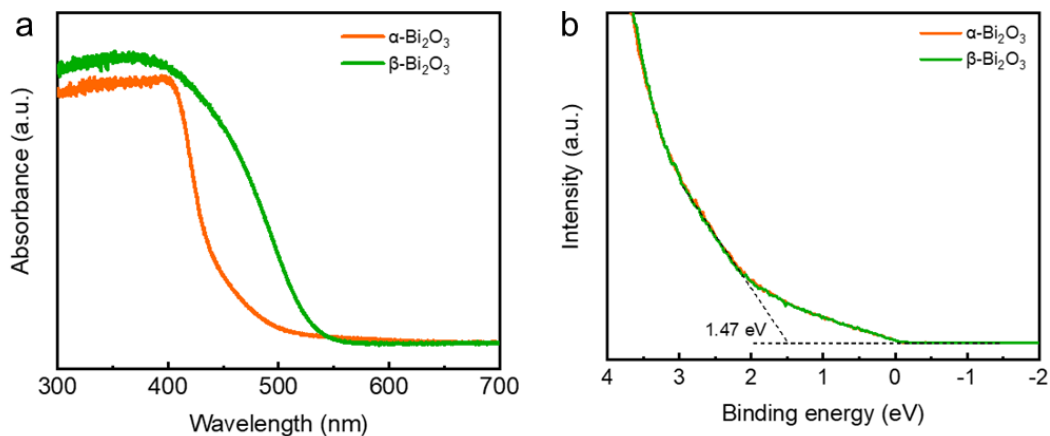
Figure S7.15 (a) UV-vis diffuse reflectance spectra of α-Bi$_2$O$_3$ and β-Bi$_2$O$_3$; (b) VB-XPS spectra of α-Bi$_2$O$_3$ and β-Bi$_2$O$_3$.

Table S7.1 Fitting parameters of the EXAFS spectra of α-Bi$_2$O$_3$ and β-Bi$_2$O$_3$.

Sample	Path	CN	R (Å)	σ^2 (Å^2)	ΔE_0 (eV)	R factor
α-Bi$_2$O$_3$	Bi-O	4.9 ± 0.2	2.15 ± 0.02	0.0015	-2.1	0.002
β-Bi$_2$O$_3$	Bi-O	3.7 ± 0.1	2.12 ± 0.01	0.0097	-2.5	0.006

Note: CN is the coordination number; R is the path distance; σ^2 is the Debye-Waller factors; ΔE_0 is the energy shift; R factor is the happiness of fit.

7.5.2 Supporting references

[1] G. Kresse, J. Hafner, *Phys. Rev. B* **1993**, 47, 558.

[2] G. Kresse, J. Hafner, *Phys. Rev. B* **1994**, 49, 14251.

[3] G. Kresse, J. Furthmüller, *Phys. Rev. B* **1996**, 54, 11169.

[4] B. Hammer, L.B. Hansen, J.K. Nørskov, *Phys. Rev. B* **1999**, 59, 7413.

[5] H. Monkhorst, J. Pack, *Phys. Rev. B* **1976**, 13, 5188.

[6] C. J. Cramer, Essentials of computational chemistry: theories and models, John Wiley & Sons, 2013.

[7] V. Tripković, E. Skúlason, S. Siahrostami, J. K. Nørskov, J. Rossmeisl, *Electrochimica Acta*. **2010**, 55, 7975.

[8] W. J. Durand, W. J.; Peterson, A. A, Studt, F.; Abild-Pedersen, F.; Nørskov, J. K. *Surf. Sci.* **2011**, 605, 1354.

Chapter 8. Unlocking Nanotubular Bismuth Oxyiodide toward Carbon-Neutral Electrosynthesis

8.1 Introduction

The ever-increasing accumulation of CO_2 in the atmosphere has caused severe climate changes that negatively impact natural environment and sustainable development of human society [1-3]. Electrochemical reduction reaction of CO_2 (CO_2RR) is regarded as an attractive technology to lower the CO_2 emission level and when powered by the electricity generated from renewable energy sources (e.g., wind, solar or tidal energy), it can eventually achieve sustainable carbon neutrality by converting CO_2 to valuable chemicals [4-6]. However, the inertness of CO_2 molecules and multi-electron transfer process during CO_2RR usually lead to high thermodynamic energy barriers and sluggish reaction kinetics [7, 8]. The low solubility of gaseous CO_2 in aqueous media and broad distributions of target products also account for the unsatisfactory CO_2RR performance [9]. In addition, the hydrogen evolution reaction (HER) always competes with CO_2RR in aqueous media and can significantly deteriorate the selectivity for specific product [10]. Thus, it is of great importance to design highly active and selective electrocatalysts for efficient CO_2RR.

Formate is one of the typical liquid products with two-electron reduction of CO_2, which can be utilized in formate fuel cells as hydrogen carriers, in textile and pharmaceutical industries [11, 12]. So far, various metal-based electrocatalysts (e.g., Pd [13, 14], Sn [15, 16], In [17, 18], Pb [19, 20] and Bi [21-24]) have been studied for formate formation, among which Bi-based materials show a great potential for CO_2RR due to their low toxicity and earth abundance. Various studies on Bi-based electrocatalysts, including Bi nanoparticles [25], Bi

dendrites [26] and two-dimensional Bi nanosheets [27-30], have demonstrated the effectiveness of structure engineering in improving the electrocatalytic performance toward formate formation. Despite some encouraging achievements, the performance of these electrocatalysts needs further improvement before meeting the requirements of their industrial applications. The commercialization of CO_2RR technologies requires much higher current densities (j) and wider potential window with higher Faradaic efficiencies (FEs) to lower the capital investment for the desired production rate [31, 32]. However, most of the reported formate Faradaic efficiencies ($FE_{formate}$) on Bi-based materials show the increased peak of over 90% at the moderate potential, while such high selectivity could only be maintained in a narrow potential window [33]. Although some reported electrocatalysts demonstrated wider potential windows with higher $FE_{formate}$, the achieved j is still far from the one for practical implementations. Therefore, it is imperative to develop effective electrocatalysts for CO_2RR-to-formate conversion with high j and FE over a wide potential window in order to realize the practical applications of the technology at industrial scale.

It is generally recognized that the structure modulation of electrocatalyst is a feasible approach to improving CO_2RR performance. Among numerous nanomaterials with various morphologies and structures, one-dimensional nanomaterials are regarded as the promising candidates for CO_2RR [34, 35]. The large surface area guarantees the substantial amount of active sites for CO_2RR to proceed, while the unique channel structure of nanotubes could significantly improve the charge transfer ability and the mass transport in aqueous media. Given the gaseous reactant in aqueous media during CO_2RR, the electrocatalyst with nanotubular structure is highly attractive to address the issues of low CO_2 solubility and sluggish multi-electron transfer kinetics. As another critical factor, defects on as-prepared

electrocatalysts can introduce massive uncoordinated sites, thereby ensuring desirable CO_2RR performance. Zhang et al. [36] demonstrated that defects could enrich reaction intermediates and OH^-, which could consequently prompt the C-C bond formation and improve the selectivity of target product. This is further confirmed by Yang et al. [37] that the defective indium/indium oxide heterostructures exhibit a high selectivity for C_1 products with the FE approaching 100% in a broad potential range. Presently, among various electrocatalysts, defects are mostly designed on bulk or two-dimensional materials but there are few studies on building defects into one-dimensional materials [38, 39]. In light of the advantages of low-dimensional materials and structure defects for CO_2RR, introducing defects into the nanotubular Bi-based architecture holds great potential to drive highly active and selective CO_2RR to produce formate.

In this work, the ultrathin Bi_5O_7I nanotubes (NTs) with nanopores and abundant oxygen vacancies are synthesized and demonstrated as a highly active, selective and stable electrocatalyst for CO_2RR toward formate formation. The as-obtained Bi_5O_7I NTs show the desirable $FE_{formate}$ within a wide potential range as well as the high formate formation rate of 1145 $\mu mol\ h^{-1}\ cm^{-2}$ at a moderate potential. More significantly, the CO_2RR performance is boosted in a flow cell that delivers a high current density of 225 mA cm^{-2} at -1.0 V versus reversible hydrogen electrode (vs. RHE) and achieves a good stability of 7 h with negligible degradation. The Bi_5O_7I NTs are further evaluated in the membrane electrode assembly system at a current density of 200 mA cm^{-2} and show the negligible change of cell voltage and FE over 140 h for CO_2RR. With the benefit of nanotubular morphology and defective structure, the massive uncoordinated active sites not only can strengthen the CO_2 adsorption and charge transfer, thereby speeding up the CO_2RR reaction kinetics, but also provide the

hydrophobic surface with a higher local pH to effectively inhibit the competing HER. Density functional theory (DFT) calculations reveal that the defective structure of the electrocatalyst can effectively modulate the electronic structure and optimize the adsorption of the reaction intermediate, thereby promoting CO_2RR performance. All the above merits collectively contribute to the enhanced electrocatalytic performance for CO_2-to-formate conversion.

8.2 Results and discussion

8.2.1 Structural characterizations of Bi_5O_7I nanotubes

The Bi_5O_7I NTs were synthesized *via* the hydrothermal method. As characterized by the high-angle annular dark-field scanning transmission electron microscopy (HAADF-STEM), the prepared catalyst shows the ultrathin nanotubular structure with a uniform diameter of about 5 nm, where the substantial amount of nanopores can be observed on the side wall (Figures 8.1a and 8.1b). The magnified HAADF-STEM image further clearly shows the wall thickness of about 1 nm with the distribution of nanopores along the wall (Figure 8.1c). It is expected that the abundant defects on ultrathin porous nanotubes are beneficial for gas adsorption and charge transfer during the electrochemical reactions. Energy dispersive X-ray spectroscopy (EDS) elemental mapping (Figures 8.1d to 8.1g) confirms the uniform distribution of Bi, O and I along the nanotubes, indicating a successful preparation of the Bi_5O_7I NTs. Moreover, Bi_5O_7I NTs were further characterized by powder X-ray diffraction (XRD) as shown in Figure 8.1h. The three peaks of XRD patterns ranging from 25 to 35 ° are assigned to the (312), (004) and (600) planes of Bi_5O_7I (JCPDS 40-0548), suggesting a high purity of the prepared Bi_5O_7I NTs. For comparison, Bi_5O_7I nanobelts (NBs) were obtained under the same condition except that the pH was increased to 12.5. The scanning electron microcopy (SEM) and TEM images (Figure S8.1) clearly show the structure of belts

with the width of around a micrometer, and the lattice fringe of 0.32 nm is assigned to the (312) plane of Bi_5O_7I, in consistency with the XRD result (Figure S8.2).
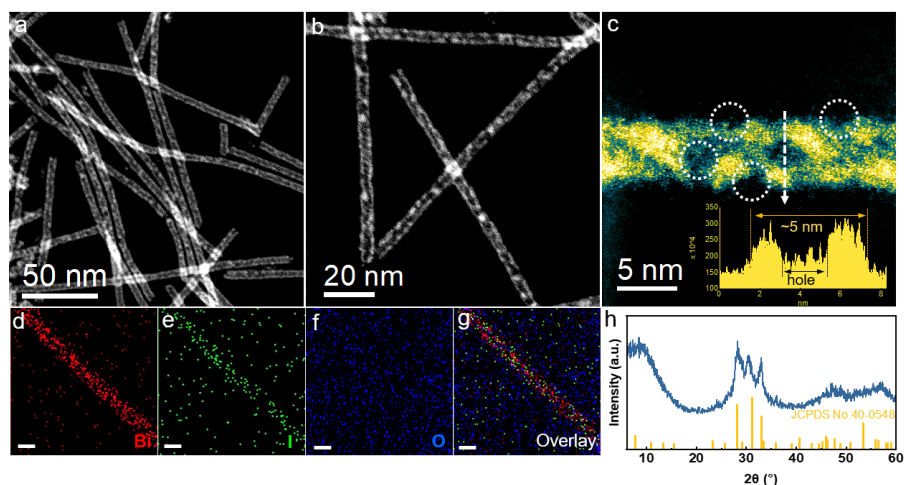
Figure 8.1 (a), (b) and (c) HADDF-STEM images of Bi_5O_7I NTs (insert is the line scan of the depth); (d) to (g) the corresponding EDS elemental mappings and overlay image of Bi_5O_7I NTs (scale bar: 5 nm); (h) XRD pattern of Bi_5O_7I NTs.

8.2.2 Electrocatalytic performance for CO₂RR

The CO₂RR electrocatalytic activities of Bi_5O_7I NTs and NBs were first evaluated in an H-type cell containing 0.5 M CO₂-saturated $KHCO_3$ with all the potentials referred to the reversible hydrogen electrode (RHE) unless specified otherwise. Firstly, linear sweep voltammetry (LSV) curves were measured in Ar- and CO₂-saturated electrolytes, respectively, to evaluate the electrocatalytic activities toward CO₂RR. As shown in Figure 8.2a, the Bi_5O_7I NTs deliver a comparably higher total current density (j) in the CO₂-saturated electrolyte than that in Ar, implying the higher preference to CO₂RR. The similar result is also obtained on Bi_5O_7I NBs, while the higher j and more positive onset potential of Bi_5O_7I NTs suggest their better electrocatalytic activity for CO₂ conversion. To exclude the preferential occurrence of HER and identify the reduction products of CO₂RR, the controlled

electrolysis was carried out (Figure S8.3) at different potentials. The gas-phase products were detected by the online gas chromatography (GC), and the liquid products were analyzed by ion chromatography (IC). The results show that formate is the dominating product, together with minor amounts of CO and H_2. As displayed in Figure 8.2b, the Bi_5O_7I NTs exhibit higher selectivity for formate formation and the $FE_{formate}$ maintains over 92% in a wide potential range from −0.8 to −1.3 V, whereas Bi_5O_7I NBs show the inferior selectivity with the maximum $FE_{formate}$ of about 80% under the same applied potentials. Specifically, the maximum $FE_{foramte}$ of 95.5% is achieved at −1.0 V where HER is significantly inhibited with the FE_{H2} of about 1%. Moreover, the FEs for C_1 products (i.e., formate and CO) are approaching near-unity within a wide potential gap of 500 mV (Figure S8.4), demonstrating the high preference to CO_2RR over the competing HER for Bi_5O_7I NTs.
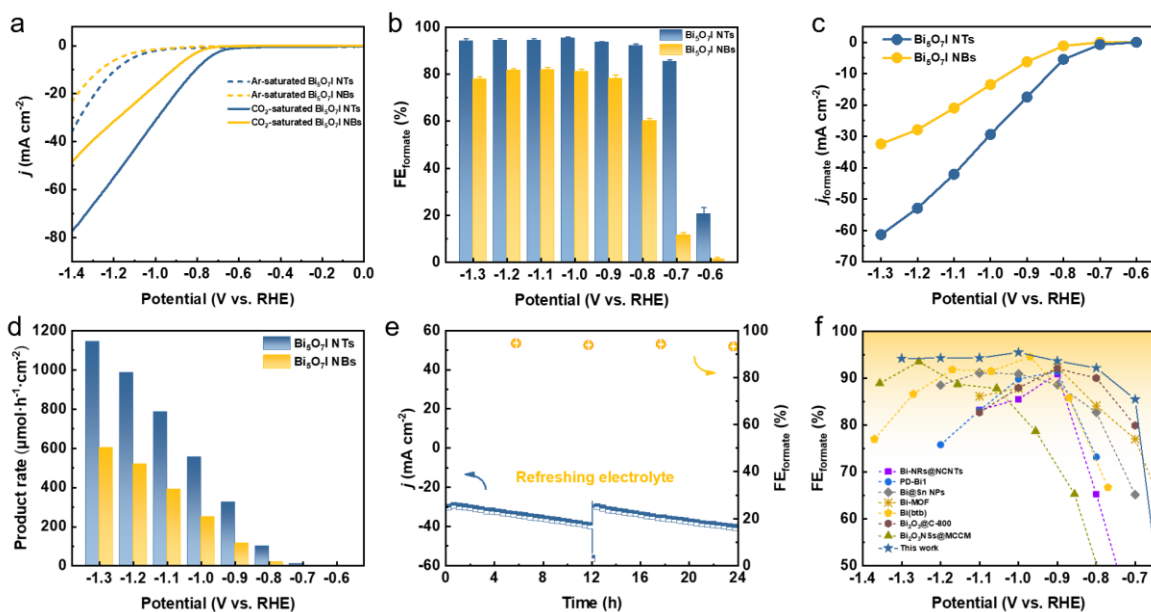
Figure 8.2 (a) LSV curves in 0.5 M CO_2- or Ar-saturated $KHCO_3$ electrolyte, (b) FEs of formate, (c) $j_{formate}$ and (d) formate formation rates of Bi_5O_7I NTs and NBs; (e) Stability test

of Bi_5O_7I NTs at -1.0 V in 0.5 M CO_2-saturated $KHCO_3$ electrolyte; (f) Comparison of $FE_{formate}$ of this work with recently reported Bi-based catalysts.

To reveal the electrocatalytic activity for CO_2RR to formate, the partial current densities of formate ($j_{formate}$) were derived from the j and $FE_{formate}$ as shown in Figure 2c. Clearly, Bi_5O_7I NTs possess better electrocatalytic activity for CO_2-to-formate conversion, where a $j_{formate}$ of about 61 mA cm^{-2} was reached at a moderate potential of -1.3 V, about two times higher than that of Bi_5O_7I NBs (32 mA cm^{-2}). Figure 8.2d shows the formate formation rate, in which Bi_5O_7I NTs exhibit a rate of 1145 μmol h^{-1} cm^{-2} at -1.3 V, comparably higher than Bi_5O_7I NBs (605 μmol h^{-1} cm^{-2}). Furthermore, a potentiostatic electrolysis measurement was conducted at -1.0 V on Bi_5O_7I NTs to evaluate the stability. As shown in Figure 8.2e, the j shows a slight increment after electrolysis for 12 h, which is mainly attributed to the accumulation of products in electrolyte. The j could go back to the original value after refreshing the electrolyte, indicating the good stability of the electrocatalyst. It is worth noting that the average $FE_{formate}$ was maintained at about 92 % over 24 h electrolysis, this further confirms the remarkable durability of Bi_5O_7I NTs for formate formation. Further post-catalysis characterizations were performed to identify the structure and composition changes of the catalyst after CO_2RR. The Bi_5O_7I NTs are fully reduced to metallic Bi after the electrolysis as confirmed by XRD result (Figure S8.5). It is worth noting that the morphologies of the nanotubular structures with surface defects are well maintained under the reduction condition as shown in TEM images (Figure S8.6). To better demonstrate the reduction of Bi_5O_7I NTs to defective metallic Bi NTs, an electrochemical activation measurement was conducted using fresh electrode at -1.0 V vs. RHE in 0.5 M CO_2-saturated $KHCO_3$ for 10 min. The XRD results show that Bi_5O_7I NTs are already fully reduced to

metallic Bi in 10 min (Figure S8.7). From the HRTEM images, some nanopores can be clearly identified on the nanotube walls. The Fourier transform pattern of selected area belongs to the zone axis [001] where the lattice fringe of 0.23 nm is well indexed to (110) facet of metallic Bi (Figure S8.8). The good structure durability accounts for the negligible degradation of the electrocatalytic performance as well as the good stability. To the best of our knowledge, the electrocatalytic performance of Bi_5O_7I NTs outperforms the recently reported Bi-based electrocatalysts for CO_2RR toward formate (Figure 8.2f and Table S8.1) [23, 28, 40-44].

Given the reduction of Bi_5O_7I NTs to defective metallic Bi NTs during CO_2RR, the similar nanotubular Bi NTs without defects were further prepared to compare the CO_2RR performance. As shown in Figure S8.9, the high purity of metallic Bi is synthesized using the hydrothermal method. The nested Bi NTs can be clearly observed by SEM and TEM images and the lattice distance of 0.33 nm is well indexed to (012) facet of metallic Bi (Figure S8.10). The EDS result further confirms the successful prepare of Bi NTs. The CO_2RR measurement was conducted under the same condition as Bi_5O_7I NTs and NBs. As shown in Figure S8.11, the selectivity for formate formation is less than 90% in all measured potentials and the maximum $FE_{formate}$ of 86.6% is achieved at -1.3 V vs. RHE. In addition, the $j_{formate}$ of Bi NTs is much lower compared to that of Bi_5O_7I NTs, demonstrating the inferior electrocatalytic activity for formate formation.

8.2.3 High-throughput CO_2RR performance

It is suggested that the economically compelling application of CO_2RR toward formate formation requires a minimum j of 200 mA cm^{-2} with the selectivity of 90 % to promote the practical CO_2 electrolysis technology [32, 45]. However, the low CO_2 gas solubility in

aqueous media (~33 mM) strongly restricts the CO_2 mass transfer, which results in the limited j. To this end, the CO_2RR performance of Bi_5O_7I NTs on gas diffusion electrode (GDE) was evaluated in a flow cell with 1.0 M KOH. As shown in Figure 8.3a, the onset potential of -0.3 V was reached in the flow cell, much more positive than -0.6 V in H-type cell. Notably, the Bi_5O_7I NTs show a high j of 390 mA cm^{-2} at -1.4 V that decreases to about 225 mA cm^{-2} at -1.0 V, demonstrating the considerably high electrocatalytic activity for CO_2RR. The shortened gas diffusion pathway on GDE facilitates the greater access to CO_2, resulting in the better performance than in H-type cell. In addition, the reduced ohmic resistance and charge transfer resistance (Figure S8.12) in the flow cell system further promote the enhanced CO_2RR electrocatalytic performance. The potential controlled electrolysis measurements were also conducted, and the results of product analysis suggest that the $FE_{formate}$ exceeds 93 % at all the applied potentials from -0.3 to -1.3 V with corresponding $j_{formate}$ increasing from 4.0 to 296 mA cm^{-2} (Figures 8.3b). Meanwhile, the Bi_5O_7I NTs also exhibit a good stability with a high j of over 200 mA cm^{-2} and an average $FE_{formate}$ of about 94 % in the flow cell system for 7 h as shown in Figure 8.3c. The high $FE_{formate}$ and j of Bi_5O_7I NTs in a wide potential window make it stand out from the recently reported electrocatalysts for formate production in flow cell systems (Table S8.2).

To evaluate the feasibility of actual application of Bi_5O_7I NTs in CO_2RR process, a custom-built two-electrode membrane electrode assembly (MEA) system was used to perform the stability test. As shown in Figure 8.3d, the electrolysis can be stably operated at 200 mA cm^{-2} for 140 h with negligible fluctuation of cell voltage, suggesting the good stability of the electrocatalyst under the MEA working conditions. Moreover, the $FE_{formate}$ was maintained over 90% in the period of 140 h, demonstrating the superb CO_2RR performance of Bi_5O_7I

NTs. Such results make it outperform many recently reported electrocatalysts for CO_2 to formate conversion in MEA systems (Figure 8.3e and Table S8.3). Conclusively, Bi_5O_7I NTs possess the strengthened electrocatalytic activity, selectivity and durability for CO_2-to-formate conversion in both the flow cell and MEA systems, thereby demonstrating the promising future for their practical applications in the field of CO_2RR technology.
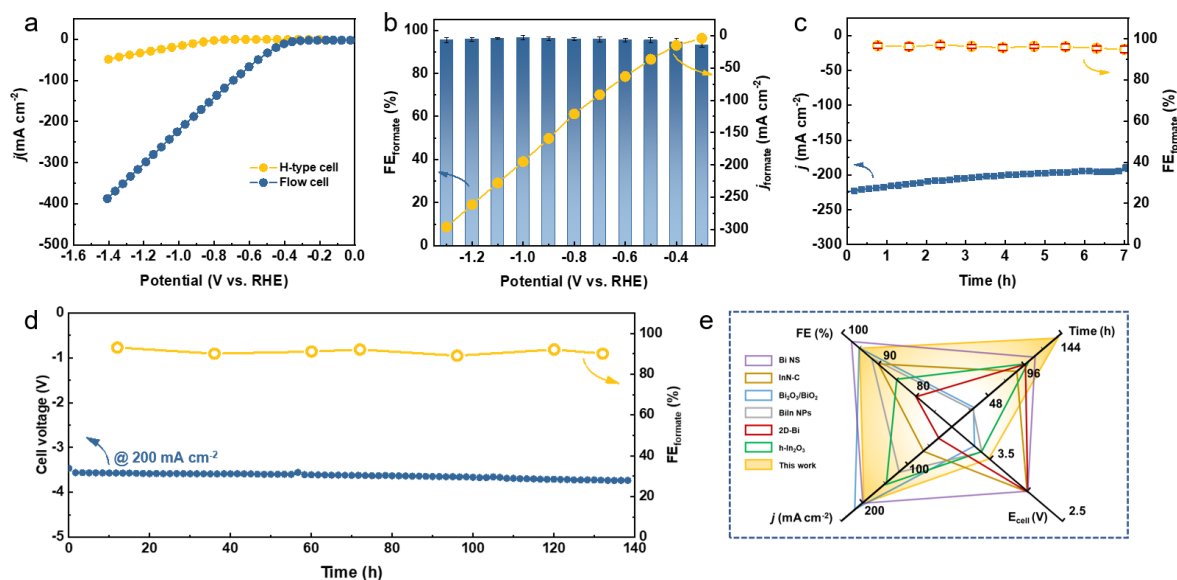
Figure 8.3 (a) LSV curves of Bi_5O_7I NTs in the H-type cell and flow cell, (b) $FE_{formate}$ and $j_{formate}$ of Bi_5O_7I NTs at all potentials in the flow cell, (c) Stability test of Bi_5O_7I NTs at -1.0 V vs. RHE in the flow cell, (d) The CO_2RR performance of Bi_5O_7I NTs at 200 mA cm^{-2} in MEA system, and (e) Comparison of $FE_{formate}$, j, E_{cell} and stability of recently reported electrocatalysts for CO_2RR to formate in MEA system.

8.2.4 Reaction kinetics and mechanistic studies for CO_2RR to formate

To investigate the reaction kinetics for CO_2RR to formate formation, Tafel plots were derived based on static state j and $FE_{formate}$ (Figure 8.4a). Compared with Bi_5O_7I NBs (70.2 mV dec^{-1}), its smaller Tafel slope of 63.4 mV dec^{-1} indicates the faster reaction kinetics process and

better stabilization for $*CO_2^-$ intermediate on Bi_5O_7I NTs, which ensures the improved CO_2RR performance. It is generally recognized that the rate-determining step (RDS) of formate formation could be identified by matching the theoretical Tafel slopes and experimentally derived values [46-48]. The theoretical Tafel slope of 118 mV dec^{-1} suggests the RDS of the initial electron transfer to the adsorbed CO_2, i.e., $* + CO_2 + e^- \rightarrow *CO_2^-$, where (*) corresponds to the active site for adsorption species, while the value of 59 mV dec^{-1} corresponds to the RDS of proton (H^+) transfer served by bicarbonate (HCO_3^-), i.e., $*CO_2^- + HCO_3^- \rightarrow OCHO* + CO_3^{2-}$. It is worth noting that the RDS for CO_2RR toward formate formation is identical for Bi_5O_7I NTs and NBs, where the Tafel slopes are close to the theoretical value of 59 mV dec^{-1}. Therefore, the electroreduction of CO_2 to formate on Bi_5O_7I follows the steps below [11].

$$* + CO_2 + e^- \rightarrow *CO_2^- \qquad \qquad (1)$$

$$*CO_2^- + HCO_3^- \rightarrow OCHO* + CO_3^{2-} \text{ (RDS)} \qquad (2)$$

$$OCHO* + e^- \rightarrow HCOO^-* \qquad \qquad (3)$$

$$HCOO^-* \rightarrow HCOO^- + * \qquad \qquad (4)$$
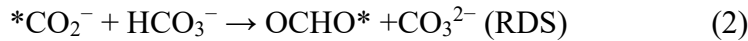
It is also noted that the initial electron transfer step to form the intermediate $*CO_2^-$, i.e., equation (1), plays a fundamental role for CO_2RR toward formate. The better stabilization ability of $*CO_2^-$ could facilitate the faster reaction process and improve the selectivity for CO_2 conversion. To evaluate the binding affinity of $*CO_2^-$ on the catalyst surface, the oxidative LSV measurements were conducted in N_2-saturated 0.1 M KOH electrolyte where the OH^- is considered as the surrogate for $*CO_2^-$. As shown in Figure 8.4b, the Bi_5O_7I NTs exhibit a higher peak intensity at more negative potential compared to Bi_5O_7I NBs, an indication of the better adsorption and stabilization capability for $*CO_2^-$ intermediate and

thus, the enhanced CO2RR performance. The reaction step (2) is further supported by the constant electrolysis performed at -1.0 V vs. RHE with different concentrations of $KHCO_3$ electrolyte ranging from 0.1 to 0.5 M (Figure S8.7b). The j increases with increasing $[HCO_3^-]$ so that the j of 32.1 mA cm^{-2} in 0.5 M $KHCO_3$ is about four times higher than that of 8.2 mA cm^{-2} in 0.1 M $KHCO_3$. The reaction order with respect to HCO_3^- concentrations was derived as displayed in Figure 8.4c. It is found that the log $j_{formate}$ shows nearly linear increase with log $[HCO_3^-]$ and the slope of 0.865 suggests the first-order relation to $[HCO_3^-]$, in consistency with the result of Tafel slope that HCO_3^- serves as the proton donor as the RDS.
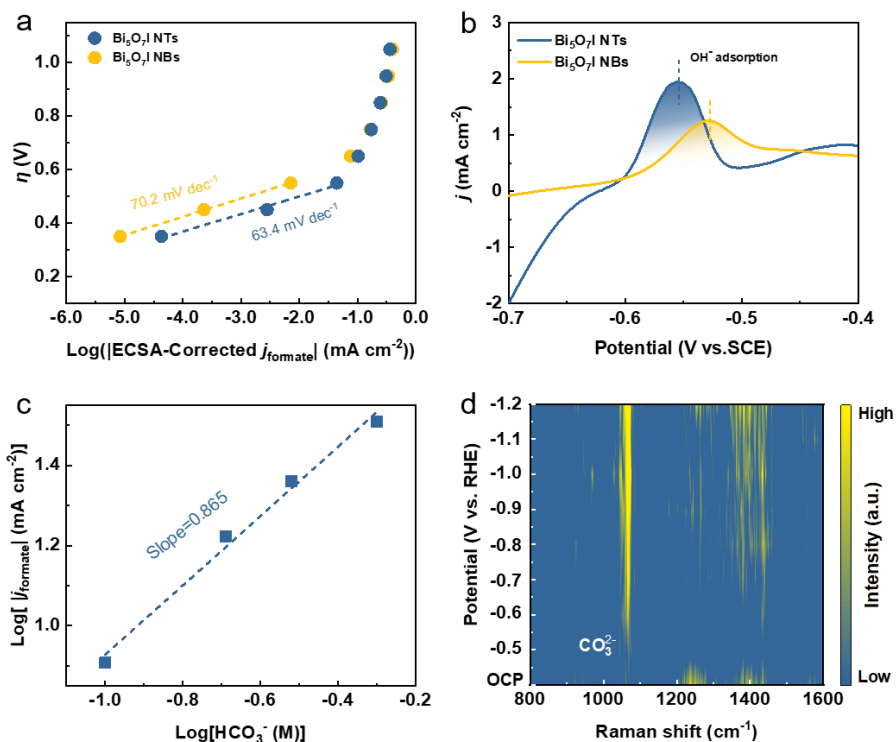
Figure 8.4 (a) ECSA-corrected Tafel plots for formate production, (b) Oxidative LSV curves in N_2-saturated 0.1M KOH, (c) $j_{formate}$ of Bi_5O_7I NTs in different concentrations of HCO_3^- at -1.0 V vs. RHE, (d) Potential-dependent Raman spectra on Bi_5O_7I NTs in 0.5 M CO_2-saturated $KHCO_3$.

The reaction mechanism for CO_2RR to formate formation was further validated by the *in situ* electrochemical Raman spectroscopy measurement (Figure S8.13). Figure 8.4d shows the Raman spectra on Bi_5O_7I NTs at different applied potentials in 0.5 M CO_2-saturated $KHCO_3$ electrolyte, in which two obvious peaks are observed at the applied negative potentials. As stated before, the initial electron transfer to form $*CO_2^-$ is the first reaction step during CO_2RR. The Raman peaks at 450 to 550 cm^{-1} start to appear when the applied potential reaches −0.6 V vs. RHE, which are assigned to the peak of carboxylate $\delta(CO_2^-)$ [49]. The increased peak intensity suggests the first stage of reaction (1) during CO_2RR. Moreover, the peak located at about 1065 cm^{-1} is ascribed to the symmetric C-O stretching vibration $v_1(CO_3^{2-})$ [50], the surface weakly adsorbed monodentate carbonate η^1-CO_3^{2-}. It is noted that the peak intensity gradually increases as the applied potential shifts to a more negative range, while no peak is observed when the applied potential is lower than −0.6 V vs. RHE. This demonstrates the occurrence of reaction step (2) during CO_2RR when the intermediate is formed and accompanied by the production of carbonate ions. Notably, the peaks of $\delta(CO_2^-)$ and $v_1(CO_3^{2-})$ disappear when the applied potential is stopped, further proving that the carbonate intermediate comes from the reaction process (Figure S8.14). All these results provide solid evidence to confirm the reaction mechanism on Bi_5O_7I NTs for electroreduction of CO_2 to formate.

Density functional theory (DFT) calculations were performed to deepen our understanding on the origins of the enhanced catalytic activity and selectivity toward CO_2RR. Given the fully reduction of Bi_5O_7I NTs to defective metallic Bi NTs during CO_2RR, the three models of perfect Bi and Bi with different defects were investigated (Bi-V_1 means Bi surface with a mono vacancy and V_2 means di-vacancy). As depicted in Figure 8.5a, the charge density

difference between Bi and the adsorbate *OCHO on perfect Bi shows relatively low interaction compared to those on Bi-V$_1$ and Bi-V$_2$. The apparent charge transfer between Bi and O atoms on defective Bi demonstrates the stronger interaction of the adsorbate on the Bi surface, which is beneficial for the formation of *OCHO intermediate. Given the structure difference of Bi, the electronic local functions were further studied (Figure 8.5b). The local charge distribution of adjacent Bi atoms can be clearly observed with the existence of defects, which is attributed to the increased orbital overlap caused by the shortened bond length between two adjacent atoms (Figure S8.15), thus resulting in electron delocalization. The p orbitals delocalization of the Bi atoms leads to orbital hybridization between the Bi atoms and the adsorbed *OCHO. The more delocalized electrons near the Bi atom with vacancies can effectively promote the formation of the intermediate *OCHO by donating electrons to the reaction, enhancing the interaction between *OCHO as evidenced by the electron density difference. In addition, the adsorbed intermediate *OCHO shift to the electron delocalized region on Bi atoms as shown in Figure S8.15, further confirming the favorable formation of intermediates over the electron delocalized region.

Furthermore, the Gibbs free energies for CO_2 to HCOOH formation were calculated over the optimized structures shown in Figure 8.5c. The formation energy of intermediate *OCHO decreases from 0.66 to 0.46 eV when introducing di-vacancy on the Bi, suggesting the lower energy barrier compared to the perfect Bi. The stronger charge interaction between Bi and O atoms and higher local charge distribution near Bi atoms synergistically contribute to better adsorption ability of *OCHO, leading to the decreased energy barrier in the rate determining step. In addition, the Gibbs free energies for CO_2 to CO formation were also calculated (Figure 8.5d). It can be found that the rate determining step is the formation of intermediate

*COOH on perfect Bi and defective Bi where no obvious energy difference is observed. The high energy barrier of about 1.47 eV for *COOH formation is significantly higher than that for *OCHO formation, leading to the unfavorable CO formation.
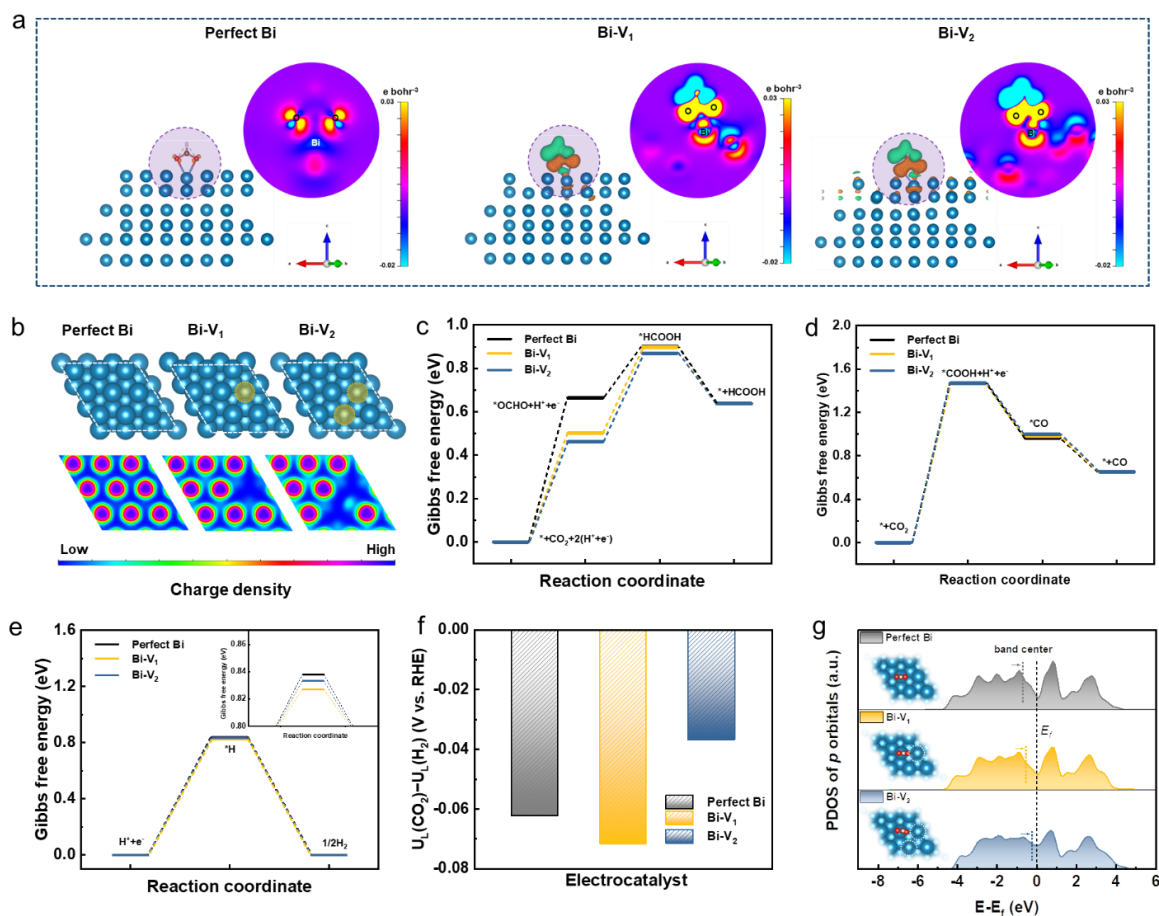
Figure 8.5 (a) The electron density difference with *OCHO adsorbates (2D view generated from the plane derived by Bi-O-O atoms), (b) Electron local functions, Gibbs free energy of CO_2RR to (c) HCOOH pathway and (d) CO pathway, (e) Gibbs free energy of HER, (f) Difference in limiting potentials for CO_2RR and HER, (g) The Bi p-PDOS with *OCHO adsorbates of perfect Bi, Bi-V_1 and Bi-V_2.

Given the competing reaction of HER during CO_2RR, the DFT calculation was further conducted on HER as shown in Figure 8.5e. When introducing defects on Bi structure, the

Gibbs free energies of the formed *H display less difference compared to that of perfect Bi. The energy barrier of over 0.8 eV on *H formation is higher than the determining step of *OCHO formation, indicating the suppression of HER during CO_2RR. Furthermore, the limiting potential difference (ΔU_L) between CO_2RR and HER was also determined to reveal the selectivity toward CO_2RR. As depicted in Figure 8.5f, Bi-V_2 has a more positive potential value (−0.036 V) than perfect Bi (−0.062 V) and Bi-V_1 (−0.072 V), demonstrating the higher selectivity for CO_2 to formate conversion. The projected density of states (PDOS) for Bi p orbitals with adsorbed *OHCO were plotted where the band center shifts upwards to Fermi level with increased vacancies, indicating the stronger interaction between *OCHO and Bi that facilitates the HCOOH formation (Figure 8.5g). Thus, the existed vacancies on Bi can effectively modulate the electronic structure and lower the energy barrier, leading to the superior catalytic performance for formate formation.

8.2.5 Structural merits of Bi$_5$O$_7$I nanotubes towards the enhanced CO$_2$RR performance

To uncover the merits of the defective nanotubular structure, the electrochemical double-layer capacitance (C_{dl}) was measured to determine the electrochemically active surface area (ECSA). As shown in Figure S8.16a, the ultrathin Bi_5O_7I NTs possess a higher C_{dl} (6.81 mF cm^{-2}) than Bi_5O_7I NBs (3.26 mF cm^{-2}), suggesting that the defective nanotubular structure offers substantial number of the active sites and thereby improves the electrocatalytic activity for CO_2RR. Moreover, the previous study [51-53] also manifests the benefits of the ultrathin nanostructure for CO_2RR performance. The thinner thickness of the electrocatalyst provides higher surface area and more active sites. Compared to the nanobelt structure, the ultrathin nanotube structure of Bi_5O_7I endows it with larger surface area and more exposed electrocatalytic active sites for CO_2RR to proceed, which improves both electrocatalytic

activity and selectivity for the conversion of CO_2 to formate. To exclude the effect of morphology on the CO_2RR performance, the $j_{formate}$ was further normalized by the ECSA. As shown in Figure S8.16b, the Bi_5O_7I NTs still deliver the higher $j_{formate}$ compared to Bi_5O_7I NBs, suggesting the higher intrinsic electrocatalytic activity of the Bi_5O_7I NTs for CO_2RR to formate conversion. In addition, the electrochemical impedance spectroscopy (EIS) measurement was conducted to evaluate the charge transfer process between the electrocatalyst and electrolyte. Apparently, the Bi_5O_7I NTs show the comparably smaller interfacial charge transfer resistance compared to NBs (Figure S8.17a), indicating a better charge transfer ability to facilitate the occurrence of CO_2RR. As stated before, the defective nanotubular structure is conducive to gas adsorption, and volumetric CO_2 adsorption isotherms prove the superb CO_2 capture ability of Bi_5O_7I NTs that is three times higher than that of Bi_5O_7I NBs (Figure 8.6a). The enhanced CO_2 adsorption capability originates from the abundant defects on the ultrathin porous nanotubes. This ensures the good mass transfer in aqueous media and benefits the reaction processes on the active sites and consequently, promotes the electrocatalytic performance for formate formation. Aside from the observed nanosized defects, the result of electron paramagnetic resonance (EPR) measurement displays an obvious signal peak at g = 2.001, which is ascribed to the oxygen vacancies in Bi_5O_7I NTs (Figure 8.6b). Previous results have demonstrated that the spare electrons at the defect sites of oxygen vacancy could serve as the electron donor to ease the activation of electron-deficient CO_2 molecules, which is beneficial for the CO_2 activation to form the *CO_2^- [38, 39, 54]. This also accounts for the improved electrocatalytic activity over Bi_5O_7I NTs for CO_2-to-formate conversion.
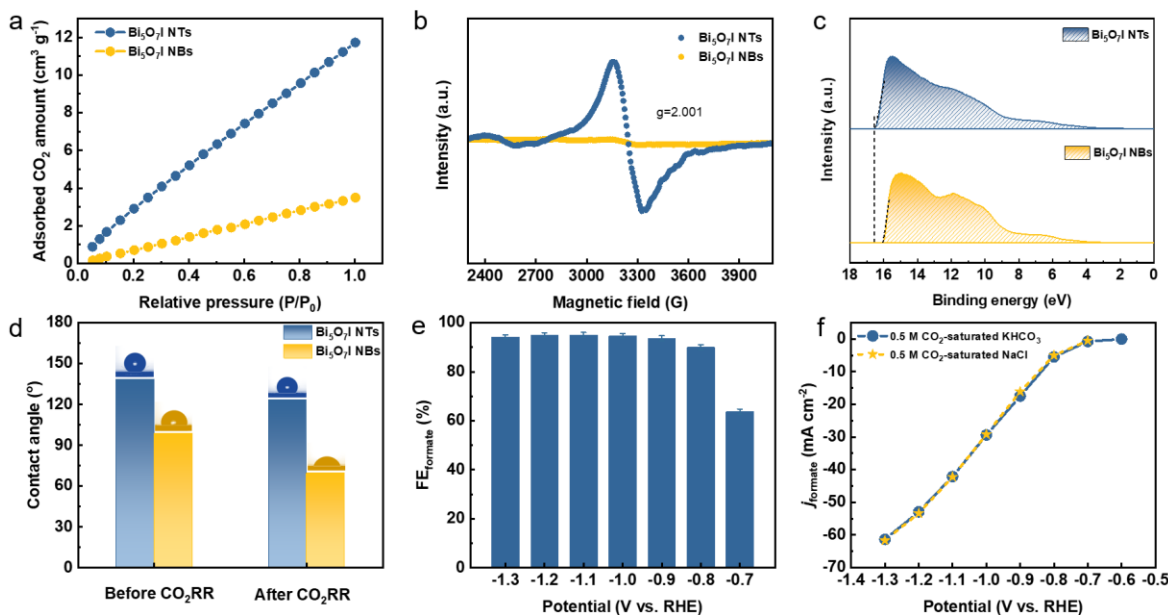
Figure 8.6 (a) CO_2 adsorption isotherms, (b) EPR spectra, (c) UPS spectra and (d) Contact angle measurements before and after CO_2RR on Bi_5O_7I NTs and NBs; (e) $FE_{formate}$ and (f) $j_{formate}$ of Bi_5O_7I NTs in CO_2-saturated 0.5 M NaCl.

Since CO_2RR is a proton-coupled electron transfer (PCET) process and the complicated multi-electron transfer steps occur on the catalyst surface, it is important to take the charge transfer ability into consideration to achieve higher activity and selectivity. Work function (WF) is regarded as an effective indicator to describe the electron transfer ability over the catalyst surface. A lower WF corresponds to the higher tunneling probability of electrons, i.e., the electrons are easier to transfer from the catalyst to the reactant and participate in the subsequent reactions of CO_2RR [55]. It can be inferred that the unique channel structure of the nanotubes with abundant nanosized defects and oxygen vacancies can serve as the charge transport pathway to ensure the faster electron transfer on the catalyst. To this end, the WFs of Bi_5O_7I NTs and NBs were measured by ultraviolet photoelectron spectroscopy (UPS) as shown in Figure 8.6c. Apparently, the defective Bi_5O_7I NTs possess the lower WF of about

4.75 eV compared to NBs (i.e., 5.25 eV), demonstrating the enhanced electron transfer ability (Figure S8.17b). The fast electron transfer on the catalyst surface facilitates the quick pre-equilibrium of CO_2 to $*CO_2^-$, thereby ensuring the formate formation from highly selective CO_2RR.

It is widely accepted that CO_2RR is a gas involved reaction and takes place at the triple-phase boundaries. The wettability of the catalyst plays an indispensable role in the reaction process and can consequently tune the product selectivity. Previous studies have suggested that the hydrophobic interface is favorable for formate formation owing to the limited supply of protons to participate in the competitive HER [56-58]. In light of the substantial amount of nanopores on the defective Bi_5O_7I NTs, the hydrophobicity is expected across the catalyst surface. Thus, the influence of wettability on CO_2RR performance was further studied (Figure S8.18). As shown in Figure 8.6d, the defective Bi_5O_7I NTs present a hydrophobic surface with the contact angle of 138.4°, while a less hydrophobicity is observed on NBs. After CO_2RR measurement, the defective nanotubular structure still maintains the hydrophobicity with the slight decrement of contact angle to 123.5°. Nevertheless, the surface of Bi_5O_7I NBs turns to be hydrophilic with the obvious change of contact angle. The hydrophobic Bi_5O_7I NTs can effectively limit the proton supply to suppress HER, which is consistent with the products distribution result. Concurrently, the enhanced CO_2 adsorption capability can promote sufficient proton donors of HCO_3^- to enhance the proton-depleted formate formation, thus improving the selectivity of CO_2RR. Moreover, the parasitic HER during CO_2RR process usually deteriorates the reaction selectivity toward the target product. The research results suggest that the higher local pH near the electrode surface can change the concentrations of proton-donating species and effectively suppress HER during CO_2RR

[36, 59, 60]. It is speculated that the higher local pH could be achieved on the catalyst surface considering the superior hydrophobicity of Bi_5O_7I NTs. To better observe the local pH effect, the phenolphthalein color transition experiment was performed on the prepared catalysts (Figure S8.19). It is found that the defective Bi_5O_7I NTs show more significant color change to pink in comparison to the NBs, demonstrating the higher local pH around its surface. This higher pH can lead to a local conversion of CO_2 to HCO_3^-, i.e., $CO_2 + OH^- \rightarrow HCO_3^-$, which facilitates the reaction process by providing more proton-donating species and simultaneously suppresses HER. Based on the abovementioned, the defective nanotubular structure of Bi_5O_7I demonstrates the advantages of creating massive uncoordinated active sites, ensuring the CO_2 adsorption capability and improving the charge transfer capability. Concurrently, the hydrophobic surface with the higher local pH effectively inhibits HER, thus achieving selective formation of formate.

8.2.6 CO_2RR performance in simulated seawater-based system

It has been shown that most CO_2RR performance is measured in bicarbonate electrolyte, typically potassium or sodium bicarbonate. To some extent, using low-carbon electrolyte is a promising approach to reducing the carbon source for CO_2RR. The natural seawater is considered as an alternative to substitute the bicarbonate-based electrolyte owing to its abundance and negligible cost [61, 62]. The chlorine evolution reaction at the anode can simultaneously produce higher-value products rather than oxygen gas when directly using seawater as the electrolyte for CO_2RR. The CO_2RR performance of defective Bi_5O_7I NTs was further evaluated in a 0.5 M NaCl solution that mimics seawater (Figure S8.20). Remarkably, the high $FE_{formate}$ is achieved over a wide potential range with a maximum value of 95 % that is comparable to the result by using $KHCO_3$ electrolyte (Figure 8.6e).

Furthermore, the derived $j_{formate}$ shows the similar value compared to the measurement in bicarbonate solution, implying the good intrinsic electrocatalytic activity of the Bi_5O_7I NTs toward formate formation (Figure 8.6f) in a 0.5 M NaCl solution. Therefore, the highly active and selective Bi_5O_7I NTs also demonstrate the promising prospect for CO_2RR application in future seawater-based electrolysis system.

8.3 Conclusions

The ultrathin Bi_5O_7I NTs with abundant nanosized defects and oxygen vacancies are successfully synthesized and exhibit the excellent electrocatalytic performance for CO_2RR toward formate with good selectivity and stability, which is further improved in the flow cell and MEA systems by overcoming the limitation of CO_2 mass transport in aqueous media. The high selectivity and current density of formate over a wide potential window, as well as the good stability, make this electrocatalyst a possible candidate for CO_2RR applications at industrial scale. The experimental results prove that the nanosized defects and oxygen vacancies can serve as the massive uncoordinated active sites and facilitate the adsorption of CO_2, which promotes the charge transfer and stabilizes the reaction intermediates toward CO_2RR. Theoretical calculations unveil that the existence of defects can effectively modulate the electronic structure, thus benefiting the formation of intermediate *OHCO toward HCOOH. Furthermore, the hydrophobic catalyst surface with higher local pH effectively suppresses the HER and results in the very efficient performance of CO_2RR. These findings highlight the importance of structure and defect engineering as an attractive strategy for designing advanced electrocatalysts for achieving carbon-neutral sustainability.

8.4 References

[1]   G. Wang, J. Chen, Y. Ding, P. Cai, L. Yi, Y. Li, C. Tu, Y. Hou, Z. Wen, L. Dai, *Chem. Soc. Rev.* **2021**, *50*, 4993-5061.

[2]   C. Xu, J. Hong, P. Sui, M. Zhu, Y. Zhang, J.-L. Luo, *Cell Reports Physical Science* **2020**, *1*, 100101.

[3]   P. De Luna, C. Hahn, D. Higgins, S. A. Jaffer, T. F. Jaramillo, E. H. Sargent, *Science* **2019**, *364*.

[4]   R. Francke, B. Schille, M. Roemelt, *Chem. Rev.* **2018**, *118*, 4631-4701.

[5]   C. Costentin, M. Robert, J. M. Saveant, *Chem. Soc. Rev.* **2013**, *42*, 2423-2436.

[6]   J. Qiao, Y. Liu, F. Hong, J. Zhang, *Chem. Soc. Rev.* **2014**, *43*, 631-675.

[7]   S. Liu, H. Tao, L. Zeng, Q. Liu, Z. Xu, Q. Liu, J. L. Luo, *J. Am. Chem. Soc.* **2017**, *139*, 2160-2163.

[8]   P.-F. Sui, S. Liu, C. Xu, J. Xiao, N. Duan, R. Feng, J.-L. Luo, *Chem. Eng. J.* **2022**, *427*, 131654.

[9]   T. Burdyny, W. A. Smith, *Energy Environ. Sci.* **2019**, *12*, 1442-1453.

[10]   Y. Y. Birdja, E. Pérez-Gallent, M. C. Figueiredo, A. J. Göttle, F. Calle-Vallejo, M. T. M. Koper, *Nat. Energy.* **2019**, *4*, 732-745.

[11]   N. Han, P. Ding, L. He, Y. Li, Y. Li, *Adv. Energy Mater.* **2019**, 1902338.

[12]   M. F. Philips, G.-J. M. Gruter, M. T. M. Koper, K. J. P. Schouten, *ACS Sustainable Chem. Eng.* **2020**, *8*, 15430-15444.

[13]   T. Gunji, H. Ochiai, T. Ohira, Y. Liu, Y. Nakajima, F. Matsumoto, *Chem. Mater.* **2020**, *32*, 6855-6863.

[14]   N. Han, M. Sun, Y. Zhou, J. Xu, C. Cheng, R. Zhou, L. Zhang, J. Luo, B. Huang, Y. Li, *Adv. Mater.* **2021**, *33*, 2005821.

[15]   Z. Chen, T. Fan, Y.-Q. Zhang, J. Xiao, M. Gao, N. Duan, J. Zhang, J. Li, Q. Liu, X. Yi, J.-L. Luo, *Appl. Catal. B-Environ.* **2020**, *261*, 118243.

[16]   S. Liu, J. Xiao, X. F. Lu, J. Wang, X. Wang, X. W. D. Lou, *Angew. Chem. Int. Ed.* **2019**, *58*, 8499-8503.

[17]   Y. Huang, X. Mao, G. Yuan, D. Zhang, B. Pan, J. Deng, Y. Shi, N. Han, C. Li, L. Zhang, L. Wang, L. He, Y. Li, Y. Li, *Angew. Chem. Int. Ed.* **2021**, *60*, 15844-15848.

[18]   W. Guo, X. Tan, J. Bi, L. Xu, D. Yang, C. Chen, Q. Zhu, J. Ma, A. Tayal, J. Ma, Y. Huang, X. Sun, S. Liu, B. Han, *J. Am. Chem. Soc.* **2021**, *143*, 6877–6885.

[19]   M. J. W. Blom, V. Smulders, W. P. M. van Swaaij, S. R. A. Kersten, G. Mul, *Appl. Catal. B-Environ.* **2020**, *268*, 118420.

[20]   C. H. Lee, M. W. Kanan, *ACS Catal.* **2014**, *5*, 465-469.

[21]   P. Deng, H. Wang, R. Qi, J. Zhu, S. Chen, F. Yang, L. Zhou, K. Qi, H. Liu, B. Y. Xia, *ACS Catal.* **2019**, *10*, 743-750.

[22]   C. W. Lee, J. S. Hong, K. D. Yang, K. Jin, J. H. Lee, H.-Y. Ahn, H. Seo, N.-E. Sung, K. T. Nam, *ACS Catal.* **2018**, *8*, 931-937.

[23]   S. Liu, X. F. Lu, J. Xiao, X. Wang, X. W. D. Lou, *Angew. Chem. Int. Ed.* **2019**, *58*, 13828-13833.

[24]   P. F. Sui, C. Xu, M. N. Zhu, S. Liu, Q. Liu, J. L. Luo, *Small* **2021**, e2105682.

[25]   Y. Qiu, J. Du, W. Dong, C. Dai, C. Tao, *J. CO_2 Util.* **2017**, *20*, 328-335.

[26]   J. H. Koh, D. H. Won, T. Eom, N.-K. Kim, K. D. Jung, H. Kim, Y. J. Hwang, B. K. Min, *ACS Catal.* **2017**, *7*, 5071-5077.

[27]   F. P. Garcia de Arquer, O. S. Bushuyev, P. De Luna, C. T. Dinh, A. Seifitokaldani, M. I. Saidaminov, C. S. Tan, L. N. Quan, A. Proppe, M. G. Kibria, S. O. Kelley, D. Sinton, E. H. Sargent, *Adv. Mater.* **2018**, *30*, e1802858.

[28]   Y. Wang, Y. Li, J. Liu, C. Dong, C. Xiao, L. Cheng, H. Jiang, H. Jiang, C. Li, *Angew. Chem. Int. Ed.* **2021**, *60*, 7681-7685.

[29]   J. Yang, X. Wang, Y. Qu, X. Wang, H. Huo, Q. Fan, J. Wang, L. M. Yang, Y. Wu, *Adv. Energy Mater.* **2020**, *10*, 2001709.

[30]   W. Ma, J. Bu, Z. Liu, C. Yan, Y. Yao, N. Chang, H. Zhang, T. Wang, J. Zhang, *Adv. Funct. Mater.* **2020**, 2006704.

[31]   Y. Cheng, P. Hou, X. Wang, P. Kang, *Acc. Chem. Res.* **2022**, *55*, 231-240.

[32]   R. I. Masel, Z. Liu, H. Yang, J. J. Kaczur, D. Carrillo, S. Ren, D. Salvatore, C. P. Berlinguette, *Nat. Nanotechnol.* **2021**, *16*, 118-128.

[33]   Y. Guan, M. Liu, X. Rao, Y. Liu, J. Zhang, *J. Mater. Chem. A* **2021**, *9*, 13770-13803.

[34]   A. Guan, C. Yang, Y. Quan, H. Shen, N. Cao, T. Li, Y. Ji, G. Zheng, *Chem. Asian J.* **2019**, *14*, 3969-3980.

[35]   S. P. Paula, M. Stefano, E. L. S. Ifan, E. E. María, *ChemCatChem* **2019**, *11*, 1-21.

[36] B. Zhang, J. Zhang, M. Hua, Q. Wan, Z. Su, X. Tan, L. Liu, F. Zhang, G. Chen, D. Tan, X. Cheng, B. Han, L. Zheng, G. Mo, *J. Am. Chem. Soc.* **2020**, *142*, 13606-13613.

[37] W. Yang, Y. Zhao, S. Chen, W. Ren, X. Chen, C. Jia, Z. Su, Y. Wang, C. Zhao, *Inorg. Chem.* **2020**, *59*, 12437-12444.

[38] Q. Wang, y. lei, D. Wang, Y. Li, *Energy Environ. Sci.* **2019**, *12*, 1730-1750.

[39] Y. Wang, P. Han, X. Lv, L. Zhang, G. Zheng, *Joule* **2018**, *2*, 2551-2582.

[40] W. Zhang, S. Yang, M. Jiang, Y. Hu, C. Hu, X. Zhang, Z. Jin, *Nano Lett.* **2021**, *21*, 2650-2657.

[41] Y. Xing, X. Kong, X. Guo, Y. Liu, Q. Li, Y. Zhang, Y. Sheng, X. Yang, Z. Geng, J. Zeng, *Adv. Sci.* **2020**, 1902989.

[42] P. Deng, F. Yang, Z. Wang, S. Chen, Y. Zhou, S. Zaman, B. Y. Xia, *Angew. Chem. Int. Ed.* **2020**, *59*, 10807-10813.

[43] F. Li, G. H. Gu, C. Choi, P. Kolla, S. Hong, T.-S. Wu, Y.-L. Soo, J. Masa, S. Mukerjee, Y. Jung, J. Qiu, Z. Sun, *Appl. Catal. B-Environ.* **2020**, *277*, 119241.

[44] P. Lamagni, M. Miola, J. Catalano, M. S. Hvid, M. A. H. Mamakhel, M. Christensen, M. R. Madsen, H. S. Jeppesen, X. M. Hu, K. Daasbjerg, T. Skrydstrup, N. Lock, *Adv. Funct. Mater.* **2020**, 1910408.

[45] H. Rabiee, L. Ge, X. Zhang, S. Hu, M. Li, Z. Yuan, *Energy Environ. Sci.* **2021**, *14*, 1959-2008.

[46] C. W. Lee, N. H. Cho, S. W. Im, M. S. Jee, Y. J. Hwang, B. K. Min, K. T. Nam, *J. Mater. Chem. A* **2018**, *6*, 14043-14057.

[47] A. Wuttig, Y. Yoon, J. Ryu, Y. Surendranath, *J. Am. Chem. Soc.* **2017**, *139*, 17109-17113.

[48] S. Zhang, P. Kang, T. J. Meyer, *J. Am. Chem. Soc.* **2014**, *136*, 1734-1737.

[49] C. He, S. Chen, R. Long, L. Song, Y. Xiong, *Sci. China Chem.* **2020**, *63*, 1721-1726.

[50] I. V. Chernyshova, P. Somasundaran, S. Ponnurangam, *Proc. Natl. Acad. Sci.* **2018**, *115*, E9261-E9270.

[51] N. Han, Y. Wang, H. Yang, J. Deng, J. Wu, Y. Li, Y. Li, *Nat Commun* **2018**, *9*, 1320.

[52] F. Yang, A. O. Elnabawy, R. Schimmenti, P. Song, J. Wang, Z. Peng, S. Yao, R. Deng, S. Song, Y. Lin, M. Mavrikakis, W. Xu, *Nat. Commun.* **2020**, *11*, 1088.

[53] P. Su, W. Xu, Y. Qiu, T. Zhang, X. Li, H. Zhang, *ChemSusChem* **2018**, *11*, 848-853.

[54]   Z. Wu, Y. Zhao, W. Jin, B. Jia, J. Wang, T. Ma, *Adv. Funct. Mater.* **2020**, 2009070.

[55]   Z.-Z. Wu, F.-Y. Gao, M.-R. Gao, *Energy Environ. Sci.* **2021**, *14*, 1121-1139.

[56]   P. Yue, Q. Fu, J. Li, L. Zhang, L. Xing, Z. Kang, Q. Liao, X. Zhu, *Chem. Eng. J.* **2021**, *405*, 126975.

[57]   Z. Xing, L. Hu, D. S. Ripatti, X. Hu, X. Feng, *Nat. Commun.* **2021**, *12*, 136.

[58]   Z. Cai, Y. Zhang, Y. Zhao, Y. Wu, W. Xu, X. Wen, Y. Zhong, Y. Zhang, W. Liu, H. Wang, Y. Kuang, X. Sun, *Nano Res.* **2018**, *12*, 345-349.

[59]   M. Alfath, C. W. Lee, *Catalysts* **2020**, *10*, 859.

[60]   Y. Yoon, A. S. Hall, Y. Surendranath, *Angew. Chem. Int. Ed.* **2016**, *55*, 15282-15286.

[61]   A. Chen, B.-L. Lin, *Joule* **2018**, *2*, 594-606.

[62]   X. Tan, C. Yu, X. Song, C. Zhao, S. Cui, H. Xu, J. Chang, W. Guo, Z. Wang, Y. Xie, J. Qiu, *Adv. Energy Mater.* **2021**, 2100075.

8.5 Supporting Information

8.5.1 Supporting figures and tables
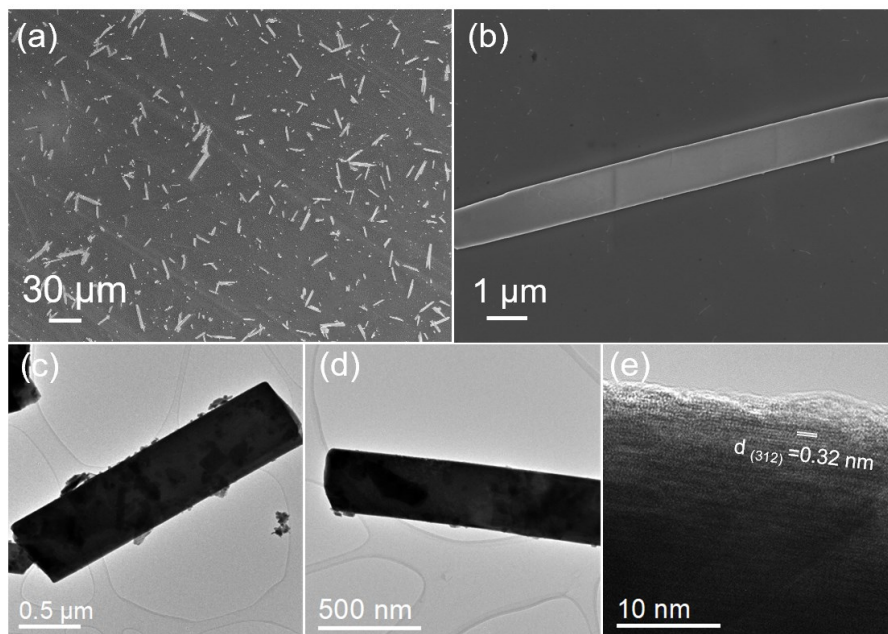
Figure S8.1 (a) and (b) SEM images, (c) and (d) TEM images and (e) HRTEM image of Bi_5O_7I NBs.
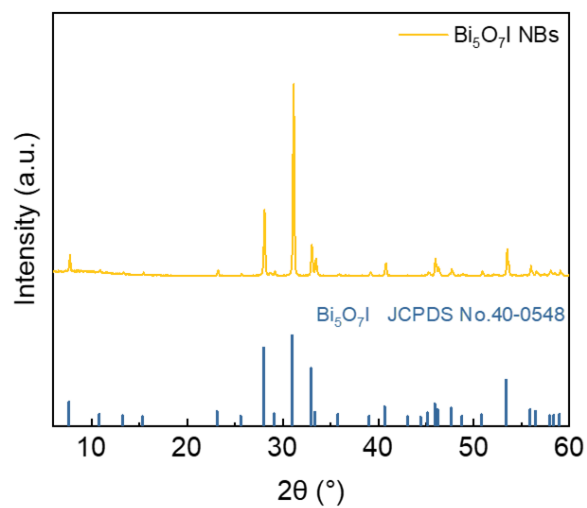
Figure S8.2 XRD pattern of Bi_5O_7I NBs.
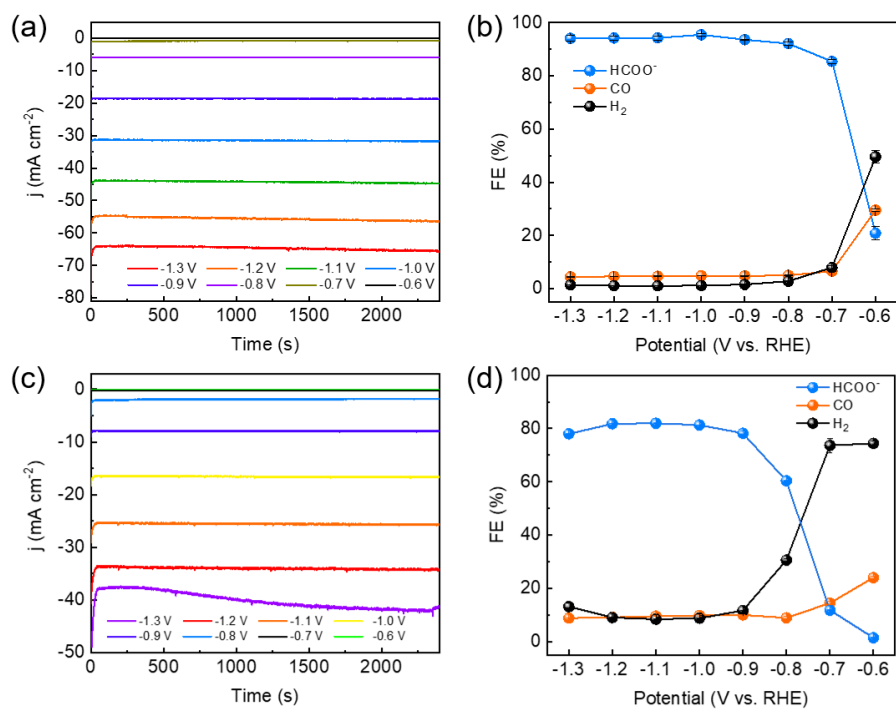
Figure S8.3 Plots of current densities as a function of time and Faradaic efficiencies at different potentials for (a) and (b) Bi_5O_7I NTs; (c) and (d) Bi_5O_7I NBs.
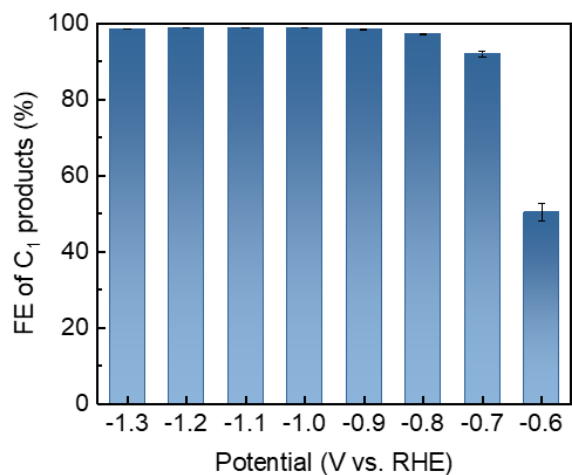
Figure S8.4 FEs of C_1 products on Bi_5O_7I NTs at different applied potentials.
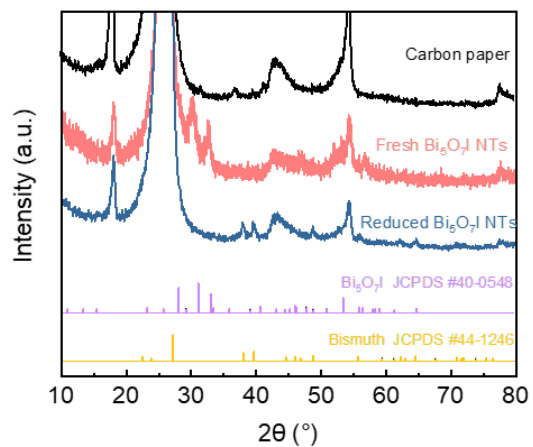
Figure S8.5 XRD result of Bi$_5$O$_7$I NTs after CO$_2$RR measurements.
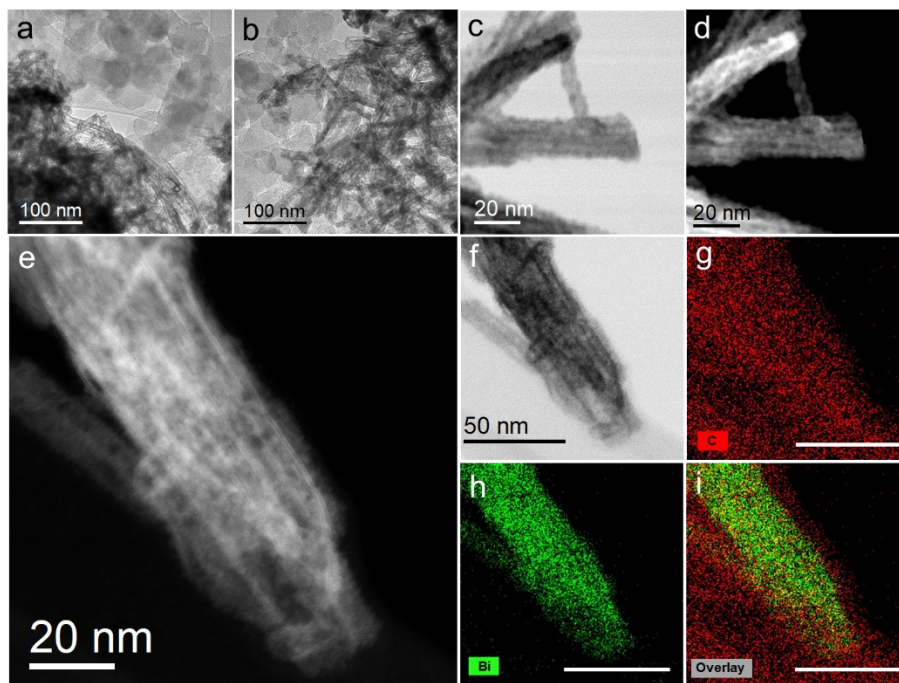
Figure S8.6 (a) and (b) TEM images; (c) to (f) HAADF-STEM and BF-STEM images; (g) to (i) the corresponding EDS elemental mappings of Bi$_5$O$_7$I NTs after CO$_2$RR stability measurements.
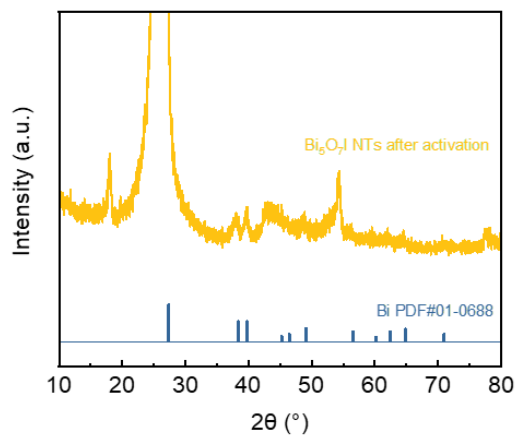
Figure S8.7 XRD result of Bi$_5$O$_7$I NTs after activation at −1.0 V in 0.5 M CO$_2$-saturated KHCO$_3$ electrolyte.
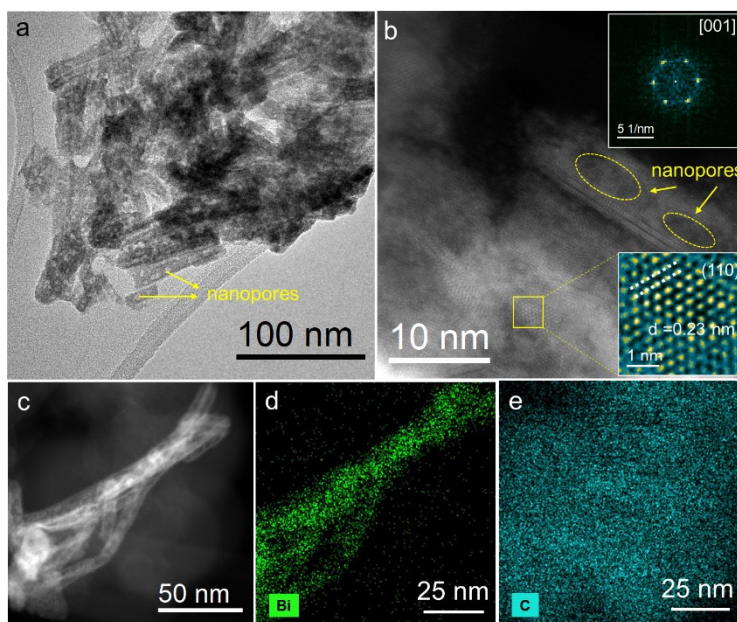
Figure S8.8 (a) HRTEM image; (b) and (c) HAADF-STEM images (insert: Fourier transform pattern and enlarged lattice image of selected area); (d) and (e) the corresponding elemental mappings of Bi$_5$O$_7$I NTs after activation at −1.0 V in 0.5 M CO$_2$-saturated KHCO$_3$ electrolyte.
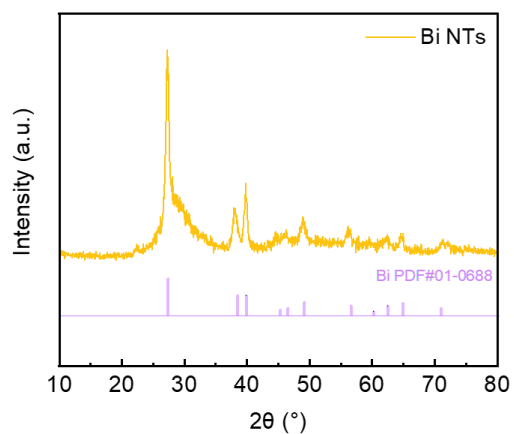
Figure S8.9 XRD pattern of the synthesized Bi NTs.
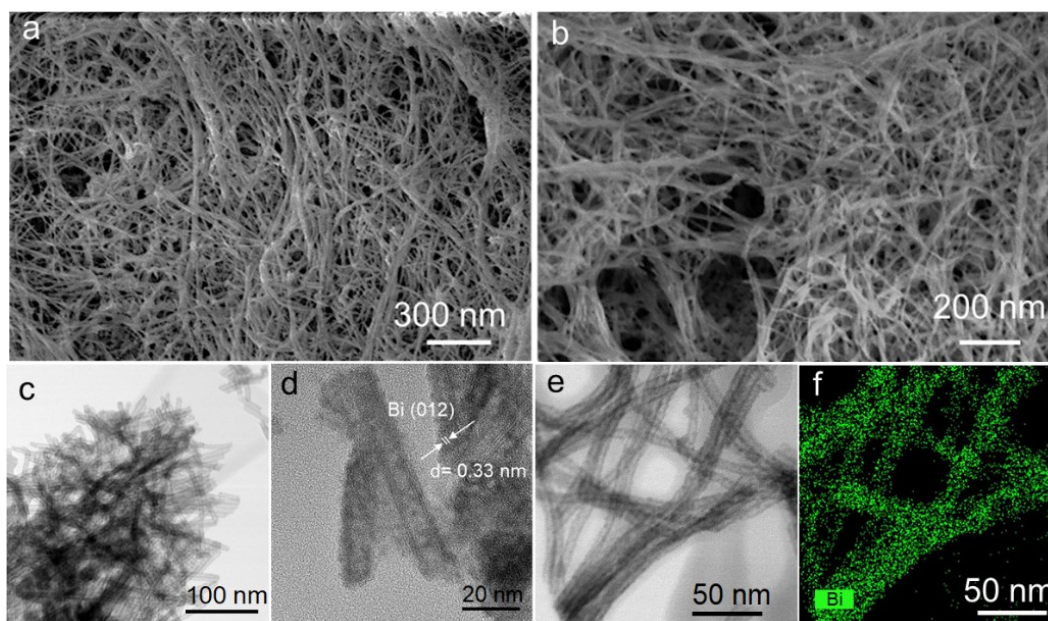
Figure S8.10 (a) and (b) SEM images; (c) TEM image; (d) HRTEM image; (e) BF-STEM

images and (f) EDS elemental mapping of the prepared Bi NTs.
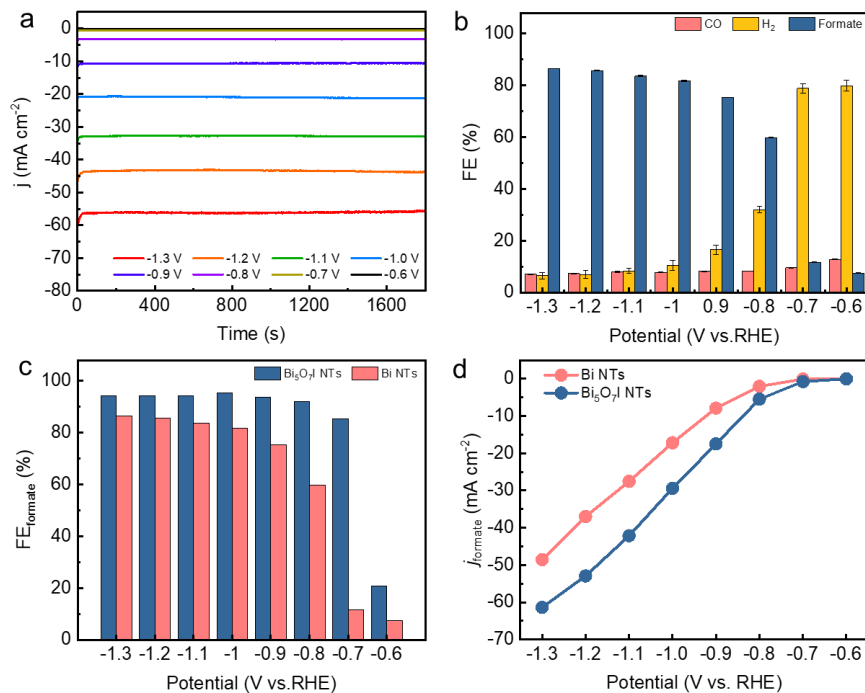
Figure S8.11 (a) Plots of current densities as a function of time; (b) Faradaic efficiencies at different potentials; (c) $FE_{formate}$ and (d) $j_{formate}$ comparison with Bi_5O_7I NTs.
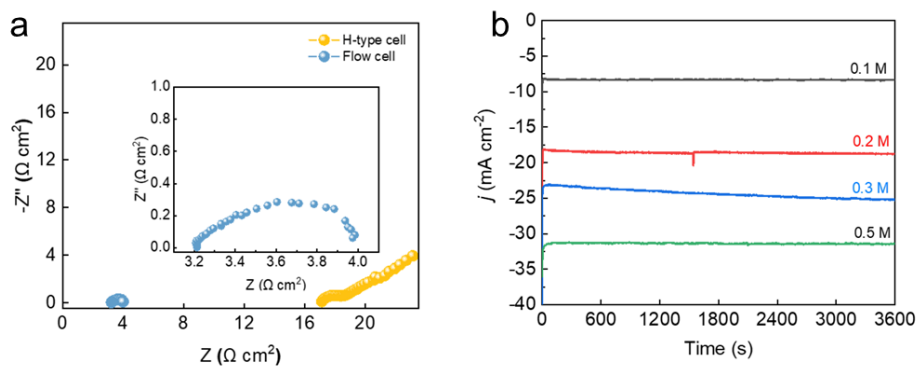
Figure S8.12 (a) Nyquist plots of Bi_5O_7I NTs (inset: the enlarge result in flow cell) in the H-type cell and flow cell; (b) Plot of current densities as a function of time in different concentrations of CO_2-saturated $KHCO_3$ at -1.0 V vs. RHE.
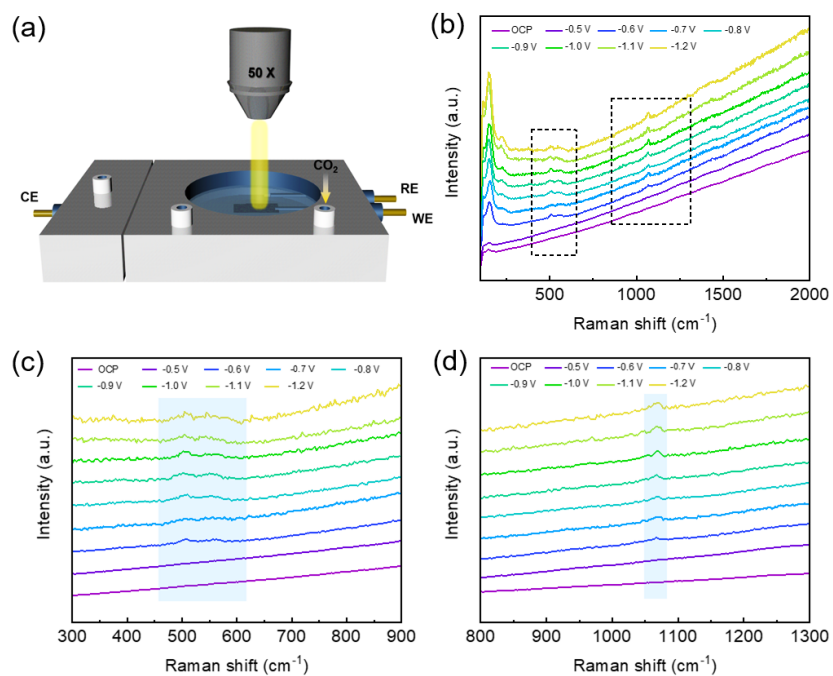
Figure S8.13 (a) Schematic illustration of the *in situ* Raman measurement device for CO_2RR, (b), (c) and (d) Potential-dependent Raman spectra on Bi_5O_7I NTs in 0.5 M CO_2-saturated $KHCO_3$.
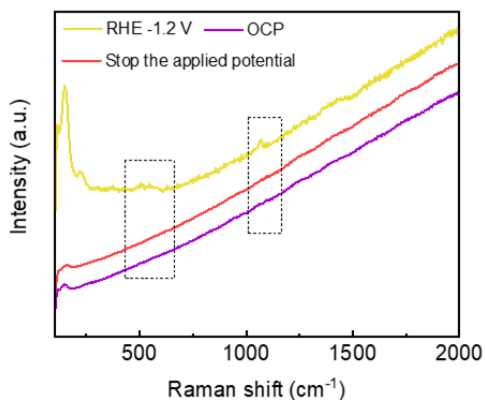
Figure S8.14 The measured Raman spectra (red) of Bi_5O_7I NTs after stopping the applied potential for 5 minutes.
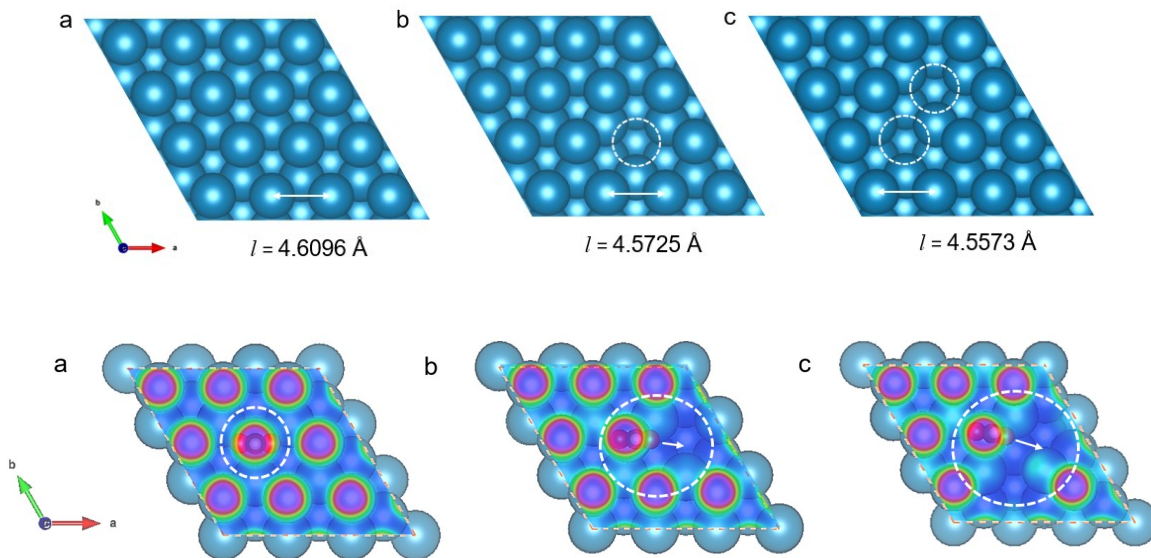
Figure S8.15 Optimized structure of perfect Bi, Bi-V$_1$ and Bi-V$_2$ (*l* is the bond length) and the overlap view of electron local functions and the optimized models of adsorbed *OHCO on Bi atoms.
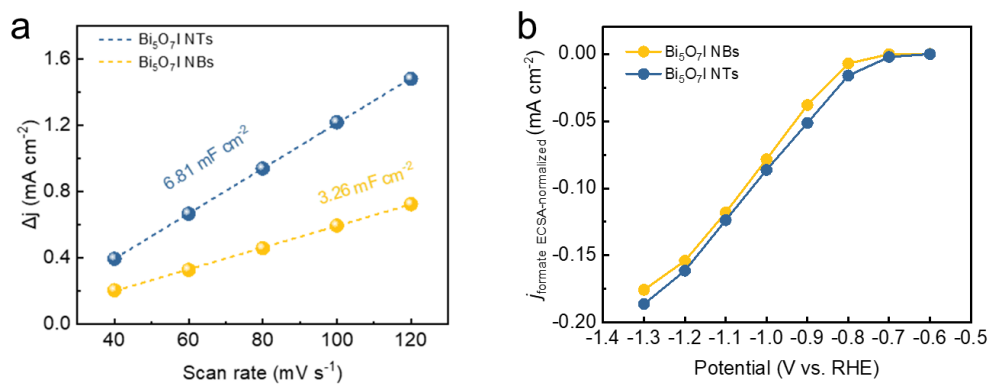
Figure S8.16 (a) Charging current density differences (Δj) plotted against scan rates and (b) ECSA normalized partial current of formate (*j*$_{formate\ ECSA-normalized}$) for Bi$_5O_7$I NTs and NBs.
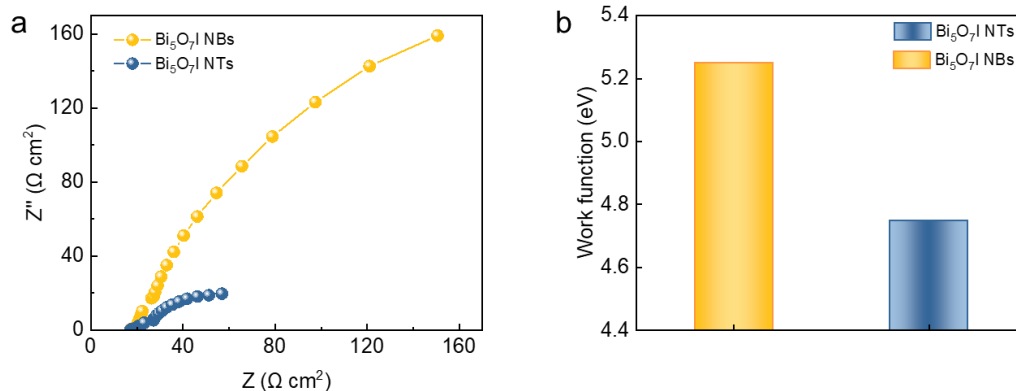
Figure S8.17 (a) Nyquist plots of the electrochemical impedance spectra for Bi_5O_7I NTs and Bi_5O_7I NBs at -1.0 V vs. RHE in CO_2-satured 0.5 M $KHCO_3$ electrolyte; (b) The calculated work functions of Bi_5O_7I NTs and NBs based on experimental measurements.
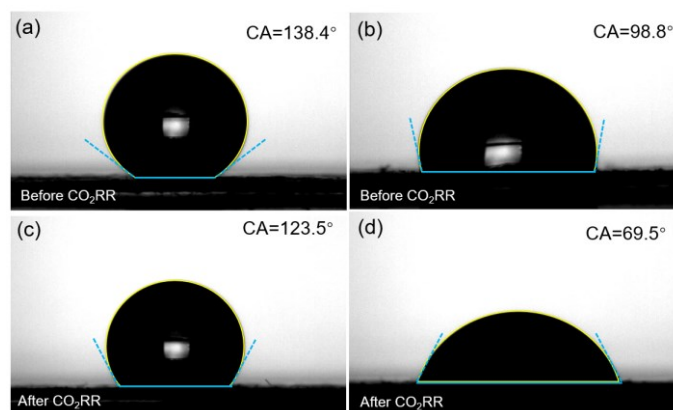
Figure S8.18 Images of contact angle measurement for (a) and (c) Bi_5O_7I NTs, (b) and (d) Bi_5O_7I NBs before and after CO_2RR.
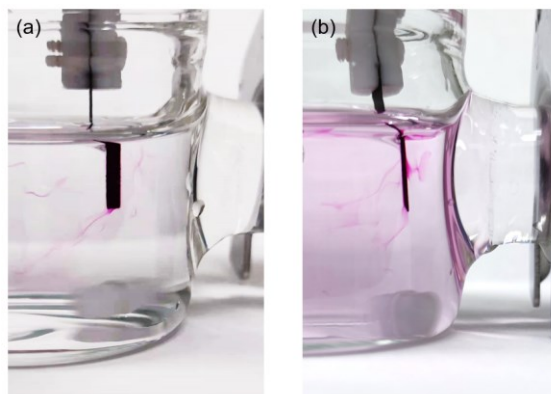
Figure S8.19 Phenolphthalein color transition experiment. Photographs of the phenolphthalein color transition experiment for (a) Bi_5O_7I NBs and (b) Bi_5O_7I NTs at -1.0 V vs RHE.

The phenolphthalein color transition experiment was performed on the catalysts to observe the local pH effect. 0.05 M phenolphthalein in ethanol was added into the CO_2-saturated 0.5 M $KHCO_3$ close to the electrode. After 15 s electrolysis at -1.0 1vs RHE, the color near the electrode changes to obvious pink on Bi_5O_7I NTs electrode, implying the higher local pH around the cathode.
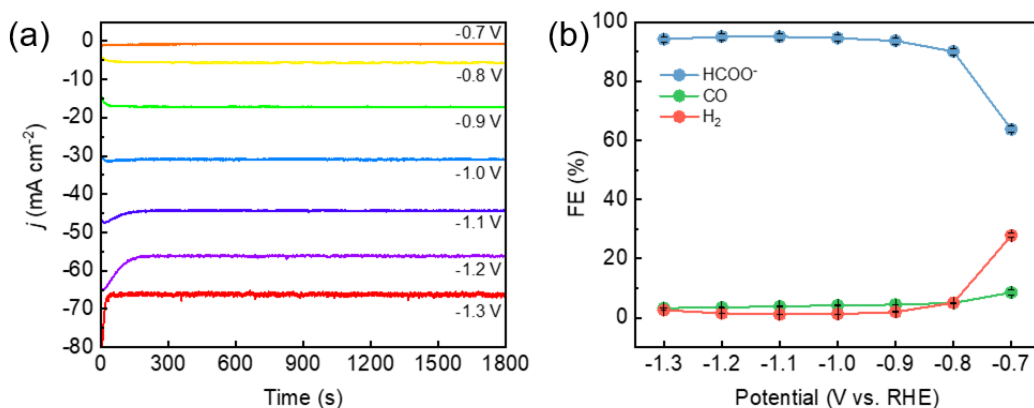
Figure S8.20 Plots of current densities as a function of time and Faradaic efficiencies at different potentials on Bi_5O_7I NTs in CO_2-saturated 0.5 M NaCl.

Table S8.1 Summary and comparison of recently reported Bi-based electrocatalysts for CO_2RR to formate formation in H-type cell.

Catalyst	Electrolyte	Maximum $FE_{formate}$ with the applied potential (vs. RHE)	Potential window for $FE_{formate} > 90\%$	Ref.
Bi-NRs@NCNTs	0.1 M $KHCO_3$	90.9 % at -0.9 V	<100	[1]
PD-Bi1	0.5 M $KHCO_3$	91.4 % at -0.9 V	<100	[2]
Bi@Sn NPs	0.5 M $KHCO_3$	91 % at -1.1 V	<100	[3]
Bi-MOF	0.1 M $KHCO_3$	92.2 % at -0.9 V	<100	[4]
Bi(btb)	0.5 M $KHCO_3$	95.3 % at -0.97 V	200	[5]
Bi_2O_3@C-800	0.5 M $KHCO_3$	92 % at -0.9 V	100	[6]
Bi NTs	0.5 M $KHCO_3$	97 % at -1.0 V	450	[7]
Bi-SnO_x	0.5 M $KHCO_3$	95.8 % at -0.88 V	250	[8]
f-Bi_2O_3	0.1 M $KHCO_3$	87 % at -1.2 V	<100	[9]
Bi_2O_3NSs@MCCM	0.1 M $KHCO_3$	93.8 % at -1.256 V	<100	[10]
Bi-Sn aerogel	0.1 M $KHCO_3$	93.9 % at -1.0 V	300	[11]
BOC@GDY	0.5 M $NaHCO_3$	95.5 % at -0.85 V	150	[12]
Bi_5O_7I NTs	**0.5 M $KHCO_3$**	**94.2 % at -1.3 V** **94.3% at -1.2 V** **94.3% at -1.1 V** **95.5% at -1.0 V** **93.6% at -0.9 V** **92.3% at -0.8 V**	**500**	**This work**

Table S8.2 Summary and comparison of recently reported electrocatalysts for CO_2RR to formate formation in a flow cell.

Catalyst	Electrolyte	Maximum FE$_{formate}$ with the applied potential (vs. RHE)	Potential window (mV)	Ref.
Bi@Sn NPs	2.0 M KHCO$_3$	95% at -1.02 V	350 (FE$_{formate}$ > 90%)	[3]
BOC NFs	1.0 M KOH	98.7% at 0.8 V	1200 (FE$_{formate}$ > 90%)	[13]
Bi$_2$O$_3$@C-800	1.0 M KOH	95% at -0.7 V	700 (FE$_{formate}$ > 90%)	[6]
S-BiVO$_4$	1.0 M KHCO$_3$	97.5 % at -1.0 V	750 (FE$_{formate}$ > 90%)	[14]
SnO$_2$-Bi$_2$O$_3$	1.0 M KOH	91% at -1.29 V	100 (FE$_{formate}$ > 90%)	[15]
BOC@GDY	1.0 M KOH	97% at -0.85 V	450 (FE$_{formate}$ > 90%)	[12]
Bi$_2$S$_3$-Bi$_2$O$_3$ NSs	1.0 M KOH	95% at -1.0 V	800 (FE$_{formate}$ > 90%)	[16]
MIL-68(In)-NH$_2$	1.0 M KOH	94.4% at -1.1 V	300 (FE$_{formate}$ > 90%)	[17]
In-Sn alloy	1.0 M KOH	94% at -0.98 V	550 (FE$_{formate}$ > 90%)	[18]
SnS	1.0 M KOH	88 ± 2% at -1.3 V	300 (FE$_{formate}$ > 80%)	[19]
SnO$_2$/Sn	1.0 M KOH	93% at -0.98 V	500 (FE$_{formate}$ > 90%)	[20]
ZnIn$_2$S$_4$	1.0 M KHCO$_3$	99.3% at -1.18 V	300 (FE$_{formate}$ > 90%)	[21]
Sn$_3$O$_4$	1.0 M KOH	91.1% at -1.02 V	300 (FE$_{formate}$ > 80%)	[22]
Bi$_5$O$_7$I NTs	**1.0 M KOH**	**97.5% (-1.0 V)**	**1000 (FE$_{formate}$ > 93%)**	**This work**

Table S8.3 Summary and comparison of recently reported electrocatalysts for CO_2RR to formate formation in MEA.

Catalyst	E_{cell} (V)	j_{cell} (mA cm^{-2})	FE_{max} (%)	Time (h)	Ref.
2D-Bi	3	30	80	100	[23]
Bi NS	3	200	97	110	[24]
Bi_2O_3/BiO_2	3.7	220	95.4	30	[25]
InN-C	3	64.2	90	88	[26]
BiIn alloy NPs	3.6	120	92	27	[27]
h-In_2O_3	3.6	150	85	100	[28]
Bi$_5$O$_7$I NTs	**3.5**	**200**	**97.5**	**140**	**This work**

8.5.2 Supporting references

[1] W. Zhang, S. Yang, M. Jiang, Y. Hu, C. Hu, X. Zhang, Z. Jin, *Nano Lett.* **2021**, *21*, 2650-2657.

[2] Y. Wang, Y. Li, J. Liu, C. Dong, C. Xiao, L. Cheng, H. Jiang, H. Jiang, C. Li, *Angew. Chem. Int. Ed.* **2021**, *60*, 7681-7685.

[3] Y. Xing, X. Kong, X. Guo, Y. Liu, Q. Li, Y. Zhang, Y. Sheng, X. Yang, Z. Geng, J. Zeng, *Adv. Sci.* **2020**, 1902989.

[4] F. Li, G. H. Gu, C. Choi, P. Kolla, S. Hong, T.-S. Wu, Y.-L. Soo, J. Masa, S. Mukerjee, Y. Jung, J. Qiu, Z. Sun, *Appl. Catal. B-Environ.* **2020**, *277*, 119241.

[5] P. Lamagni, M. Miola, J. Catalano, M. S. Hvid, M. A. H. Mamakhel, M. Christensen, M. R. Madsen, H. S. Jeppesen, X. M. Hu, K. Daasbjerg, T. Skrydstrup, N. Lock, *Adv. Funct. Mater.* **2020**, 1910408.

[6] P. Deng, F. Yang, Z. Wang, S. Chen, Y. Zhou, S. Zaman, B. Y. Xia, *Angew. Chem. Int. Ed.* **2020**, *59*, 10807-10813.

[7]   K. Fan, Y. Jia, Y. Ji, P. Kuang, B. Zhu, X. Liu, J. Yu, *ACS Catal.* **2019**, *10*, 358-364.

[8]   Q. Yang, Q. Wu, Y. Liu, S. Luo, X. Wu, X. Zhao, H. Zou, B. Long, W. Chen, Y. Liao, L. Li, P. K. Shen, L. Duan, Z. Quan, *Adv Mater* **2020**, e2002822.

[9]   T. Tran-Phu, R. Daiyan, Z. Fusco, Z. Ma, R. Amal, A. Tricoli, *Adv. Funct. Mater.* **2019**, *30*, 1906478.

[10]   S. Liu, X. F. Lu, J. Xiao, X. Wang, X. W. D. Lou, *Angew. Chem. Int. Ed.* **2019**, *58*, 13828-13833.

[11]   Z. Wu, H. Wu, W. Cai, Z. Wen, B. Jia, L. Wang, W. Jin, T. Ma, *Angew. Chem. Int. Ed.* **2021**, *60*, 12554-12559.

[12]   S.-F. Tang, X.-L. Lu, C. Zhang, Z.-W. Wei, R. Si, T.-B. Lu, *Sci. Bull.* **2021**, *66*, 1533-1541.

[13]   P. F. Sui, M. R. Gao, S. Liu, C. Xu, M. N. Zhu, J. L. Luo, *Adv. Funct. Mater.* **2022**, 2203794.

[14]   W. Ma, J. Bu, Z. Liu, C. Yan, Y. Yao, N. Chang, H. Zhang, T. Wang, J. Zhang, *Adv. Funct. Mater.* **2020**, 2006704.

[15]   X. Wang, W. Wang, J. Zhang, H. Wang, Z. Yang, H. Ning, J. Zhu, Y. Zhang, L. Guan, X. Teng, Q. Zhao, M. Wu, *Chem. Eng. J.* **2021**, *426*, 131867.

[16]   P. F. Sui, C. Xu, M. N. Zhu, S. Liu, Q. Liu, J. L. Luo, *Small* **2021**, e2105682.

[17]   Z. Wang, Y. Zhou, C. Xia, W. Guo, B. You, B. Y. Xia, *Angew. Chem. Int. Ed.* **2021**, *60*, 19107-19112.

[18]   J. Wang, S. Ning, M. Luo, D. Xiang, W. Chen, X. Kang, Z. Jiang, S. Chen, *Appl. Catal. B-Environ.* **2021**, *288*, 119979.

[19]   J. Zou, C. Y. Lee, G. G. Wallace, *Adv. Sci.* **2021**, *8*, e2004521.

[20]   S. Ning, J. Wang, D. Xiang, S. Huang, W. Chen, S. Chen, X. Kang, *J. Catal.* **2021**, *399*, 67-74.

[21]   L. P. Chi, Z. Z. Niu, X. L. Zhang, P. P. Yang, J. Liao, F. Y. Gao, Z. Z. Wu, K. B. Tang, M. R. Gao, *Nat. Commun.* **2021**, *12*, 5835.

[22]   L.-X. Liu, Y. Zhou, Y.-C. Chang, J.-R. Zhang, L.-P. Jiang, W. Zhu, Y. Lin, *Nano Energy* **2020**, *77*, 105296.

[23]   C. Xia, P. Zhu, Q. Jiang, Y. Pan, W. Liang, E. Stavitski, H. N. Alshareef, H. Wang, *Nat. Energy* **2019**, *4*, 776-785.

[24]   Y. Yuan, Q. Wang, Y. Qiao, X. Chen, Z. Yang, W. Lai, T. Chen, G. Zhang, H. Duan, M. Liu, H. Huang, *Adv. Energy Mater.* **2022**, 2200970.

[25]   X. Feng, H. Zou, R. Zheng, W. Wei, R. Wang, W. Zou, G. Lim, J. Hong, L. Duan, H. Chen, *Nano Lett* **2022**.

[26]   P. Hou, X. Wang, P. Kang, *J. CO$_2$ Util.* **2021**, *45*, 101449.

[27]   K. Yao, H. Wang, X. Yang, Y. Huang, C. Kou, T. Jing, S. Chen, Z. Wang, Y. Liu, H. Liang, *Appl. Catal. B* **2022**, *311*, 121377.

[28]   Z. Liu, X. Lv, J. Zhang, A. Guan, C. Yang, S. Yan, Y. Chen, K. Liu, G. Zheng, *Adv. Mater. Interfaces* **2022**, *9*, 2101956.

Chapter 9. Summary and Future Prospects

9.1 Summary

The work presented in this dissertation focused on applying different engineering strategies to design highly active and selective p-block metal-based electrocatalysts for CO_2RR to C1 products. Firstly, the bimetallic engineering strategy was used to design the electrocatalyst $InO_x@CuO$ through a facile method. The synthesized $InO_x@CuO$ possesses significantly higher electrocatalytic activity, considerably lower onset potential, better selectivity, and a long-term stability for CO_2RR, outperforming the state-of-the-art benchmarking Cu-In electrocatalysts. The *in situ* measurement and theoretical calculation reveal that the enhanced catalytic performance originates from the essential In species on CuO, which not only introduces more active sites, but also better stabilizes the key intermediates, accelerates electron transfer, and increases CO_2 adsorption. These findings advance the bimetallic engineering strategy for improving the electrocatalytic performance for CO formation through introducing p-block metals on Cu as an earth-abundant, cost-effective, highly active and durable electrocatalyst for CO_2RR.

Given the importance of multiple-electron transfer steps during CO_2RR, the electrocatalyst of heterostructured Bi_2S_3-Bi_2O_3 NSs was fabricated to create abundant interfaces within the two components to improve the charge transfer ability. The Bi_2S_3-Bi_2O_3 NSs possess significantly higher electrocatalytic activity, better selectivity, and good stability for CO_2RR. A wide potential window of formate Faradaic efficiencies of over 90 % with a high current density is achieved in a flow cell system. The excellent electrocatalytic activity is attributed to the fast-interfacial charge transfer induced by the electronic interaction at the interface of

Bi_2S_3-Bi_2O_3, the increased number of active sites and the improved CO_2 adsorption ability. These features collectively contribute to the faster reaction kinetics and the improved selectivity and consequently guarantee the superb CO_2RR performance towards formate formation. These outputs shed light on the interface engineering of CO_2RR electrocatalysts and offer an effective approach to designing the electrocatalysts suitable for industrial applications.

Bicarbonate/carbonate are the most common species involved in the CO_2RR process, but it is still unclear as to how the catalyst with self-contained carbonate species affects the CO_2RR performance. Thus, the BOC NFs were prepared using a one-pot synthesis method for the efficient CO_2RR to formate. The *in situ* DRITFS and Raman measurements reveal the unique self-reinforced CO_2 adsorption properties of BOC NFs, especially the chemisorption, which is further proved by theoretical calculations. The fast CO_2 adsorption-desorption kinetics on the catalyst surface in an aqueous electrolyte is further identified, which could greatly facilitate the CO_2RR process. In addition to the good charge transfer ability of BOC NFs, the layer-stacked structure also endows the catalysts with a large surface area that offers an increased number of active sites. As a result, the near-unity formate selectivity and a good stability are achieved on BOC NFs at -1.0 V with the negligible degradation. Moreover, the high throughput electrocatalytic performance of CO_2RR with the desirable selectivity of over 90% in a potential window as wide as 1200 mV and a high current density of over 230 mA cm^{-2} is achieved. These findings clearly reveal the unique properties of electrocatalyst with the self-contained carbonate species for CO_2RR, and also present a promising strategy to design highly active, efficient and robust catalysts with self-reinforced CO_2 adsorption capability for formate electrosynthesis.

To modulate physicochemical and structural properties of metal nanomaterials, phase engineering has proven to be an effective approach in electrocatalysis, but so far, metal oxides have rarely been studied from the perspective of that approach. To bridge the knowledge gap, the stable α-Bi_2O_3 and metastable β-Bi_2O_3 phases were prepared using a thermal treatment strategy, and the phase transition and morphology evolution from β- to α-Bi_2O_3 were tracked by *in situ* heating X-ray diffraction and *in situ* heating scanning electron microscope. Compared to α-Bi_2O_3, β-Bi_2O_3 possesses substantially more nanovoids, oxygen vacancies and grain boundaries, which enable better CO_2 adsorption and charge transfer abilities and consequently promote faster reaction kinetics. The β-Bi_2O_3 achieves a high Faradaic efficiency for formate formation with a maximum of 98.1% at -1.1 V and good stability of 36 h. Further computational results point out that the exothermic process of the key intermediate *OCHO formation on β-Bi_2O_3 is beneficial and leads to a high formate selectivity. Theses results underscore the effectiveness of phase engineering of metal oxides in CO_2RR and provide more opportunities for intellectual catalyst design to achieve environmental sustainability.

Finally, through introducing defects to the nanotubes, the ultrathin one-dimensional nanotubular Bi_5O_7I with substantial amounts of nanosized defects and oxygen vacancies were synthesized for CO_2RR. The abundant defects not only offer massive uncoordinated active sites for CO_2RR to proceed, but also increase the CO_2 adsorption capability. Benefiting from the prominent capillary and confinement effects, the unique channel structure of Bi_5O_7I NTs significantly enhances the charge transfer ability and the mass transport in aqueous media as well as stabilizes the reaction intermediates during CO_2RR. In addition, the hydrophobic catalyst surface with higher local pH effectively suppresses the competing

hydrogen evolution reaction, leading to the highly active and selective performance towards formate. Density functional theory calculation results further unravel the effective electronic structure modulation and the optimization of the reaction intermediates on the defective nanostructure, elucidating the origins of the enhanced CO_2RR performance. Moreover, the high throughput electrocatalytic performance of CO_2RR in the membrane electrode assembly (MEA) system achieves a high Faradaic efficiency at 200 mA cm^{-2} and high stability of 140 h with negligible performance degradation, both meet the requirement for practical implementations of CO_2RR technologies. These results exemplify the utilization of defect engineering as an attractive strategy for designing advanced electrocatalysts to achieve carbon-neutral sustainability in industrial applications.

9.2 Future prospects

The suggestions of future work are briefly listed as below and hopefully, they can serve as guidelines and inspirations for researchers dedicated to electrocatalysis studies of CO_2RR.

1. *Further studies on the design impurity tolerant catalysts*

Although CO_2RR performance has been greatly improved with the development of various highly active and selective catalysts, most laboratory tests are conducted using ultrapure CO_2. The results from such high pure gaseous CO_2 cannot be suitably adopted for industrial situations because of the high cost for gas purification. The flue gas generated from fossil fuel combustion usually contains other impurities such as SO_x and NO_x at ppm levels, which may significantly affect the CO_2RR performance. To that end, future studies are expected to be conducted using simulated flue gas to disclose the effect of impurities on CO_2RR performance so that the impurity tolerant catalysts can be designed and synthesized accordingly.

2. *Mitigation of carbon loss from carbonate crossover*

It is recognized that CO_2 crossover is one of the key challenges in CO_2RR technology. When using an anion exchange membrane under alkaline conditions, carbonate/bicarbonate species can cross from the cathode to the anode through the membrane, leading to carbon source loss. Alternative membranes, such as cation exchange membranes and bipolar membranes, offer the opportunity to prevent carbon loss in strong acidic electrolytes. However, the competing hydrogen evolution reaction can degrade the selectivity of CO_2RR, and the membrane's stability poses another critical issue. Therefore, how to mitigate carbon loss due to carbonate crossover during CO_2RR is of great importance in achieving practical implementation of the technology.

3. *Direct electrolysis of CO_2 using amine capturing solution*

The direct electrolysis of amine-based CO_2 capturing solution is attractive as an alternative to the energy-demanding CO_2 separation processes. Traditional CO_2 capture usually involves two steps: absorbing CO_2 using a basic solvent to convert it to carbamate or bicarbonate, followed by thermal or pressure swings for utilization. However, the regeneration separation process is energy-intensive and of high cost, resulting in a huge penalty on the total operating cost. Therefore, direct electrolysis of amine-based CO_2 capturing solution holds great potential to reduce the capital cost for CO_2RR, which needs further in depth studies on reaction system and catalyst design.

4. *Upgrade the electrolysis system combined with alternative anode reactions*

Most of the current CO_2RR investigations only focus on the cathode while less attention is being paid to the anode part. The common CO_2RR usually couples with the anodic oxygen evolution reaction that is high energy consumption compared to the cathode. To this end,

using other anode oxidation reactions with lower energy input to replace the oxygen evolution reaction can be an attractive strategy to reduce the overall energy consumption. Given the different reaction conditions, the effects of the anode electrolyte and catalysts are the two key points that need to be further studied to minimize the energy input and maximize the value of the total products.

Bibliography

[1]   O. S. Bushuyev, P. De Luna, C. T. Dinh, L. Tao, G. Saur, J. van de Lagemaat, S. O. Kelley, E. H. Sargent, *Joule* **2018**, *2*, 825-832.

[2]   P. De Luna, C. Hahn, D. Higgins, S. A. Jaffer, T. F. Jaramillo, E. H. Sargent, *Science* **2019**, *364*.

[3]   https://climateactiontracker.org/global/temperatures/

[4]   CARBON DIOXIDE CAPTURE AND STORAGE, Cambridge University Press, United States of America, New York, **2005**.

[5]   https://www.iea.org/reports/about-ccus

[6]   E. Alper, O. Yuksel Orhan, *Petroleum* **2017**, *3*, 109-126.

[7]   D. T. Whipple, P. J. A. Kenis, *The Journal of Physical Chemistry Letters* **2010**, *1*, 3451-3458.

[8]   R. S. Weber, *ACS Catal.* **2018**, *9*, 946-950.

[9]   S. Xu, E. A. Carter, *Chem Rev* **2018**.

[10] L. Zhang, Z. J. Zhao, T. Wang, J. Gong, *Chem. Soc. Rev.* **2018**, *47*, 5423-5443.

[11] Y. Y. Birdja, E. Pérez-Gallent, M. C. Figueiredo, A. J. Göttle, F. Calle-Vallejo, M. T. M. Koper, *Nat. Energy.* **2019**, *4*, 732-745.

[12] F. Li, D. R. MacFarlane, J. Zhang, *Nanoscale* **2018**, *10*, 6235-6260.

[13] N. Han, P. Ding, L. He, Y. Li, Y. Li, *Adv. Energy Mater.* **2019**, 1902338.

[14] S. Jin, Z. Hao, K. Zhang, Z. Yan, J. Chen, *Angew.Chem. Int. Ed.* **2021**, *60*, 20627-20648.

[15] G. Wang, J. Chen, Y. Ding, P. Cai, L. Yi, Y. Li, C. Tu, Y. Hou, Z. Wen, L. Dai, *Chem. Soc. Rev.* **2021**, *50*, 4993-5061.

[16] D. Kim, J. Resasco, Y. Yu, A. M. Asiri, P. Yang, *Nat Commun* **2014**, *5*, 4948.

[17] Q. Li, J. Fu, W. Zhu, Z. Chen, B. Shen, L. Wu, Z. Xi, T. Wang, G. Lu, J. J. Zhu, S. Sun, *J. Am. Chem. Soc.* **2017**, *139*, 4290-4293.

[18] K. Sun, T. Cheng, L. Wu, Y. Hu, J. Zhou, A. Maclennan, Z. Jiang, Y. Gao, W. A. Goddard, 3rd, Z. Wang, *J. Am. Chem. Soc.* **2017**, *139*, 15608-15611.

[19] K. Wang, D. Liu, P. Deng, L. Liu, S. Lu, Z. Sun, Y. Ma, Y. Wang, M. Li, B. Y. Xia, C. Xiao, S. Ding, *Nano Energy* **2019**, *64*, 103954.

[20] Z. Wu, H. Wu, W. Cai, Z. Wen, B. Jia, L. Wang, W. Jin, T. Ma, *Angew. Chem. Int. Ed.* **2021**, *60*, 12554-12559.

[21] K. Ye, T. Liu, Y. Song, Q. Wang, G. Wang, *Appl. Catal. B-Environ.* **2021**, *296*, 120342.

[22] B. Zhang, J. Zhang, M. Hua, Q. Wan, Z. Su, X. Tan, L. Liu, F. Zhang, G. Chen, D. Tan, X. Cheng, B. Han, L. Zheng, G. Mo, *J. Am. Chem. Soc.* **2020**, *142*, 13606-13613.

[23] W. Yang, Y. Zhao, S. Chen, W. Ren, X. Chen, C. Jia, Z. Su, Y. Wang, C. Zhao, *Inorg. Chem.* **2020**, *59*, 12437-12444.

[24] Q. Gong, P. Ding, M. Xu, X. Zhu, M. Wang, J. Deng, Q. Ma, N. Han, Y. Zhu, J. Lu, Z. Feng, Y. Li, W. Zhou, Y. Li, *Nat. Commun.* **2019**, *10*, 2807.

[25] Y. Yuan, Q. Wang, Y. Qiao, X. Chen, Z. Yang, W. Lai, T. Chen, G. Zhang, H. Duan, M. Liu, H. Huang, *Adv. Energy Mater.* **2022**, 2200970.

[26] Y. Chen, Z. Lai, X. Zhang, Z. Fan, Q. He, C. Tan, H. Zhang, *Nat. Rev. Chem.* **2020**, *4*, 269.

[27] H. Li, X. Zhou, W. Zhai, S. Lu, J. Liang, Z. He, H. Long, T. Xiong, H. Sun, Q. He, Z. Fan, H. Zhang, *Adv. Energy Mater.* **2020**, *10*, 2002019.

[28] D. Ma, Y. Ying, K. Zhang, Y. Gao, L. Zhou, A. Song, Y. Zhu, K. Xie, T. Jin, H. Huang, *Appl. Catal. B-Environ.* **2022**, *316*, 121658.

[29] Y. Ma, J. Yu, M. Sun, B. Chen, X. Zhou, C. Ye, Z. Guan, W. Guo, G. Wang, S. Lu, D. Xia, Y. Wang, Z. He, L. Zheng, Q. Yun, L. Wang, J. Zhou, P. Lu, J. Yin, Y. Zhao, Z. Luo, L. Zhai, L. Liao, Z. Zhu, R. Ye, Y. Chen, Y. Lu, S. Xi, B. Huang, C. S. Lee, Z. Fan, *Adv. Mater.* **2022**, *34*, e2110607.

[30] Y. Ge, Z. Huang, C. Ling, B. Chen, G. Liu, M. Zhou, J. Liu, X. Zhang, H. Cheng, G. Liu, Y. Du, C. J. Sun, C. Tan, J. Huang, P. Yin, Z. Fan, Y. Chen, N. Yang, H. Zhang, *J. Am. Chem. Soc.* **2020**, *142*, 18971-18980.

[31] Y. Chen, Z. Fan, J. Wang, C. Ling, W. Niu, Z. Huang, G. Liu, B. Chen, Z. Lai, X. Liu, B. Li, Y. Zong, L. Gu, J. Wang, X. Wang, H. Zhang, *J. Am. Chem. Soc.* **2020**, *142*, 12760-12766.

[32] S. Liu, J. Xiao, X. F. Lu, J. Wang, X. Wang, X. W. D. Lou, *Angew. Chem. Int. Ed.* **2019**, *58*, 8499-8503.

[33] B. Zhang, S. Chen, B. Wulan, J. Zhang, *Chem. Eng. J.* **2021**, *421*, 130003.

[34] Y. Shi, Y. Ji, J. Long, Y. Liang, Y. Liu, Y. Yu, J. Xiao, B. Zhang, *Nat. Commun.* **2020**, *11*, 3415.

[35] W. Zhang, S. Yang, M. Jiang, Y. Hu, C. Hu, X. Zhang, Z. Jin, *Nano Lett.* **2021**, *21*, 2650-2657.

[36] Y. Wang, Y. Li, J. Liu, C. Dong, C. Xiao, L. Cheng, H. Jiang, H. Jiang, C. Li, *Angew. Chem. Int. Ed.* **2021**, *60*, 7681-7685.

[37] S. Liu, X. F. Lu, J. Xiao, X. Wang, X. W. D. Lou, *Angew. Chem. Int. Ed.* **2019**, *58*, 13828-13833.

[38] W. Guo, X. Tan, J. Bi, L. Xu, D. Yang, C. Chen, Q. Zhu, J. Ma, A. Tayal, J. Ma, Y. Huang, X. Sun, S. Liu, B. Han, *J. Am. Chem. Soc.* **2021**.

[39] Z. Zhang, F. Ahmad, W. Zhao, W. Yan, W. Zhang, H. Huang, C. Ma, J. Zeng, *Nano Lett.* **2019**, *19*, 4029-4034.

[40] X. Yuan, Y. Luo, B. Zhang, C. Dong, J. Lei, F. Yi, T. Duan, W. Zhu, R. He, *Chem. Commun.* **2020**, *56*, 4212.

[41] Y. Huang, X. Mao, G. Yuan, D. Zhang, B. Pan, J. Deng, Y. Shi, N. Han, C. Li, L. Zhang, L. Wang, L. He, Y. Li, Y. Li, *Angew. Chem. Int. Ed.* **2021**.

[42] Z. Yang, F. E. Oropeza, K. H. L. Zhang, *APL Mater.* **2020**, *8*, 060901.

[43] S. Liu, H. Tao, L. Zeng, Q. Liu, Z. Xu, Q. Liu, J. L. Luo, *J. Am. Chem. Soc.* **2017**, *139*, 2160-2163.

[44] N. Han, M. Sun, Y. Zhou, J. Xu, C. Cheng, R. Zhou, L. Zhang, J. Luo, B. Huang, Y. Li, *Adv. Mater.* **2021**, *33*, 2005821.

[45] Y. Chen, C. W. Li, M. W. Kanan, *J. Am. Chem. Soc.* **2012**, *134*, 19969-19972.

[46] H. Huang, H. Jia, Z. Liu, P. Gao, J. Zhao, Z. Luo, J. Yang, J. Zeng, *Angew. Chem. Int. Ed.* **2017**, *56*, 3594-3598.

[47] J. Wang, G. Wang, J. Zhang, Y. Wang, H. Wu, X. Zheng, J. Ding, X. Han, Y. Deng, W. Hu, *Angew. Chem. Int. Ed.* **2021**, *60*, 7602-7606.

[48] J. Xiao, M. R. Gao, S. Liu, J. L. Luo, *ACS Appl. Mater. Interfaces* **2020**, *12*, 31431-31438.

[49] T. Zheng, K. Jiang, H. Wang, *Adv. Mater.* **2018**, *30*, 1802066.

[50] B. Zhang, J. Zhang, *Journal of Energy Chemistry* **2017**, *26*, 1050-1066.

[51] H. Xie, T. Wang, J. Liang, Q. Li, S. Sun, *Nano Today* **2018**, *21*, 41-54.

[52] Z. Gu, H. Shen, L. Shang, X. Lv, L. Qian, G. Zheng, *Small Methods* **2018**, *2*, 1800121.

[53] S. Liu, C. Sun, J. Xiao, J.-L. Luo, *ACS Catal.* **2020**, *10*, 3158-3163.

[54] S. Liu, X.-Z. Wang, H. Tao, T. Li, Q. Liu, Z. Xu, X.-Z. Fu, J.-L. Luo, *Nano Energy* **2018**, *45*, 456-462.

[55] K. Qi, Y. Zhang, J. Li, C. Charmette, M. Ramonda, X. Cui, Y. Wang, Y. Zhang, H. Wu, W. Wang, X. Zhang, D. Voiry, *ACS Nano* **2021**, *15*, 7682-7693.

[56] W. Luo, Q. Zhang, J. Zhang, E. Moioli, K. Zhao, A. Züttel, *Appl. Catal. B-Environ.* **2020**, *273*, 119060.

[57] M. F. Philips, G.-J. M. Gruter, M. T. M. Koper, K. J. P. Schouten, *ACS Sustainable Chem. Eng.* **2020**, *8*, 15430-15444.

[58] Z. Chen, T. Fan, Y.-Q. Zhang, J. Xiao, M. Gao, N. Duan, J. Zhang, J. Li, Q. Liu, X. Yi, J.-L. Luo, *Appl. Catal. B-Environ.* **2020**, *261*, 118243.

[59] F. Lei, W. Liu, Y. Sun, J. Xu, K. Liu, L. Liang, T. Yao, B. Pan, S. Wei, Y. Xie, *Nat Commun* **2016**, *7*, 12697.

[60] Y. J. Ko, J. Y. Kim, W. H. Lee, M. G. Kim, T. Y. Seong, J. Park, Y. Jeong, B. K. Min, W. S. Lee, D. K. Lee, H. S. Oh, *Nat Commun* **2022**, *13*, 2205.

[61] B. Kumar, V. Atla, J. P. Brian, S. Kumari, T. Q. Nguyen, M. Sunkara, J. M. Spurgeon, *Angew. Chem. Int. Ed.* **2017**, *56*, 3645-3649.

[62] F. Li, L. Chen, G. P. Knowles, D. R. Macfarlane, J. Zhang, *Angew. Chem. Int. Ed.* **2017**, *129*, 520-524.

[63] G. Liu, Z. Li, J. Shi, K. Sun, Y. Ji, Z. Wang, Y. Qiu, Y. Liu, Z. Wang, P. Hu, *Appl. Catal. B-Environ.* **2020**, *260*, 118134.

[64] W. Ma, S. Xie, X. G. Zhang, F. Sun, J. Kang, Z. Jiang, Q. Zhang, D. Y. Wu, Y. Wang, *Nat. Commun.* **2019**, *10*, 892.

[65] P. Hou, X. Wang, P. Kang, *J. CO_2 Util.* **2021**, *45*, 101449.

[66] J. Feng, H. Gao, J. Feng, L. Liu, S. Zeng, H. Dong, Y. Bai, L. Liu, X. Zhang, *ChemCatChem* **2019**, *12*, 926-931.

[67] Z. Zhang, M. Chi, G. M. Veith, P. Zhang, D. A. Lutterman, J. Rosenthal, S. H. Overbury, S. Dai, H. Zhu, *ACS Catal.* **2016**, *6*, 6255-6264.

[68] L. Jia, M. Sun, J. Xu, X. Zhao, R. Zhou, B. Pan, L. Wang, N. Han, B. Huang, Y. Li, *Angew Chem Int Ed Engl* **2021**.

[69] Y. Jiang, X. Zhang, D. Xu, W. Li, M. Liu, X. Qiu, *Chemical Communications* **2021**.

[70] M. Fan, S. Prabhudev, S. Garbarino, J. Qiao, G. A. Botton, D. A. Harrington, A. C. Tavares, D. Guay, *Appl. Catal. B-Environ.* **2020**, *274*, 119031.

[71] J. H. Koh, D. H. Won, T. Eom, N.-K. Kim, K. D. Jung, H. Kim, Y. J. Hwang, B. K. Min, *ACS Catal.* **2017**, *7*, 5071-5077.

[72] S. X. Guo, Y. Zhang, X. Zhang, C. D. Easton, D. R. MacFarlane, J. Zhang, *ChemSusChem* **2019**, *12*, 1091-1100.

[73] F. Li, G. H. Gu, C. Choi, P. Kolla, S. Hong, T.-S. Wu, Y.-L. Soo, J. Masa, S. Mukerjee, Y. Jung, J. Qiu, Z. Sun, *Appl. Catal. B-Environ.* **2020**, *277*, 119241.

[74] J. Yang, X. Wang, Y. Qu, X. Wang, H. Huo, Q. Fan, J. Wang, L. M. Yang, Y. Wu, *Adv. Energy Mater.* **2020**, *10*, 2001709.

[75] Z. Chen, K. Mou, X. Wang, L. Liu, *Angew. Chem. Int. Ed.* **2018**, *57*, 12790-12794.

[76] P. Deng, F. Yang, Z. Wang, S. Chen, Y. Zhou, S. Zaman, B. Y. Xia, *Angew. Chem. Int. Ed.* **2020**, *59*, 10807-10813.

[77] M. Li, J. Wang, P. Li, K. Chang, C. Li, T. Wang, B. Jiang, H. Zhang, H. Liu, Y. Yamauchi, N. Umezawa, J. Ye, *Journal of Materials Chemistry A* **2016**, *4*, 4776-4782.

[78] K. Liu, M. Ma, L. Wu, M. Valenti, D. Cardenas-Morcoso, J. P. Hofmann, J. Bisquert, S. Gimenez, W. A. Smith, *ACS Appl Mater Interfaces* **2019**.

[79] J. Choi, M. J. Kim, S. H. Ahn, I. Choi, J. H. Jang, Y. S. Ham, J. J. Kim, S.-K. Kim, *Chemical Engineering Journal* **2016**, *299*, 37-44.

[80] S. N. Zhang, M. Li, B. Hua, N. Duan, S. Ding, S. Bergens, K. Shankar, J. L. Luo, *ChemCatChem* **2019**, *11*, 4147-4153.

[81] L. Peng, Y. Wang, Y. Wang, N. Xu, W. Lou, P. Liu, D. Cai, H. Huang, J. Qiao, *Appl. Catal. B-Environ.* **2021**, 120003.

[82] X. Zhang, X. Sun, S.-X. Guo, A. M. Bond, J. Zhang, *Energy & Environmental Science* **2019**, *12*, 1334-1340.

[83] X. An, S. Li, A. Yoshida, T. Yu, Z. Wang, X. Hao, A. Abudula, G. Guan, *ACS Appl Mater Interfaces* **2019**, *11*, 42114-42122.

[84] Y. Wang, Z. Chen, P. Han, Y. Du, Z. Gu, X. Xu, G. Zheng, *ACS Catalysis* **2018**, *8*, 7113-7119.

[85] Y. Feng, Z. Li, H. Liu, C. Dong, J. Wang, S. A. Kulinich, X. Du, *Langmuir* **2018**, *34*, 13544-13549.

[86] Y. Peng, T. Wu, L. Sun, J. M. V. Nsanzimana, A. C. Fisher, X. Wang, *ACS Appl Mater Interfaces* **2017**, *9*, 32782-32789.

[87] X. Li, J. Yu, M. Jaroniec, X. Chen, *Chem Rev* **2019**, *119*, 3962-4179.

[88] Y. Li, M. Zhang, L. Zhou, S. Yang, Z. Wu, Y. Ma, *Acta Physico Chimica Sinica* **2020**, *0*, 2009030-2009030.

[89] L. Cheng, D. Zhang, Y. Liao, J. Fan, Q. Xiang, *Chinese Journal of Catalysis* **2021**, *42*, 131-140.

[90] J. Qiao, Y. Liu, F. Hong, J. Zhang, *Chem. Soc. Rev.* **2014**, *43*, 631-675.

[91] C. Xu, J. Hong, P. Sui, M. Zhu, Y. Zhang, J.-L. Luo, *Cell Reports Physical Science* **2020**, *1*, 100101.

[92] R. Francke, B. Schille, M. Roemelt, *Chem. Rev.* **2018**, *118*, 4631-4701.

[93] C. Chen, J. F. Khosrowabadi Kotyk, S. W. Sheehan, *Chem* **2018**, *4*, 2571-2586.

[94] M. G. Kibria, J. P. Edwards, C. M. Gabardo, C. T. Dinh, A. Seifitokaldani, D. Sinton, E. H. Sargent, *Adv. Mater.* **2019**, *31*, 1807166.

[95] Z. Chen, M.-R. Gao, N. Duan, J. Zhang, Y.-Q. Zhang, T. Fan, J. Zhang, Y. Dong, J. Li, Q. Liu, X. Yi, J.-L. Luo, *Appl. Catal. B-Environ.* **2020**, *277*, 119252.

[96] C. Costentin, M. Robert, J. M. Saveant, *Chem. Soc. Rev.* **2013**, *42*, 2423-2436.

[97] Y. Hou, Y.-L. Liang, P.-C. Shi, Y.-B. Huang, R. Cao, *Appl. Catal. B-Environ.* **2020**, *271*, 118929.

[98] J.-H. Kim, H. Woo, S.-W. Yun, H.-W. Jung, S. Back, Y. Jung, Y.-T. Kim, *Appl. Catal. B-Environ.* **2017**, *213*, 211-215.

[99] K. Liu, J. Wang, M. Shi, J. Yan, Q. Jiang, *Advanced Energy Materials* **2019**, *9*, 1900276.

[100] W. Luo, J. Zhang, M. Li, A. Züttel, *ACS Catalysis* **2019**, *9*, 3783-3791.

[101] A. Bagger, W. Ju, A. S. Varela, P. Strasser, J. Rossmeisl, *Chemphyschem* **2017**, *18*, 3266-3273.

[102] X. Su, Y. Sun, L. Jin, L. Zhang, Y. Yang, P. Kerns, B. Liu, S. Li, J. He, *Appl. Catal. B-Environ.* **2020**, *269*, 118800.

[103] Q. Zhu, X. Sun, D. Yang, J. Ma, X. Kang, L. Zheng, J. Zhang, Z. Wu, B. Han, *Nat Commun* **2019**, *10*, 3851.

[104] D. Wakerley, S. Lamaison, F. Ozanam, N. Menguy, D. Mercier, P. Marcus, M. Fontecave, V. Mougel, *Nat. Mater.* **2019**, *18*, 1222-1227.

[105] C. Choi, T. Cheng, M. Flores Espinosa, H. Fei, X. Duan, W. A. Goddard, Y. Huang, *Adv. Mater.* **2019**, *31*, 1805405.

[106] D. Wu, G. Huo, W. Chen, X.-Z. Fu, J.-L. Luo, *Appl. Catal. B-Environ.* **2020**, *271*, 118957.

[107] R. Hegner, L. F. M. Rosa, F. Harnisch, *Appl. Catal. B-Environ.* **2018**, *238*, 546-556.

[108] D. D. Zhu, J. L. Liu, S. Z. Qiao, *Adv. Mater.* **2016**, *28*, 3423-3452.

[109] B. E. Conway, G. Jerkiewicz, *Electrochimica Acta* **2000**, *45*, 4075-4083.

[110] P. Devi, K. Malik, E. Arora, S. Bhattacharya, V. Kalendra, K. V. Lakshmi, A. Verma, J. P. Singh, *Catalysis Science & Technology* **2019**, *9*, 5339-5349.

[111] W. Luo, W. Xie, R. Mutschler, E. Oveisi, G. L. De Gregorio, R. Buonsanti, A. Züttel, *ACS Catalysis* **2018**, *8*, 6571-6581.

[112] H. Xiang, S. Rasul, B. Hou, J. Portoles, P. Cumpson, E. H. Yu, *ACS Appl Mater Interfaces* **2020**, *12*, 601-608.

[113] J.Y.Kim, J. A. Rodriguez, J. C. Hanson, A. I. Frenkel, P. L. Lee, *J. Am. Chem. Soc.* **2003**, *125*, 10684-10692.

[114] X. Wang, J. C. Hanson, A. I. Frenkel, J. Y. Kim, J. A. Rodriguez, *J. Phys. Chem. B* **2004**, *108*, 13667-13673.

[115] J. F. Xu, W. Ji, Z. X. Shen, W. S. Li, S. H. Tang, X. R. Ye, X. Q. Xin, *J. Raman Spectrosc.* **1999**, *30*, 413-415.

[116] H. Zhu, X. Wang, F. Yang, X. Yang, *Cryst. Growth Des.* **2008**, *8*, 950-956.

[117] T. Li, H. Wei, T. Liu, G. Zheng, S. Liu, J. L. Luo, *ACS. Appl. Mater. Interfaces* **2019**, *11*, 22346-22351.

[118] F. L. P. Veenstra, A. J. Martin, J. Perez-Ramirez, *ChemSusChem* **2019**, *12*, 3501-3508.

[119] Y. J. Jang, J. Lee, J. H. Kim, B. J. Lee, J. S. Lee, *Journal of Power Sources* **2018**, *378*, 412-417.

[120] G. O. Barasa, T. Yu, X. Lu, X. Zhou, H. Wang, L. Qian, Y. Yu, L. Liu, P. Lei, *Electrochim. Acta* **2019**, *295*, 584-590.

[121] P. De Luna, R. Quintero-Bermudez, C.-T. Dinh, M. B. Ross, O. S. Bushuyev, P. Todorović, T. Regier, S. O. Kelley, P. Yang, E. H. Sargent, *Nat. Catal.* **2018**, *1*, 103-110.

[122] H. Mistry, A. S. Varela, C. S. Bonifacio, I. Zegkinoglou, I. Sinev, Y. W. Choi, K. Kisslinger, E. A. Stach, J. C. Yang, P. Strasser, B. R. Cuenya, *Nat. Commun.* **2016**, *7*, 12123.

[123] Y. Chen, M. W. Kanan, *J. Am. Chem. Soc.* **2012**, *134*, 1986-1989.

[124] X. Zhang, Z. Chen, M. Jiao, X. Ma, K. Mou, F. Cheng, Z. Wang, X. Zhang, L. Liu, *Appl. Catal. B-Environ.* **2020**, *279*, 119383.

[125] C. W. Lee, N. H. Cho, S. W. Im, M. S. Jee, Y. J. Hwang, B. K. Min, K. T. Nam, *J. Mater. Chem. A* **2018**, *6*, 14043-14057.

[126] L. Zhang, Z. J. Zhao, J. Gong, *Angew. Chem. Int. Ed.* **2017**, *56*, 11326-11353.

[127] G. Kresse, J. Hafner, *Phys. Rev. B* **1993**, *47*, 558-561.

[128] G. Kresse, J. Hafner, *Phys. Rev. B* **1994**, *49*, 14251-14269.

[129] G. Kresse, J. Furthmüller, *Phys. Rev. B* **1996**, *54*, 11169-11186.

[130] B. Hammer, L. B. Hansen, J. K. Nørskov, *Phys. Rev. B* **1999**, *59*, 7413-7421.

[131] T. Vo, K. Purohit, C. Nguyen, B. Biggs, S. Mayoral, J. L. Haan, *ChemSusChem* **2015**, *8*, 3853-3858.

[132] A. S. Agarwal, Y. Zhai, D. Hill, N. Sridhar, *ChemSusChem* **2011**, *4*, 1301-1310.

[133] F. Li, L. Chen, G. P. Knowles, D. R. MacFarlane, J. Zhang, *Angew. Chem. Int. Ed.* **2017**, *56*, 505-509.

[134] X. Liu, Y. Jiao, Y. Zheng, M. Jaroniec, S. Z. Qiao, *J. Am. Chem. Soc.* **2019**, *141*, 9664-9672.

[135] Q. Zhu, J. Ma, X. Kang, X. Sun, H. Liu, J. Hu, Z. Liu, B. Han, *Angew. Chem. Int. Ed.* **2016**, *55*, 9012-9016.

[136] M. J. W. Blom, V. Smulders, W. P. M. van Swaaij, S. R. A. Kersten, G. Mul, *Appl. Catal. B-Environ.* **2020**, *268*, 118420.

[137] H. W. Yoshio Hori, Toshio Tsukamoto, Osamu, Koga, *Electrochim. Acta* **1994**, *39*, 1833-1839.

[138] Z. Chen, N. Wang, S. Yao, L. Liu, *J. CO_2 Util.* **2017**, *22*, 191-196.

[139]   T. Tran-Phu, R. Daiyan, Z. Fusco, Z. Ma, R. Amal, A. Tricoli, *Adv. Funct. Mater.* **2019**, *30*, 1906478.

[140]   X. Zhang, T. Lei, Y. Liu, J. Qiao, *Appl. Catal. B-Environ.* **2017**, *218*, 46-50.

[141]   C. W. Lee, J. S. Hong, K. D. Yang, K. Jin, J. H. Lee, H.-Y. Ahn, H. Seo, N.-E. Sung, K. T. Nam, *ACS Catal.* **2018**, *8*, 931-937.

[142]   H. Ju, G. Kaur, A. P. Kulkarni, S. Giddey, *J. CO$_2$ Util.* **2019**, *32*, 178-186.

[143]   B. Endrődi, G. Bencsik, F. Darvas, R. Jones, K. Rajeshwar, C. Janáky, *Prog. Energy Combust. Sci.* **2017**, *62*, 133-154.

[144]   Y. J. Sa, C. W. Lee, S. Y. Lee, J. Na, U. Lee, Y. J. Hwang, *Chem. Soc. Rev.* **2020**, *49*, 6632-6665.

[145]   D. Wu, W. Chen, X. Wang, X.-Z. Fu, J.-L. Luo, *J. CO$_2$ Util.* **2020**, *37*, 353-359.

[146]   X. Zhang, J. Fu, Y. Liu, X.-D. Zhou, J. Qiao, *ACS Sustain. Chem. Eng.* **2020**, *8*, 4871-4876.

[147]   H. Li, C. Chen, D. Yan, Y. Wang, R. Chen, Y. Zou, S. Wang, *J. Mater. Chem. A* **2019**.

[148]   F. Pan, Y. Yang, *Energy Environ. Sci.* **2020**, *13*, 2275-2309.

[149]   A. Vasileff, C. Xu, Y. Jiao, Y. Zheng, S.-Z. Qiao, *Chem* **2018**, *4*, 1809-1831.

[150]   Z. Niu, C. Qiu, J. Jiang, L. Ai, *ACS Sustain. Chem. Eng.* **2018**, *7*, 2335-2342.

[151]   L. An, Z. Zhang, J. Feng, F. Lv, Y. Li, R. Wang, M. Lu, R. B. Gupta, P. Xi, S. Zhang, *J. Am. Chem. Soc.* **2018**, *140*, 17624-17631.

[152]   Y. Liu, X. Luo, C. Zhou, S. Du, D. Zhen, B. Chen, J. Li, Q. Wu, Y. Iru, D. Chen, *Appl. Catal. B-Environ.* **2020**, *260*, 118197.

[153]   K. Chu, Y. P. Liu, Y. B. Li, Y. L. Guo, Y. Tian, *ACS Appl. Mater. Interfaces* **2020**, *12*, 7081-7090.

[154]   Y. Wang, L. Cheng, J. Liu, C. Xiao, B. Zhang, Q. Xiong, T. Zhang, Z. Jiang, H. Jiang, Y. Zhu, Y. Li, C. Li, *ChemElectroChem* **2020**, *7*, 2864-2868.

[155]   D. Wu, X. Wang, X.-Z. Fu, J.-L. Luo, *Appl. Catal. B-Environ.* **2021**, *284*, 119723.

[156]   P. Deng, H. Wang, R. Qi, J. Zhu, S. Chen, F. Yang, L. Zhou, K. Qi, H. Liu, B. Y. Xia, *ACS Catal.* **2019**, *10*, 743-750.

[157]   K. Liu, W. A. Smith, T. Burdyny, *ACS Energy Lett.* **2019**, *4*, 639-643.

[158]   Z.-Z. Wu, F.-Y. Gao, M.-R. Gao, *Energy Environ. Sci.* **2021**, *14*, 1121-1139.

[159]   E. Pineda, M. E. Nicho, P. K. Nair, H. Hu, *Sol. Energy* **2012**, *86*, 1017-1022.

[160] Y. Huang, W. Wang, Q. Zhang, J. J. Cao, R. J. Huang, W. Ho, S. C. Lee, *Sci. Rep.* **2016**, *6*, 23435.

[161] Yong Xu, M. A. A. Schoonen, *Am. Mineral* **2000**, *85*, 543-556.

[162] Y. Xing, X. Kong, X. Guo, Y. Liu, Q. Li, Y. Zhang, Y. Sheng, X. Yang, Z. Geng, J. Zeng, *Adv. Sci.* **2020**, 1902989.

[163] Q. Yang, Q. Wu, Y. Liu, S. Luo, X. Wu, X. Zhao, H. Zou, B. Long, W. Chen, Y. Liao, L. Li, P. K. Shen, L. Duan, Z. Quan, *Adv Mater* **2020**, e2002822.

[164] F. L. Meng, Q. Zhang, Y. X. Duan, K. H. Liu, X. B. Zhang, *Chinese Journal of Chemistry* **2020**, *38*, 1752-1756.

[165] Y.-R. Wang, R.-X. Yang, Y. Chen, G.-K. Gao, Y.-J. Wang, S.-L. Li, Y.-Q. Lan, *Science Bulletin* **2020**, *65*, 1635-1642.

[166] Q. Gong, P. Ding, M. Xu, X. Zhu, M. Wang, J. Deng, Q. Ma, N. Han, Y. Zhu, J. Lu, Z. Feng, Y. Li, W. Zhou, Y. Li, *Nature Communications* **2019**, *10*, 2807.

[167] Y. Liang, W. Zhou, Y. Shi, C. Liu, B. Zhang, *Science Bulletin* **2020**, *65*, 1547-1554.

[168] Z. Li, A. Cao, Q. Zheng, Y. Fu, T. Wang, K. T. Arul, J. L. Chen, B. Yang, N. M. Adli, L. Lei, C. L. Dong, J. Xiao, G. Wu, Y. Hou, *Adv Mater* **2020**, e2005113.

[169] W. Zhang, Y. Hu, L. Ma, G. Zhu, P. Zhao, X. Xue, R. Chen, S. Yang, J. Ma, J. Liu, Z. Jin, *Nano Energy* **2018**, *53*, 808-816.

[170] L. Zhou, R. Lv, *J. Energy Chem.* **2022**, *70*, 310-331.

[171] S. Overa, B. H. Ko, Y. Zhao, F. Jiao, *Acc. Chem. Res.* **2022**, *55*, 638-648.

[172] H. Liu, Y. Zhu, J. Ma, Z. Zhang, W. Hu, *Adv. Funct. Mater.* **2020**, *30*, 1910534.

[173] T.-J. Wang, W.-S. Fang, Y.-M. Liu, F.-M. Li, P. Chen, Y. Chen, *J. Energy Chem.* **2022**, *70*, 407-413.

[174] M. Azuma, K. Hashimoto, M. Hiramoto, M. Watanabe, T. Sakata, *J. Electrochem. Soc.* **1990**, *137*, 1772-1778.

[175] J. Xiao, S. Liu, P.-F. Sui, C. Xu, L. Gong, H. Zeng, J.-L. Luo, *Chem. Eng. J.* **2022**, *433*, 133785.

[176] F. Cheng, X. Zhang, K. Mu, X. Ma, M. Jiao, Z. Wang, P. Limpachanangkul, B. Chalermsinsuwan, Y. Gao, Y. Li, Z. Chen, L. Liu, *Energy Technol.* **2021**, *9*, 2000799.

[177] Y. Guan, M. Liu, X. Rao, Y. Liu, J. Zhang, *J. Mater. Chem. A* **2021**, *9*, 13770-13803.

[178] K. Fan, Y. Jia, Y. Ji, P. Kuang, B. Zhu, X. Liu, J. Yu, *ACS Catal.* **2019**, *10*, 358-364.

[179] P. F. Sui, C. Xu, M. N. Zhu, S. Liu, Q. Liu, J. L. Luo, *Small* **2021**, e2105682.

[180] X. Jiang, X. Wang, Q. Wang, X. Xiao, J. Chen, M. Wang, Y. Shen, *ACS Appl. Energy Mater.* **2021**, *4*, 2073-2080.

[181] R. M. Aran-Ais, D. Gao, B. Roldan Cuenya, *Acc. Chem. Res.* **2018**, *51*, 2906-2917.

[182] M. Konig, J. Vaes, E. Klemm, D. Pant, *iScience* **2019**, *19*, 135-160.

[183] M. F. Baruch, J. E. Pander, J. L. White, A. B. Bocarsly, *ACS Catal.* **2015**, *5*, 3148-3156.

[184] J. E. Pander, M. F. Baruch, A. B. Bocarsly, *ACS Catal.* **2016**, *6*, 7824-7833.

[185] Z. M. Detweiler, J. L. White, S. L. Bernasek, A. B. Bocarsly, *Langmuir* **2014**, *30*, 7593-7600.

[186] L. Chen, R. Huang, S.-F. Yin, S.-L. Luo, C.-T. Au, *Chem. Eng. J.* **2012**, *193-194*, 123-130.

[187] Y. Wang, B. Wang, W. Jiang, Z. Liu, J. Zhang, L. Gao, W. Yao, *Nano Res.* **2021**, *15*, 2919-2927.

[188] L. G. Puppin, M. Khalid, G. T. T. da Silva, C. Ribeiro, H. Varela, O. F. Lopes, *J. Mater. Res.* **2020**, *35*, 272-280.

[189] T. Fan, W. Ma, M. Xie, H. Liu, J. Zhang, S. Yang, P. Huang, Y. Dong, Z. Chen, X. Yi, *Cell Reports Physical Science* **2021**, 100353.

[190] W. Lv, J. Bei, R. Zhang, W. Wang, F. Kong, L. Wang, W. Wang, *ACS Omega* **2017**, *2*, 2561-2567.

[191] Y. Cheng, P. Hou, X. Wang, P. Kang, *Acc. Chem. Res.* **2022**, *55*, 231-240.

[192] H. Rabiee, L. Ge, X. Zhang, S. Hu, M. Li, Z. Yuan, *Energy Environ. Sci.* **2021**, *14*, 1959-2008.

[193] K. Yang, R. Kas, W. A. Smith, T. Burdyny, *ACS Energy Lett.* **2020**, 33-40.

[194] R. I. Masel, Z. Liu, H. Yang, J. J. Kaczur, D. Carrillo, S. Ren, D. Salvatore, C. P. Berlinguette, *Nat. Nanotechnol.* **2021**, *16*, 118-128.

[195] Y. Yang, L. Ohnoutek, S. Ajmal, X. Zheng, Y. Feng, K. Li, T. Wang, Y. Deng, Y. Liu, D. Xu, V. K. Valev, L. Zhang, *J. Mater. Chem. A* **2019**, *7*, 11836-11846.

[196] C. Xu, X. Zhang, M.-N. Zhu, L. Zhang, P.-F. Sui, R. Feng, Y. Zhang, J.-L. Luo, *Appl. Catal. B-Environ.* **2021**, *298*, 120533.

[197] J. Baltrusaitis, J. Schuttlefield, E. Zeitler, V. H. Grassian, *Chem. Eng. J.* **2011**, *170*, 471-481.

[198] I. V. Chernyshova, P. Somasundaran, S. Ponnurangam, *Proc. Natl. Acad. Sci.* **2018**, *115*, E9261-E9270.

[199] C. He, S. Chen, R. Long, L. Song, Y. Xiong, *Sci. China Chem.* **2020**, *63*, 1721-1726.

[200] A. M. Ismail, G. F. Samu, Á. Balog, E. Csapó, C. Janáky, *ACS Energy Lett.* **2018**, *4*, 48-53.

[201] L. Li, X. Li, Y. Sun, Y. Xie, *Chem. Soc. Rev.* **2022**, *51*, 1234.

[202] Y. Wang, P. Han, X. Lv, L. Zhang, G. Zheng, *Joule* **2018**, *2*, 2551-2582.

[203] Q. Wang, y. lei, D. Wang, Y. Li, *Energy Environ. Sci.* **2019**, *12*, 1730-1750.

[204] Z. Wu, Y. Zhao, W. Jin, B. Jia, J. Wang, T. Ma, *Adv. Funct. Mater.* **2020**, 2009070.

[205] Q. Lu, A. L. Wang, H. Cheng, Y. Gong, Q. Yun, N. Yang, B. Li, B. Chen, Q. Zhang, Y. Zong, L. Gu, H. Zhang, *Small* **2018**, *14*, e1801090.

[206] J. Kim, Y. Lee, S. Sun, *J. Am. Chem. Soc.* **2010**, *132*, 4996-4997.

[207] Z. Fan, M. Bosman, Z. Huang, Y. Chen, C. Ling, L. Wu, Y. A. Akimov, R. Laskowski, B. Chen, P. Ercius, J. Zhang, X. Qi, M. H. Goh, Y. Ge, Z. Zhang, W. Niu, J. Wang, H. Zheng, H. Zhang, *Nat. Commun.* **2020**, *11*, 3293.

[208] H. Cheng, N. Yang, G. Liu, Y. Ge, J. Huang, Q. Yun, Y. Du, C. J. Sun, B. Chen, J. Liu, H. Zhang, *Adv. Mater.* **2020**, *32*, e1902964.

[209] X. Zhou, Y. Ma, Y. Ge, S. Zhu, Y. Cui, B. Chen, L. Liao, Q. Yun, Z. He, H. Long, L. Li, B. Huang, Q. Luo, L. Zhai, X. Wang, L. Bai, G. Wang, Z. Guan, Y. Chen, C. S. Lee, J. Wang, C. Ling, M. Shao, Z. Fan, H. Zhang, *J. Am. Chem. Soc.* **2022**, *144*, 547-555.

[210] M. Zhou, J. Liu, C. Ling, Y. Ge, B. Chen, C. Tan, Z. Fan, J. Huang, J. Chen, Z. Liu, Z. Huang, J. Ge, H. Cheng, Y. Chen, L. Dai, P. Yin, X. Zhang, Q. Yun, J. Wang, H. Zhang, *Adv. Mater.* **2022**, *34*, e2106115.

[211] S. Q. Liu, E. Shahini, M. R. Gao, L. Gong, P. F. Sui, T. Tang, H. Zeng, J. L. Luo, *ACS Nano* **2021**, *15*, 17757-17768.

[212] H. Cheng, B. Huang, J. Lu, Z. Wang, B. Xu, X. Qin, X. Zhang, Y. Dai, *Phys. Chem. Chem. Phys* **2010**, *12*, 15468-15475.

[213] P. F. Sui, M. R. Gao, S. Liu, C. Xu, M. N. Zhu, J. L. Luo, *Adv. Funct. Mater.* **2022**, 2203794.

[214]   Y. Shi, C. F. Wen, X. Wu, J. Y. Zhao, F. Mao, P. F. Liu, H. G. Yang, *Mater. Chem. Front.* **2022**, *6*, 1091-1097.

[215]   S.-Q. Liu, M.-R. Gao, R.-F. Feng, L. Gong, H. Zeng, J.-L. Luo, *ACS Catal.* **2021**, *11*, 7604-7612.

[216]   S. Zhang, P. Kang, T. J. Meyer, *J. Am. Chem. Soc.* **2014**, *136*, 1734-1737.

[217]   P.-F. Sui, S. Liu, C. Xu, J. Xiao, N. Duan, R. Feng, J.-L. Luo, *Chem. Eng. J.* **2022**, *427*, 131654.

[218]   R. Daiyan, W. H. Saputera, Q. Zhang, E. Lovell, S. Lim, Y. H. Ng, X. Lu, R. Amal, *Adv. Sustain. Syst.* **2018**, *3*, 1800064.

[219]   T. Liu, C. Xi, C. Dong, C. Cheng, J. Qin, S. Hu, H. Liu, X.-W. Du, *J. Phys. Chem. C* **2019**, *123*, 28319-28326.

[220]   P. Gayen, S. Saha, K. Bhattacharyya, V. K. Ramani, *ACS Catal.* **2020**, *10*, 7734-7746.

[221]   C. Zhan, F. Dattila, C. Rettenmaier, A. Bergmann, S. Kuhl, R. Garcia-Muelas, N. Lopez, B. R. Cuenya, *ACS Catal.* **2021**, *11*, 7694-7701.

[222]   E. Zhang, T. Wang, K. Yu, J. Liu, W. Chen, A. Li, H. Rong, R. Lin, S. Ji, X. Zheng, Y. Wang, L. Zheng, C. Chen, D. Wang, J. Zhang, Y. Li, *J. Am. Chem. Soc.* **2019**, *141*, 16569-16573.

[223]   T. Burdyny, W. A. Smith, *Energy Environ. Sci.* **2019**, *12*, 1442-1453.

[224]   T. Gunji, H. Ochiai, T. Ohira, Y. Liu, Y. Nakajima, F. Matsumoto, *Chem. Mater.* **2020**, *32*, 6855-6863.

[225]   C. H. Lee, M. W. Kanan, *ACS Catal.* **2014**, *5*, 465-469.

[226]   Y. Qiu, J. Du, W. Dong, C. Dai, C. Tao, *J. CO$_2$ Util.* **2017**, *20*, 328-335.

[227]   F. P. Garcia de Arquer, O. S. Bushuyev, P. De Luna, C. T. Dinh, A. Seifitokaldani, M. I. Saidaminov, C. S. Tan, L. N. Quan, A. Proppe, M. G. Kibria, S. O. Kelley, D. Sinton, E. H. Sargent, *Adv. Mater.* **2018**, *30*, e1802858.

[228]   W. Ma, J. Bu, Z. Liu, C. Yan, Y. Yao, N. Chang, H. Zhang, T. Wang, J. Zhang, *Adv. Funct. Mater.* **2020**, 2006704.

[229]   A. Guan, C. Yang, Y. Quan, H. Shen, N. Cao, T. Li, Y. Ji, G. Zheng, *Chem. Asian J.* **2019**, *14*, 3969-3980.

[230]   S. P. Paula, M. Stefano, E. L. S. Ifan, E. E. María, *ChemCatChem* **2019**, *11*, 1-21.

[231] P. Lamagni, M. Miola, J. Catalano, M. S. Hvid, M. A. H. Mamakhel, M. Christensen, M. R. Madsen, H. S. Jeppesen, X. M. Hu, K. Daasbjerg, T. Skrydstrup, N. Lock, *Adv. Funct. Mater.* **2020**, 1910408.

[232] A. Wuttig, Y. Yoon, J. Ryu, Y. Surendranath, *J. Am. Chem. Soc.* **2017**, *139*, 17109-17113.

[233] P. Yue, Q. Fu, J. Li, L. Zhang, L. Xing, Z. Kang, Q. Liao, X. Zhu, *Chem. Eng. J.* **2021**, *405*, 126975.

[234] Z. Xing, L. Hu, D. S. Ripatti, X. Hu, X. Feng, *Nat. Commun.* **2021**, *12*, 136.

[235] Z. Cai, Y. Zhang, Y. Zhao, Y. Wu, W. Xu, X. Wen, Y. Zhong, Y. Zhang, W. Liu, H. Wang, Y. Kuang, X. Sun, *Nano Res.* **2018**, *12*, 345-349.

[236] M. Alfath, C. W. Lee, *Catalysts* **2020**, *10*, 859.

[237] Y. Yoon, A. S. Hall, Y. Surendranath, *Angew. Chem. Int. Ed.* **2016**, *55*, 15282-15286.

[238] A. Chen, B.-L. Lin, *Joule* **2018**, *2*, 594-606.

[239] X. Tan, C. Yu, X. Song, C. Zhao, S. Cui, H. Xu, J. Chang, W. Guo, Z. Wang, Y. Xie, J. Qiu, *Adv. Energy Mater.* **2021**, 2100075.

[240] H. J. Monkhorst, J. D. Pack, *Phys. Rev. B* **1976**, *13*, 5188-5192.

[241] V. Tripković, E. Skúlason, S. Siahrostami, J. K. Nørskov, J. Rossmeisl, *Electrochim. Acta* **2010**, *55*, 7975-7981.

[242] C. J. Cramer, Essentials of computational chemistry: theories and models, John Wiley & Sons, England, **2013**.

[243] W. J. Durand, A. A. Peterson, F. Studt, F. Abild-Pedersen, J. K. Nørskov, *Surf. Sci.* **2011**, *605*, 1354-1359.

[244] S.-F. Tang, X.-L. Lu, C. Zhang, Z.-W. Wei, R. Si, T.-B. Lu, *Sci. Bull.* **2021**, *66*, 1533-1541.

[245] X. Wang, W. Wang, J. Zhang, H. Wang, Z. Yang, H. Ning, J. Zhu, Y. Zhang, L. Guan, X. Teng, Q. Zhao, M. Wu, *Chem. Eng. J.* **2021**, *426*, 131867.

[246] Z. Wang, Y. Zhou, C. Xia, W. Guo, B. You, B. Y. Xia, *Angew. Chem. Int. Ed.* **2021**, *60*, 19107-19112.

[247] J. Wang, S. Ning, M. Luo, D. Xiang, W. Chen, X. Kang, Z. Jiang, S. Chen, *Appl. Catal. B-Environ.* **2021**, *288*, 119979.

[248] J. Zou, C. Y. Lee, G. G. Wallace, *Adv. Sci.* **2021**, *8*, e2004521.

[249]   S. Ning, J. Wang, D. Xiang, S. Huang, W. Chen, S. Chen, X. Kang, *J. Catal.* **2021**, *399*, 67-74.

[250]   L. P. Chi, Z. Z. Niu, X. L. Zhang, P. P. Yang, J. Liao, F. Y. Gao, Z. Z. Wu, K. B. Tang, M. R. Gao, *Nat. Commun.* **2021**, *12*, 5835.

[251]   L.-X. Liu, Y. Zhou, Y.-C. Chang, J.-R. Zhang, L.-P. Jiang, W. Zhu, Y. Lin, *Nano Energy* **2020**, *77*, 105296.

[252]   C. Xia, P. Zhu, Q. Jiang, Y. Pan, W. Liang, E. Stavitski, H. N. Alshareef, H. Wang, *Nat. Energy* **2019**, *4*, 776-785.

[253]   X. Feng, H. Zou, R. Zheng, W. Wei, R. Wang, W. Zou, G. Lim, J. Hong, L. Duan, H. Chen, *Nano Lett* **2022**.

[254]   K. Yao, H. Wang, X. Yang, Y. Huang, C. Kou, T. Jing, S. Chen, Z. Wang, Y. Liu, H. Liang, *Appl. Catal. B* **2022**, *311*, 121377.

[255]   Z. Liu, X. Lv, J. Zhang, A. Guan, C. Yang, S. Yan, Y. Chen, K. Liu, G. Zheng, *Adv. Mater. Interfaces* **2022**, *9*, 2101956.